UNIVERSIDADE DE BRASÍLIA

INSTITUTO DE GEOCIÊNCIAS

PROGRAMA DE PÓS-GRADUAÇÃO EM GEOLOGIA

PROVENIÊNCIA SEDIMENTAR DO INTERVALO DEVONIANO – CARBONÍFERO DA BACIA SUBANDINA DE TARIJA (BOLÍVIA) E A RELAÇÃO COM AS BACIAS DO SETOR SW DE GONDWANA

Dissertação de Mestrado
N° 479

Arnold David García Zavaleta

Brasília – DF
2021

UNIVERSIDADE DE BRASÍLIA

INSTITUTO DE GEOCIÊNCIAS

PROGRAMA DE PÓS-GRADUAÇÃO EM GEOLOGIA

PROVENIÊNCIA SEDIMENTAR DO INTERVALO DEVONIANO – CARBONÍFERO DA BACIA SUBANDINA DE TARIJA (BOLÍVIA) E A RELAÇÃO COM AS BACIAS DO SETOR SW DE GONDWANA

Dissertação de Mestrado
N° 479

Arnold David García Zavaleta

Dissertação submetida à Coordenação do Programa de Pós-graduação em Geologia da Universidade de Brasília, como requisito parcial para a obtenção de grau de Mestre em Geologia.

Área de concentração: Geologia Regional

Orientadora:

Profa. Dra. Natalia Hauser

Co-Orientador:

Prof. Dr. Martin B. Roddaz

Comissão Examinadora:

Prof. Dr. Heinrich Bahlburg (Institute of Geology and Palaentology – Alemanha)

Prof. Dr. Carlos José Souza de Alvarenga (Instituto de Geociências - UnB)

Brasília-DF

Julho, 2021

Ficha catalográfica elaborada automaticamente,
com os dados fornecidos pelo(a) autor(a)

García Zavaleta, Arnold David
GG216pp Proveniência sedimentar do intervalo Devoniano - Carbonífero da Bacia Subandina de Tarija (Bolívia) e a relação com as Bacias do setor SW de Gondwana / Arnold David García Zavaleta; orientador Natalia Hauser; co-orientador Martin Roddaz. -- Brasília, 2021.
162 p.

Dissertação (Mestrado - Mestrado em Geologia) -- Universidade de Brasília, 2021.

1. Proveniência. 2. Bacia de Tarija. 3. Devoniano - Carbonífero. 4. Subandino Boliviano . 5. SW de Gondwana. I. Hauser, Natalia, orient. II. Roddaz, Martin, co-orient. III. Título.

AGRADECIMENTOS

- Primeiramente, gostaria de agradecer à minha família pela confiança, o carinho e por todo o suporte emocional no tempo que fiquei morando longe de casa.
- Um agradecimento muito especial para minha orientadora Dra. Natalia Hauser e para meu co-orientador Dr. Martin Roddaz pela confiança e todas as sugestões durante a realização desse trabalho.
- Ao Instituto de Geociências da Universidade de Brasília por me aceitar no programa de pós-graduação e ao Laboratório de Estudos Geodinâmicos, Geocronológicos e Ambientais (LEGGA) pelo apoio e financiamento.
- Agradeço ao equipe do LEGGA, em especial aos professores Natalia Hauser, Roberto Ventura, Guilherme Gonçalves, Elton Dantas, e colegas Gabriel Moizinho, Michele Andriolli e Mariana Rodrigues.
- Ao Dr. Patrice Baby e aos colegas do YPFB pelo apoio nos trabalhos de campo na Bolívia.
- À Dra. Pamela Aparicio Gonzalez e ao *Instituto de Geocronología y Geología Isotópica (INGEIS)* da *Universidad de Buenos Aires*, pelas análises de difratometria de raios-X.
- À banca examinadora, que contribuiu para melhorar e amadurecer essa dissertação de mestrado.
- Um agradecimento especial para todos os amigos que conheci em Brasília, que fizeram a minha estadia mais agradável.
- O presente trabalho foi realizado com apoio da Coordenação de Aperfeiçoamento de Pessoal de Nível Superior – Brasil (CAPES) – Código de Financiamento 001

Resumo

A evolução da margem sudoeste de Gondwana durante o Devoniano-Carbonífero tem sido amplamente debatida. Alguns autores propõem o estabelecimento de uma margem passiva para esse intervalo de tempo, baseado principalmente na ausência de um arco magmático devoniano na região e na escassez ou ausência de grãos de zircão devonianos no registro sedimentar. Outros autores propõem a existência de uma margem ativa baseada no magmatismo devoniano intracontinental e deformação. Uma maneira de investigar mais profundamente esta complexa situação relacionada às características geodinâmicas durante o Devoniano-Carbonífero, é mediante o estudo da proveniência sedimentar, porque as bacias sedimentares da região representam arquivos da evolução tectônica da crosta. Neste trabalho, nós estudamos as rochas sedimentares da bacia de Tarija na Zona Subandina Sul da Bolívia usando datação U-Pb e análises morfológico de zircão detrítico, análises de isótopos Sr-Nd, mineralogia de raios X de rochas peliticas, e petrografia de arenitos. A deposição dos sedimentos devonianos ocorreu em uma configuração de bacia de antepaís, com uma importante aporte desde o oeste. As formações devonianas Icla, Huamampampa, Los Monos e Iquiri apresentam valores $\varepsilon_{Nd(300)}$ de -9.65 até -6.82 e rações $^{87}Sr/^{86}Sr_{(300)}$ entre 0.71931 e 0.75565. O Carbonífero também está caracterizado pela deposição de sedimentos em uma configuração de bacia de antepaís, mas com um importante aporte desde a região intracontinental e com um aporte menor desde o oeste. As formações carboníferas Itacua, Tupambi, Tarija e Chorro apresentam valores de $\varepsilon_{Nd(300)}$ entre -8.13 y -6.54 e razões $^{87}Sr/^{86}Sr_{(300)}$ que variam entre 0.70686 y 0.71996. As unidades devonianas e carboníferas possuem principalmente populações de zircão com idades que correspondem com idades Pampeanas (700-500 Ma), famatinianas (500-420 Ma) e Sunsas/Grenvillian (1300-900 Ma). Uma fonte mais jovem com idades entre 420-320 Ma (evento Chanico?) foi determinada apenas nas unidades carboníferas. Este resultados enfatizam uma proveniência desde as *Sierras Pampeanas*, o maciço de Arequipa-Antofalla e o arco Famatiniano. No entanto, os resultados combinados de várias técnicas, com os dados de paleocorrentes sugerem que as unidades carboníferas poderiam representar o retrabalho das unidades subjacentes desde o sudeste com um contribuição menor de uma fonte mais jovem desde a parte oeste da bacia. Além disso, propõe-se que a margem relacionada à bacia de Tarija poderia ser de tipo convergente relacionada com uma subducção tipo *flat-slab* durante o Devoniano, a qual mudou para uma subducção normal durante o Carbonífero depois da delaminação

completa do *flat-slab*. Nesse sentido, a ausência ou escassez do magmatismo de arco durante o Devoniano e o passo para um magmatismo de arco durante o Carbonífero ao longo do setor SW de Gondwana pode ser explicado. Nossos dados, em conjunto com a informação publicada da bacia de Tarija e das bacias vizinhas contemporâneas, permitiram deduzir que a margem SW de Gondwana aparentemente foi uma margem ativa durante o Devoniano-Carbonífero inferior, a qual estava caracterizada por uma forte segmentação, como produto de modificações no comportamento e interações entre as placas.

Abstract

The evolution of the southwest margin of Gondwana in Devonian-Carboniferous times has been extensively debated. Some authors proposed the establishment of a passive margin during that time, based mainly on the absence of a Devonian magmatic arc in this region and the scarcity of Devonian zircon in the related sedimentary record. Others proposed the existence of an active margin based on the record for intracontinental Devonian magmatism and deformation. One way to further investigate this complex situation related to the geodynamical settings in the Devonian-Carboniferous, is through the study of sedimentary provenance, as the sedimentary basins in the region represent archives of crustal tectonic evolution. We studied the sedimentary rocks of the Tarija basin in the Southern Bolivian Subandean Zone by U-Pb dating and morphological analysis of detrital zircon, Sr-Nd isotope analysis, X-ray mineralogy of pelitic rocks, and sandstone petrography. The deposition of Devonian sediments occurred in foreland basin settings, with an important input from the west. The Devonian Icla, Huamampampa, Los Monos, and Iquiri formations gave $\varepsilon_{Nd(300)}$ values of -9.65 to -6.82 and $^{87}Sr/^{86}Sr_{(300)}$ ratios between 0.71931 and 0.75565. The Carboniferous is also characterized by deposition of sediment in foreland basin settings, but with an important input from the intracontinental region and a minor supply from the west only. The Carboniferous Itacua, Tupambi, Tarija, and Chorro formations yielded $\varepsilon_{Nd(300)}$ values of -8.13 to -6.54 and $^{87}Sr/^{86}Sr_{(300)}$ ratios from 0.70686 to 0.71996. The Devonian and Carboniferous units mainly have zircon populations with ages that correspond to Pampean (700-500 Ma), Famatinian (500-420 Ma), and Sunsas/Grenvillian (1300-900 Ma) ages. A younger source of 420-320 Ma (Chanic event?) age was only determined for the Carboniferous units. These findings emphasize a dominant provenance from the Sierras Pampeanas, the Arequipa-Antofalla Massif and the Famatinian arc. However, the combined results from various techniques, with paleocurrent data suggest that the Carboniferous units could represent reworking of lower stratigraphic units from the southeast, with a minor, younger supply from the western part of the basin. We furthermore propose that the margin related to the Tarija basin could have been a convergent margin related to flat-slab subduction during the Devonian, which could have changed to normal subduction during the Carboniferous after complete delamination of the flat-slab. In this way, the absent to scarce evidence for arc magmatism during the Devonian and the shift to arc magmatism during the Carboniferous along the SW sector of Gondwana could be explained. Our data together,

with published information for the Tarija basin and coeval neighboring basins, allow us to deduce that the SW margin of Gondwana apparently was an active margin in Devonian-lower Carboniferous times, which was characterized by strong segmentation due to changes in the behavior of, and interactions between, plates.

Resumen

La evolución del margen suroeste de Gondwana durante el Devónico-Carbonífero ha sido extensamente debatida. Algunos autores proponen el establecimiento de un margen pasivo durante ese tiempo, basado principalmente en la ausencia de una arco magmático devoniano en la región y en la escasez de granos de circón devónicos en el registro sedimentario. Otros autores proponen la existencia de un margen activo basado en el registro de magmatismo devónico intracontinental y deformación. Una manera de investigar más a fondo esta compleja situación relacionada a las características geodinámicas durante el Devónico- Carbonífero, es a través del estudio de la proveniencia sedimentaria, ya que las cuencas sedimentarias de la región representan archivos de la evolución tectónica de la corteza. En este trabajo, nosotros estudiamos las rocas sedimentarias de la cuenca Tarija en la Zona Subandina Sur de Bolivia mediante datación U-Pb y análisis morfológico de circón detrítico, análisis de isótopos Sr-Nd, mineralogía de rayos X de rocas pelíticas y petrografía de areniscas. La depositación de los sedimentos devónicos se produjo en una configuración de cuenca de antepaís, con un importante aporte desde el oeste. Las formaciones devónicas Icla, Huamampampa, Los Monos e Iquiri dieron valores $\varepsilon_{Nd(300)}$ de -9.65 hasta -6.82 y razones $^{87}Sr/^{86}Sr_{(300)}$ entre 0.71931 y 0.75565. El Carbonífero también está caracterizado por la depositación de sedimentos en una configuración de cuenca de antepaís, pero con un importante aporte desde la región intracontinental y con un aporte menor desde el oeste. Las formaciones carboníferas Itacua, Tupambi, Tarija y Chorro presentan valores de $\varepsilon_{Nd(300)}$ entre -8.13 y -6.54 y razones $^{87}Sr/^{86}Sr_{(300)}$ que varían entre 0.70686 y 0.71996. Las unidades devonianas y carboníferas tienen principalmente poblaciones de circón con edades que corresponden a edades pampeanas (700-500 Ma), famatinianas (500-420 Ma) y de Sunsas/Grenvillian (1300-900 Ma). Una fuente más joven con edades entre 420-320 Ma (evento Chanico?) fue determinado solamente en las unidades carboníferas. Estos hallazgos enfatizan una proveniencia desde las Sierras Pampeanas, el macizo de Arequipa-Antofalla y el arco Famatiniano. Sin embargo, los resultados combinados de varias técnicas, con los datos de paleocorrientes sugieren que las unidades carboníferas podrían representar el retrabajo de unidades infrayacientes desde el sudeste con un aporte menor de una fuente más joven desde la parte oeste de la cuenca. Además, se propone que el margen relacionado a la cuenca de Tarija podría ser de tipo convergente relacionado a una subducción tipo *flat-slab* durante el Devónico, la cual cambiaría para una subducción normal durante el

Carbonífero después de la delaminación completa del *flat-slab*. En ese sentido, la ausencia o escasez de magmatismo de arco durante el Devónico y el paso hacia un magmatismo de arco durante el Carbonífero a lo largo del sector SW de Gondwana puede ser explicado. Nuestros datos, en conjunto con información publicada sobre la cuenca Tarija y cuencas vecinas contemporáneas, permitieron deducir que el margen SW de Gondwana aparentemente fue un margen activo durante el Devónico-Carbonífero inferior, el cual estaba caracterizado por una fuerte segmentación, como producto de modificaciones en el comportamiento e interacciones entre las placas.

CONTEÚDO

CAPÍTULO 1

INTRODUÇÃO

O segmento atual dos Andes representa a margem sudoeste do supercontinente Gondwana (Cawood, 2005). Esse setor foi foco de uma convergência entre o continente Gondwana e a litosfera oceânica de Panthalassa durante a maior parte do Paleozoico (Gohrbandt, 1993; Vaughan et al., 2005). No entanto, até agora a evolução do continente Gondwana ainda não é muito clara em termos de geodinâmica para o intervalo Devoniano – Carbonífero. Pelo menos desde o Cambriano (Ramos e Aleman, 2000) até o Devoniano inferior, no segmento pacífico de Gondwana deveria ter existido uma margem continental ativa com subducção de tipo Andina (Chew et al., 2007).

No entanto, diversos autores (Augustsson et al., 2006; Bahlburg et al., 2009; Bahlburg e Hervé, 1997; Cawood, 2005; Chew et al., 2007; Reimann et al., 2010) sugerem que o Devoniano – Carbonífero inferior se destaca como um tempo de relativa quiescência, ou seja, um tempo sem atividade magmática, metamorfismo ou deformação. Segundo esses autores, as principais evidencias seriam 1) ausência de grãos de zircão com idades devonianas no registro sedimentar das bacias Paleozoicas próximas da margem sudoeste de Gondwana e 2) a inexistência de afloramentos de rochas ígneas de idades devonianas permitiu a interpretação da ausência de um arco magmático durante o Devoniano e o Carbonífero inferior na parte central-oeste da América do Sul. Essa situação anômala foi chamada "o problema do Devoniano" ("*The Devonian Problem*") por Bahlburg et al. (2009), o qual faz referência ao estabelecimento de uma margem passiva durante esse tempo.

No entanto, essas interpretações são opostas com o modelo de uma margem ativa proposta por outros autores (p.e. Anderson et al., 2021; Dahlquist et al., 2018; Jaillard et al., 2000; Sempere, 1995) e com a deformação compressional que ainda foi persistente durante o Devoniano e com o desenvolvimento de bacias de antepaís (Anderson et al., 2021; Diaz-Martinez et al., 1996; Isaacson e Diaz-Martinez, 1995; Jiménez et al., 2009; Ramos, 2018; Starck, 1995).

A bacia de Tarija, na parte sul da Bolívia, preserva um importante registro das sequências sedimentares do Devoniano – Carbonífero, do setor sudoeste de Gondwana (Cruz et al., 2008; Sempere, 1995). A mesma se estende desde o sul boliviano até o norte

argentino (Figura 1.1) e tem espessuras superiores a 10.000 m. Está composta por rochas sedimentares com idades estratigráficas que variam desde o Siluriano até o recente (Cruz et al., 2008). Em função dos diferentes mecanismos de subsidência e histórias de depósito, foram reconhecidos diversos ciclos sedimentares. Esses ciclos se sobrepõem em inconformidade a rochas antigas do Cambro - Ordoviciano. O Ciclo Siluriano - Devoniano está composto por sedimentos clásticos de origem marinha, onde se alternam fácies arenosa e argilosas; enquanto que o ciclo Carbonífero – Permiano está composto por facies clásticas continentais que representam eventos glaciais e periglaciais. As fácies argilosas, predominantemente de cores cinzas escuras e negras têm potencial como rocha geradora de hidrocarbonetos, sendo verificados apenas aqueles atribuídos à Fm. Los Monos (Cruz et al., 2008 e referências nele). Além de sua capacidade de geração, essas fácies finas constituem selos estratigráficos regionais. As fácies de arenitos quartzosos das formações Santa Rosa, Icla, Huamampampa e Iquiri do Devoniano, além das formações Tupambi, Tarija e Chorro do Carbonífero, constituem os reservatórios que abrigam as maiores reservas de gás nessa bacia. Embora a bacia seja de importância econômica, existem poucos estúdios focados na proveniência sedimentar das unidades que representam o sistema petrolífero (unidades Devonianas e Carboníferas), os quais permitiriam estabelecer correlações estratigráficas em diferentes setores da bacia e fornecer informação da qualidade das unidades como rochas reservatório.

Por outro lado, até agora a configuração tectônica da bacia durante o Paleozoico médio e superior é ainda incerta e motivo de debate. Diversos autores propuseram diferentes tipos de bacias, entre elas: 1) bacia de antepaís (p.e. Anderson et al., 2021; Isaacson e Diaz-Martinez, 1995; Sempere, 1995; Starck, 1995); 2) bacia relacionada com uma margem divergente (e.g. Gohrbandt, 1993); 3) bacia intracratônica (p.e. Fernández Seveso et al., 1998; Starck e Del Papa, 2006); e 4) bacia tipo back-arc sem deformação (e.g. Dalenz-Farjat et al., 2002).

De acordo com diversos autores (p.e. Cawood et al., 2012; Reimann et al., 2010), as bacias sedimentares representam arquivos da evolução crustal e tectônica ao longo do tempo, os quais são refletidos na proveniência sedimentaria. Nesse sentido, o uso das técnicas de proveniência sedimentar permite traçar as fontes de sedimentos, assim como também permite obter informação adicional sobre o crescimento crustal e a evolução geodinâmica das áreas fontes (p.e. Bahlburg et al., 2009; Chew et al., 2008; Nie et al., 2012; Reimann et al., 2010). Assim, o objetivo principal desse trabalho é determinar a

proveniência sedimentar das sequencias do Devoniano-Carbonífero da bacia de Tarija usando idades U-Pb em grãos de zircão detrítico em combinação com as análises morfológicas dos grãos de zircão dos arenitos, e isótopos de Sr-Nd e dados mineralógicos de difratometria de raios-X de rochas sedimentares de grão fino, e petrografia de arenitos. Esses dados de proveniência sedimentar foram utilizados para discutir a configuração geodinâmica da bacia de Tarija e outras bacia vizinhas relacionadas com a margem sudoeste de Gondwana. Esses dados em conjunto permitiam também discutir os conceitos relacionado com o *"Devonian problem"*.

1.1. LOCALIZAÇÃO

As amostras do intervalo Devoniano-Carbonífero da bacia de Tarija foram coletadas na Zona Subandina Sul da Bolívia, a qual representa a parte norte da bacia (Figuras 1.1 e 2.7). Essa parte da bacia envolve os departamentos de Santa Cruz e Chuquisaca. O acesso pode ser feito pela rodovia que conecta as cidades de Santa Cruz de la Sierra, Monteagudo, Camiri e Villa Montes (Figura 2.7).

1.2. JUSTIFICATIVA

Os estudos que permitiram inferir o estabelecimento de uma margem passiva do setor sudoeste de Gondwana durante o Devoniano – Carbonífero foram feitos no noroeste de Argentina e norte de Chile por Bahlburg e Hervé (1997); Bahlburg et al. (2009), nos Andes Patagônicos chilenos por Augustsson et al. (2006), no norte e centro do Peru por Chew et al. (2007); Cardona et al. (2009), e no sul do Peru por Reimann et al. (2010). No entanto, até hoje não existem estudos de proveniência sedimentar pelo método U-Pb em zircão nas unidades do Devoniano – Carbonífero, das bacias localizadas mais para o leste do margem sudoeste de Gondwana, que certamente permitiriam compreender a evolução geodinâmica no continente durante esse tempo.

As mudanças tectônicas, durante a evolução de uma bacia, influenciam diretamente sobre os processos sedimentares responsáveis pelo preenchimento da mesma, de modo que essas mudanças são registradas e evidenciadas no registro sedimentar. Para entender parte da evolução geodinâmica do Gondwana naquela época (períodos Devoniano - Carbonífero) é necessário fazer uso dos princípios da proveniência sedimentar com o objetivo de fazer uma conexão entre os processos tectônicos e sedimentares. A justificativa deste projeto de mestrado centra-se no entendimento da evolução geodinâmica durante o Devoniano – Carbonífero no continente Gondwana,

especificamente na bacia de Tarija. O entendimento das mudanças geodinâmicas e os dados de proveniência sedimentar nesse intervalo de tempo são também necessários porque as rochas sedimentares da bacia de Tarija têm uma importância desde o ponto de vista econômico, pois representam um sistema petrolífero com rocha geradora e reservatório na mesma unidade (Starck, 1999; Cruz et al., 2008).

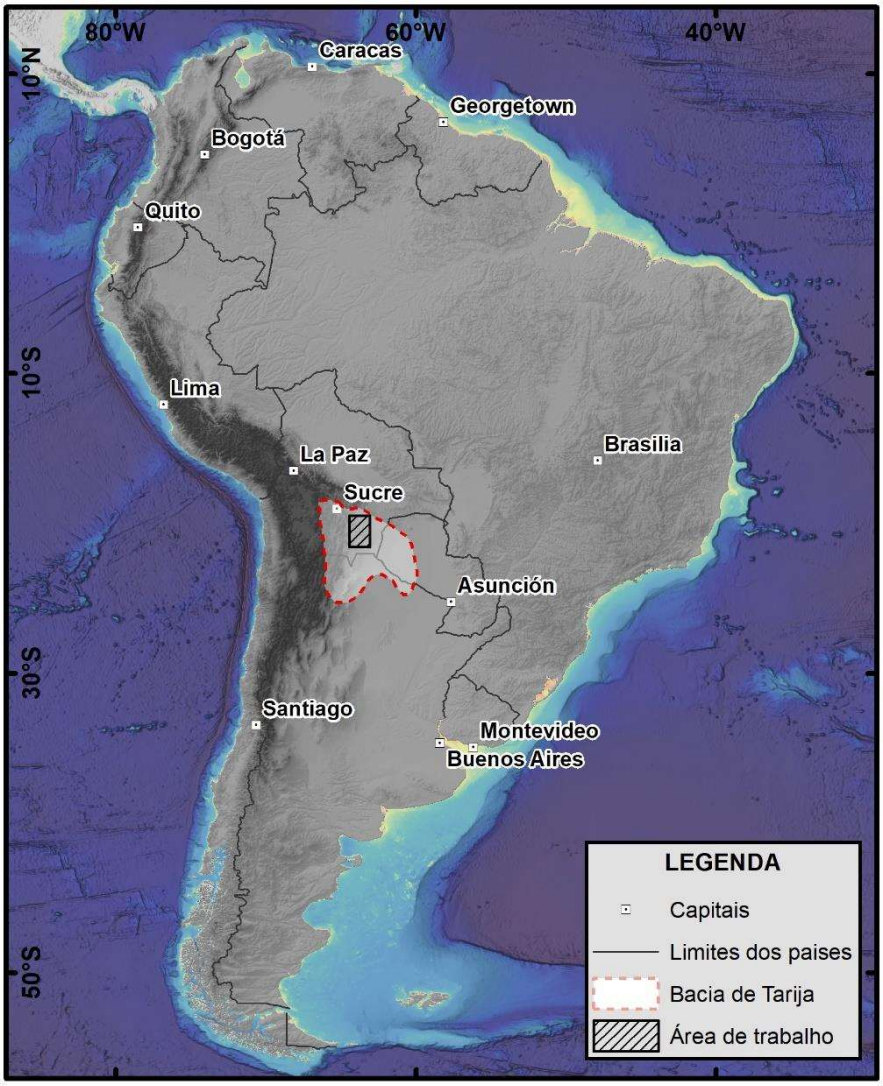

Figura 1. 1: Localização da bacia de Tarija (polígono vermelho) e a área de estudo no contexto da América do Sul.

1.3. OBJETIVOS

O objetivo principal deste projeto de mestrado é definir a proveniência sedimentar no intervalo de tempo Devoniano – Carbonífero, para estabelecer ou inferir os processos geodinâmicos que atuaram durante esse tempo na bacia de Tarija. Os dados obtidos serão

relacionados com bacias correlatas no setor sudoeste de Gondwana, usando as técnicas de proveniência sedimentar. Para atingir o objetivo principal, serão desenvolvidos os seguintes objetivos específicos:

- Reconhecimento de campo e obtenção de amostras em secções geológicas pré-definidas.
- Petrografia de arenitos para classificá-las de acordo com seu conteúdo modal.
- Análises isotópicos U-Pb em grãos zircão detrítico dos arenitos das unidades do Devoniano – Carbonífero para obter idade máxima de sedimentação e estabelecer as possíveis fontes de proveniência.
- Análises de difratometria de raios-X dos níveis pelíticos. A composição mineralógica da fração argila permitirá determinar possíveis variações nas proveniência sedimentar e nas condições de deposição.
- Isótopos de Sr-Nd dos níveis pelíticos ao longo das colunas sedimentares para obter uma variação temporal das razões $^{87}Sr/^{86}Sr$ inicial e Épsilon Nd (e T_{DM}) para estabelecer possíveis fontes e variações na proveniência sedimentar ao longo do tempo.
- Estabelecer a relação desde o ponto de vista geodinâmico das unidades do Devoniano – Carbonífero da bacia de Tarija com as bacias correlatas no setor sudoeste de Gondwana.

CAPÍTULO 2

CONCEITOS TEÓRICOS

2.1. CONTEXTO GEODINÂMICO DE GONDWANA

A história da evolução do continente Gondwana é complexa e até agora ainda incerta. Gondwana foi composto em maior parte pela união dos atuais continentes da África, América do Sul, Antártica, Austrália, Madagascar e Índia. Foi entre no final do período Proterozoico (Ediacarano) e o Paleozoico inferior (630 – 530 Ma) que ocorreu a montagem do supercontinente Gondwana (Cawood, 2005). A montagem do mesmo foi um evento geodinâmico de grande magnitude que teve influência decisiva no desenvolvimento de bacias, climas, biota e processos orogênicos (Benedetto, 2019). Segundo Zalán et al. (1990), o Gondwana foi estabelecido como resultado de um importante evento tectonomagmático conhecido como ciclo Brasiliano (na América do sul) ou a orogenia Pan-Africana (na África). A montagem do Gondwana começou há aproximadamente 630 Ma, depois do início da fragmentação do supercontinente Rodinia no final do Meso-proterozoico há ~830 Ma (Cawood, 2005). Finalmente, o Gondwana foi um supercontinente perto dos 550-530 Ma até o Carbonífero perto dos 320 Ma, depois desse tempo tornou-se parte de um setor da Pangea até depois do final do Paleozoico (Torsvik e Cocks, 2013).

De acordo com Cawood (2005), o registro do início das margens Pacifica e Iapetus do Gondwana e do subsequente início da interação de tipo convergente entre placas está preservada no cinturão orogênico do Neo-proterozoico até Paleozoico superior, o qual é denominado “Orogeno Terra Australis” e que se extendeu ao longo da margem do Gondwana. A história do orógeno Terra Australis acabou perto dos 300-230 Ma com o início do ciclo orogênico Gondwânico; isso anunciou o início do orógeno do Paleozoico superior até o Mesozoico, o qual é denominado “Orógeno Gondwanide” (Cawood, 2005).

A margem sudoeste do Gondwana, o que corresponde atualmente ao borde Pacífico dos Andes de América do Sul, foi uma região submetida a esforços compressivos durante a maior parte do Paleozoico. Esses esforços foram o resultado da convergência entre o bloco Gondwânico e a litosfera oceânica Panthalassa (Milani e Ramos, 1998; Vaughan et al., 2005; Milani e De Wit, 2008), assim a história Paleozoica deste setor do Gondwana está marcada por uma sucessão de ciclos orogênicos, que são produto de uma aglutinação de terrenos alóctones contra a margem do Gondwana (Ramos, 1988). O

regime compressivo constante influenciou na evolução de faixas dobradas e bacias de antepaís adjacentes às mesmas, mas afetou também o interior cratônico do continente (Milani e Ramos, 1998).

De acordo com Heredia et al. (2018), na margem sudoeste do Gondwana foram acrescionados fragmentos continentais de variável extensão e alóctones; isso deu como resultado seis orogenias durante o Paleozoico com diferentes intervalos de tempo e diferentes extensões espaciais: 1) Orogenia Pampeana (Ediacariano - Cambriano inferior), 2) Orogenia Famatiniana (Ordoviciano médio - Siluriano), 3) Orogenia Ocloyica (Ordoviciano médio - Devoniano), 4) Orogenia Chanica (Devoniano médio - Carbonífero inferior), 5) Orogenia Gondwânica (Devoniano médio - Permiano médio), e 6) Orogenia Tabarin (Permiano superior - Triássico), reconhecido como um orógeno de tipo não colisional localizado na Patagônia e na Península Antártica.

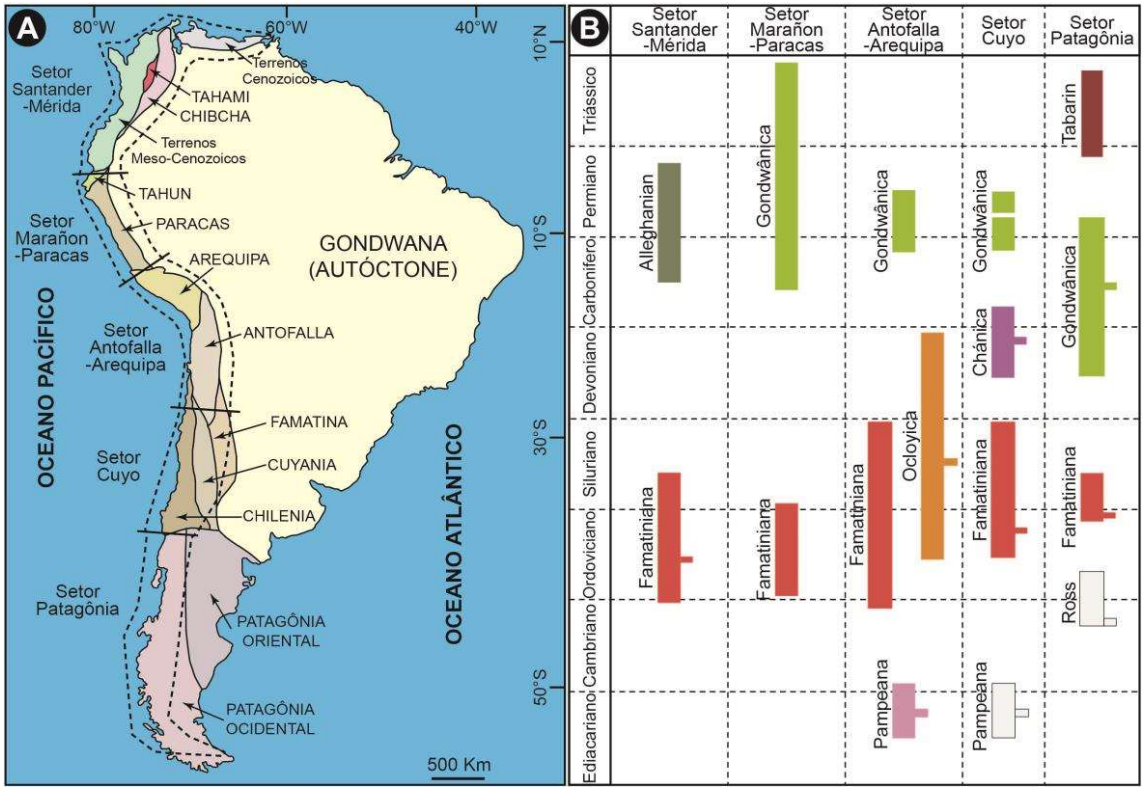

Figura 2.1: A) Terrenos paleozoicos e fragmentos continentais da América do Sul e localização dos setores Santander-Mérida, Marañon-Paracas, Antofalla-Arequipa, Cuyo e Patagônia. B) Distribuição temporal esquemática das orogenias paleozoicas. As barras sem cor representam as orogenias fora dos Andes. Os retângulos pequenos marcam o início das colisões. Adaptado de Heredia et al. (2018) *baseados nos dados de* Ramos (2015)*;* Van der Lelij et al. (2016) *e* Ramos (2018b) .

2.2. O PROBLEMA DO DEVONIANO

Segundo vários autores (p.e. Augustsson et al., 2006; Bahlburg et al., 2009; Bahlburg e Hervé, 1997; Chew et al., 2016, 2007; Reimann et al., 2010), a subducção cessou, na margem ocidental de Gondwana, no início do Devoniano e continuo até o início do Carbonífero. Nesse sentido, o Devoniano se destaca como um momento de relativa quiescência. As evidencias presentadas por esses autores para esse período de quiescência tectônica foram principalmente a ausência ou escassez de grãos de zircão com idades entre o Devoniano e o Carbonífero inferior. Consequentemente, esses autores sugeriram o desenvolvimento de uma margem passiva, a qual se estendeu desde o norte do Peru até o sul do Chile durante o Devoniano – Carbonífero inferior, essa suposição está baseada na observação feita por Chew et al. (2007). Essa situação anômala, relacionada com a ausência de um arco magmático entre o Devoniano e o Carbonífero superior, foi chamada por Bahlburg et al. (2009) como "O Problema do Devoniano".

Por outro lado, outro autores (p.e. Anderson et al., 2021; Dahlquist et al., 2018; Jaillard et al., 2000; Sempere, 1995) sugerem um modelos que envolvem uma margem ativa para a margem sudoeste de Gondwana durante o Devoniano – Carbonífero inferior. As evidencias da existência de uma margem ativa incluem a persistência da deformação por contração durante o Devoniano com o desenvolvimento de bacias de antepaís (p.e. Anderson et al., 2021; Diaz-Martinez, 1996; Isaacson e Diaz-Martinez, 1995; Jiménez et al., 2009; Ramos, 2018; Starck, 1995) e a atividade magmática continua desde o Devoniano superior até o Carbonífero inferior com uma importante variação composicional ao longo do tempo e do espaço observada no noroeste Argentino (Dahlquist et al., 2019, 2018; López de Luchi et al., 2017).

2.3. SISTEMA DE BACIAS

Existem muitas classificações de bacias sedimentares que tomam como referência os estudos da tectônica de bacias sedimentares feitos por Dickinson (1974); no entanto, de acordo com Miall (2000), a maioria das bacias sedimentares podem ser facilmente classificadas em termos de três critérios: 1) o tipo de crosta em que a bacia repousa, 2) a posição da bacia em relação às margens da placa, e 3) onde a bacia fica próximo de uma margem de placa, o tipo de interação da placa que ocorre durante a sedimentação.

A configuração tectônica da bacia de Tarija durante o Paleozoico médio e superior ainda é motivo de debate. Diversos tipos de configurações tem sido propostos por vários

autores, entre essas propostas destacam a possível existência de uma bacia de ante-país (Anderson et al., 2021; Isaacson e Diaz-Martinez, 1995; Sempere, 1995; Starck, 1995), uma bacia relacionada com uma margem divergente (Gohrbandt, 1993), uma bacia intracratônica (Fernández Seveso et al., 1998; Starck e Del Papa, 2006), ou uma bacia tipo back-arc sem deformação (Dalenz-Farjat et al., 2002). Portanto, é importante conhecer e compreender as características destes tipos de bacias sedimentares.

2.3.1. BACIAS DE ANTE-PAÍS

As bacias de antepaís são definidas como bacias sedimentares situadas entre a frente de uma cadeia montanhosa e o cráton adjacente (Allen et al., 1986). De acordo com Dickinson (1974), é possível distinguir entre bacias de antepaís *peripheral* e *retroarc*, o primeiro situado contra do arco externo do orógeno durante a colisão de placas oceânica e continental, e o segundo situado atrás de um arco magmático e relacionado à subducção da litosfera oceânica. Além disso, os sistemas de bacias de antepaís são regiões alongadas de acomodação potencial de sedimentos que se formam na crosta continental entre cinturões orogênicos compressionais e crátones em resposta a processos geodinâmicos relacionados à cinturão orogênico e um sistema de subducção associado (DeCelles e Giles, 1996). O sistemas de bacias de antepaís se formam pela flexão da litosfera pela combinação de cargas supralitosféricas e sublitosféricas (DeCelles e Giles, 1996; Catuneanu et al., 1997). A flexão da litosfera pelas cargas estáticas concentradas gera uma depressão ou *downwarp* próxima ao orógeno, denominada bacia de antepaís, e uma protuberância ou *upwarp* conhecida como f*orebulge* (Figura 2.2). Além disso, segundo Catuneanu et al. (1997), a combinação de cargas estáticas e dinâmicas influem na geração da Pro-bacia de antepaís (*pro-foreland basin*) e Retro-bacia de antepaís (*retro-foreland basin*) (Figura 2.2). A primeira ligada geneticamente a uma litosfera em subducção, e a segunda ligada a um frente de deformação chamado cinturão de dobra e cavalgamento (*fold and thrust belt*) (Figura 2.3).

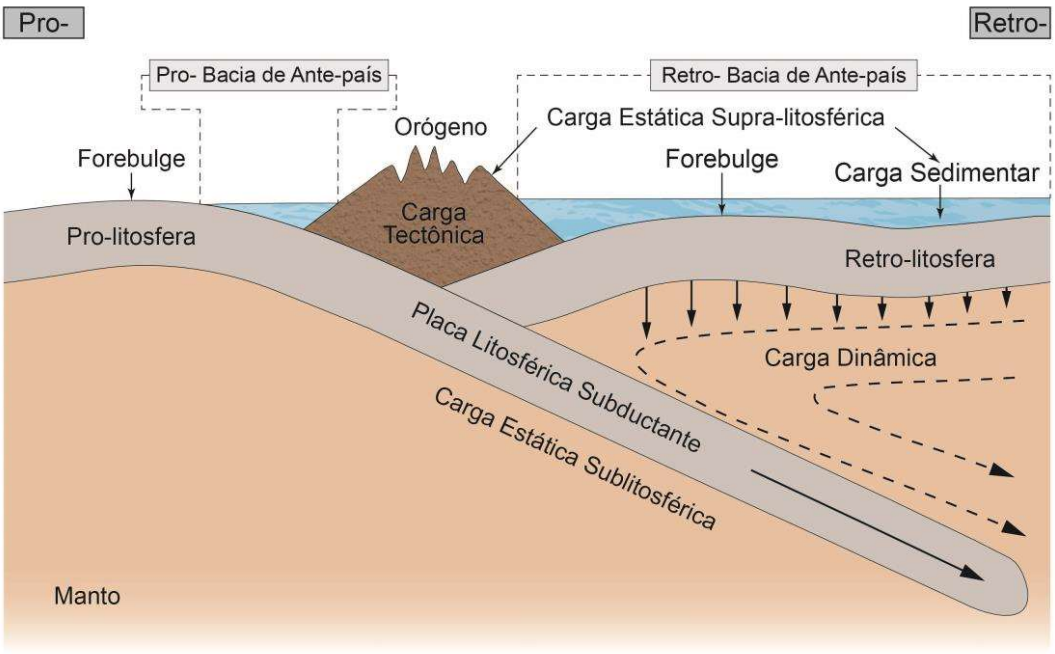

Figura 2.2: Cargas dinâmicas e estáticas que atuam sobre um sistema de Orógeno-Bacia de Ante-país. Pro- e Retro- refrem-se às litosferas subductante e subductada (Tomado de Catuneanu et al., 1997).

Zonas de deposição:

De acordo com DeCelles e Giles (1996), as bacias de antepaís podem ser divididas em quatro zonas de deposição (depozonas), entre elas estão o *wedge-top*, *foredeep*, *forebulge* e *backbulge* (Figura 2.3). Os principais mecanismo de perturbação litosférica, em sistemas de bacias de antepaís, são a flexão em resposta a carga orogênica e cargas subsuperficias, mas essa flexão pode ser manifestada diferentemente em cada depozona.

Wedge-Top:

De acordo com DeCelles (2012), inclui sedimentos que cobrem a parte frontal ativa do cinturão de empuxo. A imaturidade textural e composicional é uma característica típica dos depósitos da zona *wedge-top*, no entanto, as estruturas de crescimento (inconformidades progressivas) são sua característica definidora (Figura 2.3B). Em muitas cinturões de empuxo continentais, o limite de topografia significativa está longe da parte posterior do empuxo frontal, e uma grande quantidade de sedimento sinorogênico cobre a parte frontal do cinturão de empuxo (DeCelles e Giles, 1996). Geralmente, os empuxos frontais estão cobertos; no entanto, é possível reconhecer *duplexs*, zonas triangulares, anticlinais de rampa e dobras pela propagação de falhas (Figura 2.3B) que representam o frente de deformação.

Em ambientes subaéreos, esses depósitos consistem do material mais grosso no preenchimento da bacia, geralmente sedimentos aluviais e fluviais que se acumulam próximo ao alto relevo topográfico; por outro lado, em ambientes subaquáticos. Os depósitos do *wedge-top* consistem tipicamente de fluxos de massa e sedimentos de grãos finos de plataforma (DeCelles e Giles, 1996).

Foredee:

De acordo com Price (1973), a depozona *Foredeep* consiste em sedimentos depositados dentro do fosso de flexão formado pela carga do cinturão de empuxo (Figuras 2.3A e 2.3B). A zona *Foredeep* é a massa de sedimento que foi acumulada entre a ponta frontal da cunha orogénica e o *Forebulge* (DeCelles e Giles, 1996).

Em ambientes subaéreos, esses depósitos consistem de sedimentos de fluxos longitudinais e transversais de sistemas deposicionais fluviais e aluvias; por outro lado, em ambientes subaquáticos, estão ocupados por sistemas deposicionais marinhos o lacustrinos someros que variam entre deltas, plataformas someras e abanicos de turbiditos (DeCelles e Giles, 1996). A maior parte do sedimentos do *Foredeep* derivam do cinturão do empuxo e dobramento, no entanto, também e possível o aporte de sedimentos derivados do *Forebulge* e do Cráton.

Forebulge:

De acordo com DeCelles e Giles (1996), a depozona *Forebulge* consiste da região de potencial levantamento (Figuras 2.3A e 2.3B) pela flexão ao longo do lado cratônico do *Foredeep*. O *Forebulge* é considerada como uma zona de não-deposição o erosão porque é uma zona elevada e potencialmente migratória, que pode ser desgastado e deixar só uma inconformidade.

O *Forebulge* também pode ser uma zona de acumulação de sedimentos substancial (DeCelles e Giles, 1996). Em sistemas de bacia de antepaís submarinhas na zona de *Forebulge* pode desenvolver-se plataformas locais de carbonatos (Dorobek, 1995); por outro lado, de acordo com DeCelles e Giles (1996); DeCelles (2012), em ambientes subaéreos os sedimentos derivados do cinturão de empuxo também pode progradar além do *Foredeep*, representado por sedimentos finos fluviais e eólicos condensados depositados sobre uma ampla região.

Backbulge:

A depozona Backbulge representa os sedimentos que foram acumulados entre o Forebulge e o Cráton (Figuras 2.3A e 2.3B). De acordo com DeCelles e Giles (1996), embora a maior parte desse sedimento seja derivada do cinturão orogênico, as contribuições do cráton e o desenvolvimento de plataformas de carbonatos podem ser significativos em sistemas submarinos. Os sistemas deposicionais dominantes é o marinho somero e também não-marinho; em quanto a granulometria, geralmente, é fina pela grande distância de seu principal fonte no cinturão orogênico. No entanto, de acordo com Giles e Dickinson (1995), as acumulações de sedimentos de grão grosso podem estar presente no flanco da zona Forebulge levantada.

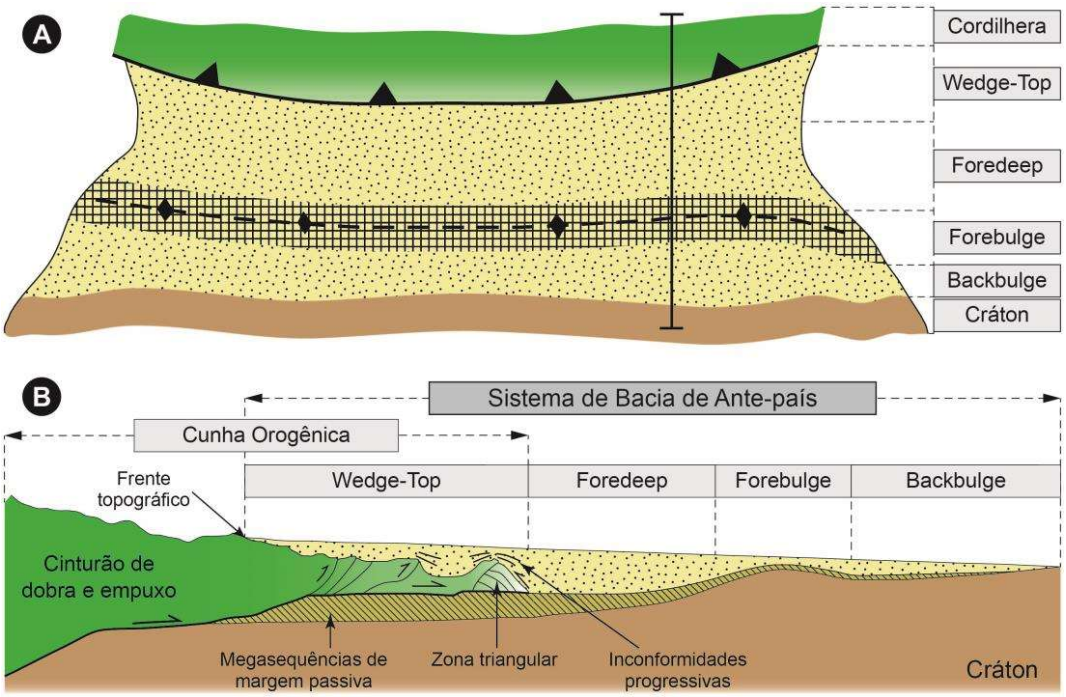

Figura 2.3: Sistema de bacia de Ante-país. A) visão em planta do sistema de bacia de ante-país; B) Secção de um sistema de bacia de ante-país ligada a um frente de deformação (Adaptado de DeCelles e Giles, 1996).

2.3.2. BACIAS INTRACRATÔNICAS

As Bacias Intracratônicas, também conhecidas como "Bacia Cratônica", "Bacia Cratônica interior", e "Afundamentos intracontinentais", são afundamentos crustais de forma circular para oval, localizada numa litosfera continental estável e relativamente espessa (Sloss e Speed, 1974; Sloss, 1988) (Figura 2.4). De acordo com Allen e Armitage (2012), as Bacias Cratônicas são aquelas bacias localizadas a alguma distância de margens continentais divergentes ou convergentes, diferentes dos rifts ligados a uma extensão continental, mas localizada em uma variedade de substratos crustais,

independentemente de serem escudos cristalinos, terrenos acrecionados, ou antigos cinturões dobrados e *rifts* complexos.

Segundo diversos autores (Sloss e Speed, 1974; Sloss, 1988; Leighton et al., 1990; Xie e Heller, 2009), as bacias cratônicas estão caracterizadas por uma subsidência e sedimentação prolongada. A primeira característica está ocasionalmente marcada por um estágio inicial de subsidência relativamente rápida, seguida por um período de decrescimento da subsidência; por outro lado, a última corresponde a uma sedimentação predominantemente de águas rasas e terrestres, e uma estratigrafia grossa de tipo *layer-cake*.

De acordo com Allen e Armitage (2012), embora que as bacias cratônicas tenham sua própria individualidade, o que é de se esperar nestas bacias longevas, há uma série de características proeminentes comuns entre elas. Estas características incluem o seguinte: 1) a área da superfície delimitada pela isopaca zero do preenchimento da bacia é comumente circular ou elíptica, e grande; 2) na seção transversal, as bacias cratônicas são simples discos, sem grandes falhas sin-tectônicas, geralmente com espessuras de sedimentos tipicamente menores que 5 km.; 3) a duração da subsidência é muito longa (centenas de milhões de anos) e as histórias de subsidência tectônicas são comumente sublineares a exponenciais suavemente negativas. Esses longos tempos de subsidência comumente compreendem várias fases de bacias separadas por inconformidades, dando como resultado megaseqüências sobrepostas que refletem padrões de mudança da tectônica; 4) a estratigrafia é predominantemente terrestre até águas rasas, indicando que a sedimentação acompanhou o ritmo da subsidência tectônica; 5) as bacias cratônicas são geralmente espaçadas com seus centros localizados a cerca de 10^3 km de distância; e 6) algumas bacias cratônicas estão associadas a magmatismos extensos, como a erupção de grandes volumes de basaltos. No entanto, as ligações causais precisas entre o vulcanismo basáltico e o desenvolvimento da bacia não são claras.

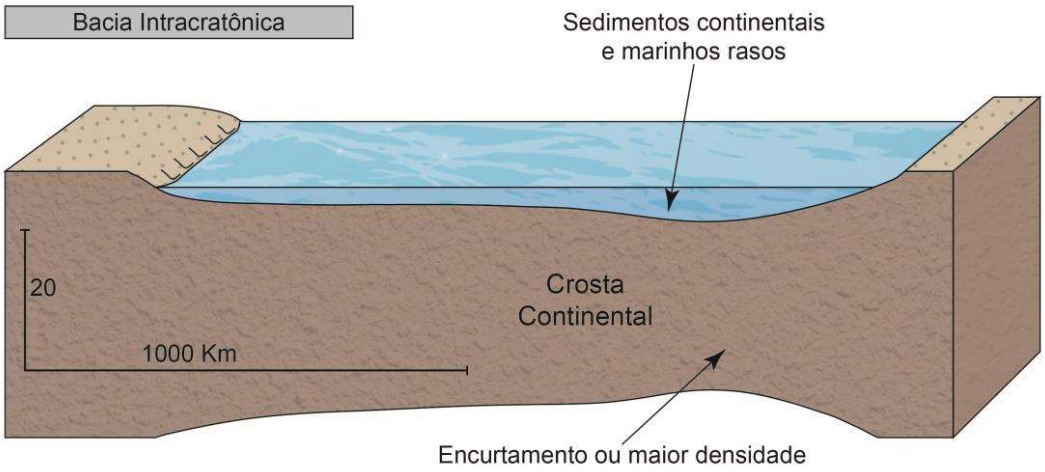

Figura 2.4: Esquema de bacias intracratônicas (tomado de Einsele, 2013*).*

Mecanismos de formação das bacias intracratônicas:

De acordo com Allen e Armitage (2012) e referencias nele, propõem diferentes mecanismos para tentar explicar a origem destes tipos de bacias. Estes mecanismos incluem: 1) Contração térmica após do aquecimento; 2) Extensão localizada relacionada à ressurgência magmática que pode estar associada à atividade da pluma mantélica; 3) Mudanças da fase crustal profunda; 4) Reativação de afundamentos pré-existentes sob esforços no plano ou carga de flexão; 5) Colocação de *underplates* basálticos durante o magmatismo anorogênico e contração térmica lenta em um ambiente não extensional; 6) Subsidência devido à topografia dinâmica negativa, resultante da transmissão à superfície da Terra de esforços causadas pelo fluxo do manto em grande escala, sobre uma instabilidade descendente ou convectiva no manto ou relacionada à subducção de placas oceânicas frias; e 7) Erosão subaerial relacionado com um aumento térmico seguido de carregamento de sedimentos.

2.3.3. BACIAS BACK-ARC

As bacias *back-arc* se desenvolvem atrás de arcos de ilhas na crosta oceânica ou na crosta continental normal e fina (Einsele, 2000). No entanto, é certo que esse tipo de bacias geralmente estão relacionadas com um arco, a presença ou preservação de um arco remanescente não é uma condição necessária para o reconhecimento de uma bacia *back-arc* (Taylor e Karner, 1983).

De acordo com Ingersoll (2011) existem dos tipos de bacias de *back-arc*: 1) bacias oceânicas atrás dos arcos magmáticos intraoceânicos, e 2) bacias continentais atrás de arcos da margem continental que não possuem cinturões de dobras e cavalgamentos.

Muitas bacias de *back-arc* são de origem extensional, formando-se por rifting e expansão do fundo oceânico (Figura 2.5A); no entanto, nem todas as bacias de *back-arc* são extensionais, elas também podem-se formar sob regimes de estresse neutro (Figura 2.5B) (Marsaglia, 1995). Segundo Ingersoll (2011), o tipo de bacia de *back-arc* não extensional mais comum consiste de bacias oceânicas antigas presas durante a reorganização da placa. Bacias de *back-arc* não extensionais também podem-se desenvolver na crosta continental (Figura 2.5C) (Ingersoll, 2011).

Em configurações de margem continental:

De acordo com Einsele (2000), o início da evolução da região de retroarco está comumente caracterizada pela extensão e rifting relacionado à subducção, o que pode ser seguido pela acreção de nova crosta oceânica. Além disso, a extensão atrás do arco magmático resulta do fato de que a taxa de subducção da placa inferior é mais rápida do que o movimento para ao frente conduzido pela subducção da placa superior. Nesse sentido, para compensar esse déficit, a região do *back-arc* da placa superior é esticada. Posteriormente, o lado arqueado da bacia de *back-arc* pode ser dobrado e desenvolver um falhamento reverso, semelhante à evolução tectônica das bacias de ante-país.

Em sistemas intraoceânicos de arco-trincheira:

A região de back-arc é uma bacia oceânica de tamanho limitado que acumula sedimentos pelágicos e hemipelágicos misturados com material vulcaniclástico (Einsele, 2000).

Bacias oceânicas marginais:

Podem ser subdividido em bacias marginais relacionadas à subducção e bacias não relacionadas à subducção (Einsele, 2000). As bacias relacionadas à subducção formam dois grupos de acordo com sua origem: 1) bacias back-arc que evoluem na região back-arc de um arco ativo pelo espalhamento do fundo oceânico seguindo o rifting do arco; 2) bacias marginais relacionadas à subducção formadas pelo aprisionamento de parte de uma bacia oceânica grande devido ao estabelecimento de uma nova zona de subducção na bacia oceânica. Enquanto que a maioria das bacias não relacionadas à subducção não estão associadas ao espalhamento ativo do back-arc, mas podem representar remanescentes de bacias back-arc mais antigas que foram presas pelo recuo de um antigo sistema ativo de arco-trincheira.

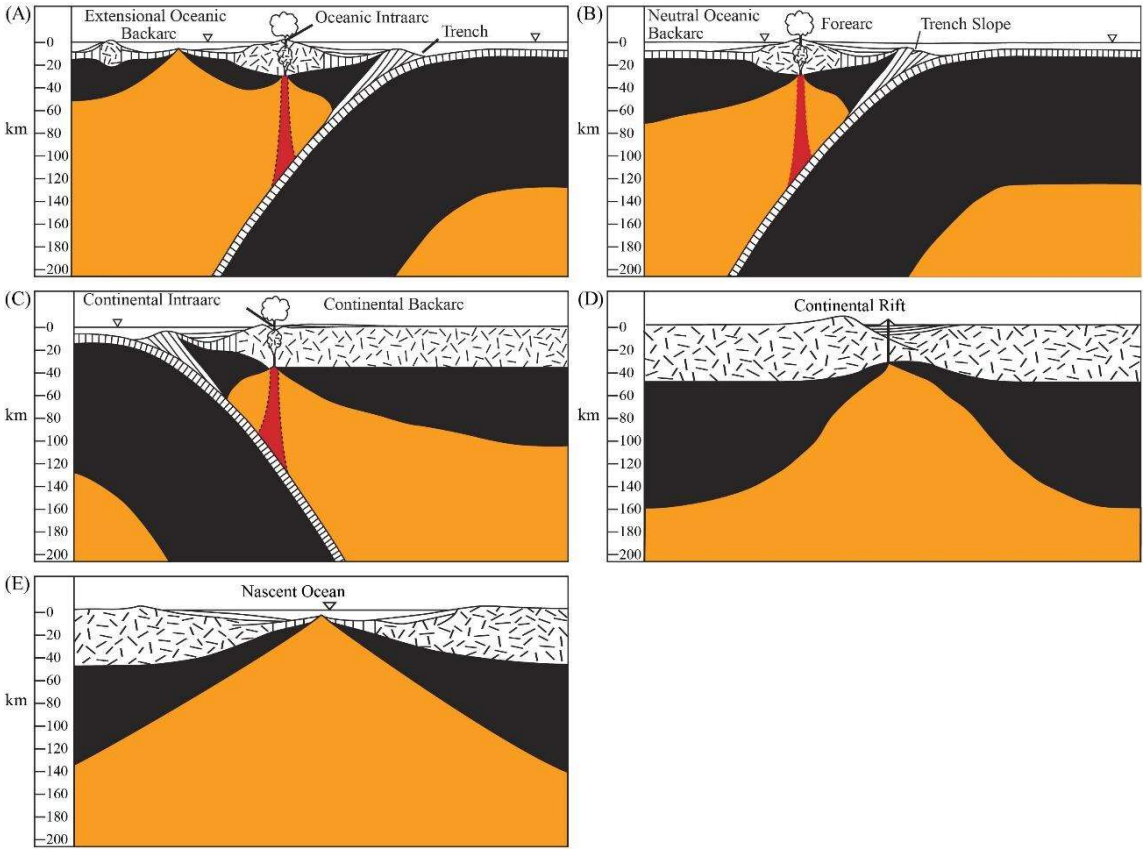

Figura 2.5: Tipos de bacias. A-C) Bacias de back-arc. D-E) Bacia divergentes. Retirado de Ingersoll (2011).

2.3.4. BACIAS DIVERGENTES

De acordo com Ingersoll (2011), de uma forma geral as bacias divergentes podem ser classificadas em dois: 1) bacias de *rift* continental (Figura 2.5D), com riftes dentro da crosta continental, comumente associadas com magmatismo bimodal, e 2) bacias oceânicas nascentes e margens continentais (Figura 2.5E), que correspondem às bacias oceânicas incipientes revestidas por uma nova crosta oceânica e rodeadas por margens continentais jovens rifteadas.

Desenvolvimento sequencial do rift e separação continental:

De acordo com Ingersoll (2011), os riftes continentais podem experimentar dois caminhos. O primeiro é o rifting "bem-sucedido" que evolui dentro da expansão do fundo oceânico para formar bacias oceânicas nascentes, que evoluem para bacias oceânicas ativas com margens intraplaca emparelhadas. Enquanto o segundo é o rifting “abortado” que não evolui para bacias oceânicas nascentes, em vez disso, produzindo rifts fósseis, comumente recobertas por bacias intracratônicas.

2.4. MARCO GEOLÓGICO DA BACIA DE TARIJA

A Bacia de Tarija desenvolveu-se próximo ao margem sudoeste do paleo-continente Gondwana; na configuração atual dos continentes, e está localizada na parte sul da Bolívia e estende-se até a parte norte da Argentina (Ver Figura 1.1). A localização, flanqueando um hipotético orógeno de colisão, além da assimetria das fácies com importantes aportes do oeste, permitiu a diversos autores (Ramos, 1986; Vistalli, 1990; Starck, 1995, 1999) classifica-la como uma bacia de antepaís.

No entanto, as características tectônicas das bacias do Paleozoico médio e superior nesse setor ainda é incerto e motivo de debate. De acordo com vários autores (Isaacson e Diaz-Martinez, 1995; Ramos, 1988a; Sempere, 1995; Starck, 1995), estão associadas com bacias marinhas de antepaís. Por outro lado, Gohrbandt (1993) consideram que estiveram ligadas com uma margem divergente; enquanto que Fernández Seveso et al. (1998) sugerem uma bacia intracratônica, e Starck e Del Papa (2006) com uma bacia intracratônica influenciada pela subsidência tectônica devido à subducção.

A evolução da bacia de Tarija é complexa e está representada por uma sobreposição de várias bacias com origens e mecanismos de subsidência distintos; no entanto, segundo Starck (1999) a delimitação no tempo da bacia de Tarija está separada por eventos diastróficos importantes. Deste jeito a bacia de Tarija é funcional depois da Fase tectônica Ocloyica, separando-se da bacia Cambriana-Ordoviciana por médio de uma discordância. Por outro lado, o fim do ciclo tectono-sedimentar da bacia de Tarija está relacionado à fase tectônica Araucana, a qual provocou o desmembramento das bacias Paleozoicas-eomesozoicas (Starck, 1995, 1999; Starck et al., 2002). O registro estratigráfico da fase diastrófica Araucama está representada pela inconformidade angular que conforma o limite superior do Registro da bacia de Tarija (Starck e Del Papa, 2006).

Entre os eventos diastróficos (Ocloyica e Araucama), foram depositados ao redor de 5000 m de sedimentos, que constituem dois paquetes estratigráficos (Siluro-Devoniano e Carbonífero-Cretáceo) separados pela fase tectônica Chanica reconhecida por Starck et al., (1993). Esta fase tectônica foi posiblemente de características compressivas e interrompeu a sedimentação desde o Devoniano superior; além disso a queda eustática, durante o Carbonífero médio, impediu que a sedimentação fosse continua até o Carbonífero superior (Starck, 1999).

2.4.1. ESTRATIGRAFÍA

A Bacia de Tarija compreende preenchimentos com espessuras maiores do que 10000 m de rochas sedimentares desde o Siluriano ao recente, onde podem ser reconhecidas vários ciclos sedimentares com hierarquia de conjunto de supersequências com diferentes mecanismos de subsidência e historias deposicionais (Cruz et al., 2002). A coluna estratigráfica da Zona Subandina Sul da Bolívia superpõem-se em relação discordante com as rochas do embasamento pre-Siluriano não deformadas e podem ser divididas em 3 ciclos sedimentares maiores (Figura 2.6): 1) Ciclo Siluriano-Devoniano; 2) Ciclo Carbonífero-Jurássico; e 3) Ciclo Cenozoico (Starck, 1995). De acordo com Fuentes et al. (2018), o embasamento pre-Siluriano e os três ciclos sedimentares compreendem sobreposições de bacias diferentes: 1) uma sequência clástica ordoviciana de plataforma, possivelmente depositada em uma bacia back-arc; 2) uma bacia intracratônica siluriana-devoniana de afinidade incerta, compreendendo principalmente estratos marinhos clásticos depositados em configurações de rampa; 3) sucessões intracratônicas de Gondwana com uma estratigrafia distinta que compreendem o Carbonífero-Permiano, o Permiano-Triássico e o Jurássico; e 4) um sistema de bacia de antepaís andinas cenozoicas.

Ciclo Siluriano-Devoniano:

Esse ciclo está composto por mais de 3000 m de sedimentos clásticos, representado por uma alternâncias de fácies arenosas e argilosas (Figura 2.6) depositadas principalmente num ambiente marinho raso e menos comumente em ambiente litoral e continental. Esse ciclo está separado do embasamento pre-Siluriano por uma inconformidade proeminente que tem uma clara expressão regional (Starck, 1995). As fácies argilosas com cores preto e cinza escuro tem potencial como rocha geradora de hidrocarbonatos, sendo comprovada as que foram assignadas à Formação Los Monos. Além da capacidade geradora, as fácies finas constituem selos regionais (Cruz et al., 2008), além de representar os níveis de descolamento (Ver Figura 2.6) que controlam a geometria das Serras Subandinas (Rocha, 2013). As fácies dos arenitos quartzosos das formações Santa Rosa, Icla, Huamampampa e Iquiri constituem as unidades reservatórios que abrigam as maiores reservas de gás dessa bacia (Cruz et al., 2002, 2008).

De acordo com Fuentes et al. (2018), os sistemas do Siluriano e do Devoniano estão representados principalmente por depósitos marinhos relativamente tabulares. Diversas configurações de bacias foram propostas para esses depósitos incluindo bacia de antepaís (Anderson et al., 2021; Sempere, 1995; Starck, 1995), bacia tipo rift e posrift

(Fernández Seveso et al., 2000), e bacia tipo back-arc (Dalenz-Farjat et al., 2002). O Siluriano está representado, da base para o topo pelas formações Cancañiri/Zapla, Kirusillas e Tarabuco (Figura 2.6); enquanto o Devoniano está representado, da base para o topo, pelas formações Santa Rosa, Icla, Huamampampa, Los Monos e Iquiri (Figura 2.6). O Devoniano da bacia de Tarija está caracterizada pela presença de palinomorfos distintintivos como *Bimerga bensonii*, *Crucidia camirense*, *Evittia sommeri*, *Evittia sommeri*, *Petrovina connata*, *Ramochitina magnifica*, *Leiotriletes balapucensis* e *Endoculeospora altobellii* (di Pasquo, 2007a; Troth et al., 2011).

Ciclo Carbonífero-Jurássico:

O ciclo Carbonífero-Jurássico está composto por hasta 2500 m de rochas formadas principalmente em ambientes continentais e deltaicos (Rocha, 2013). O contato com as sequências pre-Carboníferas é por médio de uma inconformidade angular. O topo da sucessão Carbonífera-Jurássica está marcada por outra inconformidade maior; um conjunto de paleovales profundamente erodidos sobrepõem-se a essa inconformidade regional, erodindo os diferentes níveis do Devoniano (Starck et al., 1993). As unidades mais antigas mostram uma forte influência glacial (Figura 2.6) reconhecida em distintas unidades carboníferas formadas em diferentes bacias do Gondwana (Starck, 1995; Starck e Del Papa, 2006). Enquanto que as unidades mais novas foram formadas em ambientes continentais (Figura 2.6) baixo condições climáticas mais cálidas durante o Permiano e o Jurássico do Gondwana (Starck, 1995; Starck et al., 2002).

De acordo com Starck (1995), o intervalo Carbonífero-Jurássico está caracterizado pela sucessão de sequências deposicionais, sendo que cada sequência está separada da seguinte por uma inconformidade. Assim, o ciclo está subdividido em 4 grupos que são geneticamente diferentes e separados por inconformidades: Macharetí, Mandiyutí, Cuevo, e Tacuru (Figura 2.6). O Mississíppiano da bacia de Tarija está caracterizado pela presença de palinomorfos distintintivos como *Auroraspora macra*, *Granulatisporites granulatus*, *Foveosporites appositus*, *Retusotriletes mirabilis* e *Secarisporites undatus*. Enquanto o Pennsylvániano está caracterizado pela presença de palinomorfos distintintivos como *Crassispora kosankei*, *Cristatisporites chacoparanensis*, *Cristatisporites crassilabratus*, *Dictyotriletes bireticulatus*, *Lundbladispora riobonitensis*, *Vallatisporites arcuatus*, *Cystoptychus azcuyi* e *Potonieisorites novicus* (di Pasquo et al., 2019 e referências nele).

Grupo Macharetí:

De acordo com Starck (1995) o ciclo Carbonífero-Jurássico inicia-se com a deposição do Grupo Macharetí sobre uma inconformidade existente no substrato Siluriano-Devoniano. De acordo com Suárez Soruco e Díaz Martínez (1996), de maneira geral a unidade está composta por arenitos, folhelhos e diamictitos, de variável extensão chegando até mais de 1000 m. Os cores das rochas variam desde preto e cinza escuro nos diamictitos e pelitos para uma cor cinza claro até cinza esbranquiçado nos arenitos; no entanto no topo do grupo ocorrem uns tons avermelhados relacionados com os processos de exposição e oxidação que aconteceram entre a deposição dos grupos Macharetí e Mandiyutí (Starck e Del Papa, 2006). No setor sul da Bolívia, esse grupo está composto por seis formações: Itacua, Tupambi, Itacuami, Tarija, Chorro e Taiguati (Figura 2.6).

Grupo Mandiyutí:

O Grupo Mandiyutí está separado do Grupo Macharetí por uma inconformidade proeminente (Starck, 1995). De acordo com Suárez Soruco e Díaz Martínez (1996), o grupo está composto por arenitos, folhelhos e diamictitos, de variável extensão chegando até mais de 600 m. A coloração geral desse grupo variam desde vermelho até branco, com níveis escuros isolados (Starck e Del Papa, 2006). Podem-se reconhecer duas unidades litológicas: formações Escarpment e San Telmo (Figura 2.6).

Grupo Cuevo:

De acordo Suárez Soruco e Díaz Martínez (1996), o Grupo está composto por uma sequência heterolítica (Figura 2.6) de espessuras variáveis devido a erosão, chegando até mais de 1000 m. As facies correspondem a uma bacia reduzida e parcialmente evaporítica, separada por uma discordância e coberta pelo Basalto Entre Rios com uma espessura que pode chegar até 84 m. O Grupo Cuevo está composto por três formações: Cangapi, Petaca e Ipaguazu (Figura 2.6).

Grupo Tacuru:

De acordo Suárez Soruco e Díaz Martínez (1996), esse grupo está composto por arenitos com intercalações de folhelhos e siltitos, com espessuras que podem chegar até 1500 m, e tem uma relação discordante com a unidade inferior. O Grupo Tacuru está

extensamente preservado na Bolívia e nas regiões subandinas na fronteira com a Argentina. Está composto quase na sua totalidade por arenitos com tons avermelhados e laranjas com estratificações cruzadas de grande escala, representando um grande campo de dunas (Starck et al., 1992). Esse Grupo está composto por três formações: Tapecua, Castellon e Ichoa (Figura 2.6).

Ciclo Cenozoico:

Esse ciclo está composto por rochas siliciclasticas de ambiente continental e em menor quantidade níveis de ambiente marinho marginal reconhecidos por vários autores nos níveis basais do ciclo Cenozoico (Hernández et al., 2005; Hulka et al., 2006; Uba et al., 2005, 2006, 2009a). De acordo com Rocha (2013), a acumulação de sedimentos nos sinclinais poderia superar os 5000 m de espessura. Está composto principalmente por arenitos, folhelhos, conglomerados, margas e tufos (Suárez Soruco e Díaz Martínez, 1996). Os níveis basais superpõem-se em uma ligeira discordância angular sobre as rochas do ciclo Carbonífero-Jurássico (ver Figura 2.6). As unidades que compõem o ciclo Cenozoico são sinorogênicas, desenvolvidas durante a formação da faixa de dobras e cavalgamentos da Cordilhera Oriental e das Serras Subandinas (Hernández et al., 1999; Uba et al., 2006). As formações que compõem esse ciclo são: Petacua, Yecua, Tariquia, Guandacay e Emborozu (Figura 2.6).

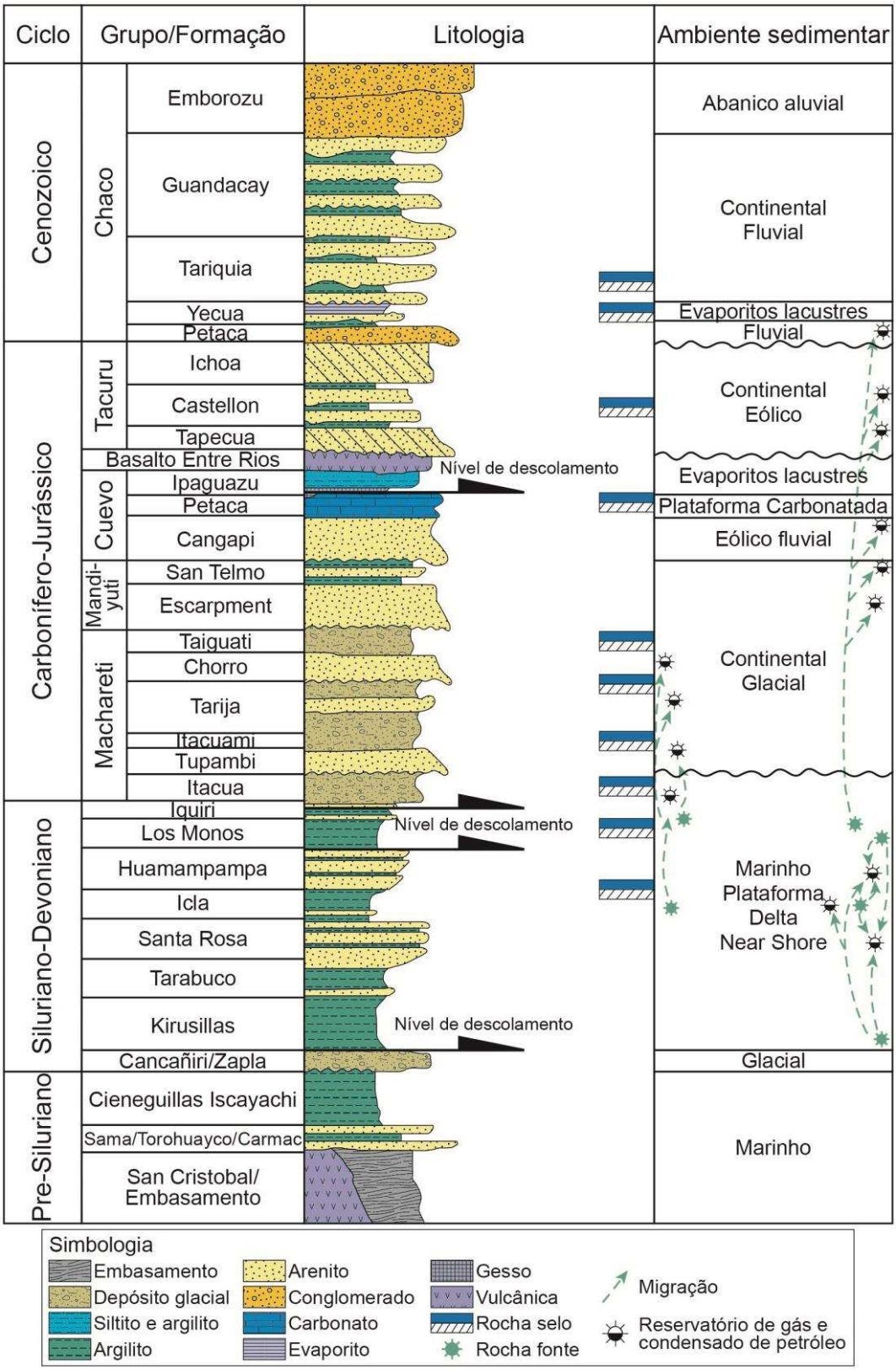

Figura 2.6: Coluna generalizada da Bacia de Tarija, ciclos sedimentares segundo Starck (1995). *Adaptado de* Giampaoli e Rojas Vera (2018).

2.4.2. GEOLOGIA ESTRUTURAL

O denominado "Subandino Sul" é uma típica faixa de dobras e cavalgamentos de pele fina (Figs. 2.7 e 2.8; Baby et al., 1992; Dunn et al., 1995) que limita ao leste com uma bacia de antepaís sem deformação e ao oeste com a região interandina (Rocha, 2013). O desenvolvimento da faixa de dobras e cavalgamentos da região subandina começou durante o Mioceno médio ao superior (Echavarria et al., 2003; Uba et al., 2009b), quando a megafalha da Cordilheira Oriental chegou até o nível de descolamento regional localizado nos folhelhos do Siluriano e o Ordoviciano superior (Fuentes et al., 2018). Essa deformação do sistema interandino e a Cordilheira Oriental pode estar associada com a reativação de estruturas pré-existentes, tais como falhas normais do Paleozoico inferior (Kley, 1996; Kley et al., 1996) ou estruturas formadas durante o Paleozoico ou Mesozoico (Allmendinger e Zapata, 2000).

A estrutura mais profunda consiste de uma falha reversa de baixo ângulo, com descolamento basal nos folhelhos da Formação Kirusillas (Siluriano) e o descolamento superior na Formação Los Monos (Devoniano) reconhecidos no setor sul da Bolívia (Baby et al., 1992; Dunn et al., 1995) e no noroeste da Argentina (Belotti et al., 1995; Echavarria et al., 2003). Os *duplexes* são o estilo estrutural dominante da faixa de dobras e cavalgamentos do Subandino, incluindo tipos de *roof-thrust* passivos, ativos e compostos (Fig. 2.8; Baby et al., 1992; Rocha, 2013).

Segundo Giampaoli e Rojas Vera (2018), as sequência estratigráfica da bacia de Taija pode ser divide mecanicamente em três intervalos estruturais: 1) embasamento pre-Siluriano; 2) nível estrutural inferior; e 3) nível estrutural superior. O topo do embasamento pre-Siluriano está definido pela presença da primeira camada incompetente que corresponde à Formação Kirusillas. Essa unidade está composta por um pacote de folhelhos que mostram um forte contraste reológico com o embasamento pre-Siluriano e controla o descolamento basal das estruturas maiores. O nível estrutural inferior está composto pelas formações Kirusillas, Tarabauco, Santa Rosa, Icla e Huamampampa; o horizonte medianamente incompetente corresponde à base da Formação Los Monos. Enquanto que o nível estrutural superior está composto pelas unidades competentes do Carbonífero até o Plioceno, descoladas do topo da Formação Iquiri ou dos folhelhos da Formação Los Monos (Giampaoli e Rojas Vera, 2018).

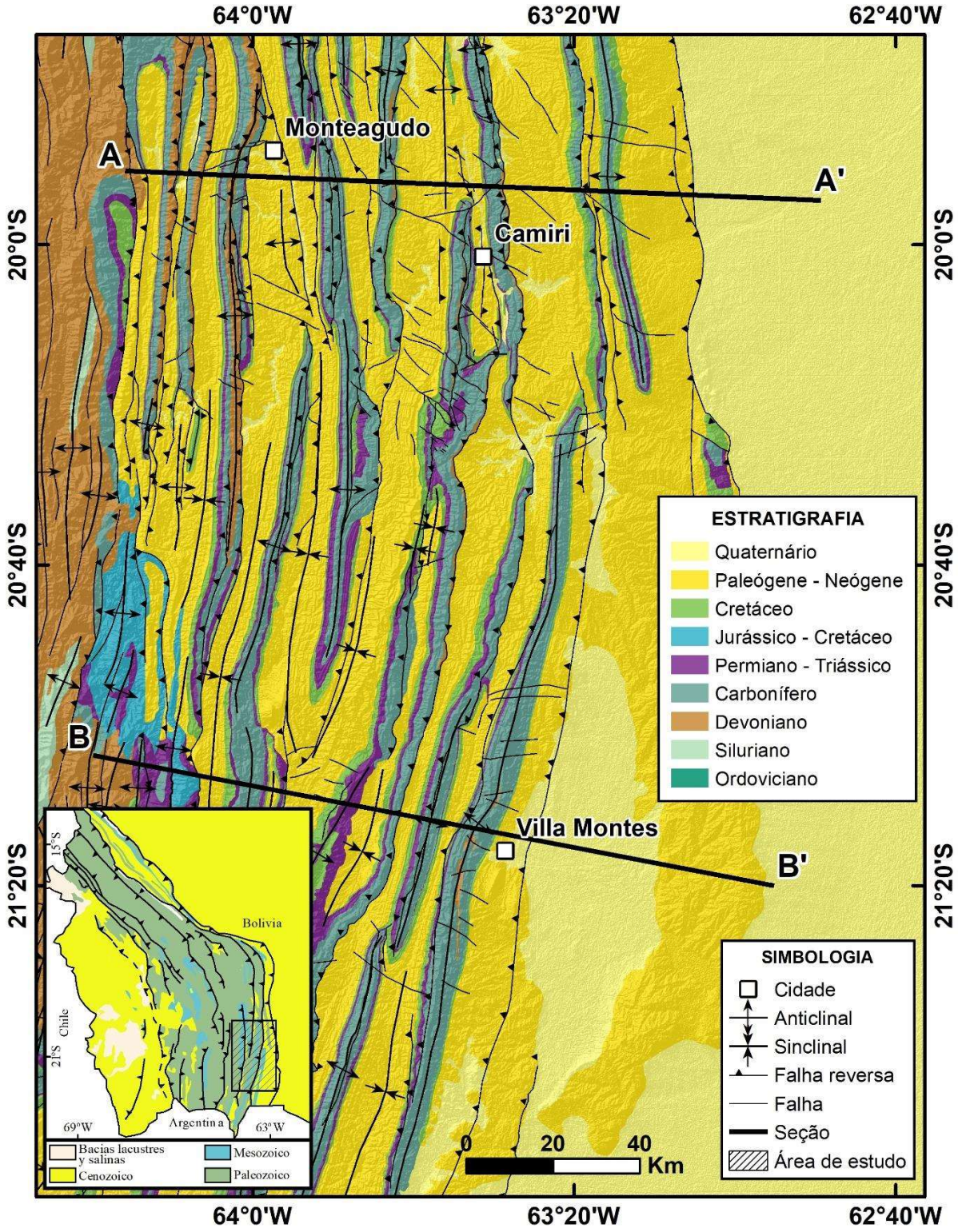

Figura 2.7: Mapa geológico simplificado da área de trabalho, Zona Subandina Sul da Bolívia, Bacia de Tarija. Adaptado de Anderson et al. (2017); Giampaoli e Vera (2018). A-A' e B-B' representam as seções geológicos apresentados na Fig. 2.8.

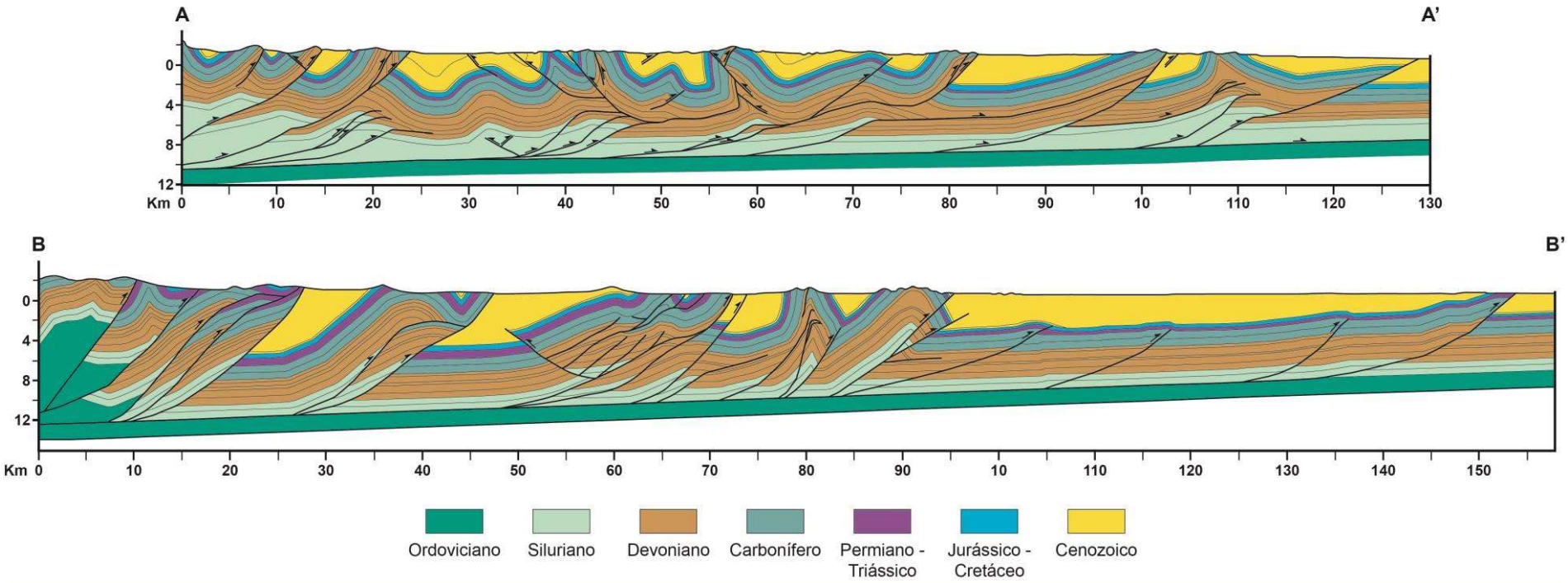

Figura 2.8: Seções geológicas A-A' e B-B' da Zona Subandina Sul da Bolívia. Tomado de Fuentes et al. (2018). *Os traços da seções geológicas estão representados na Fig. 2.7.*

2.5. CORRELAÇÃO DAS BACIAS DO SETOR SUDOESTE DO GONDWANA

De acordo com Milani e De Wit (2008), a evolução das bacias do setor oeste do Gondwana (Figura 2.9) esteve ligada com o crescimento externo da litosfera continental do orógeno Gondwanides durante o Paleozoico. As importantes similitudes dessas bacias foram motivo de estudos e discussões ao longo do tempo (Milani e De Wit, 2008; Rapela et al., 2003) como o intuito de melhorar as correlações feitas por *du Toit* no libro "*Our Wandering Continents*". Vários autores (p.e. Limarino e Spalletti, 2006; Linol et al., 2015; Milani e De Wit, 2008; Sempere, 1995; Vargas et al., 2020) reconheceram e estabeleceram a interconexão entre diferentes bacias da parte sudoeste de Gondwana como as bacias Tarija, Paraná, Chaco-Paraná, Sauce Grande, Paganzo, Navidad Arizaro, Madre de Dios e Karoo. Assim, importantes eventos regionais puderam ser reconhecidos nas bacias coetâneas nesse setor de Gondwana mediante o estudo e comparação das sequencias sedimentarias (Figura 2.10) e dos dados de proveniência sedimentar. A compilação de dados U-Pb em grãos de zircão detrítico dessas bacias será apresentada no Capitulo 4.

De acordo com Vargas et al. (2020) os padrões de empilhamento semelhantes identificados nessas bacias durante o Devoniano (Figura 2.10) sugerem que elas formaram parte de um sistema marinho interconectado e foram afetados similarmente por eventos transgressivos e regressivos coetâneos. A presencia desses eventos transgressivos e regressivos coetâneos que abrangem várias bacias em toda América do Sul, e sua correlação com a curva global do nível do mar, demostram que a eustasia foi o componente predominante da flutuação do nível base nas bacias do setor sudoeste de Gondwana durante o Devoniano médio e superior (Haq e Schutter, 2008). No entanto, existem evidencias que sugerem que durante o Devoniano inferior, essas bacias foram mais afetadas por tectonismo do que pela eustasia (Vargas et al., 2020). Segundo alguns autores (Heredia et al., 2018b; Milani e De Wit, 2008), esses processos tectônicos foram provavelmente relacionados com os fenômenos orogênicos da Precordillera que afetaram as bacias do setor sudoeste de Gondwana durante o ciclo Famatiniano.

Por outro lado, segundo Valdez et al. (2020) durante o Carbonífero, Gondwana formou uma extensa massa de terra do hemisférios sul que foi afetada por vários episódios glaciais, o que resultou na deposição de sedimentos glaciais, periglaciais e deglaciais em bacias em uma grande parte do Gondwana (Figura 2.10) (Craddock et al., 2019; Fedorchuk et al., 2021; Linol et al., 2016; Milani e De Wit, 2008; Valdez et al., 2020).

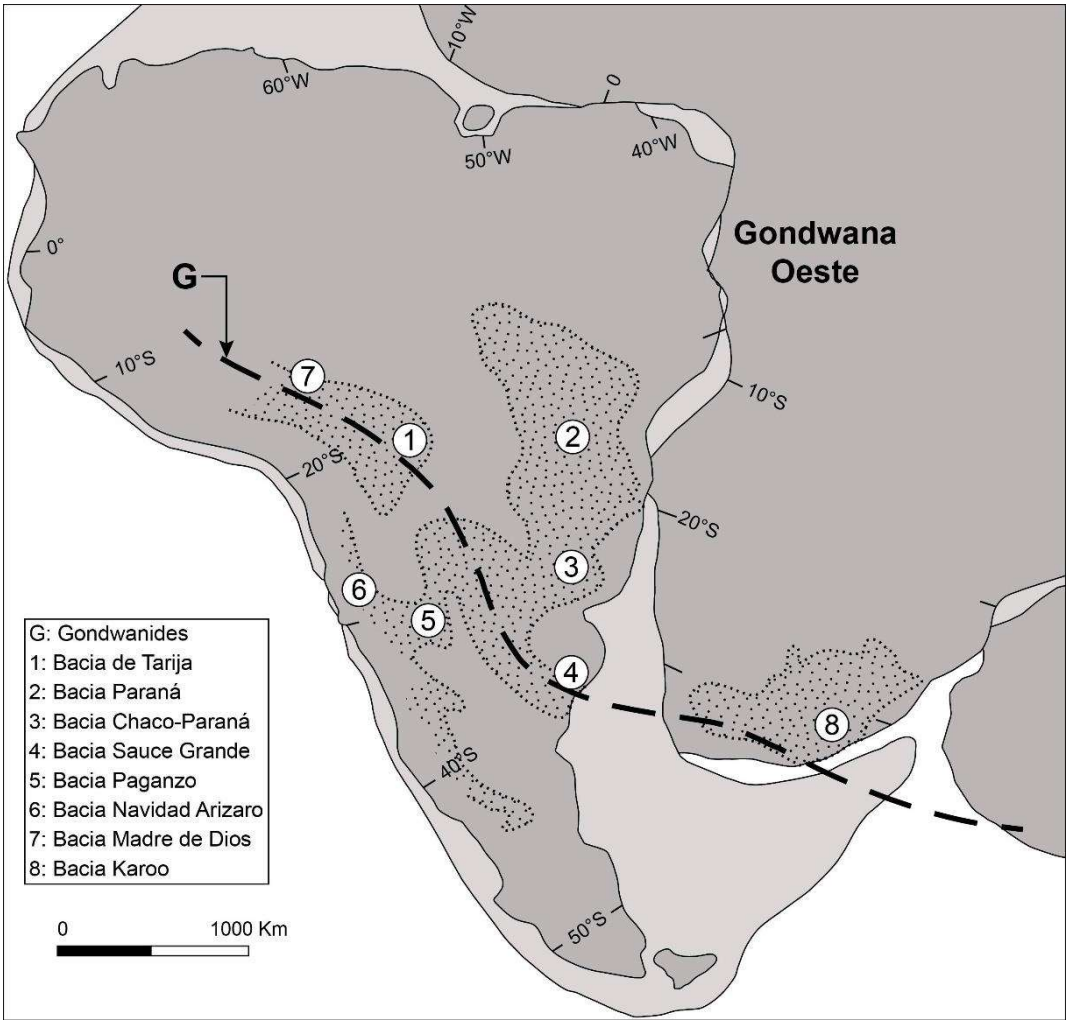

Figura 2.9: Distribuição das principais bacias ligadas ao orógeno no interior do Gondwana durante o Paleozoico, tomado de Milani e De Wit (2008).

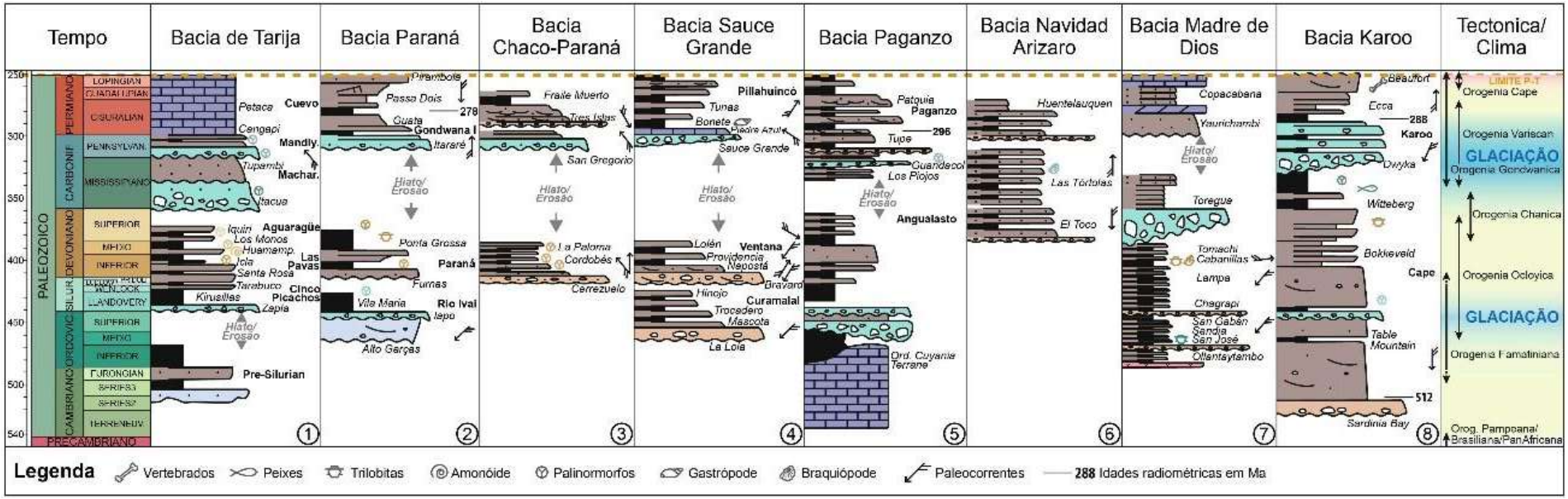

Figura 2.10: Sequências estratigráficas do Paleozoico das bacias Tarija, Paraná, Cape-Karoo, Sauce Grande, e Precordillera-Paganzo presentadas na Fig. 2.8, e correlação de tempo com os eventos tectônicos do oeste do Gondwana. Retirado e modificada de Linol et al. (2016) *com dados estratigráficos e paleontológicos de diversos autores* (Bahlburg et al., 2009; Fedorchuk et al., 2021; Grahn, 2003; Gulbranson et al., 2010; Kołtonik et al., 2019; Milani e De Wit, 2008; Ramos et al., 2014; Reimann et al., 2015; Uriz et al., 2016).

2.6. PROVENIÊNCIA SEDIMENTAR

A composição isotópica Sr-Nd de sedimentos de grão fino (argilitos e siltitos) podem ser importantes para estabelecer uma integração completa das rotas de drenagem das áreas cratônicas mais distantes para as bacias oceânicas (Patchett et al., 1999). Uma das razões é que esses tipos de rochas não são influenciadas pelo selecionamento do tamanho de grão (Cullers, 2000; McLennan et al., 1993) quando são comparadas com fracções maiores (Bouchez et al., 2011; McLennan et al., 1993; Roddaz et al., 2014). Outra razão é a concentração e em consequência as razões desses isótopos não são substancialmente afetados por processos sedimentares e secundários (McLennan et al., 1993). Assim é possível traçar a proveniência sedimentar usando o mesmo critério que dos sedimentos atuais. Nesse sentido, vários autores têm sido usados a composição isotópica de Nd e Sr de sedimentos e rochas sedimentares das Zonas Subandinas e cratônicas para determinar sua proveniência e paleodrenagem (p.e. Basu et al., 1990; Hurtado et al., 2018; Nie et al., 2012; Roddaz et al., 2005; Viers et al., 2008)

De maneira semelhante, as idades U-Pb de grãos de zircão detrítico tem sido usados para traçar a proveniência de rochas sedimentares na região andina, considerando as diferentes idades dos terrenos e eventos geocronológicos que compõem os Andes e o Cráton Amazônico (p.e. Bahlburg et al., 2009; Calle et al., 2018; Hurtado et al., 2018; Reimann et al., 2010). O tamanho e forma dos grãos de zircão detrítico podem ser correlacionados com suas idades, permitindo avaliar efeitos hidrodinâmicos nas populações das idades dos grãos de zircão. Outra maneira interessante de complementar essas informações é mediante as análises da morfologia e texturas internas e externas, porque essas características podem refletir a história geológica do zircão, especialmente os episódios relevantes de cristalização e recristalização magmática e metamórfica (Corfu et al., 2003).

2.7. POTENCIAIS AREAS FONTES

As principais potencias fontes das unidades sedimentares devonianas-carboníferas incluem rochas pré-cambrianas do Cráton Amazônico, o maciço Arequipa-Antofalla, rochas das Sierras Pampeanas e as rochas do magmatismo Paleozoico dos Andes centrais (Figura 2.11).

O CRÁTON AMAZÔNICO:

Segundo vários autores (p.e. Basu et al., 1990; Roddaz et al., 2005) é possível distinguir entre uma fonte cratônica e uma andina fazendo uso da composição isotópica Sr-Nd de sedimentos de grão fino, além das idades U-Pb em grãos de zircão detrítico em arenitos. As rochas sedimentares derivadas de áreas cratônicas têm valores de $\varepsilon_{Nd(0)} > -13.8$ (Figueiredo et al., 2009; Hurtado et al., 2018; Roddaz et al., 2005). Não existe um *cut-off* estrito para a composição isotópica de Sr, mas em geral as rochas sedimentares derivadas do cráton estão caracterizadas por razões $^{87}Sr/^{86}Sr$ mais radiogênicas do que as rochas sedimentares derivadas dos Andes (e.g. Basu et al., 1990; Roddaz et al., 2005). De uma maneira similar, as idades U-Pb dos grãos de zircão detrítico tem sido usadas para traçar a proveniência sedimentar das rochas sedimentarias porque os terrenos do Cráton Amazonico e dos Andes têm diferentes idades. De uma maneira geral, as rochas derivadas do Cráton Amazônico possuem populações com idades > 900 Ma, enquanto que as rochas derivas dos Andes possuem populações com idades < 900 Ma (p.e. Bahlburg et al., 2009; Calle et al., 2018; Chew et al., 2008; Hurtado et al., 2018; Reimann et al., 2010). No entanto, idades > 900 Ma também podem ser encontradas no setor dos Andes como produto de uma superposição múltipla de eventos tectônicos como é o caso do Maciço de Arequipa-Antofalla (e.g. Loewy et al., 2004).

O MACIÇO AREQUIPA-ANTOFALLA:

O Maciço de Arequipa-Antofalla, de acordo com Loewy et al. (2004), está dividido em três domínios: domínio Norte, Centro e Sul. Eles representam uma superposição múltipla de eventos tectônicos que afetaram a região. Os domínios possuem diferentes idades e composições isotópicas, com um decrescimento nas idades desde norte para o sul. O domínio norte está composto por rochas com idades entre 500 – 420 Ma, 1300 – 900 Ma, 2000 – 1820 Ma e também pode ter componentes > 2200 Ma (*pre-Andean inliers*). Os valores iniciais de ε_{Nd} variam entre -4.3 e -1.0 (Loewy et al., 2004). Além disso, o domínio norte também está superposto pelo batólito de San Nicolas com idades U-Pb (*lower intercept*) de 425 e 394 – 388 Ma (Mukasa e Henry, 1990).

Por outro lado, os domínios centro e sul estão compostos por componentes com idades entre 500 – 420 Ma, 1300 – 900 Ma e também poder ter componentes com idades > 2200 Ma (*pre-Andean inliers*). O valores inicias de ε_{Nd} de esses domínios podem atingir valores entre -10.3 e +3.9 (Loewy et al., 2004).

AS SIERRAS PAMPEANAS:

As rochas formadas durante o evento Pampeano estão representadas pelo terreno denominado "Sierras Pampeanas". Essa unidade morfoestrutural consiste das subprovíncias geológicas Orientais e Ocidentais, as quais são uma serie de terrenos acrescionados. As Sierras Pampeanas Orientais estão compostas por rochas do Neoproterozoico até o Paleozoico superior, com idades que variam entre 700 – 500 Ma (p.e. Pankhurst e Rapela, 1998; Rapela et al., 1998). Enquanto que as Sierras Pampeanas Ocidentais estão compostas por rochas do Mesoproterozoico até o Paleozoico superior, com idades que variam entre 1300 – 900 e 700 – 500 Ma (p.e. Casquet et al., 2008, 2001; Morata et al., 2010; Pankhurst e Rapela, 1998; Varela et al., 2003). De uma maneira geral, os valores inicias de ε_{Nd} das Sierras Pampeanas atingem um rango entre -9.9 e +5.4, e razões inicias $^{87}Sr/^{86}Sr$ entre 0.702 e 0.731 (p.e. Casquet et al., 2008; Morata et al., 2010; Rapela et al., 1998; Varela et al., 2003).

2.7.1. O MAGMATISMO PALEOZOICO

O magmatismo Paleozoico como potencial fonte de sedimentos da bacia, está composto pelo Arco Magmático Famatiniano e o magmatismo intracontinental e de retroarco do Paleozoico superior no noroeste da Argentina. As rochas ígneas relacionadas com esse arco possuem idades entre 500 – 4200 Ma; com valores inicias de ε_{Nd} que podem atingir um rango entre -12.6 e -4.2 (Bock et al., 2000; Cardona, 2006; Pankhurst et al., 1998), e razões inicias $^{87}Sr/^{86}Sr$ que variam entre 0.706 e 0.716 (Pankhurst et al., 1998). Enquanto que o magmatismo intracontinental e de retroarco do Paleozoico superior (batólitos Chacras-Potrerillos, Renca e Achala) possuem idades entre 420 – 320 Ma (Dahlquist et al., 2019, 2018; López de Luchi et al., 2017); com valores inicias de ε_{Nd} que variam entre -4.8 e -0.6, e razões iniciais $^{87}Sr/^{86}Sr$ que variam entre 0.703 e 0.707 (Dahlquist et al., 2019; López de Luchi et al., 2017).

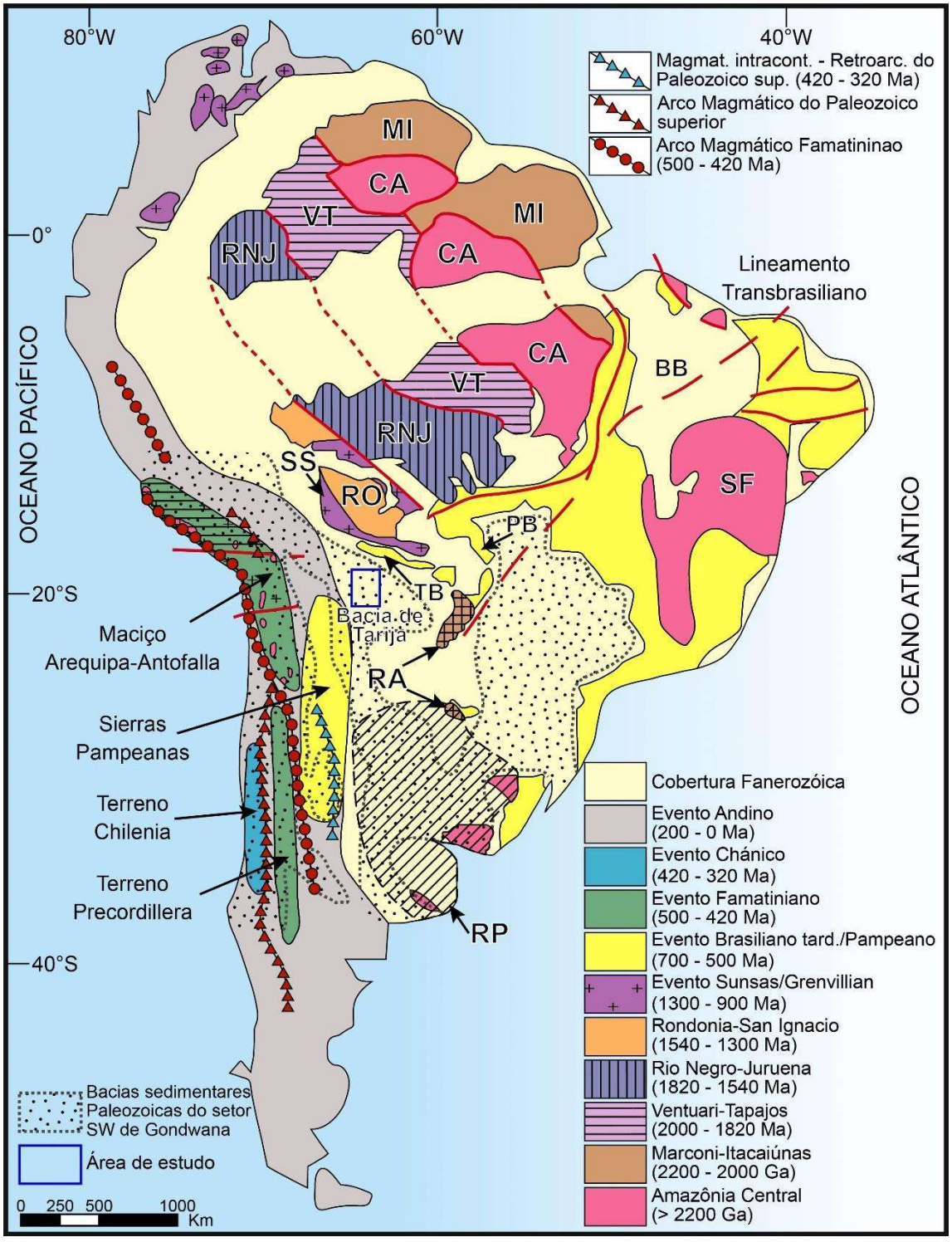

Figura 2.11: Mapa esquemático das províncias geocronológicas de América do Sul. Modificado de Bahlburg et al. (2009); Chew et al. (2008) e Reimann et al. (2010). *CA: Amazônia Central, MI: Marconi-Itacaiúnas, VT: Ventuari-Tapajos, RNJ: Rio Negro – Juruena, Ro: Rondonia-San Ignacio, SS: Sunsas/Grenvillian, SF: Cráton São Francisco, RP: Cráton Río de la Plata, RA: Rio Apa, BB: Faixa Brasilia, PB: Faixa Paraguai, e TB: Faixa Tucavaca.*

CAPÍTULO 3

AMOSTRAGEM E MÉTODOS

3.1. AMOSTRAGEM

3.1.1. ESTRATEGIA DE AMOSTRAGEM

Os trabalhos de campo foram feitos com o objetivo de reconhecer e coletar amostras das rochas sedimentares das unidades do intervalo Devoniano-Carbonífero da bacia de Tarija. Na parte sul da bacia de Tarija, no sul da Bolívia, foram feitos 3 perfis de campo nas proximidades das cidades de Camiri, Monteagudo (Figura 3.1A) e Villa Montes (Figura 3.1B). A amostragem teve como intuito atingir o registro sedimentar completo do intervalo Devoniano-Carbonífero (Figura 3.2).

3.1.2. LOCALIZAÇÃO E COLETA DAS AMOSTRAS

As amostras foram coletadas nas unidades do intervalo Devoniano-Carbonífero com o objetivo de observar as variações dos dados isotópicos e as mudanças das fontes dos sedimentos ao longo das colunas estratigráficas. Os dados das amostras estão resumidos na Tabela 3.1 e nas figuras 3.1, 3.2 e 3.3. A amostragem para cada tipo de análise foi feita no mesmo nível estratigráfico, de tal forma que os resultados possam ser complementados.

- U-Pb em zircão detrítico: foram coletadas um total de 7 amostras de arenitos. Cada amostra coletada possuía um peso que variou ente 4 e 5 Kg.
- Sr-Nd em rocha total: foram coletadas um total de 19 amostras de rochas sedimentares de granulometria fina (argilitos e siltitos). Cada amostra coletada possuía um peso não maior do que 0.5 Kg.
- Difratometria de Raios-X: foram coletadas um total de 15 amostras de rochas sedimentares de granulometria fina (argilitos e siltitos). Cada amostra possuía um peso não maior do que 0.5 Kg.
- Petrografia de arenitos: foram coletadas um total de 12 amostras de arenitos.

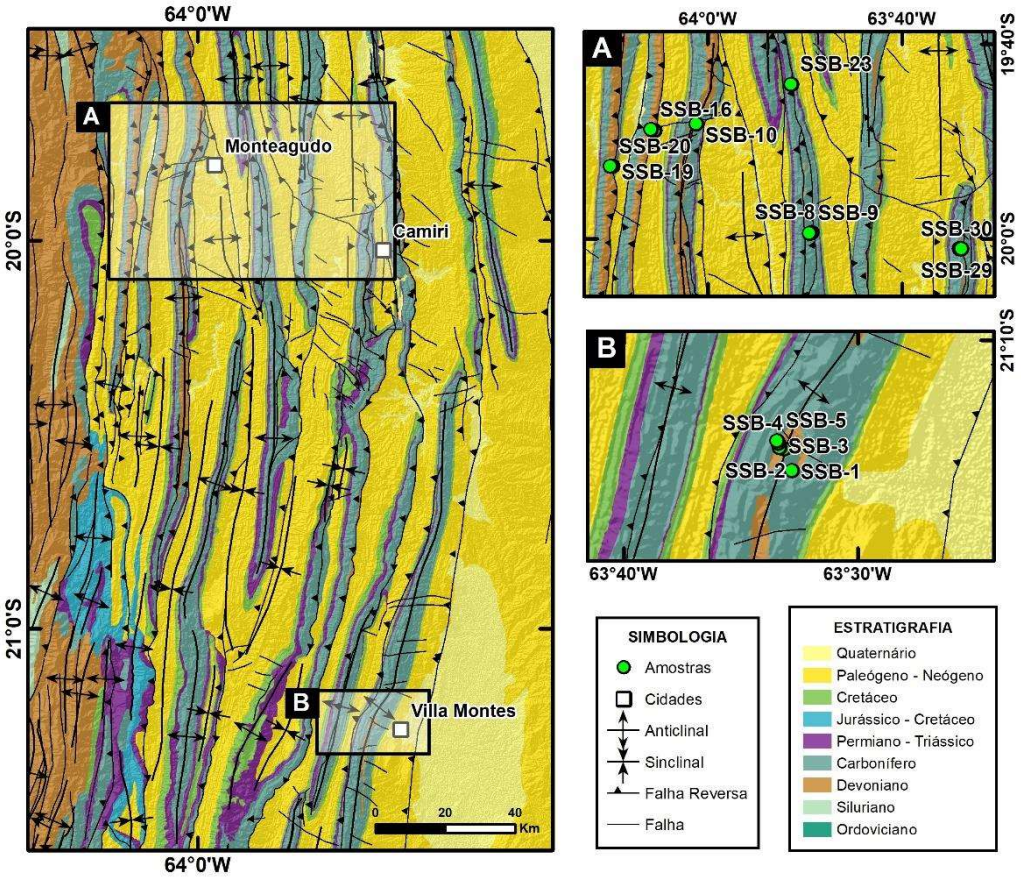

Figura 3.1. Mapa geológico simplificado da área de trabalho, Zona Subandina Sul da Bolívia, Bacia de Tarija. Adaptado de Anderson et al. (2017); Giampaoli e Vera (2018). A e B representam o mapas geológicos detalhados dos perfis realizados.

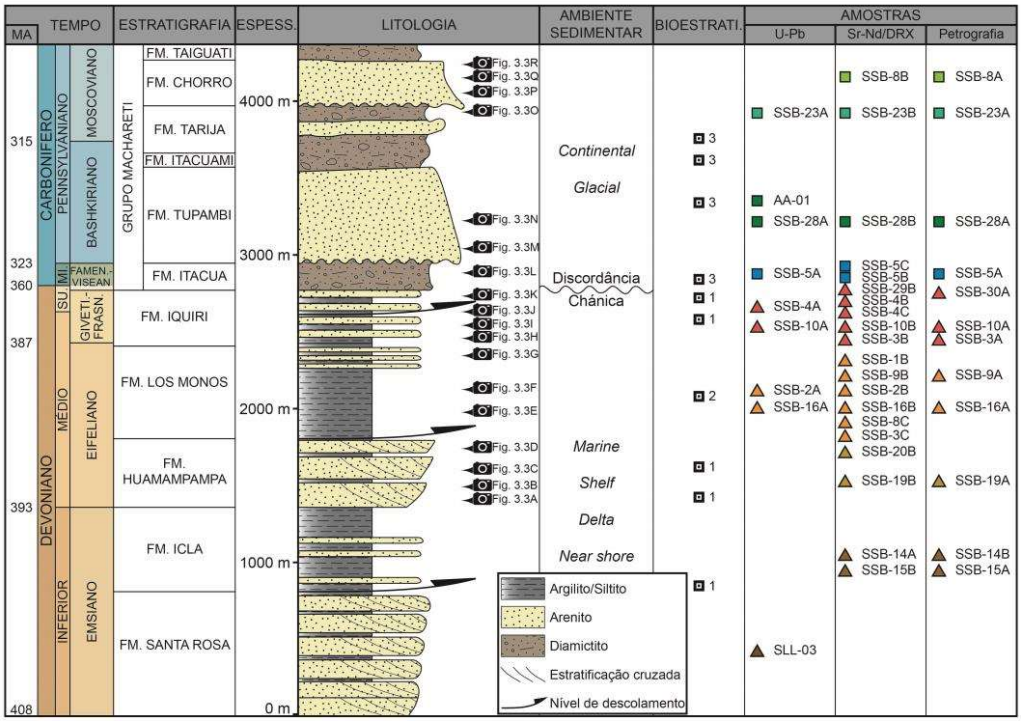

Figura 3.2: Coluna estratigráfica generalizada das unidades do Devoniano - Carbonífero da Bacia de Tarija. Retirada e adaptada de Giampaoli e Vera (2018). Bioestratigrafia: 1- Troth et al. (2011); 2- di Pasquo (2007b); e 3- di Pasquo et al. (2019). As amostras SLL-03 e AA-01 foram tomadas de Calle (2013).

Código	Formação	Idade	Long. (X)	Lat. (Y)	U-Pb	Sr-Nd	DRX	Petrografia
SSB-8A	Chorro	Carbonífero	-63.82281	-19.98934				X
SSB-8B	Chorro	Carbonífero	-63.82281	-19.98934		X	X	
SSB-23A	Tarija	Carbonífero	-63.85761	-19.73476	X			X
SSB-23B	Tarija	Carbonífero	-63.85761	-19.73476		X	X	
SSB-28A	Tupambi	Carbonífero	-63.56830	-20.01733	X			
SSB-28B	Tupambi	Carbonífero	-63.56830	-20.01733		X	X	X
SSB-5A	Itacua	Carbonífero	-63.55794	-21.23814	X			X
SSB-5C	Itacua	Carbonífero	-63.55794	-21.23814		X	X	
SSB-5B	Itacua	Carbonífero	-63.55794	-21.23814		X	X	
SSB-29B	Iquiri	Devoniano	-63.56745	-20.01780		X	X	
SSB-30A	Iquiri	Devoniano	-63.56530	-20.01802				X
SSB-4A	Iquiri	Devoniano	-63.55717	-21.24005	X			
SSB-4B	Iquiri	Devoniano	-63.55717	-21.24005		X	X	
SSB-4C	Iquiri	Devoniano	-63.55717	-21.24005		X		
SSB-10A	Iquiri	Devoniano	-64.02048	-19.80269	X			X
SSB-10B	Iquiri	Devoniano	-64.02048	-19.80269		X	X	
SSB-3A	Iquiri	Devoniano	-63.55608	-21.24305				X
SSB-3B	Iquiri	Devoniano	-63.55608	-21.24305		X	X	
SSB-1B	Los Monos	Devoniano	-63.54731	-21.25947		X	X	
SSB-9A	Los Monos	Devoniano	-63.82641	-19.99056				X
SSB-9B	Los Monos	Devoniano	-63.82641	-19.99056		X	X	
SSB-2A	Los Monos	Devoniano	-63.55295	-21.24416	X			
SSB-2B	Los Monos	Devoniano	-63.55295	-21.24416		X	X	
SSB-16A	Los Monos	Devoniano	-64.09835	-19.81271	X			X
SSB-16B	Los Monos	Devoniano	-64.09835	-19.81271		X	X	
SSB-8C	Los Monos	Devoniano	-63.82281	-19.98934		X	X	
SSB-3C	Los Monos	Devoniano	-63.55608	-21.24305		X	X	
SSB-20B	Huamampampa	Devoniano	-64.16868	-19.87594		X	X	
SSB-19A	Huamampampa	Devoniano	-64.16473	-19.87589				X
SSB-19B	Huamampampa	Devoniano	-64.16473	-19.87589		X	X	
SSB-14A	Icla	Devoniano	-64.09370	-19.81412		X	X	
SSB-14B	Icla	Devoniano	-64.09370	-19.81412				X
SSB-15A	Icla	Devoniano	-64.09282	-19.81441				X
SSB-15B	Icla	Devoniano	-64.09282	-19.81441			X	

Tabela 3.1: Dados das amostras coletadas na bacia de Tarija e as análises feitas em cada uma delas.

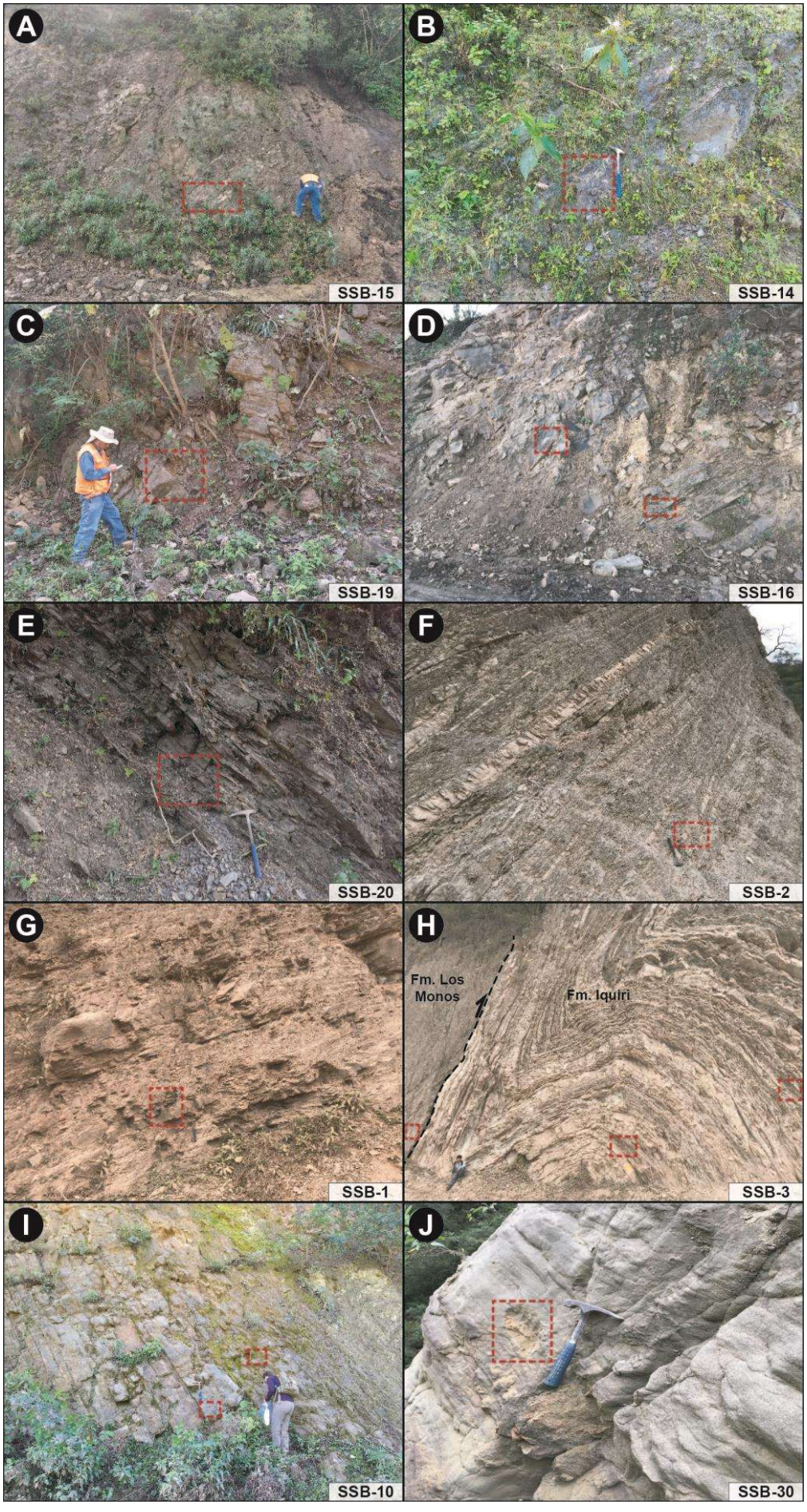
A
SSB-15
B
SSB-14
C
SSB-19
D
SSB-16
E
SSB-20
F
SSB-2
G
SSB-1
H
Fm. Los Monos
Fm. Iquiri
SSB-3
I
SSB-10
J
SSB-30

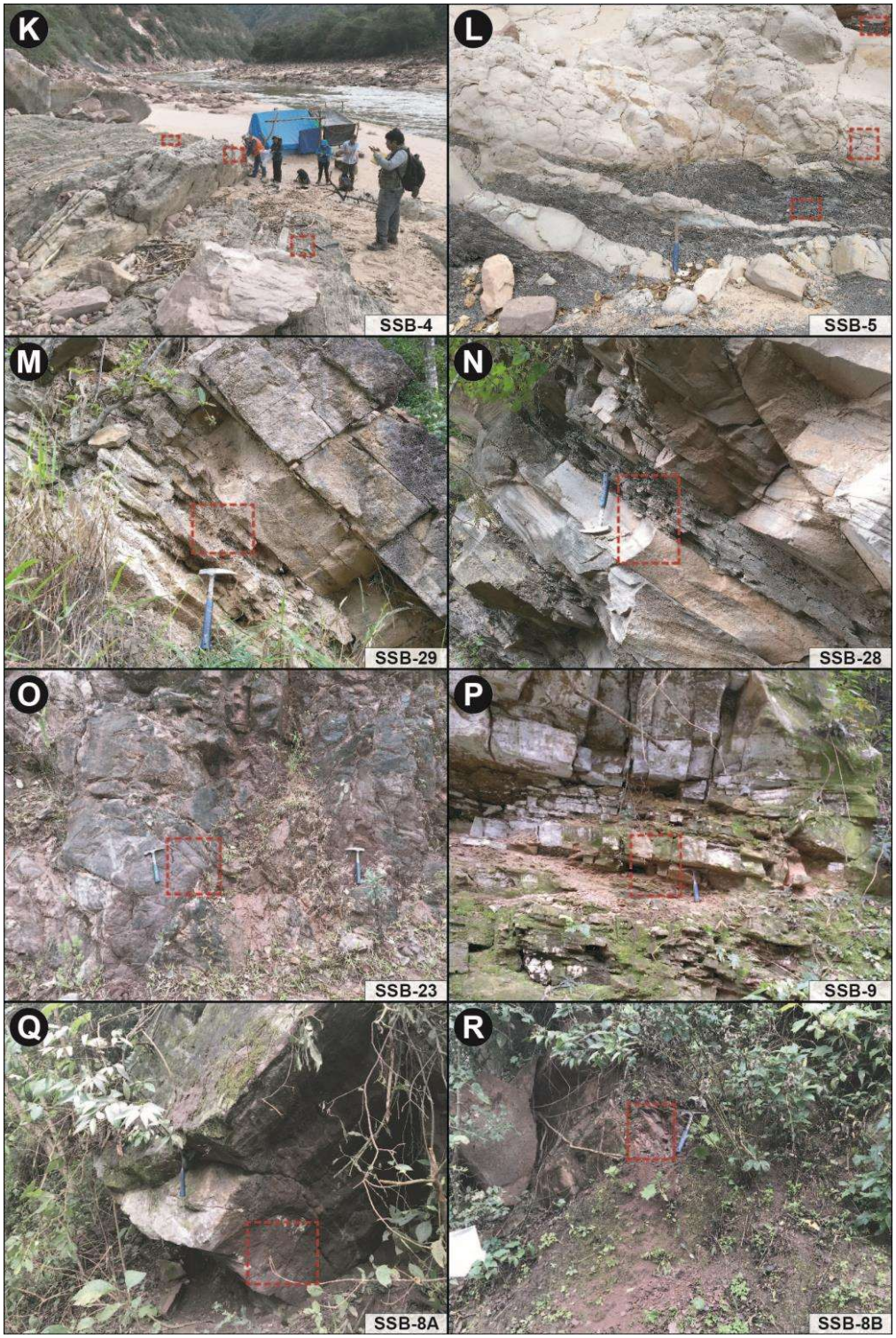

Figura 3.3: Imagens dos afloramentos onde foi feita a coleta das unidades devonianas e carboníferas da bacia de Tarija. A-D) Formação Huamampampa. E-G) Formação Los Monos. H) Afloramentos das formações Los Monos e Iquiri, postas em contato por uma falha reversa. I-K) Formação Iquiri. L) Formação Itacua. M-N) Formação Tupambi. O) Formação Tarija. P-R) Formação Chorro. As áreas vermelhas pontilhadas representam os pontos de amostragem dos afloramentos. A localização das amostras e a posição estratigráfica delas estão representadas na Tabela 3.1 e nas figuras 3.1 e 3.2, respectivamente.

3.2. PREPARAÇÃO DAS AMOSTRAS

Todas as amostras foram preparadas e processadas no Laboratório de Estudos Geodinâmicos, Geocronológicos e Ambientais (LEGGA) da Universidade de Brasília (UnB).

O processo de preparação dos arenitos para a separação dos grãos de zircão detrítico pode ser observado na Figura 3.4. A britagem manual das rochas foi feita utilizando o martelo, seguido da britagem mecânica feita no *Jaw crusher* para reduzir o tamanho das amostras até um tamanho aproximado de 3 cm, logo foram britadas novamente no moinho de panela *Herzog* até reduzir ao tamanho de areia. Após de que as amostras foram britadas, foram lavadas com água para retirar a argila, logo foram secadas na lâmpada e peneiradas em intervalos de > 250 µm, 250 – 164 µm e < 164 µm. Durante a separação percebeu-se que a concentração maior dos grãos de zircão estava na fração < 164 µm, no entanto foram selecionadas as duas frações menores para a separação em todas as amostras, enquanto a fração maior foi armazenada.

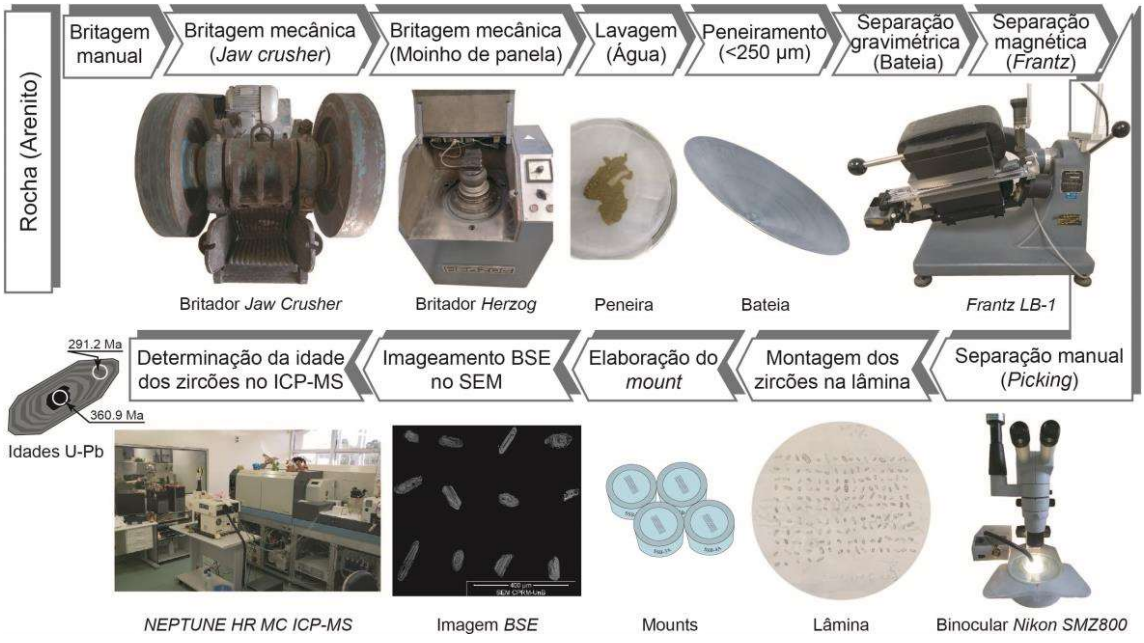

Figura 3.4: Fluxo de trabalho da preparação e a análise U-Pb das amostras de zircão em arenitos.

Nas frações 250 – 164 e < 164 µm, iniciou-se o processo de separação gravimétrica dos minerais pesados utilizando uma bateia galvanizada e uma tigela grande com água, onde foram realizados movimentos oscilatórios que permitiram separar a fração de minerais pesados dos minerais ligeiros. A água da bacia foi trocada para cada amostra com o objetivo de recuperar a fração que ficava no fundo e realizar uma posterior

recuperação no caso fosse necessário. O concentrado de minerais pesados foi passado pelo separador magnético *Frantz* modelo *LB-1*, com uma amperagem de 1.5 A°, para separar os minerais magnéticos (com susceptibilidades magnéticas menores do que 1.5 A°) dos minerais não magnéticos. A fração não magnética foi colocada em uma placa de Petri, e foi realizado o microbateamento com álcool etílico hidratado, realizando movimentos oscilatórios para concentrar os minerais pesados na borda da placa. Nessa área foi feito o *picking* do mineral zircão com uma agulha e com ajuda de uma lupa binocular *Nikon SMZ800*. Os grãos de zircão foram coletados aleatoriamente, posteriormente foram montados em uma lâmina e foram recobertos com resina *epoxy* e endurecedor para obter o *mount*. A superfície do *mount* foi polida e metalizada por uma película de carbono para a realização das imagens de elétrons retroespalhados (*Back Scattered Electrons*, BSE) no microscópio eletrônico de varredura (MEV). Essas imagens ajudaram na determinação tipológica e morfológica dos grãos de zircão, além de definir áreas alvo (núcleo e borda) para realizar as datações U-Pb.

Por outro lado, o processo de preparação das amostras de rochas sedimentares finas (argilitos e siltitos) para aobtenção das razões isotópicas Sr-Nd pode ser observado na Figura 3.5. As amostras coletadas foram lavadas com água, colocadas em placas de Petri e secadas na estufa até uma temperatura de 70 °C durante 24 horas para retirar todo resíduo de água. Após o secado, as amostras foram britadas no moinho de panela *Herzog* até a pulverização completa. Entre cada processo de pulverização foi feita a lavagem da panela, além disso, foi feito a pulverização de um branco (quartzo) entre cada amostra, seguida da pulverização de uma pequena porção da amostra antes de pulverizar ela, isso foi feito com o objetivo de evitar a contaminação entre as diferentes amostras. Finalmente, as amostras foram coletadas em potes para posteriormente realizar os análises isotópicos Sr-Nd e análises de difratometria de raios-X.

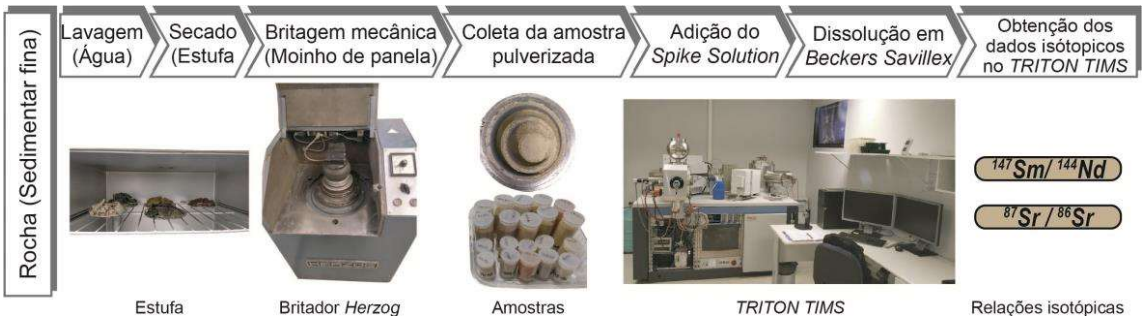

Figura 3.5: Fluxo de trabalho da preparação e análise Sr-Nd das amostras sedimentares de granulação fina.

3.3. MÉTODOS

3.3.1. PETROGRAFIA DE ARENITOS

Os estudos petrográficos dos arenitos foram realizados tomando em conta a metodologia *Gazzi-Dickinson* de contagem por pontos proposta por Ingersoll et al. (1984), a classificação de arenitos proposta por Garzanti (2019) e o esquema genético proposto por Dickinson (1985). O espaçamento considerado entre pontos foi de 1 mm e foram contabilizados um total de 400 pontos por lâmina delgada, além de realizar uma descrição da fração clástica e os componentes dela. A descrição petrográfica dos arenitos foi realizada num microscópio petrográfico de luz polarizada modelo *Zeiss* e com ajuda do *XY stage* do microscópio. Os dados foram parametrizados para cada amostra e calculados como quartzo total [Q = quartzo monocristalino (Qm) + quartzo policristalino (Qp)], feldspar [F = plagioclase (P) + feldspar potássico (Fk)] e fragmentos líticos [L = líticos sedimentares (Ls) + líticos vulcânicos (Lv) + líticos plutônicos (Lp) + líticos metamórficos (Lm) + fragmentos de chert (Lch)].

3.3.2. DIFRATOMETRIA DE RAIOS-X (XRD)

As análises de difratometria de raios-X foram realizadas para determinar de forma qualitativa a mineralogia das argilas existentes nas unidades devonianas (formações Icla, Huamampampa, Los Monos e Iquiri) e carboníferas (formações Itacua, Tupambi, Tarija e Chorro). Foram analisadas um total de 19 amostras de rochas sedimentares finas (argilitos e siltitos). A preparação das amostras paras as análises de difratometria de raios-X foram feitas no Laboratório de Estudos Geodinâmicos, Geocronológicos e Ambientais (LEGGA) como foi detalhado na Secção 3.2. Enquanto que as análises de DRX foram realizadas no *Laboratório de Rayos X* do *Instituto de Geocronología y Geología Isotópica* (INGEIS) da Universidade de Buenos Aires, e no Laboratório de Difração de Raios-X (LARIX) do Instituto de Geociências da Universidade de Brasília. O INGEIS e o LARIX realizaram a preparação da fracção argila seguindo a metodologia sugerida por Moore e Reynolds (1997) e Alves (1987), respectivamente.

A fracção < 2 μm foi usada convencionalmente para as medições do índice cristalográfico. As medições foram feitas nas fracções de argilas orientadas secas ao ar (AD), solvatadas com etileno-glicol (EG), solvatadas com glicerol (G) e depois do aquecimento (H).

Os componentes mineralógicos da fracção argila foram estabelecidos como componentes majores (M), menores (m) e traços (tr). Essa codificação foi estabelecida pelas comparações das intensidades das reflexões em *d*. Para os componentes não filosilicaticos foram considerados os valores ~2.7 Å para a hematita, ~3.18 Å para o plagioclásio, ~3.25 Å para o feldspato potássico, ~4.18 Å para a goethita e ~4.26 Å para o quartzo. Por outro lado, para os componentes filosilicaticos foram considerados os valores ~7 Å para a caulinita, ~10 Å para a illite e ~14 Å para a clorita, esmectite ou vermiculita, quando se expandem o cambiam na solvatação com etileno-glicol/glicerol ou são aquecidas.

3.3.3. ISÓTOPOS DE Sm-Nd

As análises isotópicas de Sm-Nd das rochas sedimentares finas foram realizadas utilizando o *TRITON Plus thermal Ionization Mass Spectrometer* (TIMS), instalado no Laboratório de Estudos Geodinâmicos, Geocronológicos e Ambientais (LEGGA) da Universidade de Brasília. O TIMS possui uma fonte termo-iônica e está dotado de coletores tipo copo Faraday móveis e uma multiplicadora de elétrons central.

As análises realizadas seguiram o procedimento sugerido por Gioia e Pimentel (2000). As amostras pulverizadas foram previamente pesadas (50 até 100 mg) e foi adicionada uma solução isotópica traçadora de ^{149}Sm e ^{150}Nd (*Spike Solution*) com concentrações conhecidas. A mistura foi dissolvida em cápsulas de Savillex com ataques sucessivos de ácidos (HNO_3, HF e HCl) em diferentes proporções até que a solução seja clara e homogênea como é sugerido por Gioia e Pimentel (2000). A separação dos elementos Sm e Nd foram feitas através de colunas cromatográficas com resina de intercambio catiônico, confeccionadas de teflon e envolvida com resina LN-Spec, que consiste de teflon revestido por *di-ethylexil phosphoric acid* (HDEHP). A coluna primaria consegue realizar a separação dos elementos de terras raras, dos elementos restantes. Posteriormente foi feita uma cromatografia em fase reversa, a fim de separar o Sm e Nd das terras raras. As soluções com concentrações dos elementos Sm e Nd são depositados por separados nos filamentos de rênio para realizar a vaporização, finalmente os filamentos são colocados no tambor do espectrômetro e são feitos os análises dos elementos Sm e Nd por separado junto com um padrão (BHVO-2).

As incertezas para as rações de $^{147}Sm/^{144}Nd$ e $^{143}Nd/^{144}Nd$ são melhores do que ± 0.1% (2σ) e ± 0.003% (2σ), respectivamente, de acordo com as análises repetidas do padrão BHVO-2 (Nd=25.2 ppm e Sm=6.2 ppm; Govindaraju, 1994). A constante de

decaimento utilizada foi $\lambda^{147}Sm = 6.54 \times 10^{-12}\ y^{-1}$. As razões $^{143}Nd/^{144}Nd_{sample}$ foram expressadas como ε_{Nd}. Foi realizada a correção de tempo (t = 300 Ma) do ε_{Nd} para o diagrama $^{87}Sr/^{86}Sr$ vs ε_{Nd}, enquanto que outra correção de tempo (t = 314 – 397 Ma) foi utilizada para o diagrama ε_{Nd} *evolution*. O T_{DM} (*Single-stage model*) foi calculado de acordo com Goldstein et al. (1984) e o T_{DM}* (*Two-stage model*) foi calculado de acordo com (Liew e Hofmann, 1988). O T_{DM} e o T_{DM}* foram calculados para propósitos comparativos.

3.3.4. ISÓTOPOS DE $^{87}Sr/^{86}Sr$

As análises isotópicas de Sr das rochas sedimentares finas foram realizadas utilizando o *TRITON Plus thermal Ionization Mass Spectrometer* (TIMS), instalado no Laboratório de Estudos Geodinâmicos, Geocronológicos e Ambientais (LEGGA) da Universidade de Brasília. Para a determinação da ração $^{87}Sr/^{86}Sr$ foram seguidos os procedimentos internos do próprio laboratório. Foi usado entre 50 e 100 mg da rocha pulverizada, a qual é dissolvida com ataques sucessivos com ácidos (HCl) até que se torne uma solução clara e homogênea. A separação do Sr foi feita através de colunas cromatográficas com resina de intercambio catiônico, confeccionadas de teflon e envolvida com resina Sr-Spec (Dt Bu CH18-c6 em 1-octanol). A solução com concentração de Sr é depositada num filamento para realizar a vaporização, finalmente o filamento é colocado no tambor e elevado no espectrômetro para realizar as análises, ao igual do que o processo do análise Sm-Nd. As análises repetitivas do material de referencia NBS 987 atingiram um valor médio de $^{87}Sr/^{86}Sr = 0.71028 \pm 0.000035$ (2SE). Foi feita a correção de tempo (t = 300 Ma) das razões $^{87}Sr/^{86}Sr$ para o diagrama $^{87}Sr/^{86}Sr$ vs ε_{Nd}. Como as razões $^{87}Rb/^{86}Sr$ não foram medidas, foram usados os conteúdos de Rb = 125 e Sr = 142 ppm dos valores referenciais da NASC para rochas de grão fino obtidas do trabalho de Gromet et al. (1984).

3.3.5. MORFOLOGIA DO ZIRCÃO

As análises da morfologia, núcleos reabsorvidos dos grãos de zircão detrítico foram realizadas com a ajuda das imagens de elétrons retroespalhados (*Back Scattered Electrons*, BSE) feitas no Microscópio Eletrônico de Varredura (MEV) *FEI QUANTA 450* instalado no LEGGA da Universidade de Brasília. Previamente à aquisição das imagens, foi feita a metalização com carbono da superfície do *mount* que contém os grãos

de zircão. A metalização permite que a superfície seja condutora, de tal forma que exista interação entre o feixe de elétrons emitidos e a amostra. Assim como foi sugerido por Goldstein et al. (1992), podem-se adquirir imagens nítidas das amostras analisadas. As imagens de BSE foram usadas para: 1) identificar os núcleos e zonas de crescimento intermediarias e bordas em grãos de zircão, 2) para selecionar áreas adequadas para realizar as análises de U-Pb, e 3) para realizar a análise morfológica dos grãos de zircão. As classes de arredondamento e alongamento consideradas nesse trabalho seguiram a classificações consideradas no trabalho de Augustsson et al. (2018). Essas classificações só consideram os grãos de zircão inteiros com idades U-Pb concordantes. A classes de arredondamento representa uma versão simplificada da proposta por Powers (1953), assim os grãos foram classificados como euhedral, subangular até subarredondado e arredondado. Enquanto que as classes de alongamento usam as rações comprimento/largura para dividi-las em alongado (< 1.3), ovalado (entre 1.3 e 1.8) e redondo (> 1.8).

Por outro lado, a combinação das características das imagens BSE, as idades U-Pb dos pares núcleo-borda e as rações Th/U foram usadas para traçar o possível retrabalho crustal dos grãos de zircão e relacioná-los com importantes eventos geocronológicos. Além disso, as rações Th/U são comumente usadas para distinguir entre uma origem magmática ou metamórfica, donde os grãos de zircão com rações Th/U < 0.1 são mais prováveis que sejam metamórficos, enquanto que rações Th/U > 0.1 podem ser ígneos o metamórficos (Rubatto, 2017; Yakymchuk et al., 2018).

3.3.6. ISÓTOPOS DE U-Pb

As análises isotópicas de U-Pb foram realizadas nos grãos de zircão detrítico usando o espectrômetro de massa *Thermo Finnigan Neptune High Resolution Multicollector Inductively Coupled Plasma* (NEPTUNE HR MC ICP-MS) acoplado a um sistema de ablação laser *Nd-YAG 213 nm New Wave*, instalado no LEGGA da Universidade de Brasília. O Neptune está equipado com 9 detectores tipo copo Faraday, uma multiplicadora de elétrons central e 5 contadoras de íons do tipo *Multi Ion Channel* (MIC).

A ablação dos grãos de zircão foi realizada com um *spot* de 25 μm com uma frequência de 10 Hz e uma energia de ~90%, resultando numa energia de 3 – 3.5 J/cm^2. As análises foram realizadas tomando em conta o método *Standard Bracketing* sugerido por Albarède et al. (2004) para a correção pela deriva do equipamento e o viés da massa.

Foram utilizados os padrões GJ-1 (Jackson et al., 2004) e o 91500 (Wiedenbeck et al., 1995). O padrão GJ-1 foi utilizado para quantificar o fraccionamento do equipamento, enquanto o padrão 91500 foi analisado como padrão externo.

As massas sintonizadas foram 232, 238, 208, 207, 206, 204 e 202. O tempo total de integração por *output data point* foi ~1.049 segundos e o tempo de ablação foi de 40 segundos, com um total de 45 ciclos por evento de análise. O procedimento do *Standard Bracketing* foi: 2 análises no GJ-1 e 2 análises no 91500 antes e depois das amostras (10 grãos de zircão) e um branco entre cada evento de análise.

O monitoramento do chumbo comum ^{204}Pb foi feito usando as massas ^{202}Hg e (^{204}Hg + ^{204}Pb). A correção por chumbo comum não foi necessária devido ao sinal de massa muito baixo ^{204}Pb (< 30 cps) e altas rações de ^{206}Pb/^{204}Pb (> 600). As idades estão cotadas em 2s absoluto, os erros foram propagados pela adição quadrática. A reprodutibilidade externa (2 $SD^2_{analized}$; SD: *Standard deviation)* está representada pelo desvio padrão obtido a partir das análises repetidas do padrão GJ-1 durante as aquisições analíticas. A precisão interna (2 $SE^2_{analized}$; SE: *Standard error*) é o erro padrão calculado para cada análise. Os dados foram processados usando o software Iolite v.4.0 (Paton et al., 2011) e o VizualAge (Petrus e Kamber, 2012), usando a modelagem *exponential plus linear* para *LIEF correction*.

As análises ligeiramente discordantes (< 10%) foram reportadas em termos de idades aparentes ^{206}Pb/^{238}U versus ^{207}Pb/^{235}U para grãos de zircão mais jovens que 1.3 Ga, e para grãos de zircão mais velhos que 1.3 Ga, as idades aparentes foram calculadas usando ^{206}Pb/^{238}U versus ^{207}Pb/^{206}Pb. As estimativas de densidade *Kernel* foram calculadas usando o pacote *detritalPy* desenvolvido em *Python* por Sharman et al. (2018). As idades máximas de deposição (MDAs) consideradas nesse trabalho foram o *youngest single grain* (YSG) e *youngest cluster* (YCσ), os quais foram calculados de acordo com Dickinson e Gehrels (2009).

CAPÍTULO 4

ARTIGO:

Geodynamic evolution of the southwestern margin of Gondwana during Devonian-Carboniferous time inferred by sedimentary provenance from Tarija basin: Active or passive margin?

Arnold García Zavaleta[1], Natalia Hauser[1], Martin Roddaz[2], Patrice Baby[2], Roberto Santos Ventura[1], Guilherme Gonçalves[1], Pamela Aparicio González[3], Felipe Puma[4], Elton Luiz Dantas[1], Patricia Bravo[4], Melvy Humerez[4]

[1] Laboratório de Geocronologia e Geoquímica Isotópica, Instituto de Geociências, Universidade de Brasília, Brasília, DF 70910-900, Brazil
[2] Géosciences-Environnement Toulouse, Université de Toulouse, UPS (SVT-OMP), CNRS, IRD, 14 Avenue Édouard Belin, F-31400 Toulouse, France
[3] UBA - INGEIS Universidad de Buenos Aires, Facultad de Ciencias Exactas y Naturales, Departamento de Geología, Instituto de Geocronología y Geología Isotópica, Ciudad Universitaria, C1428EHA, Buenos Aires, Argentina
[4] Yacimientos Petrolíferos Fiscales Bolivianos (YPFB), Doble Vía a la Guardia, Esq. Regimiento Lanza, Santa Cruz, Bolivia

Abstract

This paper presents the combined results for several sedimentary provenance techniques (U-Pb in zircon, Sr-Nd and XRD in politic rocks) applied on the Devonian – Carboniferous sedimentary units of the Tarija basin, in the Southern Bolivian Subandean Zone. We use our data to constrain the provenance and tectonic settings of the basin, as well as compare it with other neighboring basins to deduce the geodynamic context of the SW margin of Gondwana during that time. The U-Pb provenance analyses from the Devonian and Carboniferous units pointed out that the dominant areas that provide sediments for the Tarija Basin were the Sierras Pampeanas to the southwest, the Arequipa-Antofalla Massif and Famatinian arc to the west. Few zircon grains (< 18%) possibly derived from pre-Andean inliers (> 1800 Ma), were also analyzed. In addition, the Carboniferous

units show the reworking of youngest sources with ages between 420 – 320 Ma that correspond with the denominated Chanic event, related with the collision of the Chilenia terrane against the western margin of Gondwana. The combined Sr-Nd isotope data and XRD techniques on pelites and the MDS analysis allow us to establish that the Carboniferous units represent the reworking of the underlying units with a minor supply from the western part of the basin. Our data, together with published information, allowed us to propose the existence of a foreland basin related to the convergent margin during the Devonian – Carboniferous times, with an important sedimentary input from the continent during the Carboniferous. The comparison of the detrital record from the Tarija basin and the neighboring basins, like Paraná, Chaco-Paraná, Sauce Grande, Paganzo, Navidad Arizaro, Madre de Dios and Karoo allowed us to establish that the SW margin of Gondwana apparently was an active margin during the considered interval of time. Furthermore, this convergent margin could have been related to a flat-slab subduction during the Devonian, which changed to a normal subduction during the Carboniferous after the complete delamination of the flat-slab. In this way, the absent or scarce magmatism observed during the Devonian and the shift to the arc magmatism during the Carboniferous along the SW sector of Gondwana can be explained.

1. Introduction

The evolution of SW margin of Gondwana during Devonian and Carboniferous times has been extensively studied for several authors (e.g. Bahlburg et al., 2009; Bahlburg and Hervé, 1997; Dahlquist et al., 2018; Hervé et al., 2013; Reimann et al., 2010; Willner et al., 2011). Nevertheless, until now the geodynamic setting of the Andean margin during the Devonian-Carboniferous time is still debated.

The Andean border of South America, that represent the western margin of the SW

paleo-continent of Gondwana, was the focus of an active convergence margin between the Gondwana shield and the oceanic lithosphere of Panthalassa ocean during the almost part of the Paleozoic time (Gohrbandt, 1993; Vaughan et al., 2005). However, several studies (e.g. Augustsson et al., 2006; Bahlburg et al., 2009; Bahlburg and Hervé, 1997; Cawood, 2005; Chew et al., 2007; Hervé et al., 2013; Reimann et al., 2010) suggested that the Devonian - Early Carboniferous stands out as a time of relative quiescence, in another words, a time without magmatic activity, metamorphism or deformation. This anomalous situation, related to the absence of a magmatic arc between the Devonian and Early Carboniferous times, was called by Bahlburg et al. (2009) as "The Devonian Problem". Other authors, in contraposition, proposed a model that involved an active margin for the western margin of the SW Gondwana during Devonian-Early Carboniferous (e.g. Anderson et al., 2021; Dahlquist et al., 2018; Jaillard et al., 2000; Sempere, 1995).

On the view of this two possible situations, one way to distinguish between a passive from an active margin is trouthg the provenance study of the sedimentary basins of Devonian-Carboniferous ages that bodered the Andean margin. In effect, sediments deposited in back-arc or retroarc foreland basin settings are dominated by U-Pb zircon ages that approximate the depositional age of the samples (Cawood et al., 2012; Stern and Dickinson, 2010) and radiogenic Nd isotopic compositions that reflect the dominant contribution from the volcanic arc (McLennan et al., 1993). In contrast, sediments deposited in basins from a passive margin setting will show an U-Pb zircon age distribution that lack syn-depositional magmatic components (Cawood et al., 2012; Cawood and Nemchin, 2000) as well as low radiogenic Nd isotopic composition that reflect contribution from older rocks (McLennan et al., 1993).

One example of this type of basins is the Tarija basin (Figs. 1 and 2). It is located in the southern Bolivia and preserves an important part of the Phanerozoic stratigraphic record

of the SW Gondwana, including units from Silurian to Quaternary. Especially for the Devonian-Carboniferous time the basin has no less than 4000 m of sedimentary rocks (Cruz et al., 2008; Sempere, 1995; Starck, 1995). As far as we know, the provenance of these Devonian – Carboniferous rocks still remain to be determined.

Besides that, the tectonic setting of the Tarija basin during the Devonian-Carboniferous is still debated. Several types of basin have been proposed, like: 1) a retroarc foreland basin (Anderson et al., 2021; Isaacson and Diaz-Martinez, 1995; Ramos, 1988; Sempere, 1995; Starck, 1995); 2) a basin related to a divergent margin (Gohrbandt, 1993); 3) an intracratonic basin (Fernández Seveso et al., 1998; Starck and Del Papa, 2006); or 4) a back-arc basin without deformation (Dalenz-Farjat et al., 2002).

The goal of this paper is to determine the provenance of the Devonian – Carboniferous sedimentary sequence for the Tarija basin trough zircon U-Pb provenance analyses, morphological examination of detrital zircon, Sr-Nd isotopes and X-ray mineralogical data on fine grained sedimentary rocks, and sandstone petrographic analyses. These provenance data are further used to discuss the geodynamic setting of the Tarija basin in the context of other neighboring basins and discuss to resolve the so-called “Devonian Problem” of the Andean margin of the SW Gondwana.

2. Geological setting

2.1. Tectonic evolution of South America

The Amazonian craton is a largely a Proterozoic crust that is surrounded by Neoproterozoic orogenic belts (Tucavaca in Bolivia, Araguaia-Cuiabá in Central Brazil and Tocantins in northern Brazil), and it has been relatively stable since 1000 Ma (Tassinari et al., 2000). The evolution of the Amazonian Craton correspond to the diachronous foramtion of continental blocks or paleo-plate by collision during Archean and

Paleproterozoic times that resulted in the agglutination of a megacontinent (Tassinari et al., 2000). The Amazonian craton is composed by several geochronological provinces, which may contain anorogenic and orogenic rocks of widely different ages (Fig. 1, e.g. Santos et al., 2008, 2000; Tassinari et al., 2000). The Amazonian craton can be subdivided into six major geochronological provinces based on the age determinations, structural trends, relative proportions of rock-types, and some geophysical evidence (Tassinari et al., 2000 and references therein). The recognized geochronological provinces of the craton comprise the Central Amazonia (> 2200 Ma), Maroni-Itacaiúnas (2200 – 2000 Ma), Ventuari-Tapajós (2000 – 1820 Ma), Rio Negro-Juruena (1820 – 1540 Ma), Rondonia-San Ignacio (1540 – 1300 Ma) and Sunsas/Grenvillian (1300 – 900 Ma) (e.g. Bahlburg et al., 2009; Chew et al., 2008; Cordani et al., 2000; Reimann et al., 2010; Tassinari et al., 2000).

Important cratonic units was also described in the South America, like São Francisco, Rio de la Plata and Rio Apa. The São Francisco Craton correspond to internal parts of plates that amalgamated to form West Gondwana by the end of the Neoproterozic and beginning of the Paleozoic (Heilbron et al., 2017). The São Francisco Craton is situated in the central eastern part of South America and comprises Archean and Paleoproterozoic rocks (4100 to 1900 Ma; Teixeira et al., 2017, 2000). The Rio de la Plata Craton have crystallization ages on zircon ranges between 3100 and 570 Ma, which is evidence for long-lived crustal reworking (Oyhantçabal et al., 2011). The Rio de la Plata Craton consists of voluminous granite-gneissic terrains (2200 – 2100 Ma) that represent magmatism during the accretional stage of the orogeny. Coeval volcano-sedimentary basins are preserved as relics of supracrustal rocks, deformed and metamorphosed during a collisional event that occurred at ca. 2100 Ma (Oyhantçabal et al., 2018). The Rio Apa Craton formed between 2070 and 1740 (Teixeira et al., 2020), furthermore, two collisional events took place, the first at 1700 Ma related to the collision with the Paragua block and at 1300 Ma related to

the Amazonian Craton (Redes et al., 2020).

On the other hand, During the late Neoproterozoic and Paleozoic times, the southern part of the Andean Cordillera and nearby areas, formed part of the southwestern margin of Gondwana (Heredia et al., 2018a). Accretion of allochthonus or parautochthonous terranes has been signaled by several authors as the main tectonic process in this sector, resulting in several Paleozoic orogenies with different temporal and spatial extension (e.g. Heredia et al., 2018b, 2018a; Ramos, 2008; Rapela et al., 2007). According to Heredia et al. (2018a), during this period of time, the set of continental the Paleozoic orogenies are: Pampean (Ediacaran-early Cambrian), Famatinian (Middle Ordovician-Silurian), Ocloyic (Middle Ordovician-Devonian), Chanic (Middle Devonian-Early Carboniferus) Gondwanan (Middle Devonian-middle Permian), and Tabarian (late Permian-Triassic). All these orogenies culminate with collisional events, with the exception of the Tabarin and a part of the Gondwanan orogenies that are subduction-related.

2.2. Structure and stratigraphy of the Tarija basin

The Tarija basin is part of the Bolivian Subandean Zone (SAZ) which is considered as a type example of thin skin fold and thrust belt (Fig. 2) developed in a retroarc foreland basin (Baby et al., 1992; Dunn et al., 1995). It is limited to the east by the Sub-Andean thrust front and to the west by the inter-Andean zone (Rocha, 2013). The deformation of the SAZ started during the Middle to Late Miocene (Echavarria et al., 2003; Uba et al., 2009). The major detachment surface is located into the Silurian and Ordovician levels (Fuentes et al., 2018). According to (Fuentes et al., 2018), the sub-Andean fold-thrust belt was constructed on sedimentary rocks from several superposed sedimentary basins related with different geodynamic settings, where each one represent different sedimentary cycles (Starck, 1995). According to Fuentes et al. (2018), the superposed sedimentary basins are: 1) an Ordovician clastic shelf sequence possibly deposited in a back-arc setting; 2) a Silurian-Devonian basin

of uncertain affinity, mostly comprising clastic marine strata deposited on a ramp setting; 3) intracratonic successions with a distinctive stratigraphy comprising Carboniferous to Cretaceous times; and 4) a Cenozoic Andean foreland basin system.

The Silurian-Devonian and Carboniferous-Permian sedimentary cycles, that constitute approximately 5 Km of thickness of sedimentary rocks, were bracketed between the Ocloyic and Araucana diastrophic events (Starck, 1999). The two cycles were separated by the compressive Chanic tectonic event (Starck et al., 1993), that would interrupted the sedimentation in the Tarija basin in the upper Devonian. In addition, the eustatic sea level fall, during the Carboniferous, also prevented the sedimentation from being continued up to the upper Carboniferous (Starck, 1999).

The Silurian - Devonian sequence of the Tarija basin is represented by a relatively tabular, mostly marine deposits (Fuentes et al., 2018), which is composed by the intercalation of sandstone and pelitic facies and separated to the basement by the regional Ocloyic unconformity (Starck, 1995). In the Devonian stratigraphic record of the Tarija basin five major units can be recognized which are, from oldest to youngest; the Santa Rosa, Icla, Huamampampa, Los Monos and Iquiri formations (Fig. 3). The stratigraphic ages for these units are based mainly on palynological data (Fig. 3), which contain distinctive Devonian palynomorphs *Bimerga bensonii*, *Crucidida camirense*, *Evittia sommeri*, *Petrovina connate*, *Ramochitina magnifica*, *Leiotriletes balapucensis* and *Endoculeospora altobellii* (di Pasquo, 2007a; Troth et al., 2011).

The Carboniferous - Permian cycle is separated from the Silurian – Devonian cycle by the Chanic unconformity. The Machareti group represent part of the Carboniferous record of the Tarija basin and are composed mainly by continental clastic facies that represent the glacial and periglacial sequences (Fuentes et al., 2018). The glacial and periglacial sequences are composed by an alternation of diamictites, shales with and without

dropstones, striated paviments and sandstones among other lithologies, interpreted to be deposited in intracratonic settings (di Pasquo, 2007b; Starck and Del Papa, 2006). In the Machareti Group five formations can be recognized that, from oldest to youngest are; Itacua, Tupambi, Itacuami, Tarija, Chorro and Taiguati formations (Fig. 3). The stratigraphic ages for these units are also based on palynological data (Fig. 3), which contain distinctive Mississippian palynomorphs *Auroraspora macra*, *Granulatisporites granulatus*, *Foveosporites appositus*, *Retusotriletes mirabilis* and *Secarisporites undatus*. They also contain distinctive Pennsylvanian palynomorphs such as *Crassispora kosankei*, *Cristatisporites chacoparanensis*, *Cristatisporites crassilabratus*, *Dictyotriletes bireticulatus*, *Lundbladispora riobonitensis*, *Vallatisporites arcuatus*, *Cystoptychus azcuyi* and *Potonieisorites novicus* (di Pasquo et al., 2019 and references therein). According to Craddock et al. (2019), during the Visean (Mississippian) – Capitaniana/earliest Wuchiapingian (Middle-earliest Late Permian), in this sector of Gondwana, occurred the Late Paleozoic Ice Age (LPIA), wich was among the longest episodes of glaciation in Earth history, and the longest of the Phanerozoic. The LPIA had profound effects on the Earth's physical, chemical and biological environments at all southern latitudes (Craddock et al., 2019 and references therein).

2.3. Tectonic models and proposed classification of the Tarija basin

Most of the authors who have studied this basin define it as a retroarco foreland basin from the Middle Silurian until the Late Carboniferous (e.g. Anderson et al., 2021; Isaacson and Diaz-Martinez, 1995; Ramos, 1988; Sempere, 1995; Starck, 1995). The main argument is the strong asymmetry of the Silurian – Devonian sequences in the basin, with important sedimentary contributions from the western part of the basin. In addition to that, according to Sempere (1995), there is a greater subsidence in the western part of the basin. The presence of a magmatic arc to the west of the Silurian-Devonian basin in central-

northwestern Argentina and in southern Peru (e.g. Bahlburg, 1990; Mukasa and Henry, 1990; Rapela et al., 1992) is also in agreement with a retroarco foreland basin. In addition, on the basis of thermometry data, Anderson et al. (2021) suggest a shortening-related flexural subsidence driven by cratonward growth of a pre-Andean orogenic wedge along the western margin of Gondwana, with peak temperature conditions attained during eastward advance of a foreland basin between ~ 420 and ~ 318 Ma occurred during the Devonian – Carboniferous Gondwanide Orogeny.

On another hand, Gohrbandt (1993) suggest that the continental margin of Gondwana was quiescent from during the Cordilleran Cycle, durinf latest Ordovician – Devonian. The boundary between Gondwana and the proto-Pacific Plate was converted into a divergent margin during this period. A land ridge consisting of the Puna Arch and a proto-Cordillera became the new and dominant topographic feature on the outer margin of Gondwana. This ridge separated an interior epicontinental sea from the proto-Pacific Ocean (Gohrbandt, 1993 and references therein). Whereas Starck and Del Papa (2006) suggest that during the Carboniferous the widespread basin development over cratonic areas and homogeneous subsidence may classify it as an intracratonic basin. During this time, the basin was subjected to continuous advances and retreats of glaciers. The complex facies distribution and recurrent erosive unconformities recorded in the Tarija basin were interpreted as products of continuous changes in accommodation as a consequence of glacially driven subsidence and postglacial isostatic rebound (Starck and Del Papa, 2006).

Another tectonic setting for the Tarija basin was proposed by Dalenz-Farjat et al. (2002), who suggested the existence of a back-arc basin without deformation, which would be related to the presence and development of a magmatic arc prior to the Silurian-Devonian. The main arguments to supporting this type of basin is: 1) the inexistence of a fold-thrust belt in the region formed during the Devonian time and 2) absence of migration

of the depocenter during the formation of unconformities between the Ludlow and the Frasnian (Dalenz-Farjat et al., 2002).

2.4. Potential sources characteristics

The main potential sources areas for the studied sedimentary units include Precambrian rocks of the Amazonian craton to the east of the basin (Fig. 1), Arequipa-Antofalla massif, the Sierras Pampeanas, the Famatinian magmatic arc and the Late Paleozoic intracontinental and retroarc magmatism to the west of the basin (Fig. 1). It is possible to distinguish these source rocks bases on the Sr-Sm-Nd isotopic composition of the fine-grained sedimentary rocks and U-Pb dating on zircon grains.

According to Loewy et al. (2004), the Arequipa-Antofalla massif, is divided into northern, central and southern domains. The domains show multiple tectonic events overlap and a decreasing age from north to south (Fig. 1). The Northern domain is composed by rocks with ages between 500 – 420 Ma, 1300– 900 Ma, 2000 – 1820 Ma and may have old components with ages > 1800 Ma (pre-Andean inliers). Its initial ε_{Nd} values range between -4.3 and -1.0 (Loewy et al., 2004). In addition, the Northern domain also is overlapped by the San Nicolas batholith with lower intercept ages of 425 and 394 – 388 Ma (Mukasa and Henry, 1990). The Central–Southern domain is composed by rocks with ages between 500 – 420 Ma, 1300 – 900 Ma and may have old components with ages > 2200 Ma (inliers). Its initial ε_{Nd} values varying between -10.3 and +3.9 (Loewy et al., 2004).

The Sierras Pampeanas is a morphostructural unit that is composed by the Eastern and Western geological subprovinces. The Eastern Sierras Pampeanas is composed of Neoproterozoic to Late Paleozoic rocks (700 - 500 Ma; e.g. Pankhurst and Rapela, 1998; Rapela et al., 1998), whereas the Western Sierras Pampeanas is composed by rocks of Mesoproterozoic to Late Paleozoic ages (1300 - 500 Ma; e.g. Casquet et al., 2008, 2001;

Morata et al., 2010; Pankhurst and Rapela, 1998; Varela et al., 2003). Its initial ε_{Nd} values varying between -9.9 and +5.4, and with initial values of $^{87}Sr/^{86}Sr$ ratios between 0.702 and 0.731 (Casquet et al., 2008; Morata et al., 2010; Ortiz et al., 2019, 2017; Rapela et al., 1998; Varela et al., 2003).

The rocks of Famatinian magmatic arc have ages between 500 – 420 Ma; initial ε_{Nd} values between -12.6 and -4.2 (Bock et al., 2000; Cardona, 2006; Pankhurst et al., 1998), and with initial values of $^{87}Sr/^{86}Sr$ ratios between 0.706 and 0.716 (Pankhurst et al., 1998). Whereas the Late Paleozoic intracontinental and retroarc magmatism (Chacras-Potrerillos, Renca and Achala batholiths) have ages between 420 to 320 Ma (Dahlquist et al., 2019, 2018; López de Luchi et al., 2017); initial ε_{Nd} values between -4.8 and -0.6, and initial $^{87}Sr/^{86}Sr$ ratios range from 0.703 to 0.707 (Dahlquist et al., 2019; López de Luchi et al., 2017).

In addition, it is possible to distinguish between cratonic and Andean sources using the Nd-Sr isotopic composition of fine-grained sediments (e.g. Basu et al., 1990; Roddaz et al., 2005). Cratonic-derived sedimentary rocks have $\varepsilon_{Nd(o)}$ values between -14.5 to -20, while Andean-derived sediments yields $\varepsilon_{Nd(o)}$ values > -13.8 (Figueiredo et al., 2009; Hurtado et al., 2018; Roddaz et al., 2005). There is no strict cutoff value for the Sr isotopic composition but in general cratonic derived sedimentary rocks are characterized by more radiogenic $^{87}Sr/^{86}Sr$ ratios than Andean derived sedimentary rocks (i.e. Basu et al., 1990; Roddaz et al., 2005). In similar way, U-Pb ages of detrital zircon have been used to trace the provenance of the sedimentary rocks in the Andean region because terranes of the Andes and of the Amazon craton have distinct ages (Fig. 1) (Bahlburg et al., 2009; Calle et al., 2018; Hurtado et al., 2018; Reimann et al., 2010).

Sedimentological and stratigraphic studies (e.g. Albariño et al., 2002; Bache et al., 2012; Isaacson and Diaz-Martinez, 1995; Sempere, 1995; Starck et al., 2021; Starck and Del Papa,

2006) of the Tarija basin, suggested different areas as potential sources for the Devonian – Carboniferous sedimentary sequences. According to Isaacson and Diaz-Martinez (1995), the Devonian sedimentation derived from the west and was influenced by at least two different tectonic sources: 1) the Arequipa-Antofalla massif, with a superimposed Early Devonian arc, and 2) the western Argentinian Famatinian magmatic arc of Late Ordovician ages. The same authors postulated that the Early Carboniferous sedimentation could have three potential source areas: 1) the orogenic belt formed during the Devonian and Carboniferous to the east; 2) the early Paleozoic Puna magmatic arc to the south; or 3) the Arequipa-Antofalla massif to the west.

2.5. The Devonian Problem

According to several authors (e.g. Augustsson et al., 2006; Bahlburg et al., 2009; Bahlburg and Hervé, 1997; Chew et al., 2016, 2007; Reimann et al., 2010), from the Early Devonian until the Early Carboniferous, the subduction style ceased on the western margin of Gondwana because of the scarcity or absence of zircon with Devonian-Early Carboniferous ages found in the stratigraphic record or magmatic rock of these ages. Consequently, these authors suggested that during this time (Devonian-Early Carboniferous) a passive margin was developed between northern Peru to southern Chile. According to Bahlburg et al. (2009), if that observation is corroborated by further data, this would eliminate the main evidence in favor of the Devonian active margin models. This anomalous quiescence situation, related to the absence of a magmatic arc between the Devonian and Early Carboniferous times, was called by Bahlburg et al. (2009) as “The Devonian Problem”.

In contrast, other authors, proposed a model that involved an active margin for the western margin of the SW Gondwana during Devonian-Early Carboniferous (Dahlquist et al., 2018; Jaillard et al., 2000; Sempere, 1995). Evidences in favor of this model include

persistence of the contractional deformation during the Devonian with the development of a foreland basin (Anderson et al., 2021; Diaz-Martinez, 1996; Isaacson and Diaz-Martinez, 1995; Jiménez et al., 2009; Ramos, 2018; Starck, 1995) and continuous magmatic activity from Late Devonian to Early Carboniferous time (Dahlquist et al., 2018).

2.6. Correlation with other Paleozoic basins of SW Gondwana

Several authors (e.g. Limarino and Spalletti, 2006; Linol et al., 2016, 2015; Milani and De Wit, 2008; Sempere, 1995; Vargas et al., 2020) have recognized the interconnection between different basins (e.g., Tarija, Paraná, Chaco-Paraná, Sauce Grande, Paganzo, Navidad Arizaro, Madre de Dios, Karoo basins and others) of the southwestern Gondwana. Important regional events can be recognized in those basins.

The similar stacking patterns identified in those basins during the Devonian time suggested that they were part of an interconnected marine system and were similarly affected by coetaneous transgressive and regressive events (Vargas et al., 2020). According to Haq and Schutter (2008), the presence of coeval Devonian transgressive and regressive events that encompass several basins throughout the South America, and their correlation with the global sea-level curve, demonstrated that eustasy was the predominant mechanism that controlled base-level fluctuation in the SW Gondwana's basins during the Middle and Late Devonian. Nevertheless, according to Vargas et al. (2020), there is evidence suggesting that during the Early Devonian, those basins were more affected by tectonism than eustasy (e.g. the Transgressive-Regressive cycles of the basin of the SW sector of Gondwana have only a weak correlation with the eustatic curve). Those tectonic processes, according to some authors (e.g. Heredia et al., 2018; Milani and De Wit, 2008), were probably linked to the Precordilleran orogenic phenomena that affected the basins of SW Gondwana during the Famatinian geodynamic cycle.

Whereas during the Carboniferous time the Gondwana formed an extensive Southern

Hemisphere landmass that was affected by multiple glacial episodes, resulted in the deposition of glacial, periglacial and deglacial sediments recorded across the Gondwana supercontinent (Valdez et al., 2020).

3. Sampling and methodology

3.1. Sampling

From the Southern Bolivian Sub-Andean Zone, that expose the northern Tarija Basin (Figs. 2 and 3), thirty-four fine- to coarse-grained sandstone samples were collected near to three localities, Monteagudo, Camiri and Villamontes (Fig. 2). Among these samples, seven sandstones were prepared for detrital zircon U-Pb analyses, twelve sandstones for petrographic studies, nineteen siltstones and claystones were prepared for Sr-Nd isotopic composition and nineteen samples were prepared for X-ray diffractometry analyses (see Fig. 3).

3.2. Petrography:

The petrography study of sandstone rocks were done taking into account the Gazzi-Dickinson point-counting method proposed by Ingersoll et al. (1984), the petrographic classification of sandstones proposed by Garzanti (2019), and the genetic scheme propose by Dickinson (1985). A total of twelve thin sections were counted using the XY stage of the petrographic microscope *Zeiss* model. For each sample, 400 framework sand grains were counted and categorized according to Garzanti (2019). Raw data were parameterized for each sample and calculated as total quartz [Q = monocrystalline quartz (Qm) + polycrystalline quartz (Qp)], feldspar [F = plagioclase feldspar (P) + potassium feldspar (Fk)] and lithic fragments [L = sedimentary (Ls) + volcanic (Lv) + plutonic (Lp) + metamorphic (Lm) + chert fragments (Lch)].

3.3. X-ray diffractometry:

Were analyzed 19 samples of very fine sedimentary rock (siltstone and claystone size)

by X-ray diffraction (XRD) to determine the clay mineralogy of the Icla, Huamampampa, Los Monos, Iquiri, Itacua, Tupambi, Tarija and Chorro formations. The preparation of samples were done in the Geochronology Laboratory of the University of Brasília. Whereas, the XDR analysis were carried out at the Laboratorio de Rayos X of the Instituto de Geocronología y Geología Isotópica (INGEIS) of the University of Buenos Aires, and at the Laboratório de Difração de Raios-X (LARIX) of the Institute of Geosciences of the University of Brasília. Clay fraction, for each laboratory, was prepared following the methodology suggested by Moore and Reynolds (1997) and Alves (1987), respectively.

The fraction < 2 μm was conventionally used for crystallographic index measurements. The measurements were done in oriented clay fractions in air-dried (AD), solvated with ethylene-glycol (EG), solvated with glycerol (G) and after heating (H). The operating conditions and instrument settings of each laboratory is detailed in the Table 1.

The mineralogical components of the clay fraction were established like major (M), minor (m) and trace (tr) components, which were established by comparing the reflection intensities in d. For the non-phyllosilicate components were used ~2.7 Å for hematite, ~3.18 Å for plagioclase, ~3.25 Å for potassium feldspar, ~4.18 Å for goethite, and ~4.26 Å for quartz. Whereas, for the phyllosilicates components were used ~7 Å for kaolinite, ~10 Å for illite, and ~14 Å for chlorite, smectite or vermiculite, when expansive or change with ethylene-glycol/glycerol or heating. The mineral abbreviations were used according to Whitney and Evans (2010).

3.4. Sr-Nd analysis:

The preparation of samples and the isotopic analyses were carried out at the Geochronology Laboratory of the University of Brasília. The samples were washed and weathered parts were removed, then were crushed and pulverized to a very fine size powder. Analytical procedures following Gioia and Pimentel (2000). Between 50 – 100 mg

of sample, were mixed with ^{149}Sm – ^{150}Nd spike solution, and then dissolved in Teflon Savillex beakers by successive acid attack (HNO_3, HF and HCl). A separation of Nd, Sm and Sr were done using chromatographic columns. Sr and Rare-Earth Elements (REEs) were separated in a primary column filled with AG 50W-X8 cation exchange resin, whereas that Sm and Nd elements were isolated following conventional cation exchange chromatography techniques, with Teflon columns filling by LN-Spec resin (HDEHP - di-2-ethylhexyl phosphoric acid supported on Teflon powder). Sr, Sm and Nd fractions were deposited on double Re evaporation filaments, and the isotopic measurements were carried out with a multicollector TRITON Plus thermal Ionization Mass Spectrometer (TIMS). Analysis of NBS 987 standard reference material yield an average value of $^{87}Sr/^{86}Sr$ = 0.71028 ± 0.000035 (2SE). Uncertainties of Sm/Nd and $^{143}Nd/^{144}Nd$ ratios were considered to be better than ± 0.05% (1σ) and ± 0.0015% (1σ), respectively, based on repeated analyses of international rock standard BHVO-2.

The measured $^{143}Nd/^{144}Nd_{sample}$ ratios are expressed in Epsilon Neodymium notation (ε_{Nd}) as the fractional deviation in part per 10^4 (units) from $^{143}Nd/^{144}Nd$ value of the Chondritic Uniform Reservoir (CHUR). In this work was used the time correction (t = 300 Ma). As the $^{87}Rb/^{86}Sr$ ratios were not measured, were taken contents of Rb = 125 and Sr = 142 ppm from the NASC reference values for fine-grained rocks given by Gromet et al. (1984). Whereas the time correction (t = 314 – 397 Ma) was used only for the ε_{Nd} evolution diagram (Fig. 8).

3.5. Morphology of zircon:

Imaging in the Back Scattered Electron (BSE) mode was carried out using a FEI QUANTA 450 Scanning Electron Microscope (SEM) installed at the Laboratory of Geochronology of the University of Brasília. The BSE images were used to identify the growth areas and zoning in the zircon, to select suitable areas for U-Pb analysis and to

perform the morphological analysis of detrital zircon grains. The roundness and elongation classes used in this work follow the classification proposed by Augustsson et al. (2018). This classification is only possible for unbroken grains with concordant U-Pb apparent ages. The roundness classification is based in the scheme of Powers (1953) in a simplified way, that divided in euhedral, subangular to subrounded, and rounded classes. The elongation classification uses the length/width ratios to differentiate between elongated (less than 1.3), oval (between 1.3 and 1.8), and round (higher than 1.8) crystals.

The BSE images were used to identify zircon morphologies, reabsorbed cores and xenocrysts. The Th/U ratio of zircon is a commonly employed criterion to distinguish between magmatic and metamorphic origin for zircon, where Th/U ratios < 0.1 are more likely to be metamorphic and zircon with Th/U ratios > 0.1 can be igneous or metamorphic (Rubatto, 2017; Yakymchuk et al., 2018). The Supplementary Figure 3 shows the core-rim age pairs plotted in a scatter plot, where the X-axis represents the crystallization age of the core, while the Y-axis represents the crystallization age of the rim. The core-rim age pair located close to the diagonal line represent zircon grains that crystallized from a youngest magmatic episode or from an earlier episode of the same magmatic system and incorporated into a later magmatic episode. In contrast, the core-rim pairs located away from diagonal line represent zircon grains that were assimilated into the magma from surrounding host rocks or crystals derived from partially melted crust. In this way, is possible to trace the crustal reworking of the zircon and relate it to important geochronological events.

3.6. U-Pb analysis:

For U-Pb analyses on detrital zircon grains seven samples of the Devonian – Carboniferous interval were selected. Four samples from Los Monos and Iquiri formations were selected from the Devonian and three samples from the Itacua, Tupambi and Tarija

formations were selected from the Carboniferous. Zircon concentrates were extracted from 5 – 8 Kg of sandstone samples, then crushed and sieved to 250 and 164 μm grain sizes. From the fraction between 250 – 164 and <164 μm, the heavy mineral were concentrated by hydraulic methods and magnetic separation using a Frantz isodynamic separator at 1.5 A°. The zircon grains were hand-picked and placed on epoxy mount, polished and cleaned with 3% nitric acid before analysis. The back scattered electrons (BSE) images were used to select the best place for U-Pb analyses. When the zircon was complex, with different core and rings, both areas were analyzed.

The U-Pb isotopic analyses were done using a Thermo-Fisher Neptune HR-MC-ICP-MS coupled with Nd:YAG UP-213 New Wave Research laser ablation system, installed in the Laboratory of Geochronology of the University of Brasília. The U-Pb analysis in zircon grains were carried out using the standard sample bracketing method (Albarède et al., 2004) using the GJ-1 standard zircon (Jackson et al., 2004) in order to quantify the amount of ICP-MS instrumental fraction. The tuned masses were 232, 238, 208, 207, 206, 204 and 202. Total integration time per output data point was ~1.049 seconds and the time of ablation was 40 seconds, with a total of 45 cycles for each analysis event. A 25 μm spot size was used and the laser settings were 10 Hz and 3-3.5 J/cm^2. Approximately ten unknowns were analyzed between two GJ-1 analyses. $^{206}Pb/^{207}Pb$ and $^{206}Pb/^{238}U$ ratios have been time corrected. During the analytical sessions zircon standards 91500 (Wiedenbeck et al., 1995) has also been analyzed twice as an unknowns, and a blank was analyzed between each zircon analysis.

The monitoring of common lead ^{204}Pb was done using the ^{202}Hg and (^{204}Hg + ^{204}Pb) masses. The common Pb correction was not necessary due to the very low signal of mass ^{204}Pb (<30 cps) and high $^{206}Pb/^{204}Pb$ ratios (>600). Ages are quoted at 2s absolute, propagation is by quadratic addition. Excess variance and age uncertainty of reference

material are propagated where appropriate. The data processing package used were Iolite v.4.0 (Paton et al., 2011) and VizualAge (Petrus and Kamber, 2012), using exponential plus linear modelling for LIEF correction.

The slightly discordant analyses (< 10%) were reported in terms of the $^{206}Pb/^{238}U$ versus $^{207}Pb/^{235}U$ apparent ages for zircon grains younger than 1.3 Ga, and for zircon grains older than 1.3 Ga, the correlated discordance was calculated using the $^{206}Pb/^{238}U$ versus $^{207}Pb/^{206}Pb$ apparent ages. The Kernal density estimations were calculated using the detritalPy, a Python-based approach (Sharman et al., 2018). For this work, two types of Maximum Depositional Ages (MDAs) were considered. The MDAs considered were the youngest single grain (YSG) and youngest cluster (YC2σ), both were calculated according to Dickinson and Gehrels (2009). The YSG is calculated by sorting all analyses by their U-Pb age plus 2σ uncertainty and selecting the first analysis in the list (Sharman and Malkowski, 2020). While the YC2σ(3+) is defined by sorting all analyses by their U-Pb age plus 2σ uncertainty, and identifying the youngest cluster of 3 or more analyses with overlapping 2σ error (Sharman et al., 2018).

4. Results

4.1. Sandstone petrography

Modal analyses were made on twelve sandstones from the Devonian Icla (2), Huamampampa (1), Los Monos (2) and Iquiri (3) and from the Carboniferous Itacua (1), Tupambi (1), Tarija (1) and Chorro (1) formations. The grain size of the samples varies from medium (0.5 mm) to very fine (0.062 mm); the textures of the sandstones are framework-supported. The studied samples (Table 2, Fig. 4) comprise mainly sandstones of quartzose (58%) and pure quartzose (42%) composition. In a general way, the sandstone grains of the Devonian units (Supplementary Figure I1A-H) are very well sorted and consist of subrounded to subangular grains intensely fractured with concave-convex contacts. The

sandstone grains of the Carboniferous units (Supplementary Figure I1I-L) are well to poorly sorted and consist of rounded to subrounded grains with concave-convex to punctual contact. Accessory mineral mainly are muscovite micas (Supplementary Figure I1A, C-G, J and L). The matrix consists of authigenic clays, and the cement is composed mainly by clay minerals. The samples also were used for the interpretation of provenance on the ternary diagram of Dickinson (1985).

Quartz grains (Q) comprise ranges from 91.00 to 100.00% of the total rock components. Quartz grains percentages do not show any significant trend; however, it slightly increases in the sandstone samples of the Carboniferous units (Table 2).

Feldspars grains (F) represent less than 6.50% of the total rock components (Table 2). It occurs either as potassic feldspars (Fk) or as plagioclase feldspars (P).

Total lithic fragments (L) are less than 3.25% of the total rock components (Table 2). Sedimentary rock and chert fragments are dominant (Supplementary Figure I1I); volcanic (Supplementary Figure I1K) and metamorphic fragments are present only in the Tarija and Itacua formations, respectively. Plutonic fragments are absent in all analyzed samples.

4.2. Clay Mineralogy (X-ray diffractometry)

The clay fraction of the Devonian-Carboniferous claystones have distinct mineralogical assemblages. The phyllosilicates like illite, kaolinite and chlorite are present as major, minor and trace components in almost all units; the vermiculite was identified as minor and trace components only in some samples of the Icla, Huamampampa, Los Monos, Iquiri, Itacua, and Chorro formations. The interstratified clays (Chlorite/Vermiculite or Illite/Smectite) are present as minor components only in some samples of the Icla, Los Monos and Tupambi formations (See Table 3 and Supplementary Fig. I2).

The non-phyllosilicates like quartz, plagioclase and potassium feldspar are present as major, minor and trace components in almost all units. The goethite is only present in some

samples of Los Monos Formation as minor and trace components, whereas that hematite is present in all Carboniferous units (Itacua, Tupambi, Tarija and Chorro formations) as minor and trace components (See Table 3 and Supplementary Fig. I2).

4.3. Sr-Nd isotopes

Sr and Nd concentrations and isotopic compositions of 19 fine-grained sedimentary rocks from analyzed units from the Tarija basin are available in Table 4. Present-day $^{87}Sr/^{86}Sr$ isotopic ratios of the analyzed samples range between 0.71775 – 0.76659 and present-day $^{147}Sm/^{144}Nd$ and $^{143}Nd/^{144}Nd$ isotopic composition range between 0.10899 – 0.12395 and 0.511882 – 0.512173 respectively, which yield $\varepsilon_{Nd(0)}$ between -14.8 to -9.1, and $\varepsilon_{Nd(300)}$ between -11.4 to -6.3 (Table 4, Figs. 5 and 6). $^{143}Nd/^{144}Nd$ isotopic composition recalculated at the depositional age (Ts) of the analyzed sample (T_s = 397 – 314 Ma) range between 0.5116 and 0.5119 which yield $\varepsilon_{Nd(Ts)}$ between -10.4 to -5.5 (Table 4, Fig. 7). The single-stage model ages (T_{DM}) were calculated according to Goldstein et al. (1984), the T_{DM} range from 1.48 to 1.78 Ga (Table 4 and Fig. 5). In order to take into account the evolution of the continental crust and for comparative purposes, the two-stage model ages (T_{DM}*) were calculated according to Liew and Hofmann (1988). The T_{DM}* can be used as an indication of the mean formation age of the source components, which range from 1.45 to 1.80 Ga (Table 4 and Fig. 5).

In general, the Devonian unit samples can be split into three groups. The Icla and Huamampampa formations have $\varepsilon_{Nd(300)}$ values between -8.45 and -6.82, $^{87}Sr/^{86}Sr_{(300)}$ ratios ranging from 0.73943 to 0.75565, T_{DM} values from 1.53 to 1.60 and T_{DM}* values from 1.47 to 1.48 Ga. The Los Monos Formation has $\varepsilon_{Nd(300)}$ values between -9.65 and -8.02, $^{87}Sr/^{86}Sr_{(300)}$ ratios ranging from 0.72526 to 0.73133, T_{DM} values from 1.64 to 1.74 and T_{DM}* values from 1.56 to 1.68. Some exceptions in the $\varepsilon_{Nd(300)}$, T_{DM} and T_{DM}* values can be observed in the samples SSB-9B ($\varepsilon_{Nd(300)}$: -11.40, T_{DM}: 1.78 and T_{DM}*: 1.80) and SSB-8C

($\varepsilon_{Nd(300)}$: -6.29, T_{DM}: 1.60 and T_{DM}*: 1.44) of Los Monos Formation. The Iquiri Formation has $\varepsilon_{Nd(300)}$ values between -9.45 and -8.35, $^{87}Sr/^{86}Sr_{(300)}$ ratios ranging from 0.71931 to 0.73181, T_{DM} values from 1.61 to 1.76 and T_{DM}* values from 1.58 to 1.66 (Table 4 and Fig. 6). On the other hand, the Carboniferous unit samples (Itacua, Tupambi, Tarija and Chorro formations) have $\varepsilon_{Nd(300)}$ values between -8.13 and -6.54, $^{87}Sr/^{86}Sr_{(300)}$ ratios ranging from 0.70686 to 0.71996, T_{DM} values from 1.48 to 1.64 and T_{DM}* values from 1.45 to 1.56 (Table 4 and Fig. 6).

4.4. U-Pb analysis

Detrital zircon ages with ± 10% of concordance from the Devonian – Carboniferous units of the Tarija Basin are reported in the Fig. 8 and Table 5. Results are compared with plotted together with colored areas/bars that represents the different to highlight potential sources (Figs. 1 and 8; Table 5). Those age groups include Central Amazonian (> 2200 Ma), Maroni – Itacaiúnas (2200 – 2000 Ma), Ventuari – Tapajós (2000 – 1820 Ma), Rio Negro – Juruena (1820 – 1540 Ma), Rondonia – San Ignacio (1540 – 1300 Ma), Sunsas/Grenville (1300 – 900 Ma), Early Brazilian (900 – 700 Ma), Late Brazilian/Pampean (700 – 500 Ma), Famatinian (500 – 420 Ma), and Chanic (420 – 320 Ma) events.

4.4.1. Los Monos Formation (Eifelian – Middle Devonian)

Sample SSB-16A: from seventy-nine (79) analyses on zircon grains, sixty-four (64) analyses presented a concordance between 90 – 110%. Was observed a polymodal age distribution with main age peak at 530 Ma, 2nd order age peaks at 483, 1039 and 1127 Ma, and 3rd order age peaks at 663 and 749 Ma. The distribution has two main zircon populations with ages between 668 – 506 Ma (Late Brazilian/Pampean, 39%) and 1293 – 981 Ma (Sunsas/Greenville, 34%). Minor zircon population between 492 – 456 Ma (Famatinian, 11%), subordinate zircon populations between 814 – 742 Ma (Early Brazilian, 6 %), > 2200 Ma (Central Amazonian, 5%), 1889 Ma (Ventuari – Tapajós, 3%) and an

isolated zircon at 1788 Ma (Rio Negro – Juruena, 2%). The YSG is 456 ± 10 Ma, while the YC2σ(3+) is 463 ± 6 Ma.

Sample SSB-2A: from seventy (70) analyses on zircon grains, fifty-two (52) analyses yield an adequate concordance between 90-110%. Similar to sample SSB-16A, the data shown a polymodal age distribution with main age peak at 538 Ma, 2nd order age peaks at 498 and 1039 Ma, and 3rd order age peaks at 618 and 1224 Ma. The distribution also shows two main zircon populations with ages at 683 – 514 Ma (Late Brazilian/Pampean, 36%) and 1291 – 913 Ma (Sunsas/Grenville, 35%) and a minor zircon peak at 500 – 477 Ma (Famatinian, 13%) ages. Subordinate populations include ~1873 Ma (Ventuari – Tapajós, 4%), 892 – 726 Ma (Early Brazilian, 4%), > 2200 Ma (Central Amazonian, 4%) and 2002 – 2025 Ma (Maroni – Itacaiúnas, 4%). The YSG is 477 ± 7 Ma, while the YC2σ(3+) is 485 ± 4 Ma.

4.4.2. Iquiri Formation (Givetian-Frasnian – Middle-Upper Devonian)

Sample SSB-10A: from sixty (60) analyses on zircon grains fifty (50) analyses presented the adequate level of concordance between 90-110%. The data shown a polymodal age distribution with main age peak at 540 Ma, 2nd order age peaks at 473 and 1028 Ma, and 3rd order age peaks at 435 and 637 Ma. The distribution shows three main zircon populations with ages between 647 – 518 Ma (Late Brazilian/Pampean, 50%), 1189 – 920 Ma (Sunsas/Grenville, 20%) and 484 – 432 Ma (Famatinian, 20%). subordinate zircon populations at ~393 Ma (Chanic event, 4%), 2132 – 2037 Ma (Maroni – Itacaiúnas, 4%) and an isolated zircon with age 1889 Ma (Ventuari – Tapajós). The maximum zircon depositional age is younger than those of the Los Monos Formation with YSG at 393 ± 9 Ma and YC2σ(3+) is 434 ± 5 Ma.

Sample SSB-4A: from one hundred and twenty (120) analyses on zircon grains one hundred and four (104) analyses presented the adequate level of concordance between 90%

and 110%. The data shown a polymodal age distribution with main age peak at 485 Ma, 2nd order age peaks at 534 and 1006 Ma, and 3rd order age peaks at 604 and 786 Ma. Similar to sample SSB-10A, the distribution includes three dominant zircon populations between 693 – 501 Ma (Late Brazilian/Pampean, 31%), 1178 – 950 Ma (Sunsas/Grenville, 30%) and 498 – 425 Ma (Famatinian, 24%). Subordinate populations include 849 – 701 Ma (Early Brazilian, 6%) and 2180 – 2015 Ma (Maroni – Itacaiúnas, 5%) zircon ages. Isolated zircon grains with ages 1385 Ma (Rondonia – San Ignacio), 1751 Ma (Rio Negro – Juruena), 1878 Ma (Ventuari – Tapajós) and 2742 Ma (Central Amazonian) were also identified. The maximum zircon depositional age is also younger than those of the Los Monos Formation with YSG at 425 ± 7 Ma, and YC2σ(3+) is 470 ± 4 Ma.

4.4.3. Itacua Formation (Famenian-Visean – Mississippian)

Sample SSB-5A: from sixty-nine (69) analyses on zircon grains sixty (60) analyses presented the adequate level of concordance between 90% and 110%. The data shown a polymodal age distribution with main age peak at 537 Ma, 2nd order age peaks at 495 and 1043 Ma, and 3rd order age peaks at 639, 828 and 1200 Ma. The distribution presents 645 – 526 Ma (Late Brazilian/Pampean, 37%) and 1231 – 929 Ma (Sunsas/Grenville, 27%) dominant zircon populations. Other minor zircon populations include 499 – 457 Ma (Famatinian, 8%), 833 – 731 MA (Early Brazilian, 8%), and 2185 – 2025 Ma (Maroni – Itacaiúnas, 7%). Subordinate populations include > 2200 (Central Amazonian, 5%), 380 – 365 Ma (Chanic event, 3%) and 1993 – 1973 Ma (Ventuari – Tapajos, 3%). Isolated zircon grains with age 1353 Ma (Rondonia – San Ignacio) was also identified. The YSG is 365 ± 7 Ma, while the YC2σ(3+) is 493 ± 4 Ma.

4.4.4. Tupambi Formation (Bashkirian – Pennsylvanian)

Sample SSB-28A: from sixty (60) analyses on zircon grains fifty-seven (57) analyses

presented the adequate level of concordance between 90% and 110%. The data shown a polymodal age distribution with main age peak at 543 Ma, 2nd order age peak at 484 Ma, and 3rd order age peak at 812 Ma. The distribution includes two dominant zircon populations between 670 – 500 Ma (Late Brazilian/Pampean, 56%), 493 – 468 Ma (Famatinian, 16%) and 817 – 763 Ma (Early Brazilian, 11%). Minor population includes 1261 – 1055 Ma (Sunsas/Grenville, 9%), whereas subordinate zircon population includes 1807 – 1753 Ma (Rio Negro – Juruena, 5%). Isolated zircon grains with ages 1428 Ma (Rondonia – San Ignacio) and 2029 Ma (Maroni – Itacaiúnas) were also identified. The YSG is 468 ± 8 Ma, while the YC2σ(3+) is 477 ± 2 Ma.

4.4.5. Tarija Formation (Moscovian – Pennsylvanian)

Sample SSB-23A: from eighty (80) analyses on zircon grains seventy-four (74) analyses presented the adequate level of concordance between 90% and 110%. The data shown a polymodal age distribution with main age peak at 538 Ma, 2nd order age peaks at 399 and 613 Ma, and 3rd order age peaks at 865, 963 and 1033 Ma. The distribution includes three dominant zircon populations between 685 – 520 Ma (Late Brazilian/Pampean, 54%), 1224 – 941 Ma (Sunsas/Grenville, 15%), and 410 – 332 Ma (Chanic event, 13%). Minor population includes 868 – 712 Ma (Early Brazilian, 8%), whereas subordinate zircon populations include 494 – 459 Ma (Famatinian, 4%), 1944 – 1870 Ma (Ventuari – Tapajos, 3%), and > 2200 Ma (Central Amazonia, 3%). The YSG is 332 ± 5 Ma, while the YC2σ(3+) is 401 ± 4 Ma.

4.5. Morphology of zircon

The zircon morphology data of unbroken grains and with concordant ages is summarized in Table 6. The analyzed zircon grains have mean length between 102 - 147 μm. The Devonian Los Monos and Iquiri formations contain 54.7 – 83.7% subangular to subrounded, 2.3 – 34.5% euhedral, and 6.5 – 14.1% rounded grains. In terms of elongation,

58.1 – 71.0% are elongated grains, 21.9 – 34.9% are oval grains, and 3.2 – 13.8% are round grains (Table 6; Fig. 9). The Carboniferous Itacua, Tupambi and Tarija formations contain 58.1 – 83.8% subangular to subrounded, 5.4 – 34.9% rounded, and 6.0 – 10.8% euhedral grains. They are composed by 46.5 – 86.5% elongated, 13.5 – 41.9% oval, and < 11.6% round grains (Table 6; Fig. 9).

Ninety percent (90%) of unbroken zircon grains with concordant age are younger than 1540 Ma, and ~ 65% are younger than 900 Ma (Fig. 10), and the two main group age peaks are at 320 – 900 Ma and 900 – 1400 Ma (Fig. 8). The youngest age groups are at 320 – 420 Ma while the oldest age groups are at 1700 – 3600 Ma (Fig. 10).

Zircons with grain-size < 125 μm, present in all analyzed samples, shows all the age populations. Oldest zircon population (1700– 3600 Ma) are rarely present to absent in coarser zircon grains (125 – 300 μm) (Fig. 10A).

The grain shapes are partly correlate with the ages (Fig. 10B). Generally, the age interval of 320 – 1540 Ma shows all range of elongation, except sample SSB-28A (Tupambi Formation) which only present oval and elongated grains with elongation ratios of 1.1 to 5.2. The oldest age groups (1700 – 3600 Ma) show low ratios of elongation between 1.1 – 3.5, including round, oval and elongated grains (Fig. 10B).

Additionally, the BSE images were analyzed to select suitable areas for U-Pb analysis. Taking into account that the majority of zircon grains did not shown any complex inherited core bordered by a youngest rim, the selected target areas for U-Pb analyses, were the core of zircon grains, however, core and rim areas were also analyzed when was possible in order to confirm.

Fifty-one (51) core-rim age pairs of the Devonian – Carboniferous units, with the adequate level of concordance (90% to 110%), are presented here (Fig. 11 and

Supplementary Fig. I3). The BSE images (zircon grains with relatively regular, dark and light zonation) in combination with the core-rim ages pairs and Th/U ratios (> 0.1) allowed us to relate the rim crystallization to igneous growths during several magmatic episodes.

Twenty-seven (27) core-rim pairs of the Devonian sedimentary units, Los Monos (SSB-16A and SSB-2A) and Iquiri (SSB-10A and SSB-4A) correspond to zircon grains formed in the same magmatic system and zircon grains that were assimilated into the magma from host rocks or crystals derived from partially melted crust. The cores have ages between 393 and 2462 Ma with Th/U ratios range from 0.37 to 3.37, whereas the rims have ages between 392 and 2441 Ma with Th/U ratios range from 0.15 to 2.03 (Fig. 11 and Supplementary Fig. I3). On the other hand, twenty-four (24) core-rim pairs of the Carboniferous Itacua (SSB-5A), Tupambi (SSB-28A) and Tarija (SSB-23A) formations also correspond to zircon grains formed in the same magmatic system and zircon grains that were assimilated into the magma from host rocks or crystals derived from partially melted crust. The cores have ages between 400 and 1993 Ma with Th/U ratios range from 0.14 to 3.61, whereas the rims have ages between 410 and 1978 Ma with Th/U ratios range from 0.03 to 3.89 (Fig. 11 and Supplementary Fig. I3).

5. Discussion

5.1. Maximum depositional ages (MDAs)

The U-Pb detrital zircon ages of the Devonian – Carboniferous units provided consistent MDAs that are mainly older than the estimated depositional ages based in palynological data (di Pasquo, 2007a; di Pasquo et al., 2019; Troth et al., 2011) and presented in the Fig. 3. From all analyzed formations, the Carboniferous units as Tupambi (AA-01: YSG = 340 ± 6 Ma;from Calle (2013)), and Tarija (SSB-23A: YSG = 332 ± 5 Ma) presented the youngest MDAs (Mississippian). One sample of the Devonian Iquiri Formation (SSB-10A: YSG = 393 ± 9 Ma), stratigraphically located under the erosional unconformity related with

the Chanic Event, and the Carboniferous Itacua Formation (SSB-5A: YSG = 365 ± 7 Ma) show Devonian MDAs.

The Devonian units, Santa Rosa (SLL-03: YSG = 444 ± 2 Ma; from Calle, 2013), Los Monos (SSB-16A: YSG = 456 ± 10 Ma; SSB-2A: YSG = 477 ± 7 Ma), Iquiri (SSB-4A: YSG = 425 ± 7 Ma), and one sample of the Carboniferous Tupambi Formation (SSB-28A: YSG = 468 ± 8 Ma), displayed Silurian and Ordovician MDAs. Although the younger cluster, 2 sigma overlap (YC2σ(3+)) is a more conservative MDA method (Sharman and Malkowski, 2020 and references therein), we considered the youngest single grain (YSG) method because it is consistent when consider the biostratigraphic ages proposed by several authors (Fig. 3; e.g. di Pasquo, 2007a; di Pasquo et al., 2019; Troth et al., 2011).

Although most samples do not present MDAs corresponding to their depositional age, this does not imply that there are no zircon grains of that age at was explained by Sharman and Malkowski (2020), for youngest zircon grains in recently deposits. The global rarity of the youngest zircon in ancient deposits is likely due to the combined effects of several contributing factors. Some of those factors could be the relatively low abundance of active volcanic cover rock exposed at the Earth's surface in that moment, low zircon fertility of many of these volcanic rocks, complex age histories in volcanic zircon crystals, and potentially grain size biases.

Nevertheless the analyzed Devonian units, almost in their entirety, did not show any Devonian MDAs attempting to infer that the magmatism was absent or scarce during this time, those registered in southern Peru by Mukasa and Henry (1990) and in central northwestern Argentina (Dahlquist et al., 2019, 2018; López de Luchi et al., 2017) must be taking into account. In addition, the samples from the Carboniferous units show zircon populations of Devonian ages (Table 5 and Fig. 8). This could indicate that, in addition to Devonian magmatism not being expressive in this sector of Gondwana; Devonian igneous

rocks could remain below the surface during this time. Apparently, the behavior and interaction between plates in this sector of Gondwana changed after the Carboniferous, making possible the exhumation of these Devonian igneous rocks and the erosion and transport to the Tarija Basin during Carboniferous time. . An important erosional exhumation event would have occurred in this sector of Gondwana between ~352 and ~294 Ma (Anderson et al., 2021). On the other hand, the samples from the Carboniferous units show Mississippian MDAs, which is consistent with the widely developed arc magmatism in the southwestern margin of Gondwana as a product of a major geodynamic modification around 345 Ma (e.g. Bahlburg et al., 2009; Creixell et al., 2021).

5.2. Interpretation of the provenance

Before interpreting the provenance based on U-Pb zircons ages and Sr-Nd isotopic compositions of the analyzed sedimentary rocks, the effect of weathering and hydrodynamic sorting on the isotopic composition should be carefully evaluated as it could be the primary factor controlling the isotopic composition of sediments (e.g. Augustsson et al., 2018; Johnsson, 1993; Lawrence et al., 2011; McLennan et al., 1993). Sr-Nd isotopic composition of fine grained sediments may be preferred to establish a complete integration of drainage pathways from the most distant cratonic areas to oceanic basins (Patchett et al., 1999) because they are not biased by grain-size sorting and weathering processes (e.g. Cullers, 2000; McLennan et al., 1993) when compared with coarser fractions (Bouchez et al., 2011; McLennan et al., 1993; Roddaz et al., 2014). Furthermore, the zircon-grain sizes and shapes may be correlated with their ages, thus significantly can improve provenance interpretation (Augustsson et al., 2018); this is the most simple way to evaluate hydrodynamics effects on zircon age populations (Lawrence et al., 2011). In our data, it is important to note that the dominant zircon population with ages between 320 and 1400 Ma is present in both fraction size (< 125 and 125 – 300 μm). Whereas the minor zircon

population with ages between 1700 and 3600 Ma is present in fraction size < 125 μm and rarely present to absent in fraction size 125 – 300 μm (Fig. 11A). On the other hand, it is also to highlight that the most part of zircon grains with ages > 2200 Ma are mainly present only in the fraction < 125 μm. However, the age group > 2200 Ma does not represent a relevant zircon population in the detrital record of the Devonian – Carboniferous units (Fig. 11A), so we consider that there is no clear relationship between the size of the zircon grains and the ages. In this way, we consider that the hydrodynamic sorting effect can be obviated.

Our multidisciplinary data set show a change in provenance between Devonian and Carboniferous. The transition between Devonian and Carboniferous times in the Tarija basin is marked by a change in the Sr-Nd isotopes and T_{DM} ages (Fig. 6). The Carboniferous sedimentary rocks are characterized by lower radiogenic $^{87}Sr/^{86}Sr_{(300)}$ ratios and less scattered $\varepsilon_{Nd(300)}$ values. When plotted on $^{87}Sr/^{86}Sr_{(300)}$ vs. $\varepsilon_{Nd(300)}$ (Fig. 7) and $\varepsilon_{Nd(Ts)}$ evolution (Fig. 8) diagrams and compared with several relevant sources, the Sr and Nd isotopic compositions of the Devonian-Carboniferous sedimentary rocks are similar to the Sierras Pampeanas and Famatinian arc (see Fig. 7). Furthermore, the lowest $^{87}Sr/^{86}Sr_{(300)}$ ratios of the Carboniferous units (Itacua, Tupambi, Tarija and Chorro formations) may indicate the presence of a slightly more juvenile source for these sedimentary rocks (see Fig. 7). The younger T_{DM} and T_{DM}* ages of the Carboniferous units (Table 4 and Fig. 6) are also indicating a contribution of juvenile source during the Carboniferous. A potential candidate for this juvenile source could be the Devonian magmatic rocks recognized by Dahlquist et al. (2019) and López de Luchi et al. (2017).

The estimated depositional age and T_{DM}* ages (Table 4) indicate that the Devonian detritus had been recycled in the crust for at least 1050 – 1420 my before deposition, while the Carboniferous detritus had been recycled in the crust for at least 1130 – 1250 my before deposition in the basin. It might indicate that the Carboniferous units was supplied in a

minor way by sources with youngest T_{DM}*.

Figure 9 shows that the $\varepsilon_{Nd(Ts)}$ values for Devonian to Carboniferous pelitic rocks are plotted in the range of the Nd isotopic composition for Sierras Pampeanas, Famatinian arc and for Central-Southern domains of the Arequipa-Antofalla basement. Alternatively, these values could also indicate a mixture between two compositional end members, the Arequipa-Antofalla Domains with more negative Epsilon Nd values and the Devonian magmatic arc, with more positive Epsilon Nd values.

Taking into account the paleocurrents to the east and northeast (Albariño et al., 2002; Isaacson and Diaz-Martinez, 1995) and the U-Pb zircon ages spectra (Fig. 9), that indicate that the main sources has ages between 700 – 500 Ma (Late Brazilian/Pampean); the Eastern Sierras Pampeanas (Rapela et al., 1998) looks to be the main sources. Populations with Famatinian (500 – 420 Ma) and Sunsas/Grenvillian (1300 – 900 Ma) ages also represent an important quantity of detritus that was supplied to the basin. These populations can be either derived from the Famatinian arc localized in the Eastern-Central Sierras Pampeanas (Bock et al., 2000; Pankhurst and Rapela, 1998), and from the Western Sierras Pampeanas (Casquet et al., 2008; Morata et al., 2010; Varela et al., 2003), respectively. In addition, the 500 – 420 Ma and 1300 – 900 Ma populations could also be derived from the Arequipa-Antofalla Central-Southern domain (Loewy et al., 2004). Nevertheless, the Sunsas-Grenville province could be a potential provenance area from the east (Fig. 1), the paleocurrents did not indicate any provenance from this area. It is also supported by the absence of zircon population with ages typical from the SW Amazonian Craton, between 1300 and 1700 Ma (Boger et al., 2005; Litherland et al., 1986; Redes et al., 2020; Teixeira et al., 2020).

Whereas the subordinate population of zircon grains with ages > 1700 Ma are not represented by zircons with inherited cores (Fig. 12 and Supplementary Figs. 2), that could

indicate the inliers inside the Arequipa-Antofalla massif with ages > 1800 Ma (Ramos, 2008 and references therein) (See Fig. 1) as a subordinate potential source.

The main zircon group ages for Carboniferous sandstones correspond to the Late Brazilian/Pampean (700 – 500 Ma), the Famatinian (500 – 420 Ma) and Sunsas/Greenvillian (1300 – 900 Ma) orogenic events. It might suggest that the source areas for the Carboniferous units are the same as the Devonian units, but with the addition of areas related with the Chanic event (420 – 320 Ma). However, taking into account the paleocurrents to the northwestern (Sempere, 1995; Starck and Del Papa, 2006) the source that supplied sediments probably was located to the south and/or southeastern part of the basin for Carboniferous times. In a recently work, Starck et al. (2021) suggest the Rio de la Plata Craton as the most-likely potential source area for the Tarija Formation. The main source area, proposed by Starck et al. (2021), taking into account the U-Pb age of a granitic boulder (2070 Ma) from a diamictite rock, and the direction and sense of glacial movements indicators described in the Tarija basin (Starck and Del Papa, 2006) and in Uruguay (Assine et al., 2018). Nevertheless, in this work important populations of U-Pb ages of zircon grains with ages > 1700 Ma were not found in any of the Carboniferous units (See Table 5 and Fig. 10). Based on the detrital age data (Fig. 9), the dissimilarity comparison (Fig. 13), and the isotopic composition (Figs. 7 and 8), we can infer that the probably main detrital supply of the Carboniferous units could belong to the reworking of underlying units (see Fig. 13) localized to the south and southeastern part. In addition, the Carboniferous units could also have been fed by a minor supply of sediments from the northwestern in accordance with the model of glacial-controlled sedimentation proposed by Starck and Del Papa (2006). The minor source could include the igneous Devonian rocks that could be the San Nicolas batholith (Mukasa and Henry, 1990) and/or the Chacras-Potrerillos, Renca and Achala batholiths (Dahlquist et al., 2019, 2018; López de Luchi et

al., 2017).

5.3. Maturity and reworking

The petrographic analyses (Table 2 and Fig. 4) revealed that quartz grains percentages do not show any significant trend; however, these percentages slightly increases in the sandstone samples of the Carboniferous units. Furthermore, a notably increase in the roundness of the quartz grains (Supplementary Fig. I1) and of the zircon grains (Fig. 9) from sandstones samples indicate a major mineralogical and textural maturity for the Carboniferous units.

On the basis of the genetic scheme proposed by Dickinson (1985), the samples are plotted on the Craton interior near to the boundary with recycled orogen (Fig. 4). In this way, the modal composition indicate that the analyzed sandstone were likely derived mainly from the Craton interior; but a source of a recycled orogenic cannot be discarded. This assumption is supported by the provenance data presented above that indicated provenance from the different orogenic rocks located in the western part of South America.

The X-ray diffractometry data, on the other hand, show that the Devonian and Carboniferous pelitic rocks have a similar mineralogical composition (Table 3 and Supplementary Fig. I2), with illite and kaolinite been the most abundant. In contraposition, hematite is only present in the Carboniferous units, which may indicate an oxidative depositional context.

According to Chamley (1989), the kaolinite formation under near-surface/meteoric conditions at a regional scale is correlated to humid-subtropical to tropical climates, whereas illite-mica prevails under dry climate conditions typically related with low hydrolyzing condition. For that reason, the presence of kaolinite, means that a contrasting humidity and temperature conditions were required for its formation. Considering that the Carboniferous units from the Tarija Basin were formed under glacial conditions, the

presence of kaolinite in the Carboniferous units is unusual. However, the type of clays suites transported and deposited by glaciers also depends on the compositional nature of substrates (Chamley, 1989). In this way, it is more plausible that the presence of kaolinite in Carboniferous units has been incorporated by the glacier from Devonian units rich in Kaolinite, which have also been recognized in several Paleozoic basins along of this sector of Gondwana (Aparicio González et al., 2020b; Uriz et al., 2016; Zeballos et al., 2016). The presence of kaolinite from the underlying reworked units has also been identified by Kołtonik et al. (2019) in Carboniferous diamictite units from northern part of Bolivia. In addition, the relative increase of oval zircon grains, as well as the rounded and subangular to subrounded grains for the Carboniferous units (Figs. 9 and 10B) is in accordance with our interpretation of the reworking of the underlying units as a potential source.

5.4. Tectonic setting of the Tarija Basin between Devonian and Carboniferous

Different tectonic settings were proposed for the Tarija basin during the Middle and Upper Paleozoic. However, the majority of authors defined it as a foreland basin (Anderson et al., 2021; Gohrbandt, 1993; Isaacson and Diaz-Martinez, 1995; Ramos, 1988; Sempere, 1995; Starck, 1995), intracratonic basin (Fernández Seveso et al., 1998; Starck and Del Papa, 2006) or a back-arc basin (Dalenz-Farjat et al., 2002). Our data together combined with the published ones allowed us to propose a model for the tectonic setting of the Tarija basin during the Devonian – Carboniferous time on the basis of the obtained data.

According to Cawood et al. (2012), it is possible to predict the tectonic settings of a particular basin taking into account the cumulative proportion of the function of the difference between the measured crystallization age (CA) for a detrital zircon grain and the depositional age (DA). For example, basins from extensional (including intracratonic and passive margin) settings have CA-DA greater than 150 Ma in the youngest 5% of the zircon grains (step 1 in Fig. 14), whereas basins from collisional settings (including Appalachian

and Cordillera foreland basins types) have CA-DA less than 150 Ma and greater than 100 Ma in the youngest 5% and 30% of the zircon grains, respectively (step 1 and 2 in Fig. 14).

In this way, when the cumulative proportion of analyzed zircon grains are plotted as a function (CA – DA) for each unit from the Tarija basin (following the step 1 and 2 in the Fig. 14), the most part of them plot in the collisional settings field (foreland basins types). However, apparently the cumulative proportion of analyzed zircon grains plotted in a transition zone between convergent setting and collisional setting, this could be indicative that sedimentary rocks were formed in a foreland basin related to a convergent setting (Cordillera foreland basin type).

According to Dalenz-Farjat et al. (2002), the development of a foreland-type basin during Devonian times in this sector of SW Gondwana, could not be possible because a Silurian-Devonian thrust belt was not identified to the west of the basin. In general, the foreland basin system would subside as a response of the adjacent thrust belt load development (DeCelles, 2012) and this type of subsidence has been recognized in the Tarija basin by several authors like Milani and De Wit (2008) and recently by Anderson et al. (2021). Anderson et al. (2021) suggested, on the basis of thermometry data plus cross-section reconstructions, the existence of a Paleozoic folding and trust faulting belt in this sector. This argument allows the authors to suggest the existence of a foreland basin between ~420 and ~318 Ma.

Our multidisciplinary provenance dataset reinforced by available sedimentological information suggest a change in the configurations between Devonian and Carboniferous times. The Devonian time would characterized mainly by marine clastic sedimentation (Fuentes et al., 2018). The paleocurrents (e.g Albariño et al., 2002; Isaacson and Diaz-Martinez, 1995) indicated direction toward the east and northeast. In this way, the potential source areas could be located to the west of the basin (Sierras Pampeanas, Arequipa-

Antofalla massif and Famatinian arc). As it was said before, there are evidences of subsidence (e.g. Anderson et al., 2021; Milani and De Wit, 2008) and the development of a fold and thrust belt during this time at the western part of the basin (Anderson et al., 2021). Those facts, together with the tectonic collisional setting reflected by the detrital zircon record (Fig. 14), reaffirm the existence of a foreland basin related to a convergent margin setting for the Tarija basin during the Devonian time.

The geodynamic setting of that margin during the Devonian apparently correspond to a flat-slab subduction (Fig. 15). As is shown in the model proposed by Dai et al. (2020), the flat slab subduction trough slab break-off, slab delamination and eclogitization processes, could explain: 1) the absence of a magmatic arc during the Devonian time (e.g Augustsson et al., 2006; Bahlburg et al., 2009; Chew et al., 2007; Reimann et al., 2010), 2) the tectonic shortening (Anderson et al., 2021), 3) the subsidence in the western part of the basin (e.g. Anderson et al., 2021; Milani and De Wit, 2008), and 4) the Devonian magmatism A-Type in central northwestern Argentina (Dahlquist et al., 2019, 2018).

In contrast, the Carboniferous time is characterized by deposits related to glacial settings and paleocurrents toward north and/or northwest and by fluvial and deltaic facies related to the stages of ice retreatment with paleocurrents toward the east south and southeastern (Starck and Del Papa, 2006). In this way, considering the shortening proposed by Anderson et al. (2021), the bimodal paleocurrent data and the possible reworking of underlying units, it is plausible to think in the existence of a foreland basin related to a convergent margin and with an important sedimentary contribution from the intracontinent for the Carboniferous (Fig. 15). In addition, the spatial and temporal distribution of the Carboniferous magmatism (I-and A-Type granites; see Fig. 15) in the central northwest Argentina (Dahlquist et al., 2018) and the erosional exhumation between ~352 and ~294 Ma (Anderson et al., 2021) is in accordance with the model proposed by

Dai et al. (2020). Those authors explain that after the complete delamination of flat-slab the remnant slab migrates backward to the trench. As a result, the negative topography in the foreland basin begins to uplift rapidly and eventually evolves into a positive topographic feature. At the same time, the upwelling of the asthenospheric mantle induces large-scale magmatism in the continental interior of the overriding slab (bimodal volcanism and I-and A-Type granites) that became youngest toward the coastline (Dai et al., 2020).

5.5. Geodynamic settings of the Southwestern margin of Gondwana

As the sedimentary basins could register the existence of an arc, still when it disappeared by erosion, the sedimentary provenance for the Devonian and Carboniferous units from the Tarija basin were compared again others SW Gondwanan basins of the same ages as Paraná, Chaco-Paraná, Sauce Grande, Paganzo, Navidad Arizaro, Madre de Dios and Karoo basins (Fig. 15). In general, the detrital zircon spectra of all basin show differences between the Devonian and Carboniferous units. A relative decrease in age populations occurs in the Carboniferous units of the Tarija, Paraná, Paganzo, Madre de Dios and Karoo basins. Whereas a relative increase in age populations occurs in the Carboniferous units of the Chaco-Paraná, Sauce Grande and Navidad basins (Fig. 15). A special case is the Karoo basin, which shows a similar spectrum for the Devonian and Carboniferous units, which suggests a similar provenance patterns (Fig. 15).

The Devonian detrital record of those basins show unimodal to polymodal zircon distributions, with a main range in ages between 400 – 700 Ma (Fig. 15) with many younger and older 2nd and 3rd order range peaks. Nevertheless, the Paganzo, Karoo and Madre de Dios basins show an important range peak between 900 – 1200 Ma. In addition, the Madre de Dios basin also show an important range peak between 1600 – 1900 Ma, with important peaks at 1774 and 17730 Ma, and two minor zircon population between 1200 – 1600 Ma and 350– 400 Ma, with peak ages at 1349 and 384 Ma, respectively (Fig. 15). The Paganzo

basin also show a minor zircon population between 1200 – 1600 Ma, with peak ages at 1343 and 1455 Ma. The Karoo and Navidad Arizaro basins have a subordinate zircon population between 400 and 350 Ma, with peak ages at 366 Ma for the Karoo basin and 361 Ma for the Navidad Arizaro basin. Apparently, these peak ages could represent an almost synsedimentary origin.

On another hand, the Carboniferous detrital record of those basins also show polymodal zircon distributions, with a demonstrable range peak between 400 – 700 Ma with many younger and older 2nd and 3rd order range peaks. However, the Karoo basin shows also a main population between 900 – 1200 Ma with several peaks (954, 1001 and 1066 Ma), while the Navidad Arizaro and Madre de Dios basins show minor population ranges between 300 – 350 Ma with peak ages at 325 and 312, respectively. Other minor population ranges between 900 – 1200 Ma with peak ages at 966, 1056, 1094 and 1162 Ma for the Navidad Arizaro basin and at 988, 1041 and 1180 Ma for the Madre de Dios basin (Fig. 15). Furthermore, the zircon population between 350 and 300 Ma, apparently, could also represent an almost synsedimentary origin.

The Madre de Dios basin, located to the north of 20° S (see Fig. 1), shows a minor peak ages at 384 and 367 Ma for the Devonian and Carboniferous sedimentary units, respectively (Fig. 15). This fact could suggest that the San Nicolas batholith (425 and 394 – 388; Mukasa and Henry, 1990) as a potential source. This idea is in accordance which the mainly provenance area suggested by some authors (Kołtonik et al., 2019; Reimann et al., 2010) for the Devonian and Carboniferous units of the Madre de Dios basin. In addition, the Carboniferous units also show an important peak age of ~312 Ma, which is indicative of the Carboniferous arc magmatism in the region, which apparently started after ~ 345 Ma (e.g. Bahlburg et al., 2009; Chew et al., 2007). Another interesting point is about the important zircon population between 1600 and 1900 Ma for the Devonian units and the minor zircon

population between 1900 and 2200 Ma for the Carboniferous units, both present in the Madre de Dios basin, but absent in the other basins (Fig. 15). As already indicated by Kołtonik et al. (2019) and Reimann et al. (2010), the provenance data indicate the Northern domain of Arequipa-Antofalla massif as the main source of sediment for the Devonian and Carboniferous units. These ages populations represent the oldest rocks in that region (See Fig. 1). In contrast, the Paraná basin also show these range ages like a minor zircon population, however a provenance is associated to cratonic sources.

The Tarija basin, located between 20° - 28° S, also show a minor peak age in the Devonian time with zircon grains between 365 and 410 Ma (Fig. 15), which could indicate mainly two source areas, the San Nicolas batholith suggested by Mukasa and Henry (1990) and/or the intracontinental magmatism described by Dahlquist et al. (2019, 2018). Both cases suggest an incipient magmatic activity during the Devonian, which can not be explained with a passive margin in that sector of Gondwana.

On another hand, to the south of 28° S, the geodynamic settings are more complex. According to several authors (e.g. Heredia et al., 2018; Willner et al., 2011), the interruption of the subduction margin along western Cuyania was related to the collision of a suspected exotic terrane from the west (Chilenia) accreted to the continent during the mid or late Devonian (Heredia et al., 2018b; Willner et al., 2011). Another hypothetical idea was proposed by Heredia et al. (2016), whom proposed that Chilenia and Cuyania formed a single terrane (Chi-Cu) with different settings in the north and south part. Furthermore, Dahlquist et al. (2018) suggest that late Devonian-Early Carboniferous magmatism at this latitude represents continuous magmatic activity (322 to 379 Ma), in this way those authors proposed that the magmatic evolution was mainly controlled by episodic fluctuations in the angle of subduction of the oceanic plate (between flat-slab and normal subduction), supporting by a geodynamic switching model.

The basins located to the south of 28° S (Navidad Arizaro, Paganzo, Karoo, Paraná, Chaco-Paraná and Sauce Grande basins) detailed in the Figure 16 show a minor peak age in the Devonian time for the Devonian and Carboniferous units, except for the Paraná and Chaco-Paraná basins, which detrital spectra reflect intracratonic settings (Fig. 15), for this reason the absence of that peak could be understandable. The Devonian zircon ages at this latitude could come from the Guarguaraz complex described by Willner et al. (2011) and/or Devonian intracontinental magmatism (Achala, Las Chacras-Potrerillos and Renca batholiths) described by Dahlquist et al. (2018). The Guarguaraz complex, according to Willner et al. (2011) represent the age of the metamorphic peak that indicate the age of maximum subduction of this complex, which was followed by the Chilenia collision and subsequent obduction of the Guarguaraz complex during Devonian time (ca. 374 Ma). Nonetheless, according to Dahlquist et al. (2018), the higher pressure metamorphism (7 – 14 kbar) under a low thermal gradient (10 – 13° C/km) registered by those authors is comparable with subduction zone geothermal gradients.

The development of an Early Devonian subduction setting on the proto-Pacific margin was proposed by Willner et al. (2011), although no magmatic arc is known at this time and latitude and there is no evidence for granites with a post-collisional signature (Dahlquist et al., 2018). In the same way, that proposed middle–late Devonian collision does not explain the extensive magmatism developed in the retro-arc region proposed by Dahlquist et al. (2018).

Therefore, it is plausible to think in a strong segmentation of the SW margin of Gondwana as was also proposed by Creixell et al. (2021), this segmentation could have generated modifications in the behavior and interactions between the plates. We propose a segmentation located to the north of 20° S, between 20° S to 28° S, and to the south of 28° S. To the north of 20° S, Mukasa and Henry (1990) present an ambiguous geochemical data

that reveal affinities to volcanic arc or late- to post-collisional calc-alkaline intrusions. However, no other evidence of post-collisional magmatism has been found, so the arc magmatism and segmentation hypothesis could be supported during the Devonian time in this region. Apparently, between 20° S to 28° S, until now there are no magmatism data in this sector; nevertheless, these characteristics could correspond to a flat subduction. According to Kearey et al. (2009), the flat-slab subduction in extreme cases can cause the absence or suppression of magmatism over the subduction zone, as well as significant shortening with consequent intracontinental subsidence, which has been widely recognized in the Tarija basin and neighboring sectors (i.e. Precordillera) during the Devonian (Milani and De Wit, 2008).

Furthermore, to the south of 28° S, according to Dahlquist et al. (2018), the absence of middle-late Devonian arc magmatism was a result of flat-slab subduction associated with high P-T metamorphism in the continental outboard margin at ~390 Ma. At the same time, intracontinental magmatism (Achala, Las Chacras-Potrerillos and Renca batholiths) occurred at this latitude due to anomalous mantle upwelling in the intracontinental region. We are in accordance with that observation, however we consider that a flat-slab subduction and slab delamination model proposed by Dai et al. (2020) allows considering and integrating the flat-slab subduction characteristics suggested by Dahlquist et al. (2019, 2018) with intracontinental subsidence patterns. Besides that, this model allows to explain the presence and the transition of Devonian magmatism A-type towards the Carboniferous magmatism A-type and I-type in the continental interior.

6. Conclusions

The sedimentary provenance for the Devonian – Carboniferous units of the Tarija basin have been assessed trough multidisciplinary studies. The analyzed samples of the Devonian units are mainly quartzose sandstones; pelitic composed mainly by illite, kaolinite, quartz

and feldspars minerals. The integration of provenance techniques allows us to point out the Sierras Pampeanas as a main source, the southern-central domain of Arequipa-Antofalla massif and the Famatinian as a secondary source. The analyzed samples of the Carboniferous units are mainly quartzose and pure quartzose sandstones and pelitic rocks composed by illite, kaolinite, quartz and feldspars minerals. Our data could suggest that the Carboniferous units were formed by the same sources that the Devonian units and by an additional less contribution of younger rocks. Thus, the potential sources are composed by the Sierras Pampeanas as a main source, the southern-central domain of Arequipa-Antofalla massif and the Famatinian arc as a secondary source and the rocks forming during the Chanic event provided a minor supply to the basin. However, the paleocurrent data toward the north and northwest, clay mineralogy, sandstone petrography and zircon morphology could sustain the reworking of the underlying units as a potential source with a minor supply of sources located to the west like Sierras Pampeanas, southern-central domain of Arequipa-Antofalla massif, Famatinian arc and the Devonian magmatic rocks. In contrast, the scarce Paleoproterozoic ages in the detrital record indicate that cratonic areas, like the Amazonian Craton or the Río de la Plata Craton were not important sources for the Devonian – Carboniferous units.

Our provenance data in combination with published information like paleocurrent data, subsidence patterns and Paleozoic folding and trust faulting data, allowed us to interpret the existence of a foreland basin related to a convergent margin with modifications in the behavior and interactions of the plates during the Devonian and Carboniferous times. Furthermore, the Carboniferous time is represent by an important sedimentary supply of the intracontinental area like a product of glacial transport.

The analysis of the detrital record for different basins located in the SW part of Gondwana together with our provenance data allow us to interpret that the SW margin of

Gondwana had a strong segmentation, like is observed today, that generated modifications in the behavior and interactions of the plates during the Devonian. To the north of 20° S, Considering the available data of Devonian magmatism, the existence of a magmatic arc can not be discard. In the segment located between 20° S and 28° S there is no evidence of Devonian magmatic activity so far; however, there is evidence of an important subsidence and shortening in the Tarija basin during Devonian and Carboniferous times; these evidences are in accordance to the flat-slab subduction. Finally, to the south of 28° S, the existence of a flat-slab subduction is possible, which was characterized by the development of intracontinental magmatism during the Devonian that switched to an arc magmatism during the Carboniferous as consequence of the flat-slab subduction and slab delamination processes.

Finally, the geodynamic setting during the Devonian time is complex; however, the establishment of a passive margin in this sector of Gondwana is confused. In our interpretation, the absence of Devonian magmatism in the region is consequence of the flat-slab subduction settings.

Acknowledgments:

The authors are thankful to the *Coordenação de Aperfeiçoamento de Pessoal de Nível Superior – Brasil* (CAPES) for granting a Master scholarship to the first author. We also thank the *Laboratório de Estudos Geodinâmicos, Geocronológicos e Ambientais* (LEGGA) of the University of Brasília for the technical support. We also thank the *Institut de recherche pour le développement* (IRD) for the financial support and the *Yacimientos Petrolíferos Fiscales Bolivianos* (YPFB) for help us in the fieldwork.

Figure captions:

Figure 1: Schematic map of geochronological provinces of the South American Continent. Adapted from Bahlburg et al. (2009); Chew et al. (2008) and Reimann et al. (2010). The ages of the geochronological provinces are indicate in the figure. The extention of Paleozoic

sedimentary basins of SW Gondwana are represented by dotted lines, and the numbers represent the basins with data available of the Devonian – Carboniferous units. 1) Tarija basin (study area); 2) Paraná basin; 3) Chaco-Paraná basin; 4) Sauce Grande basin; 5) Paganzo basin; 6) Navidad Arizaro basin; 7) Madre de Dios basin. CA: Central Amazonian, MI: Marconi-Itacaiúnas, VT: Ventuari-Tapajos, RNJ: Rio Negro – Juruena, Ro: Rondonia-San Ignacio, SS: Sunsas/Grenvillian, SF: São Francisco Craton (4100 – 1900 Ma), RP: Rio de la Plata Craton (3100 – 570 Ma), RA: Rio Apa (2070 – 1700, 1300 Ma), BB: Brasilia belt, PB: Paraguay belt, and TB: Tucavaca belt.

Figure 2: Simplified geological map of the Southern Bolivian Subandean Zone, where the outcrops corresponding with the southern part of the Tarija basin are also shown. A and B represent the areas from which the samples were collected. Adapted from Anderson et al. (2017) and Giampaoli and Rojas Vera (2018).

Figure 3: Schematic stratigraphic column of the Devonian-Carboniferous sequences of the Tarija basin, adapted from Giampaoli and Rojas Vera (2018). Green triangles represent U-Pb analysis from Calle (2013). References of the palynological data: 1- Troth et al. (2011); 2- di Pasquo (2007b); and 3- di Pasquo et al. (2019).

Figure 4: Ternary plot of Q (total quartz), F (feldspars) and L (lithic fragments) of the Devonian-Carboniferous interval of the Tarija Basin. Ternary diagram of sandstone classification is from Garzanti (2019) and genetic scheme from Dickinson (1985).

Figure 5: Stratigraphic variation of Nd and Sr isotope compositions (ε_{Nd} and $^{87}Sr/^{86}Sr$), single-stage model age (T_{DM}) and two-stage model age (T_{DM}*) of analyzed samples from the Devonian – Carboniferous units of the Tarija basin. The lengths of the horizontal bars for ε_{Nd} and $^{87}Sr/^{86}Sr$ values correspond to 2SE (standard error, see Table 4). All the samples are claystones, except the sample from Chorro Formation that is a siltstone.

Figure 6: $^{87}Sr/^{86}Sr_{(300)}$ vs $\varepsilon_{Nd(300)}$ values of analyzed samples compared with data obtained from potential sources. Sierras Pampeanas (Rapela et al., 1998); Famatinian arc (Bock et al., 2000); Devonian magmatism (Dahlquist et al., 2019; López de Luchi et al., 2017).

Figure 7: Time (Ga) vs $\varepsilon_{Nd(T)}$ diagram of the Devonian - Carboniferous units of the Tarija Basin. Epsilon Nd (ε_{Nd}) values were calculated to the time of deposition based in the biostratigraphic age presented in Figure 2. CHUR: Chondritic uniform reservoir; DM: Depleted mantle. For comparison are also shown the Nd isotopic composition of: Arequipa-Antofalla domains (after Loewy et al., 2004); Devonian magmatism (after Dahlquist et al.,2019 and López de Luchi et al.,2017) and Famatinian arc (after Bock et al., 2000; Cardona, 2006 and Pankhurst et al., 1998) .

Figure 8: Detrital age distributions show as a CKDEs (top), Kernel density estimates, histograms, and pie plot of detrital zircon U-Pb ages from the Tarija basin (plots generated using detritalPy; Sharman et al., 2018). Samples were arranged in ascending stratigraphic order as presented in Fig. 2. U-Pb ages of the samples SLL-03 and AA-01 are from Calle (2013). The colors bars include Central Amazonian (> 2200 Ma), Maroni – Itacaiúnas (2200 – 2000 Ma), Venturi – Tapajos (2000 – 1820 Ma), Rio Negro – Juruena (1820 – 1540 Ma),

Rondonia – San Ignacio (1540 – 1300 Ma), Sunsas/Greenvillian (1300 – 900 Ma), Early Brazilian (900 – 700 Ma), Late Brazilian/Pampean (700– 500 Ma), Famatinian (500 – 420 Ma), and Chanic event (420 – 320 Ma) events. The notation N = (a/b/c) represent the number of zircon grains, where: a = number of zircon grains shown in the graphic, b = number of zircon grains with concordant ages, and c = total number of zircon grain analyzed. Histograms to the left side represent a zoom between 500 and 300 Ma.

Figure 9: Elongation and roundness features of unbroken zircon grains with concordant U-Pb ages of the Devonian and Carboniferous units of the Tarija basin.

Figure 10: A) Zircon-grain length vs. concordant age. Dash line indicate the limit between grain length < 125 μm and grain length between 125-300 μm. B) Zircon-grain elongation vs. concordant age. The field gray represents oval grains (length/width = 1.3-1.8), the lower gray field represent the round grains (length/width < 1.3), and the upper grey field represent the elongated grains (length/width > 1.8). Unbroken grains and only rims in zircon grains dated were taken into consideration.

Figure 11: Scatter plot of the U-Pb ages of the core-rim pairs related to important geochronological events. The X-axis represents the crystallization age of the core (step 1) and the Y-axis represent the crystallization age of the rim (step 2). Core-rim pairs located close to the diagonal line represent autocryst or antecryst zircon grains, whereas the core-rim pairs located away from diagonal line represent xenocryst or inherited zircon grains. The data shows a minor quantity of xenocryst or inherited zircon grains, which suggest minor recycling events presents in the detrital zircon record. The lengths of the horizontal and vertical bars for U-Pb ages of the core-rim pairs correspond to 2SE.

Figure 12: Multidimensional scaling (MDS) configuration of detrital zircon U-Pb dataset of the Devonian – Carboniferous units and underlying units. In this case, the MDS method take a matrix of pairwise dissimilarities between the statistical distance (Kolmogorov-Smirnov) of the age distribution of samples (Vermeesch, 2018). Similar samples cluster closely together and dissimilar samples plot far apart. The shading colored areas in the diagram represent potential sources. They were established from the data of the Silurian units (Aparicio González et al., 2020b; Augustsson et al., 2015; Calle, 2013), Ordovician units (Aparicio González et al., 2020a; Calle, 2013), Middle – Upper Cambrian Mesón Group (Adams et al., 2011), and Neoproterozoic – Cambrian Puncoviscana Formation (Adams et al., 2011; Aparicio González et al., 2014; Escayola et al., 2011; Hauser et al., 2011) from the NW Argentinian basement. Each sample is connected to its closest neighbor in Kolmogorov-Smirnov space with a solid line, and to its second-closest neighbor with a dashed line.

Figure 13: Tectonic discrimination diagram for convergent, collisional and extensional basins (After Cawood et al. 2012) showing the possible tectonic setting of the Tarija basin based on differences between the crystallization and depositional ages (CA – DA) of the zircon grains. Extensional settings (including intracratonic) have CA – DA > 150 Ma at 5% of the zircon population (step 1), convergent settings have CA – DA < 150 Ma and CA – DA < 100 Ma (step 2) Ma at 5% and 30% of zircon populations, respectively. Whereas the collisional setting have CA – DA < 150 Ma and CA – DA > 100 Ma at 5% and 30% of zircon populations, respectively.

The notation N = (a/b/) represent the number of zircon grains, where: a = number of zircon grains with concordant ages, and c = total number of zircon grain analyzed.

Figure 14: Schematic evolutionary model for detrital transportation for the Devonian and Carboniferous time of the Tarija basin and its relationship with the change in the proposed geodynamic settings for the SW margin of Gondwana between the Devonian and Carboniferous. The changes in the geodynamic setting during Devonian and Carboniferous time is based on the Flat-slab subduction and slab delamination model proposed by Dai et al. (2020). Data of Devonian and Carboniferous magmatism were taken from Dahlquist et al. (2019, 2018) and López de Luchi et al. (2017).

Figure 15: Kernel density plots for the Devonian and Carboniferous sedimentary units of the Tarija basin and other units for neighboring basins of the SW part of Gondwana. The detrital zircon data correspond to the Tarija (Aparicio González et al., 2020; Calle, 2013; this study), Paraná (Canile et al., 2016; Craddock et al., 2019; Fedorchuk et al., 2021, 2019; Santos et al., 2015; Tedesco et al., 2019), Chaco-Paraná (Fedorchuk et al., 2021; Uriz et al., 2016), Sauce Grande (Ramos et al., 2014; Uriz et al., 2011; Vorster, 2013), Paganzo (Arnol et al., 2020; Craddock et al., 2019; Enkelmann et al., 2014; Pauls et al., 2021), Navidad Arizaro (Bahlburg et al., 2009), Madre de Dios (Kołtonik et al., 2019; Reimann et al., 2010), and Karoo (Andersen et al., 2016; Craddock et al., 2019; Fourie et al., 2011; Vorster, 2013) basins.

Table list:

Table 1: Operating conditions and instrument settings of the diffractometers in each laboratory.

Table 2: Summary of the percentages of the petrography composition of the sandstone study. Q: total quartz, Qm: monocrystalline quartz, Qp: Polycrystalline quartz, F: total feldspar, P: plagioclase, Fk: Potassium feldspar, L: total lithics, Lv: volcanic lithic, Lp; plutonic lithic, Ls: sedimentary lithic, Lch: Chert fragment, and Lm: metamorphic lithic.

Table 3: Mineral composition defined by XRD of the pelitic samples collected from the Devonian – Carboniferous units. Kln: kaolinite, Chl: chlorite, Ilt: illite, Vrm: vermiculite, Sme: smectite, Qz: quartzo, Pl: plagioclase, FspK: Potassium feldspar, Hem: hematite, Gth: Goethite; M: major component, m: minor component, and tr: trace component.

Table 4: $\varepsilon_{Nd(Ts)} = [^{143}Nd/^{144}Nd_{sample\ (Ts)}/^{143}Nd/^{144}Nd_{CHUR\ (Ts)} - 1] \times 10^4$. $T_{DM} = ln[(^{143}Nd/^{144}Nd_{sample,\ today} - ^{143}Nd/^{144}Nd_{DM,\ today})/(^{147}Sm/^{144}Nd_{sample,\ today} - ^{147}Sm/^{144}Nd_{DM,\ today}) + 1]/\lambda$. $T_{DM}^* = ln[(^{143}Nd/^{144}Nd_{sample,\ today} - (e^{\lambda Ts}-1) \times (^{147}Sm/^{144}Nd_{sample,\ today} - ^{147}Sm/^{144}Nd_{crust,\ today}) - ^{143}Nd/^{144}Nd_{DM,\ today})/(^{147}Sm/^{144}Nd_{crust,\ today} - ^{147}Sm/^{144}Nd_{DM,\ today}) + 1]/\lambda$. Where T_s is the estimated depositional age based in published palynological data, $^{147}Sm/^{144}Nd_{crust,\ today} = 0.11$ (Albarède and Brouxel, 1987). The T_{DM} and T_{DM}^* were calculated for comparative purposes. The single-stage model of Goldstein et al. (1984) and the two-stage model of Liew and Hofmann (1988), *with* $\lambda(^{147}Sm) = 6.54 \times 10^{-12}a^{-1}$, $^{143}Nd/^{144}Nd_{DM,\ today} = 0.51315$, $^{147}Sm/^{144}Nd_{DM,\ today} = 0.217$, $^{143}Nd/^{144}Nd_{CHUR,\ today} = 0.512638$ *and* $^{147}Sm/^{144}Nd_{CHUR,\ today} = 0.1967$ (Jacobsen and Wasserburg, 1980), were used. The $^{87}Sr/^{86}Sr_{(300)}$ ratios were

calculated from the NASC references values for fine-grained rocks given by Gromet et al. (1984), where Rb: 125 ppm and Sr: 142 ppm.

Table 5: U-Pb geochronological events (bold) recognizes in the Amazonian craton, the Arequipa-Antofalla massif and the Central Andes. The U-Pb percentages identified of them recognized in each analyzes formation. Ages ranges are according to Bahlburg et al. (2009); Chew et al. (2008) and Reimann et al. (2010). (*) Data from Calle (2013), n = number of zircon concordant ages. For complementary information see Figure 1.

Table 6: Zircon morphology statistics of the Devonian-Carboniferous units. (*) Calculated in zircon unbroken grains only. Elo: Elongated; Ova: Oval; Rou: Round; Euh: Euhedral; Sa-sr: Subangular to subrounded; Roun: Rounded.

Supplementary data:

Supplementary Figure I1: Thin-section photomicrographs of the sandstone samples. (A-C) Monocrystalline quartz, potassium feldspar (microcline and pertite) and muscovite grains and of the Iquiri Formation (samples SSB-30A, SSB-10A and SSB-3A). (D-E) Monocrystalline quartz and muscovite grains of Los Monos Formation (samples SSB-16A and SSB-9A). (F) Monocrystalline quartz and muscovite grains of the Huamampampa Formation (Sample SSB-19A). (G-H) Monocrystalline quartz and muscovite grains of the Icla Formation (Samples SSB-14B and SSB-15A). (I) Monocrystalline quartz and muscovite of the Chorro Formation (Sample SSB-8A). (J) Monocrystalline quartz grains and a volcanic lithic of the Tarija Formation (Sample SSB-23A). (K) Monocrystalline quartz and muscovite grains and volcanic lithic fragment of the Tupambi Formation (Sample SSB-28A). (L) Monocrystalline quartz and plagioclase grains and chert fragment of the Itacua Formation (Sample SSB-5A). Mu: muscovite; Lv: volcanic lithic; Lch: chert fragment; Fk: potassium feldspar; Plg: plagioclase. The mineral abbreviations were used according to Garzanti (2019).

Supplementary Figure I2: Diffractograms of the Devonian – Carboniferous units of the Tarija basin organized by age. Chl: Chlorite; FspK: Potassium feldspar; Gth: Goethite; Hem: Hematite; Ilt: Illite; Kln: Kaolinite; Pl: Plagioclase; Qz: Quartz; Sme: Smectite; Vrm: Vermiculite.

Supplementary Figure I3: BSE images of the core-rim age pairs of Devonian Los Monos (SSB-16A and SSB-2A) and Iquiri (SSB-10A and SSB-4A) formations, and the Carboniferous Itacua (SSB-5A), Tupambi (SSB-28A) and Tarija (SSB-23A) formations. Yellow letters represent the U-Pb ages, whereas blue letters represent Th/U ratios. Figure inset: histogram shoing the Age relationship between rims and cores.

Supplementary Table 1: Conditions and instrumentation for U-Pb analyses by LA-ICP-MS – Laboratory of Geochronology and Isotope Geochemistry, University of Brasília.

Supplementary Table 2: Zircon U–Pb data for Devonian – Carboniferous sedimentary units of the Tarija basin, Southern Bolivian Subandean Zone. Results of U-Pb isotope analysis by LA-ICP-MS on zircon from samples SSB-16A, SSB-2A, SSB-10A, SSB-4A, SSB-5A, SSB-28A

and SSB-23A. Data in black were used for Concordia diagrams. Data in red, were excluded. (*) Data are grouped according to $^{207}Pb/^{206}Pb$ apparent ages. See text for discussion.

References

Adams, C.J., Miller, H., Aceñolaza, F.G., Toselli, A.J., Griffin, W.L., 2011. The Pacific Gondwana margin in the late Neoproterozoic–early Paleozoic: Detrital zircon U–Pb ages from metasediments in northwest Argentina reveal their maximum age, provenance and tectonic setting. Gondwana Res. 19, 71–83. https://doi.org/10.1016/j.gr.2010.05.002

Albarède, F., Brouxel, M., 1987. The Sm/Nd secular evolution of the continental crust and the depleted mantle. Earth Planet. Sci. Lett. 82, 25–35. https://doi.org/10.1016/0012-821X(87)90104-X

Albarède, F., Telouk, P., Blichert-Toft, J., Boyet, M., Agranier, A., Nelson, B., 2004. Precise and accurate isotopic measurements using multiple-collector ICPMS. Geochim. Cosmochim. Acta 68, 2725–2744. https://doi.org/10.1016/j.gca.2003.11.024

Albariño, L., Dalenz-Farjat, A., Alvarez, L., Hernandez, R., Pérez-Leyton, M., 2002. Las secuencias sedimentarias del Devónico en el Subandino Sur y el Chaco. Bolivia y Argentina. V Congr. Explor. y Desarro. Hidrocarburos 21.

Alves, D.B., 1987. Desenvolvimento da metodologia de preparação de amostras para análise difratométrica de argilominerais no Centro de Pesquisas da Petrobrás. Bol. Geociências da Petrobrás 1, 157–175.

Andersen, T., Kristoffersen, M., Elburg, M.A., 2016. How far can we trust provenance and crustal evolution information from detrital zircons? A South African case study. Gondwana Res. 34, 129–148. https://doi.org/10.1016/j.gr.2016.03.003

Anderson, R.B., Long, S.P., Horton, B.K., Calle, A.Z., Ramirez, V., 2017. Shortening and structural architecture of the Andean fold-thrust belt of southern Bolivia (21°S): Implications for kinematic development and crustal thickening of the central Andes. Geosphere 13, 538–558. https://doi.org/10.1130/GES01433.1

Anderson, R.B., Long, S.P., Horton, B.K., Calle, A.Z., Soignard, E., 2021. Late Paleozoic Gondwanide deformation in the Central Andes: Insights from RSCM thermometry and thermal modeling, southern Bolivia. Gondwana Res. 94, 222–242. https://doi.org/10.1016/j.gr.2021.03.002

Aparicio González, P., Hauser, N., de Oliveira Carvalho, M., de Morisson Valeriano, C., Eric Cayo, L., Barrientos, A., Impiccini, A., Reimold, W.U., Heilbron, M., Pimentel, M.M., 2020a. The Neoproterozoic-lower Paleozoic sequence of the Sierra de Mojotoro, Eastern Cordillera: Sedimentary provenance (Sr–Nd, U–Pb, and clay mineralogy) and its tectonic implications for western Gondwana. J. South Am. Earth Sci. 104, 102818. https://doi.org/10.1016/j.jsames.2020.102818

Aparicio González, P., Uriz, N., Arnol, J., Dopico, C.M., Cayo, L.E., Cingolani, C., Impiccini, A., Stipp Basei, M.A., 2020b. Sedimentary provenance analysis of the ordovician to devonian siliciclastic units of the Subandean Ranges and Santa Barbara System, northwestern Argentina. J. South Am. Earth Sci. 101, 102629. https://doi.org/10.1016/j.jsames.2020.102629

Aparicio González, P.A., Pimentel, M.M., Hauser, N., Moya, M.C., 2014. U–Pb LA-ICP-MS geochronology of detrital zircon grains from low-grade metasedimentary rocks (Neoproterozoic – Cambrian) of the Mojotoro Range, northwest Argentina. J. South Am. Earth Sci. 49, 39–50. https://doi.org/10.1016/j.jsames.2013.10.002

Arnol, J.A., Uriz, N.J., Cingolani, C.A., Basei, M.A.S., Abre, P., 2020. Provenance analysis of Devonian peripheral foreland basins in SW Gondwana, case of the Gualilán Group, Precordillera Argentina. Int. J. Earth Sci. 109, 2467–2494. https://doi.org/10.1007/s00531-020-01914-9

Assine, M.L., de Santa Ana, H., Veroslavsky, G., Vesely, F.F., 2018. Exhumed subglacial landscape in Uruguay: Erosional landforms, depositional environments, and paleo-ice flow in the context of the late Paleozoic Gondwanan glaciation. Sediment. Geol. 369, 1–12. https://doi.org/10.1016/j.sedgeo.2018.03.011

Augustsson, C., Münker, C., Bahlburg, H., Fanning, C.M., 2006. Provenance of late Palaeozoic metasediments of the SW South American Gondwana margin: a combined U–Pb and Hf-isotope

study of single detrital zircons. J. Geol. Soc. London. 163, 983–995. https://doi.org/10.1144/0016-76492005-149
Augustsson, C., Rüsing, T., Niemeyer, H., Kooijman, E., Berndt, J., Bahlburg, H., Zimmermann, U., 2015. 0.3 byr of drainage stability along the Palaeozoic palaeo-Pacific Gondwana margin; a detrital zircon study. J. Geol. Soc. London. 172, 186–200. https://doi.org/10.1144/jgs2014-065
Augustsson, C., Voigt, T., Bernhart, K., Kreißler, M., Gaupp, R., Gärtner, A., Hofmann, M., Linnemann, U., 2018. Zircon size-age sorting and source-area effect : The German Triassic Buntsandstein Group. Sediment. Geol. 375, 218–231. https://doi.org/10.1016/j.sedgeo.2017.11.004
Baby, P., Hérail, G., Salinas, R., Sempere, T., 1992. Geometry and kinematic evolution of passive roof duplexes deduced from cross section balancing: Example from the foreland thrust system of the southern Bolivian Subandean Zone. Tectonics 11, 523–536. https://doi.org/10.1029/91TC03090
Bache, F., Moreau, J., Rubino, J.L., Gorini, C., Van-Vliet Lanoë, B., 2012. The subsurface record of the Late Palaeozoic glaciation in the Chaco Basin, Bolivia. Geol. Soc. London, Spec. Publ. 368, 257–274. https://doi.org/10.1144/SP368.11
Bahlburg, H., 1990. The Ordovician basin in the Puna of NW Argentina and N-Chile: geodynamic evolution from back-arc to foreland basin. Geotekt. Forsch 75, 1–107.
Bahlburg, H., Hervé, F., 1997. Geodynamic evolution and tectonostratigraphic terranes of northwestern Argentina and northern Chile. Geol. Soc. Am. Bull. 109, 869–884. https://doi.org/10.1130/0016-7606(1997)109<0869:GEATTO>2.3.CO;2
Bahlburg, H., Vervoort, J.D., Du Frane, S.A., Bock, B., Augustsson, C., Reimann, C., 2009. Timing of crust formation and recycling in accretionary orogens: Insights learned from the western margin of South America. Earth-Science Rev. 97, 215–241. https://doi.org/10.1016/j.earscirev.2009.10.006
Basu, A.R., Sharma, M., DeCelles, P.G., 1990. Nd, Sr-isotopic provenance and trace element geochemistry of Amazonian foreland basin fluvial sands, Bolivia and Peru: implications for ensialic Andean orogeny. Earth Planet. Sci. Lett. 100, 1–17. https://doi.org/10.1016/0012-821X(90)90172-T
Bock, B., Bahlburg, H., Worner, G., Zimmermann, U., 2000. Tracing crustal evolution in the Southern Central Andes from Late Precambrian to Permian with geochemical and Nd and Pb isotope data. J. Geol. 108, 515–535. https://doi.org/10.1086/314422
Boger, S., Raetz, M., Giles, D., Etchart, E., Fanning, C., 2005. U-Pb age data from the Sunsas region of Eastern Bolivia, evidence for the allochthonous origin of the Paragua Block. Precambrian Res. 139, 121–146. https://doi.org/10.1016/j.precamres.2005.05.010
Bouchez, J., Gaillardet, J., France-Lanord, C., Maurice, L., Dutra-Maia, P., 2011. Grain size control of river suspended sediment geochemistry: Clues from Amazon River depth profiles. Geochemistry, Geophys. Geosystems 12, n/a-n/a. https://doi.org/10.1029/2010GC003380
Calle, A.Z., 2013. Neogene sedimentation and provenance record of the Subandean zone and Chaco foreland basin, southern Bolivia. The University of Texas at Austin.
Calle, A.Z., Horton, B.K., Limachi, R., Stockli, D.F., Uzeda-Orellana, G. V., Anderson, R.B., Long, S.P., 2018. Cenozoic Provenance and Depositional Record of the Sub-Andean Foreland Basin during Growth of the Central Andean Fold-Thrust Belt, Southern Bolivia, in: Zamora, G., McClay, K.R., Ramos, V.A. (Eds.), Petroleum Basins and Hydrocarbon Potential of the Andes of Perú and Bolivia. The American Association of Petroleum Geologist and Repsol, pp. 483–530. https://doi.org/10.1306/13622132M1173777
Canile, F.M., Babinski, M., Rocha-Campos, A.C., 2016. Evolution of the Carboniferous-Early Cretaceous units of Paraná Basin from provenance studies based on U-Pb, Hf and O isotopes from detrital zircons. Gondwana Res. 40, 142–169.
Cardona, A., 2006. Reconhecimento da evolução tectônica da proto-margem andina do centro-norte peruano, baseada em dados geoquímicos e isotópicos do embasamento da Cordilheira Oriental na região de Huánuco-La Unión. Universidade de São Paulo.
Casquet, C., Baldo, E., Pankhurst, R.J., Rapela, C.W., Galindo, C., Fanning, C.M., Saavedra, J., 2001. Involvement of the Argentine Precordillera terrane in the Famatinian mobile belt: U-Pb SHRIMP and metamorphic evidence from the Sierra de Pie de Palo. Geology 29, 703.

https://doi.org/10.1130/0091-7613(2001)029<0703:IOTAPT>2.0.CO;2
Casquet, C., Pankhurst, R.J., Rapela, C.W., Galindo, C., Fanning, C.M., Chiaradia, M., Baldo, E., González-Casado, J.M., Dahlquist, J.A., 2008. The Mesoproterozoic Maz terrane in the Western Sierras Pampeanas, Argentina, equivalent to the Arequipa–Antofalla block of southern Peru? Implications for West Gondwana margin evolution. Gondwana Res. 13, 163–175. https://doi.org/10.1016/j.gr.2007.04.005
Cawood, P.A., 2005. Terra Australis Orogen: Rodinia breakup and development of the Pacific and Iapetus margins of Gondwana during the Neoproterozoic and Paleozoic. Earth-Science Rev. 69, 249–279. https://doi.org/10.1016/j.earscirev.2004.09.001
Cawood, P.A., Hawkesworth, C.J., Dhuime, B., 2012. Detrital zircon record and tectonic setting. Geology 40, 875–878. https://doi.org/10.1130/G32945.1
Cawood, P.A., Nemchin, A.A., 2000. Provenance record of a rift basin: U/Pb ages of detrital zircons from the Perth Basin, Western Australia. Sediment. Geol. 134, 209–234. https://doi.org/10.1016/S0037-0738(00)00044-0
Chamley, H., 1989. Clay Sedimentology, 1st ed. Springer-Verlag Berlin Heidelberg, Berlin, Heidelberg. https://doi.org/10.1007/978-3-642-85916-8
Chew, D.M., Magna, T., Kirkland, C.L., Mišković, A., Cardona, A., Spikings, R., Schaltegger, U., 2008. Detrital zircon fingerprint of the Proto-Andes : Evidence for a Neoproterozoic active margin? Precambrian Res. 167, 186–200. https://doi.org/10.1016/j.precamres.2008.08.002
Chew, D.M., Pedemonte, G., Corbett, E., 2016. Proto-andean evolution of the eastern Cordillera of Peru. Gondwana Res. 35, 59–78.
Chew, D.M., Schaltegger, U., Kosler, J., Whitehouse, M.J., Gutjahr, M., Spikings, R.A., Miskovic, A., 2007. U-Pb geochronologic evidence for the evolution of the Gondwanan margin of the north-central Andes. Geol. Soc. Am. Bull. 119, 697–711. https://doi.org/10.1130/B26080.1
Cordani, U.G., Sato, K., Teixeira, W., Tassinari, C.C.G., Basei, M.A.S., 2000. Crustal evolution of the South American platform, in: Cordani, U.G., Milani, E.J., Thomaz Filho, A.M., Campos, D.A. (Eds.), Tectonic Evolution of South America. 31st International Geological Congress Rio de Janeiro, Brazil, Rio de Janeiro, pp. 19–40.
Craddock, J.P., Ojakangas, R.W., Malone, D.H., Konstantinou, A., Mory, A., Bauer, W., Thomas, R.J., Affinati, S.C., Pauls, K., Zimmerman, U., Botha, G., Rochas-Campos, A., Santos, P.R. dos, Tohver, E., Riccomini, C., Martin, J., Redfern, J., Horstwood, M., Gehrels, G., 2019. Detrital zircon provenance of Permo-Carboniferous glacial diamictites across Gondwana. Earth-Science Rev. 192, 285–316. https://doi.org/10.1016/j.earscirev.2019.01.014
Creixell, C., Sepúlveda, F., Álvarez, J., Vásquez, P., Velásquez, R., 2021. The Carboniferous onset of subduction at SW Gondwana revisited: Sedimentation and deformation processes along the late Paleozoic forearc of north Chile (21°–33° S). J. South Am. Earth Sci. 107, 103149. https://doi.org/10.1016/j.jsames.2020.103149
Cruz, C.E., Veramendi, J.O., Di Benedetto, M., Pereira, M., Villar, H.J., 2008. Los Sistemas Petroleros Devonicos Del Subandino Sur Y Pie De Monte De La Cuenca De Tarija. Bolivia, in: Cruz, C.E., Rodríguez, J.F., Hechem, J.J., J, V.H. (Eds.), VII Congreso de Exploración y Desarrollo de Hidrocarburos (Simposio de Sistemas Petroleros de Las Cuencas Andinas). Instituto Argentino del Petróleo y del Gas, Buenos Aires, p. 29.
Cullers, R.L., 2000. The geochemistry of shales, siltstones and sandstones of Pennsylvanian–Permian age, Colorado, USA: implications for provenance and metamorphic studies. Lithos 51, 181–203. https://doi.org/10.1016/S0024-4937(99)00063-8
Dahlquist, J.A., Alasino, P.H., Basei, M.A.S., Morales Cámera, M.M., Macchioli Grande, M., da Costa Campos Neto, M., 2018. Petrological, geochemical, isotopic, and geochronological constraints for the Late Devonian–Early Carboniferous magmatism in SW Gondwana (27–32°LS): an example of geodynamic switching. Int. J. Earth Sci. 107, 2575–2603. https://doi.org/10.1007/s00531-018-1615-9
Dahlquist, J.A., Macchioli Grande, M., Alasino, P.H., Basei, M.A.S., Galindo, C., Moreno, J.A., Morales Cámera, M.M., 2019. New geochronological and isotope data for the Las Chacras – Potrerillos and Renca batholiths: A contribution to the Middle-Upper Devonian magmatism in the pre-Andean foreland (Sierras Pampeanas, Argentina), SW Gondwana. J. South Am. Earth Sci. 93, 348–363. https://doi.org/10.1016/j.jsames.2019.04.026

Dai, L., Wang, L., Lou, D., Li, Z., Dong, H., Ma, F., Li, F., Li, S., Yu, S., 2020. Slab Rollback Versus Delamination: Contrasting Fates of Flat-Slab Subduction and Implications for South China Evolution in the Mesozoic. J. Geophys. Res. Solid Earth 125, 18. https://doi.org/10.1029/2019JB019164

Dalenz-Farjat, A., Alvarez, L.A., Hernández, R.M., Albariño, L.M., 2002. Cuenca Siluro-Devónica del sur de Bolivia y del noroeste argentino: algunas interpretaciones. V Congr. Explor. y Desarro. Hidrocarburos 18.

di Pasquo, M., 2007a. Asociaciones palinológicas en las formaciones Los Monos (Devónico) e Itacua (Carbonífero Inferior) en Balapuca (Cuenca Tarija), sur de Bolivia: Parte 1. Formación Los Monos. Rev. geológica Chile 34. https://doi.org/10.4067/S0716-02082007000100006

di Pasquo, M., 2007b. Asociaciones palinológicas en las formaciones Los Monos (Devónico) e Itacua (Carbonífero Inferior) en Balapuca (Cuenca Tarija), sur de Bolivia: Parte 2. Asociaciones de la Formación Itacua e interpretación estratigráfica y cronología de las formaciones Lo. Rev. geológica Chile 34. https://doi.org/10.4067/S0716-02082007000200001

di Pasquo, M.M., Anderson Folnagy, H. j, Isaacson, P.E., Grader, G.W., 2019. Late Paleozoic carbonates and glacial deposits in Bolivia and Northern Argentina: Significant paleoclimatic changes, in: Latitudinal Controls on Stratigraphic Models and Sedimentary Concepts. Society for Sedimentary Geology, Tulsa, Olkahoma, pp. 185–203. https://doi.org/10.2110/sepmsp.108.10

Diaz-Martinez, E., 1996. Síntesis Estratigráfica y Geodinámica del Carbonífero de Bolivia. Memorias del XII Congr. Geológico Boliv. (Tarija, Boliv. 1, 355–367.

Dickinson, W.R., 1985. Interpreting Provenance Relations from Detrital Modes of Sandstones, in: Provenance of Arenites. Springer Netherlands, Dordrecht, pp. 333–361. https://doi.org/10.1007/978-94-017-2809-6_15

Dickinson, W.R., Gehrels, G.E., 2009. Use of U–Pb ages of detrital zircons to infer maximum depositional ages of strata: A test against a Colorado Plateau Mesozoic database. Earth Planet. Sci. Lett. 288, 115–125. https://doi.org/10.1016/j.epsl.2009.09.013

Dunn, J.F., Hartshorn, K.G., Hartshon, P.W., 1995. Structural Styles and Hydrocarbon Potential of the Sub-Andean Thrust Belt of Southern Bolivia, in: Tankard, A.J., Suárez, S., Welsink, H.J. (Eds.), Petroleum Basins of South America. American Association of Petroleum Geologist Memoir 62. pp. 523–543.

Echavarria, L., Hernández, R., Allmendinger, R., Reynolds, J., 2003. Subandean thrust and fold belt of northwestern Argentina: Geometry and timing of the Andean evolution. Am. Assoc. Pet. Geol. Bull. 87, 965–985. https://doi.org/10.1306/01200300196

Enkelmann, E., Ridgway, K.D., Carignano, C., Linnemann, U., 2014. A thermochronometric view into an ancient landscape: Tectonic setting, development, and inversion of the Paleozoic eastern Paganzo basin, Argentina. Lithosphere 6, 93–107. https://doi.org/10.1130/L309.1

Escayola, M.P., Staal, C.R. Van, Davis, W.J., 2011. The age and tectonic setting of the Puncoviscana Formation in northwestern Argentina : An accretionary complex related to Early Cambrian closure of the Puncoviscana Ocean and accretion of the Arequipa-Antofalla block. J. South Am. Earth Sci. 32, 438–459. https://doi.org/10.1016/j.jsames.2011.04.013

Fedorchuk, N.D., Griffis, N.P., Isbell, J.L., Goso, C., Rosa, E.L.M., Montañez, I.P., Yin, Q.-Z., Huyskens, M.H., Sanborn, M.E., Mundil, R., Vesely, F.F., Iannuzzi, R., 2021. Provenance of late Paleozoic glacial/post-glacial deposits in the eastern Chaco-Paraná Basin, Uruguay and southernmost Paraná Basin, Brazil. J. South Am. Earth Sci. 106, 102989. https://doi.org/10.1016/j.jsames.2020.102989

Fedorchuk, N.D., Isbell, J.L., Griffis, N.P., Montañez, I.P., Vesely, F.F., Iannuzzi, R., Mundil, R., Yin, Q.-Z., Pauls, K.N., Rosa, E.L.M., 2019. Origin of paleovalleys on the Rio Grande do Sul Shield (Brazil): Implications for the extent of late Paleozoic glaciation in west-central Gondwana. Palaeogeogr. Palaeoclimatol. Palaeoecol. 531, 108738. https://doi.org/10.1016/j.palaeo.2018.04.013

Fernández Seveso, F., Vistalli, M.C., Viñes, R., 1998. The Silurian-Devonian Chaco Basin: A review for reservoir correlation in Argentina and Bolivia. Ext. Abstr. Vol. AAPG Int. Conf. Exhib. 452–453.

Figueiredo, J., Hoorn, C., van der Ven, P., Soares, E., 2009. Late Miocene onset of the Amazon River and the Amazon deep-sea fan: Evidence from the Foz do Amazonas Basin. Geology 37, 619–622. https://doi.org/10.1130/G25567A.1

Fourie, P.H., Zimmermann, U., Beukes, N.J., Naidoo, T., Kobayashi, K., Kosler, J., Nakamura, E., Tait, J., Theron, J.N., 2011. Provenance and reconnaissance study of detrital zircons of the Palaeozoic Cape Supergroup in South Africa: revealing the interaction of the Kalahari and Río de la Plata cratons. Int. J. Earth Sci. 100, 527–541. https://doi.org/10.1007/s00531-010-0619-x

Fuentes, F., Rocha, E., Starck, D., 2018. Geometry and kinematics of structures of the southern sub-Andean fold-thrust belt of Bolivia. AAPG Mem. 117, 443–463. https://doi.org/10.1306/13622130M1173775

Garzanti, E., 2019. Petrographic classification of sand and sandstone. Earth-Science Rev. 192, 545–563. https://doi.org/10.1016/j.earscirev.2018.12.014

Giampaoli, P., Rojas Vera, E., 2018. Fold Growth and Lateral Linkage in the Southern Sub-Andean Fold-and-Thrust Belt of Argentina and Bolivia, in: AAPG Memoir 117: Petroleum Basins and Hydrocarbon Potential of the Andes of Peru and Bolivia. AAPG Special Volumes.

Gioia, S.M.C.., Pimentel, M.., 2000. The Sm-Nd isotopic method in the geochronology laboratory of the University of Brasília. An. Acad. Bras. Cienc. 72, 219–245. https://doi.org/10.1590/S0001-37652000000200009

Gohrbandt, K.H.A., 1993. Paleozoic paleogeographic and depositional developments on the central proto-Pacific margin of Gondwana: Their importance to hydrocarbon accumulation. J. South Am. Earth Sci. 6, 267–287.

Goldstein, S.L., O'Nions, R.K., Hamilton, P.J., 1984. A Sm-Nd isotopic study of atmospheric dusts and particulates from major river systems. Earth Planet. Sci. Lett. 70, 221–236. https://doi.org/https://doi.org/10.1016/0012-821X(84)90007-4

Gromet, L.P., Haskin, L.A., Korotev, R.L., Dymek, R.F., 1984. The "North American shale composite": Its compilation, major and trace element characteristics. Geochim. Cosmochim. Acta 48, 2469–2482. https://doi.org/10.1016/0016-7037(84)90298-9

Haq, B.U., Schutter, S.R., 2008. A chronology of Paleozoic sea-level changes. Science (80-.). 322, 64–68.

Hauser, N., Matteini, M., Omarini, R.H., Pimentel, M.M., 2011. Combined U–Pb and Lu–Hf isotope data on turbidites of the Paleozoic basement of NW Argentina and petrology of associated igneous rocks: Implications for the tectonic evolution of western Gondwana between 560 and 460Ma. Gondwana Res. 19, 100–127. https://doi.org/10.1016/j.gr.2010.04.002

Heilbron, M., Cordani, U.G., Alkmim, F.F., 2017. The São Francisco Craton and Its Margins, in: Heilbron, M., Cordani, U.G., Alkminn, F. (Eds.), São Francisco Craton, Eastern Brazil. pp. 3–13. https://doi.org/10.1007/978-3-319-01715-0_1

Heredia, N., García-Sansegundo, J., Gallastegui, G., Farias, P., Giacosa, R., Hongn, F., Tubía, J.M., Alonso, J.J., Busquets, P., Charrier, R., Clariana, P., Colombo, F., Cuesta, A., Gallastegui, J., Giambiagi, L., González-Menéndez, L., Limarino, O., Martín-González, F., Pedreira, D., Quintana, L., Rodríguez-Fernández, L.R., Rubio-Ordóñez, Á., Seggiaro, R., Serra-Varela, S., Spalletti, L., Cardó, R., Ramos, V.A., 2018a. The Pre-Andean Phases of Construction of the Southern Andes Basement in Neoproterozoic–Paleozoic Times, in: Folguera, A., Contreras-Reyes, E., Heredia, N., Encinas, A., B. Iannelli, S., Oliveros, V., M. Dávila, F., Collo, G., Giambiagi, L., Maksymowicz, A., Iglesia Llanos, M.P., Turienzo, M., Naipauer, M., Orts, D., D. Litvak, V., Alvarez, O., Arriagada, C. (Eds.), The Evolution of the Chilean-Argentinean Andes. Springer International Publishing, Cham, pp. 111–131. https://doi.org/10.1007/978-3-319-67774-3_5

Heredia, N., García-Sansegundo, J., Gallastegui, G., Farias, P., Giacosa, R.E., Giambiagi, L.B., Busquets, P., Colombo, F., Charrier, R., Cuesta, A., Rubio-Ordóñez, Á., Ramos, V.A., 2018b. Review of the geodynamic evolution of the SW margin of Gondwana preserved in the Central Andes of Argentina and Chile (28°-38° S latitude). J. South Am. Earth Sci. 87, 87–94. https://doi.org/10.1016/j.jsames.2017.11.019

Heredia, N., García Sansegundo, J., Gallastegui, G., Farias, P., Giacosa, R.E., Alonso, J.L., Busquets, P., Charrier, R., Clariana, P., Colombo, F., 2016. Evolución Geodinámica de los Andes de Argentina, Chile y la Península Antártica durante el Neoproterozoico tardío y el Paleozoico. Trab. Geol. 36, 237–278.

Hervé, F., Calderón, M., Fanning, C.M., Pankhurst, R.J., Godoy, E., 2013. Provenance variations in the Late Paleozoic accretionary complex of central Chile as indicated by detrital zircons. Gondwana Res. 23, 1122–1135. https://doi.org/10.1016/j.gr.2012.06.016

Hurtado, C., Roddaz, M., Santos, R.V., Baby, P., Antoine, P.-O., Dantas, E.L., 2018. Cretaceous-early Paleocene drainage shift of Amazonian rivers driven by Equatorial Atlantic Ocean opening and Andean uplift as deduced from the provenance of northern Peruvian sedimentary rocks (Huallaga basin). Gondwana Res. 63, 152–168.

Ingersoll, R. V, Bullard, T.F., Ford, R.L., Grimm, J.P., Pickle, S.W., 1984. The Effect of Grain Size on Detrital Modes: A Test of the Gazzi-Dickinson Point-Counting Method. SEPM J. Sediment. Res. 54, 103–116. https://doi.org/10.1306/212F83B9-2B24-11D7-8648000102C1865D

Isaacson, P.E., Diaz-Martinez, E., 1995. Evidence for a Middle-Late Paleozoic Foreland Basin and Significant Paleolatitudinal Shift, Central Andes. Pet. Basins South Am. https://doi.org/10.1306/M62593C10

Jackson, S.E., Pearson, N.J., Griffin, W.L., Belousova, E.A., 2004. The application of laser ablation-inductively coupled plasma-mass spectrometry to in situ U–Pb zircon geochronology. Chem. Geol. 211, 47–69. https://doi.org/10.1016/j.chemgeo.2004.06.017

Jacobsen, S.B., Wasserburg, G.J., 1980. Sm-Nd isotopic evolution of chondrites. Earth Planet. Sci. Lett. 50, 139–155. https://doi.org/10.1016/0012-821X(80)90125-9

Jaillard, E., Hérail, G., Monfret, T., Díaz-Martínez, E., Baby, P., Lavenu, A., Dumont, J.F., 2000. Tectonic evolution of the Andes of Ecuador, Peru, Bolivia and northernmost Chile. Tecton. Evol. South Am. 31, 481–559.

Jiménez, N., López-Velásquez, S., Santiváñez, R., 2009. Evolución tectonomagmática de los Andes Bolivianos. Rev. la Asoc. Geol. Argentina 65, 36–67.

Johnsson, M.J., 1993. The system controlling the composition of clastic sediments, in: Johnsson, M., Basu, A. (Eds.), Processes Controlling the Composition of Clastic Sediments. Geological Society of America Special Paper, p. Vol. 285, 1-20. https://doi.org/10.1130/SPE284-p1

Kearey, P., Klepeis, K.A., Vine, F.J., 2009. subduction zones, in: Global Tectonics. John Wiley & Sons, pp. 249–285.

Kołtonik, K., Isaacson, P., Pisarzowska, A., Paszkowski, M., Augustsson, C., Szczerba, M., Slama, J., Budzyń, B., Stachacz, M., Krawczyński, W., 2019. Provenance of upper Paleozoic siliciclastics rocks from two high-latitude glacially influenced intervals in Bolivia. J. South Am. Earth Sci. 92, 12–31. https://doi.org/10.1016/j.jsames.2019.02.023

Lawrence, R.L., Cox, R., Mapes, R.W., Coleman, D.S., 2011. Hydrodynamic fractionation of zircon age populations. GSA Bull. 123, 295–305. https://doi.org/10.1130/B30151.1

Liew, T.C., Hofmann, A.W., 1988. Precambrian crustal components, plutonic associations, plate environment of the Hercynian Fold Belt of central Europe: Indications from a Nd and Sr isotopic study. Contrib. to Mineral. Petrol. 98, 129–138. https://doi.org/10.1007/BF00402106

Limarino, C.O., Spalletti, L.A., 2006. Paleogeography of the upper Paleozoic basins of southern South America : An overview. J. South Am. Earth Sci. 22, 134–155. https://doi.org/10.1016/j.jsames.2006.09.011

Linol, B., de Wit, M.J., Milani, E.J., Guillocheau, F., Scherer, C., 2015. New regional correlations between the Congo, Paraná and Cape-Karoo basins of southwest Gondwana, in: Geology and Resource Potential of the Congo Basin. Springer, pp. 245–268.

Linol, Bastien, de Wit, M.J., Kasanzu, C.H., da Silva Schmitt, R., Corrêa-Martins, F.J., Assis, A., 2016. Correlation and paleogeographic reconstruction of the Cape-Karoo Basin sequences and their equivalents across central west Gondwana, in: Linol, B, de Wit, M. (Eds.), Origin and Evolution of the Cape Mountains and Karoo Basin. Springer, pp. 183–192.

Litherland, M., Annells, R.N., Llanos, A., Mitchell, W.I., O'Connor, E.A., 1986. The geology and mineral resources of the Bolivian Precambrian shield.

Loewy, S.L., Connelly, J.N., Dalziel, I.W.D., 2004. An orphaned basement block: The Arequipa-Antofalla Basement of the central Andean margin of South America. Geol. Soc. Am. Bull. 116, 171. https://doi.org/10.1130/B25226.1

López de Luchi, M.G., Siegesmund, S., Wemmer, K., Nolte, N., 2017. Petrogenesis of the postcollisional Middle Devonian monzonitic to granitic magmatism of the Sierra de San Luis, Argentina. Lithos 288–289, 191–213. https://doi.org/10.1016/j.lithos.2017.05.018

McLennan, S.M., Hemming, S., McDaniel, D. K.Hanson, G., 1993. Geochemical approaches to sedimentation, provenance, and tectonics, in: Johnsson, M.J., Basu, A. (Eds.), Processes Controlling the Composition of Clastic Sediments. Geological Society of America, Boulder,

Colorado, pp. 21–40.
Milani, E.J., De Wit, M.J., 2008. Correlations between the classic Paraná and Cape–Karoo sequences of South America and southern Africa and their basin infills flanking the Gondwanides: du Toit revisited. Geol. Soc. London, Spec. Publ. 294, 319–342.
Moore, D.M., Reynolds, R.C., 1997. X-ray Diffraction and the Identification and Analysis of Clay Minerals. Oxford University Press, New York.
Morata, D., Castro de Machuca, B., Arancibia, G., Pontoriero, S., Fanning, C.M., 2010. Peraluminous Grenvillian TTG in the Sierra de Pie de Palo, Western Sierras Pampeanas, Argentina: Petrology, geochronology, geochemistry and petrogenetic implications. Precambrian Res. 177, 308–322. https://doi.org/10.1016/j.precamres.2010.01.001
Mukasa, S.B., Henry, D.J., 1990. The San Nicolás batholith of coastal Peru: early Palaeozoic continental arc or continental rift magmatism? J. Geol. Soc. London. 147, 27–39. https://doi.org/10.1144/gsjgs.147.1.0027
Ortiz, A., Hauser, N., Becchio, R., Suzaño, N., Nieves, A., Sola, A., Pimentel, M., Reimold, W., 2017. Zircon U-Pb ages and Hf isotopes for the Diablillos Intrusive Complex, Southern Puna, Argentina: Crustal evolution of the Lower Paleozoic Orogen, Southwestern Gondwana margin. J. South Am. Earth Sci. 80, 316–339. https://doi.org/10.1016/j.jsames.2017.09.031
Ortiz, A., Suzaño, N., Hauser, N., Becchio, R., Nieves, A., 2019. New hints on the evolution of the Eastern Magmatic Belt, Puna Argentina. SW Gondwana margin: Zircon U-Pb ages and Hf isotopes in the Pachamama Igneous-Metamorphic Complex. J. South Am. Earth Sci. 94, 102246. https://doi.org/10.1016/j.jsames.2019.102246
Oyhantçabal, P., Cingolani, C.A., Wemmer, K., Siegesmund, S., 2018. The Río de la Plata Craton of Argentina and Uruguay, in: Siegesmund, S., Basei, M.A.S., Oyhantçabal, P., Oriolo, S. (Eds.), Geology of Southwest Gondwana. Springer, Cham, pp. 89–105. https://doi.org/10.1007/978-3-319-68920-3_4
Oyhantçabal, P., Siegesmund, S., Wemmer, K., 2011. The Río de la Plata Craton: a review of units, boundaries, ages and isotopic signature. Int. J. Earth Sci. 100, 201–220. https://doi.org/10.1007/s00531-010-0580-8
Pankhurst, R.J., Rapela, C.W., 1998. The proto-Andean margin of Gondwana: an introduction. Geol. Soc. London, Spec. Publ. 142, 1–9.
Pankhurst, R.J., Rapela, C.W., Saavedra, J., Baldo, E., Dahlquist, J., Pascua, I., Fanning, C.M., 1998. The Famatinian magmatic arc in the central Sierras Pampeanas : an Early to Mid-Ordovician continental arc on the Gondwana margin. Early to Mid-Ordovician Cont. arc Gondwana margin 343–367.
Patchett, P.J., Roth, M.A., Canale, B.S., de Freitas, T.A., Harrison, J.C., Embry, A.F., Ross, G.M., 1999. Nd isotopes, geochemistry, and constraints on sources of sediments in the Franklinian mobile belt, Arctic Canada. Geol. Soc. Am. Bull. 111, 578–589. https://doi.org/10.1130/0016-7606(1999)111<0578:NIGACO>2.3.CO;2
Paton, C., Hellstrom, J., Paul, B., Woodhead, J., Hergt, J., 2011. Iolite: Freeware for the visualisation and processing of mass spectrometric data. J. Anal. At. Spectrom. 26, 2508. https://doi.org/10.1039/c1ja10172b
Pauls, K.N., Isbell, J.L., Limarino, C.O., Alonso-Murauga, P.J., Malone, D.H., Schencman, L.J., Colombi, C.E., Moxness, L.D., 2021. Constraining late paleozoic ice extent in the Paganzo basin of western Argentina: Provenance of the lower Paganzo group strata. J. South Am. Earth Sci. 106, 102899. https://doi.org/10.1016/j.jsames.2020.102899
Petrus, J.A., Kamber, B.S., 2012. VizualAge: A Novel Approach to Laser Ablation ICP-MS U-Pb Geochronology Data Reduction. Geostand. Geoanalytical Res. 36, 247–270. https://doi.org/10.1111/j.1751-908X.2012.00158.x
Powers, M.C., 1953. A New Roundness Scale for Sedimentary Particles. J. Sediment. Res. 23, 117–119. https://doi.org/https://doi.org/10.1306/D4269567-2B26-11D7-8648000102C1865D
Ramos, V.A., 2018. Tectonic evolution of the Central Andes: from terrane accretion to crustal delamination, in: Zamora, G., McClay, K.M., Ramos, V.A. (Eds.), Petroleum Basins and Hydrocarbon Potential of the Andes of Perú and Bolivia. AAPG Memoir 117, pp. 1–34. https://doi.org/10.1306/13622115M1172855
Ramos, V.A., 2008. The Basement of the Central Andes: The Arequipa and Related Terranes. Annu.

Rev. Earth Planet. Sci. 36, 289–324. https://doi.org/10.1146/annurev.earth.36.031207.124304
Ramos, V.A., 1988. Late Proterozoic - Early Paleozoic of South America - a Collisional History. Episodes 11, 168–174.
Ramos, V.A., Chemale, F., Naipauer, M., Pazos, P.J., 2014. A provenance study of the Paleozoic Ventania System (Argentina): Transient complex sources from Western and Eastern Gondwana. Gondwana Res. 26, 719–740. https://doi.org/10.1016/j.gr.2013.07.008
Rapela, C.W., Coira, B., Toselli, A.J., Saavedra Alonso, J., 1992. El magmatismo del Paleozoico inferior en el Sudoeste de Gondwana, in: Paleozoico Inferior de Iberoamérica. Universidad de Extremadura, pp. 21–68.
Rapela, C.W., Pankhurst, R.J., Casquet, C., Baldo, E., Saavedra, J., Galindo, C., Fanning, C.M., 1998. The Pampean Orogeny of the southern proto-Andes: Cambrian continental collision in the Sierras de Córdoba. Geol. Soc. London, Spec. Publ. 142, 181–217. https://doi.org/10.1144/gsl.sp.1998.142.01.10
Rapela, C.W., Pankhurst, R.J., Casquet, C., Fanning, C.M., Baldo, E.G., González-Casado, J.M., Galindo, C., Dahlquist, J., 2007. The Río de la Plata craton and the assembly of SW Gondwana. Earth-Science Rev. 83, 49–82. https://doi.org/10.1016/j.earscirev.2007.03.004
Redes, L.A., Hauser, N., Ruiz, A.S., Matos, R., Reimold, W.U., Dantas, E.L., Schmitt, R.-T., Lima, B.A.F., Zacchi, E.N.P., Silva Chaves, J.G., Baumotte Osorio, L.F., Pimentel, M.M., 2020. U–Pb and Hf isotopes in granitoids from the Eastern Bolivian basement: Insights into the Paleoproterozoic evolution of the western part of South America. J. South Am. Earth Sci. 104, 102806. https://doi.org/10.1016/j.jsames.2020.102806
Reimann, C.R., Bahlburg, H., Kooijman, E., Berndt, J., Gerdes, A., Carlotto, V., López, S., 2010. Geodynamic evolution of the early Paleozoic Western Gondwana margin 14°–17°S reflected by the detritus of the Devonian and Ordovician basins of southern Peru and northern Bolivia. Gondwana Res. 18, 370–384. https://doi.org/10.1016/j.gr.2010.02.002
Rocha, E., 2013. Estilos estructurales del Subandino Sur de Bolivia. Universidad de Buenos Aires, Tese de Doutoramento, 204 p.
Roddaz, M., Viers, J., Brusset, S., Baby, P., Hérail, G., 2005. Sediment provenances and drainage evolution of the Neogene Amazonian foreland basin. Earth Planet. Sci. Lett. 239, 57–78. https://doi.org/10.1016/j.epsl.2005.08.007
Roddaz, M., Viers, J., Moreira-Turcq, P., Blondel, C., Sondag, F., Guyot, J.-L., Moreira, L., 2014. Evidence for the control of the geochemistry of Amazonian floodplain sediments by stratification of suspended sediments in the Amazon. Chem. Geol. 387, 101–110. https://doi.org/10.1016/j.chemgeo.2014.07.022
Rubatto, D., 2017. Zircon: the metamorphic mineral. Rev. Mineral. geochemistry 83, 261–295.
Santos, J.O.S., Hartmann, L.A., Gaudette, H.E., Groves, D.I., Mcnaughton, N.J., Fletcher, I.R., 2000. A New Understanding of the Provinces of the Amazon Craton Based on Integration of Field Mapping and U-Pb and Sm-Nd Geochronology. Gondwana Res. 3, 453–488. https://doi.org/10.1016/S1342-937X(05)70755-3
Santos, J.O.S., Rizzotto, G.J., Potter, P.E., McNaughton, N.J., Matos, R.S., Hartmann, L.A., Chemale, F., Quadros, M.E.S., 2008. Age and autochthonous evolution of the Sunsás Orogen in West Amazon Craton based on mapping and U–Pb geochronology. Precambrian Res. 165, 120–152. https://doi.org/10.1016/j.precamres.2008.06.009
Santos, T.B., Mancini, F., Cury, L.F., Ferreira, F.J.F., 2015. Proveniência de zircões detríticos e implicações para a paleogeografia da Formação Furnas no noroeste da Bacia do Paraná. Geol. USP. Série Científica 15, 25–59.
Sempere, T., 1995. Phanerozoic evolution of Bolivia and adjacent regions, in: Petroleum Basins of South America. American Association of Petroleum Geologist Memoir 62. pp. 207–230. https://doi.org/https://doi.org/10.1306/M62593C9
Sharman, G.R., Malkowski, M.A., 2020. Needles in a haystack: Detrital zircon U Pb ages and the maximum depositional age of modern global sediment. Earth-Science Rev. 203, 103109. https://doi.org/10.1016/j.earscirev.2020.103109
Sharman, G.R., Sharman, J.P., Sylvester, Z., 2018. detritalPy: A Python-based toolset for visualizing and analysing detrital geo-thermochronologic data. Depos. Rec. 4, 202–215. https://doi.org/10.1002/dep2.45

Starck, D., 1999. Los sistemas petroleros de la Cuenca de Tarija, in: IV Congreso de Exploración y Desarrollo de Hidrocarburos. Mar del Plata, pp. 63–82.
Starck, D., 1995. Silurian-Jurassic stratigraphy and basin evolution of northwestern Argentina, in: Tankard, A.J., Suárez, R., Welsink, H.J. (Eds.), Petroleum Basins of South America. American Association of Petroleum Geologists Memoir 62, pp. 251–267. https://doi.org/https://doi.org/10.1306/M62593C11
Starck, D., Bordese, S., Guibaldo, C., Hernández, R., 2021. Size and style of the Gondwana late Paleozoic ice cover: Insights from U-Pb dating of the Tarija Formation granitic boulders. J. South Am. Earth Sci. 106, 102954. https://doi.org/10.1016/j.jsames.2020.102954
Starck, D., Del Papa, C., 2006. The northwestern Argentina Tarija Basin: Stratigraphy, depositional systems, and controlling factors in a glaciated basin. J. South Am. Earth Sci. 22, 169–184. https://doi.org/10.1016/j.jsames.2006.09.013
Starck, D., Gallardo, E., Schulz, A., 1993. The pre-Carboniferous unconformity in the Argentine portion of the Tarija Basin, in: International Congress of Carboniferous-Permian. pp. 373–384.
Stern, R.J., Dickinson, W.R., 2010. The Gulf of Mexico is a Jurassic backarc basin. Geosphere 6, 739–754. https://doi.org/10.1130/GES00585.1
Tassinari, C.C.G., Bettencourt, J.S., Geraldes, M.C., Macambira, M.J.B., Lafon, J.M., 2000. The Amazonian Craton, in: Cordani, U.G., Milani, E.J., Thomaz Filho, A.M., Campos, D.A. (Eds.), Tectonic Evolution of South America. 31st International Geological Congress, Rio de Janeiro, pp. 41–95.
Tedesco, J., Cagliari, J., Chemale Júnior, F., Girelli, T.J., Lana, C., 2019. Provenance and paleogeography of the Southern Paraná Basin: Geochemistry and U Pb zircon geochronology of the Carboniferous-Permian transition. Sediment. Geol. 393–394, 105539. https://doi.org/10.1016/j.sedgeo.2019.105539
Teixeira, W., Cordani, U.G., Faleiros, F.M., Sato, K., Maurer, V.C., Ruiz, A.S., Azevedo, E.J.P., 2020. The Rio Apa Terrane reviewed: U Pb zircon geochronology and provenance studies provide paleotectonic links with a growing Proterozoic Amazonia. Earth-Science Rev. 202, 103089. https://doi.org/10.1016/j.earscirev.2020.103089
Teixeira, W., Oliveira, E.P., Marques, L.S., 2017. Nature and Evolution of the Archean Crust of the São Francisco Craton, in: Heilbron, M., Cordani, U.G., Alkminn, F. (Eds.), São Francisco Craton, Eastern Brazil. pp. 29–56. https://doi.org/10.1007/978-3-319-01715-0_3
Teixeira, W., Sabaté, P., Barbosa, J., Noce, C.M., Carneiro, M.A., 2000. Archean and Paleoproterozoic tectonic evolution of the São Francisco craton, Brazil, in: Cordani, U.G., Milani, E.J., Thomaz Filho, A.M., Campos, D.A. (Eds.), Tectonic Evolution of South America. 31st International Geological Congress, Rio de Janeiro, pp. 101–137.
Troth, I., Marshall, J.E.A., Racey, A., Becker, R.T., 2011. Devonian sea-level change in Bolivia: A high palaeolatitude biostratigraphical calibration of the global sea-level curve. Palaeogeogr. Palaeoclimatol. Palaeoecol. 304, 3–20. https://doi.org/10.1016/j.palaeo.2010.10.008
Uba, C.E., Kley, J., Strecker, M.R., Schmitt, A.K., 2009. Unsteady evolution of the Bolivian Subandean thrust belt: The role of enhanced erosion and clastic wedge progradation. Earth Planet. Sci. Lett. 281, 134–146. https://doi.org/10.1016/j.epsl.2009.02.010
Uriz, N.J., Cingolani, C.A., Basei, M.A.S., Blanco, G., Abre, P., Portillo, N.S., Siccardi, A., 2016. Provenance and paleogeography of the Devonian Durazno Group, southern Paraná Basin in Uruguay. J. South Am. Earth Sci. 66, 248–267.
Uriz, N.J., Cingolani, C.A., Chemale, F., Macambira, M.B., Armstrong, R., 2011. Isotopic studies on detrital zircons of Silurian–Devonian siliciclastic sequences from Argentinean North Patagonia and Sierra de la Ventana regions: comparative provenance. Int. J. Earth Sci. 100, 571–589. https://doi.org/10.1007/s00531-010-0597-z
Valdez, V., Pablo, J., Sergio, P., Paim, G., Paulo, R., Danielski, C., Cagliari, J., Chemale, F., Kneller, B., 2020. Timing of the Late Palaeozoic glaciation in western Gondwana : New ages and correlations from Paganzo and Paraná basins. Palaeogeogr. Palaeoclimatol. Palaeoecol. 544, 23. https://doi.org/10.1016/j.palaeo.2020.109624
Varela, R., Sato, A.M., Basei, M.A.S., Siga Jr, O., 2003. Proterozoico medio y Paleozoico inferior de la sierra de Umango, antepaís andino (29 S), Argentina: edades U-Pb y caracterizaciones isotópicas. Rev. geológica Chile 30, 265–284.

Vargas, M., Santos, A., Bressane, A., Francisco, R.S., Faccion, J.E., Paim, P.S., 2020. The Devonian of the Paraná Basin, Brazil: Sequence stratigraphy, paleogeography, and SW Gondwana interregional correlations. Sediment. Geol. 408, 14. https://doi.org/10.1016/j.sedgeo.2020.105768

Vaughan, A.P.M., Leat, P.T., Pankhurst, R.J., 2005. Terrane processes at the margins of Gondwana: introduction. Geol. Soc. London, Spec. Publ. 246, 1–21.

Vermeesch, P., 2018. IsoplotR: A free and open toolbox for geochronology. Geosci. Front. 9, 1479–1493. https://doi.org/https://doi.org/10.1016/j.gsf.2018.04.001

Vorster, C., 2013. Laser ablation ICP-MS afe determination of detrital zircon population in the Phanerozoic Cape and Lower Karoo Supergroups (South Africa) and correlatives in Argentina. University of Johannesburg, Tese de Doutorado, 627 p.

Whitney, D.L., Evans, B.W., 2010. Abbreviations for names of rock-forming minerals. Am. Mineral. 95, 185–187. https://doi.org/10.2138/am.2010.3371

Wiedenbeck, M., Allé, P., Corfu, F., Griffin, W.L., Meier, M., Oberli, F., Quadt, A. Von, Roddick, J.., Spiegel, W., 1995. Three natural zircon standards for U-Th-Pb, Lu-Hf, trace element and REE analyses. Geostand. Geoanalytical Res. 19, 1–23. https://doi.org/10.1111/j.1751-908X.1995.tb00147.x

Willner, A.P., Gerdes, A., Massonne, H.-J., Schmidt, A., Sudo, M., Thomson, S.N., Vujovich, G., 2011. The geodynamics of collision of a microplate (Chilenia) in Devonian times deduced by the pressure-temperature-time evolution within part of a collisional belt (Guarguaraz Complex, W-Argentina). Contrib. to Mineral. Petrol. 162, 303–327. https://doi.org/10.1007/s00410-010-0598-8

Yakymchuk, C., Kirkland, C.L., Clark, C., 2018. Th/U ratios in metamorphic zircon. J. Metamorph. Geol. 36, 715–737. https://doi.org/10.1111/jmg.12307

Zeballos, A., Weihed, P., Blanco, M., Machaca, V., 2016. Geological, mineralogical and chemical characterization of Devonian kaolinite-bearing sediments for further applications in the ceramic (tiles) industry in La Paz, Bolivia. Environ. Earth Sci. 75, 546. https://doi.org/10.1007/s12665-015-5212-y

Tables

Laboratory	LARIX	INGEIS
Solvation	Ethylene-glycol (eg); glycerol (gl)	Ethylene-glycol (eg)
Heating	4H30min; 490°C	4H; 500°-550°C
Diffractometer	Rigaku Ultima IV	BRUKER-binary V4
Radiation	Cu Kα; 35 kV; 15 mA	Cu Kα; 30 kV; 10 mA
Step size; scanning speed	0.05° 2ɵ; 5°/min	0.05° 2ɵ; 0.02°/min
Stepping range	2° to 40° 2ɵ (Clay fraction)	4° to 40° 2ɵ (Clay fraction)

Table 1

Formation	Sample	**Q**	Qm	Qp	**F**	P	Fk	**L**	Lv	Lp	Ls	Lch	Lm	**Total**
Chorro	SSB-8A	**97.50**	95.75	1.75	**1.00**	0.75	0.25	**1.50**	0.00	0.00	1.00	0.50	0.00	**100.00**
Tarija	SSB-23A	**95.75**	94.50	1.25	**2.00**	1.25	0.75	**2.25**	0.50	0.00	0.00	1.75	0.00	**100.00**
Tupambi	SSB-28A	**98.73**	98.73	0.00	**0.76**	0.00	0.76	**0.51**	0.00	0.00	0.25	0.25	0.00	**100.00**
Itacua	SSB-5A	**96.00**	96.00	0.00	**1.75**	0.50	1.25	**2.25**	0.00	0.00	0.50	1.25	0.50	**100.00**
Iquiri	SSB-30A	**92.48**	92.48	0.00	**4.76**	0.25	4.51	**2.76**	0.00	0.00	1.50	1.25	0.00	**100.00**
Iquiri	SSB-10A	**93.65**	93.65	0.00	**3.97**	2.12	1.85	**2.38**	0.00	0.00	0.79	1.59	0.00	**100.00**
Iquiri	SSB-3A	**95.00**	95.00	0.00	**4.50**	0.75	3.75	**0.50**	0.00	0.00	0.00	0.50	0.00	**100.00**
Los Monos	SSB-9A	**100.00**	100.00	0.00	**0.00**	0.00	0.00	**0.00**	0.00	0.00	0.00	0.00	0.00	**100.00**
Los Monos	SSB-16A	**91.00**	90.75	0.25	**6.50**	2.25	4.25	**2.50**	0.00	0.00	1.50	1.00	0.00	**100.00**
Huamampampa	SSB-19A	**92.50**	92.50	0.00	**4.50**	1.50	3.00	**3.00**	0.00	0.00	2.50	0.50	0.00	**100.00**
Icla	SSB-14B	**92.25**	92.00	0.25	**4.50**	1.75	2.75	**3.25**	0.00	0.00	2.25	1.00	0.00	**100.00**
Icla	SSB-15A	**95.50**	95.25	0.25	**3.25**	2.50	0.75	**1.25**	0.00	0.00	0.50	0.75	0.00	**100.00**

Table 2

Sample (< 2 µm)	Unit	Lithotype	Kln	Chl	Ilt	Vrm	Chl/Vrm	Ilt/Sme	Qz	Pl	FspK	Others
SSB-8B	Chorro	Pelite	m	-	M	m	-	-	tr	tr	tr	Hem (tr)
SSB-23B	Tarija	Pelite	M	m	M	-	-	-	m	tr	tr	Hem (m)
SSB-28B	Tupambi	Pelite	M	tr	M	-	-	tr	m	tr	tr	Hem (m)
SSB-5C	Itacua	Pelite	M	tr	M	-	-	-	m	tr	tr	-
SSB-5B	Itacua	Pelite	m	tr	M	tr	-	-	m	tr	tr	Hem (tr)
SSB-29B	Iquiri	Pelite	M	-	m	-	-	-	tr	tr	tr	-
SSB-4B	Iquiri	Pelite	M	tr	M	tr	-	-	m	m	tr	-
SSB-10B	Iquiri	Pelite	m	tr	M	-	-	-	M	m	tr	-
SSB-3B	Iquiri	Pelite	M	tr	M	-	-	-	m	m	tr	-
SSB-1B	Los Monos	Pelite	m	tr	M	-	-	-	m	m	tr	-
SSB-9B	Los Monos	Pelite	M	-	M	tr	-	tr	-	-	-	Gth (m)
SSB-2B	Los Monos	Pelite	m	tr	M	-	-	-	M	m	tr	-
SSB-16B	Los Monos	Pelite	m	-	M	m	-	-	m	m	tr	-
SSB-8C	Los Monos	Pelite	M	-	M	m	tr	-	tr	-	tr	Gth (tr)
SSB-3C	Los Monos	Pelite	M	tr	M	-	-	tr	m	tr	tr	-
SSB-20B	Huamampampa	Pelite	m	tr	M	tr	-	-	m	tr	-	-
SSB-19B	Huamampampa	Pelite	tr	-	M	tr	-	-	m	m	tr	-
SSB-14A	Icla	Pelite	tr	-	M	tr	-	-	m	tr	-	-
SSB-15B	Icla	Pelite	tr	-	M	m	tr	-	tr	tr	-	-

Table 3

Sample	Formation	Age	Estimated depositional age (Ma)	Sm (ppm)	Nd (ppm)	$^{147}Sm/^{144}Nd$	$^{143}Nd/^{144}Nd$	±2SE (10^{-6})	ε_{Nd} (0)	±2SE	ε_{Nd} (300)	$^{143}Nd/^{144}Nd$ (T_s)	ε_{Nd} (T_s)	T_{DM} (Ga)	±2SE	T_{DM}* (Ga)	±2SE	$^{87}Sr/^{86}Sr(0)$	±2SE (10^{-5})	$^{87}Sr/^{86}Sr(300)$
SSB-8B	Chorro	Carboniferous	314	7.75	39.59	0.1183	0.512149	±18	-9.54	0.35	-6.54	0.511906	-6.40	1.54	0.03	1.45	0.03	0.71775	±2	0.70686
SSB-23B	Tarija	Carboniferous	314	6.35	34.85	0.1101	0.512114	±19	-10.22	0.37	-6.91	0.511888	-6.76	1.48	0.03	1.47	0.03	0.72202	±3	0.71113
SSB-28B	Tupambi	Carboniferous	321	10.88	57.53	0.1143	0.512060	±18	-11.28	0.35	-8.13	0.511820	-7.90	1.61	0.03	1.56	0.03	0.72729	±1	0.71639
SSB-5C	Itacua	Carboniferous	354	9.79	50.45	0.1173	0.512074	±16	-11.00	0.31	-7.97	0.511802	-7.42	1.64	0.02	1.55	0.02	0.73086	±10	0.71996
SSB-5B	Itacua	Carboniferous	354	9.94	52.95	0.1135	0.512061	±20	-11.26	0.39	-8.07	0.511798	-7.50	1.60	0.03	1.56	0.03	0.72876	±2	0.71786
SSB-29B	Iquiri	Devonian	380	12.36	63.09	0.1184	0.512008	±8	-12.29	0.16	-9.30	0.511714	-8.50	1.76	0.01	1.65	0.01	0.74261	±2	0.73170
SSB-4B	Iquiri	Devonian	380	9.36	50.02	0.1131	0.512012	±13	-12.21	0.25	-9.01	0.511731	-8.17	1.67	0.02	1.63	0.02	0.73138	±1	0.72048
SSB-4C	Iquiri	Devonian	380	8.97	47.24	0.1148	0.511993	±7	-12.58	0.14	-9.45	0.511708	-8.62	1.72	0.01	1.66	0.01	0.73021	±2	0.71931
SSB-10B	Iquiri	Devonian	380	8.45	45.20	0.1129	0.512046	±20	-11.55	0.39	-8.35	0.511765	-7.50	1.61	0.03	1.58	0.03	0.74272	±3	0.73181
SSB-3B	Iquiri	Devonian	380	8.98	45.84	0.1185	0.512013	±7	-12.19	0.14	-9.20	0.511719	-8.41	1.75	0.01	1.65	0.01	0.73023	±3	0.71933
SSB-1B	Los Monos	Devonian	385	9.74	51.04	0.1153	0.511984	±9	-12.76	0.18	-9.65	0.511694	-8.77	1.74	0.01	1.68	0.01	0.73826	±2	0.72735
SSB-9B	Los Monos	Devonian	385	7.46	41.39	0.1090	0.511882	±16	-14.75	0.31	-11.40	0.511608	-10.45	1.78	0.02	1.80	0.02	0.73917	±4	0.72826
SSB-2B	Los Monos	Devonian	385	9.44	46.83	0.1219	0.512077	±20	-10.94	0.39	-8.08	0.511770	-7.28	1.72	0.03	1.57	0.03	0.73776	±1	0.72685
SSB-16B	Los Monos	Devonian	385	10.14	52.55	0.1166	0.512070	±8	-11.08	0.16	-8.02	0.511776	-7.15	1.64	0.01	1.56	0.01	0.73840	±4	0.72749
SSB-8C	Los Monos	Devonian	385	10.93	53.32	0.1239	0.512173	±19	-9.07	0.37	-6.29	0.511861	-5.50	1.60	0.03	1.44	0.03	0.74224	±8	0.73133
SSB-3C	Los Monos	Devonian	385	10.36	54.21	0.1155	0.512017	±18	-12.11	0.35	-9.01	0.511726	-8.13	1.70	0.03	1.63	0.03	0.73617	±3	0.72526
SSB-20B	Huamampampa	Devonian	393	9.45	50.28	0.1136	0.512062	±5	-11.24	0.10	-8.06	0.511770	-7.07	1.60	0.01	1.56	0.01	0.75035	±9	0.73943
SSB-19B	Huamampampa	Devonian	393	7.61	39.69	0.1159	0.512130	±17	-9.91	0.33	-6.82	0.511832	-5.86	1.53	0.03	1.47	0.02	0.75077	±3	0.73985
SSB-14A	Icla	Devonian	397	9.01	49.55	0.1100	0.512035	±21	-11.76	0.41	-8.45	0.511749	-7.38	1.58	0.03	1.58	0.03	0.76659	±7	0.75565

Table 4

Time Interval (Ga)	Province/Terrane/Event	Tarija Basin (Southern Sub-Andean Zone)								
		Devonian					Carboniferous			
		SLL-03*	SSB-16A	SSB-2A	SSB-10A	SSB-4A	SSB-5A	SSB-28A	AA-01*	SSB-23A
		n = 40	n = 64	n = 52	n = 50	n = 104	n = 60	n = 57	n = 92	n = 74
		% Sample	% Sample	% Sample	% Sample	% Sample	% Sample	% Sample	% Sample	% Sample
0.32 - 0.29	**Pennsylvanian**	**0.00**	**0.00**	**0.00**	**0.00**	**0.00**	**0.00**	**0.00**	**0.00**	**0.00**
0.42 - 0.32	**Chanic event**	**0.00**	**0.00**	**0.00**	**4.00**	**0.00**	**3.33**	**0.00**	**3.26**	**13.51**
0.36 - 0.32	Missippian	0.00	0.00	0.00	0.00	0.00	0.00	0.00	2.17	2.70
0.42-0.36	Devonian	0.00	0.00	0.00	4.00	0.00	3.33	0.00	1.09	10.81
0.50 - 0.42	**Famatinian**	**20.00**	**10.94**	**13.46**	**20.00**	**24.04**	**8.33**	**15.79**	**2.17**	**4.05**
0.46 - 0.42	Ocloyic event	5.00	3.13	0.00	8.00	0.96	1.67	0.00	0.00	1.35
0.50 -0.46		15.00	7.81	13.46	12.00	23.08	6.67	15.79	2.17	2.70
0.70 - 0.50	**Late Brazilian/Pampean**	**37.50**	**39.06**	**36.54**	**50.00**	**30.77**	**36.67**	**56.14**	**54.35**	**54.05**
0.90 - 0.70	**Early Brazilian**	**2.50**	**6.25**	**3.85**	**0.00**	**6.73**	**8.33**	**10.53**	**9.78**	**8.11**
1.30 - 0.90	**Sunsas/Grenville**	**22.50**	**34.38**	**34.62**	**20.00**	**29.81**	**26.67**	**8.77**	**19.57**	**14.86**
1.54 - 1.30	**Rondonia - San Ignacio**	**0.00**	**0.00**	**0.00**	**0.00**	**0.96**	**1.67**	**1.75**	**0.00**	**0.00**
1.82 -1.54	**Rio Negro - Juruena**	**2.50**	**1.56**	**0.00**	**0.00**	**0.96**	**0.00**	**5.26**	**1.09**	**0.00**
2.00 - 1.82	**Ventuari - Tapajós (Transamazonian)**	**5.00**	**3.13**	**3.85**	**2.00**	**0.96**	**3.33**	**0.00**	**2.17**	**2.70**
2.20 - 2.00	**Maroni - Itacaiúnas**	**5.00**	**0.00**	**3.85**	**4.00**	**4.81**	**6.67**	**1.75**	**4.35**	**0.00**
> 2.20	**Central Amazonian**	**5.00**	**4.69**	**3.85**	**0.00**	**0.96**	**5.00**	**0.00**	**3.26**	**2.70**

Table 5

Sample	Formation	Rock type	Roundness (%)*			Elongation (%)*			Mean (interval of grain lenght [μm])*	Unbroken concordant grains / Total concordant ages
			Euh.	Sa-sr	Roun.	Elo.	Ova.	Rou.		
SSB-23A	Tarija	Pure quartzose sandstone	7.0	58.1	34.9	46.5	41.9	11.6	147 (87-250)	43/74
SSB-28A	Tupambi	Pure quartzose sandstone	10.8	83.8	5.4	86.5	13.5	0.0	119 (73-191)	37/57
SSB-5A	Itacua	Pure quartzose sandstone	6.0	66.0	28.0	60.0	34.0	6.0	102 (63-201)	50/60
SSB-4A	Iquiri	Quartzose sandstone	31.3	54.7	14.1	70.3	21.9	7.8	107 (61-198)	64/104
SSB-10A	Iquiri	Quartzose sandstone	16.1	77.4	6.5	71.0	25.8	3.2	105 (59-179)	31/50
SSB-2A	Los Monos	Pure quartzose sandstone	34.5	55.2	10.3	58.6	27.6	13.8	110 (44-237)	29/52
SSB-16A	Los Monos	Quartzose sandstone	2.3	83.7	14.0	58.1	34.9	7.0	106 (64-164)	43/64

Table 6

Figures

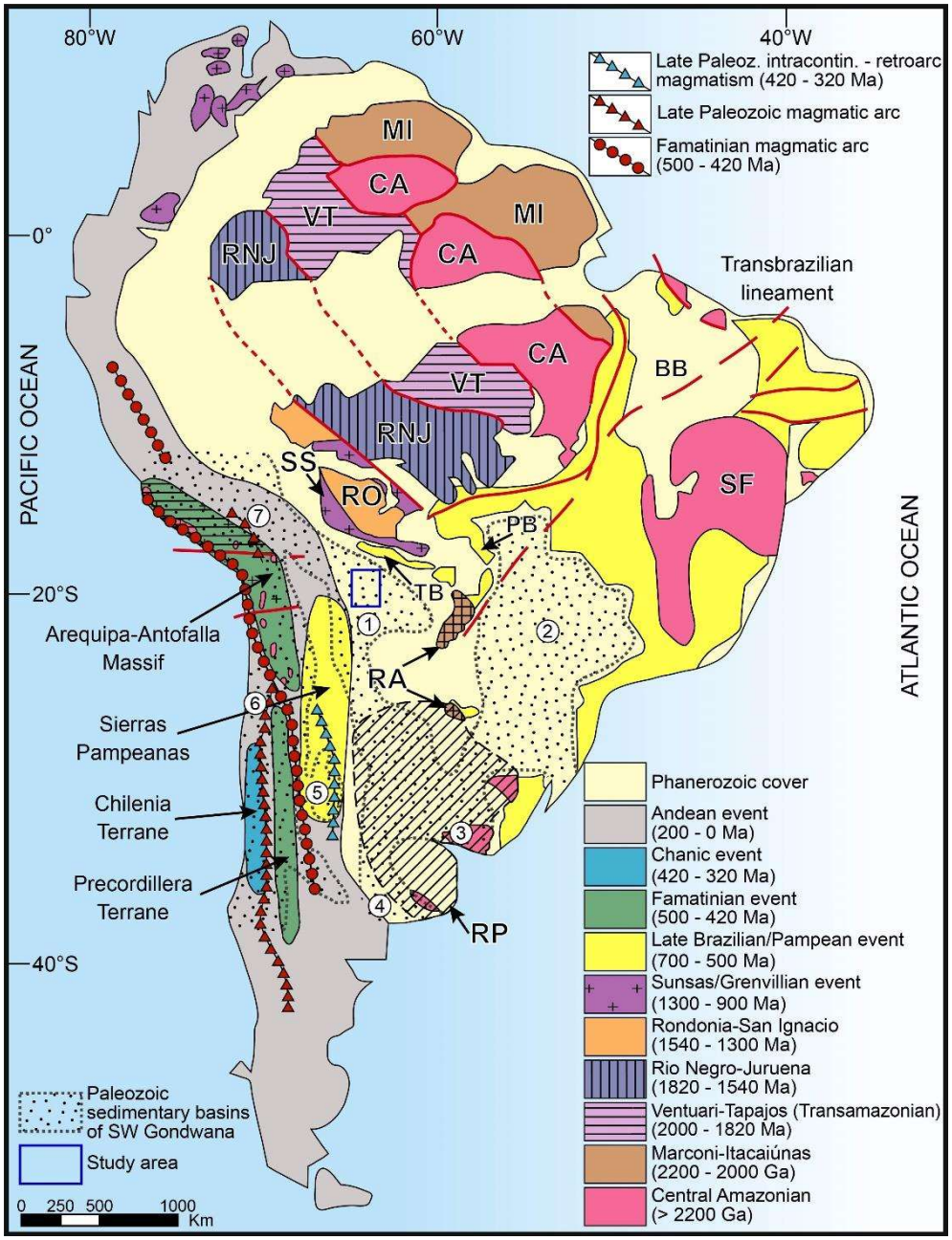

Fig. 1

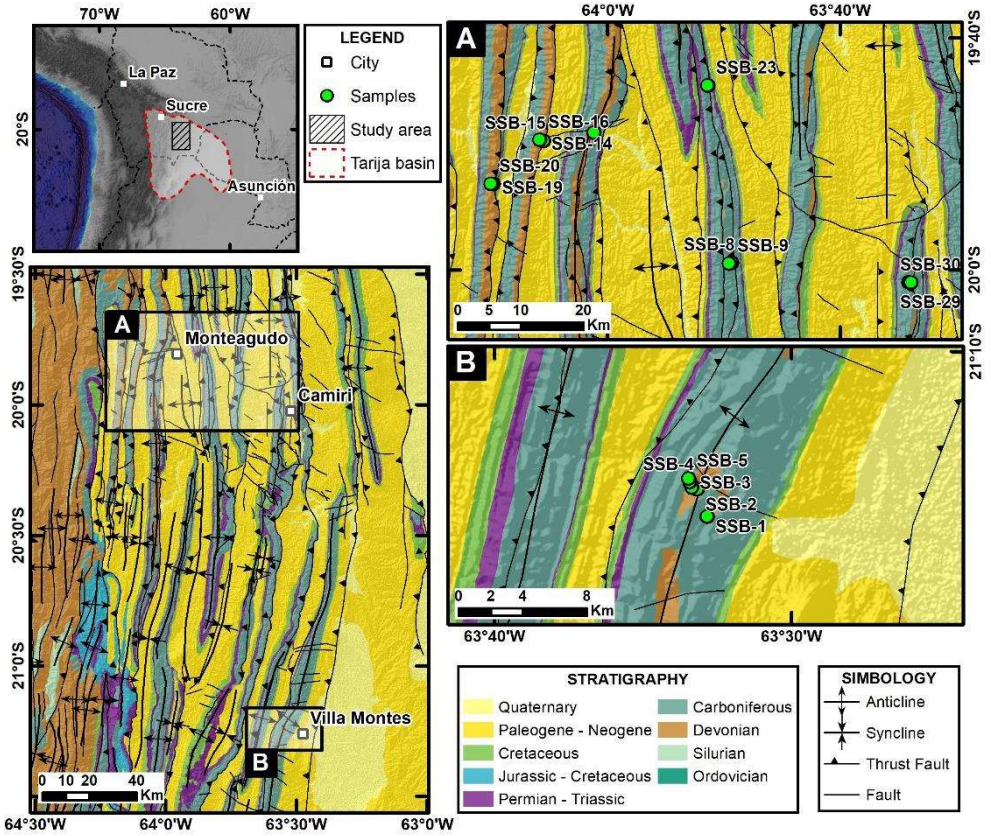
70°W
60°W
La Paz
Sucre
Asunción
20°S
LEGEND
City
Samples
Study area
Tarija basin
64°0'W
63°40'W
19°40'S
20°0'S
21°10'S
A
SSB-23
SSB-15
SSB-16
SSB-14
SSB-20
SSB-19
SSB-8
SSB-9
SSB-30
SSB-29
0 5 10 20 Km
B
SSB-4
SSB-5
SSB-3
SSB-2
SSB-1
0 2 4 8 Km
63°30'W
19°30'S
20°30'S
21°0'S
Monteagudo
Camiri
Villa Montes
0 10 20 40 Km
64°30'W
64°0'W
63°30'W
63°0'W
STRATIGRAPHY
Quaternary
Paleogene - Neogene
Cretaceous
Jurassic - Cretaceous
Permian - Triassic
Carboniferous
Devonian
Silurian
Ordovician
SIMBOLOGY
Anticline
Syncline
Thrust Fault
Fault

Fig. 2

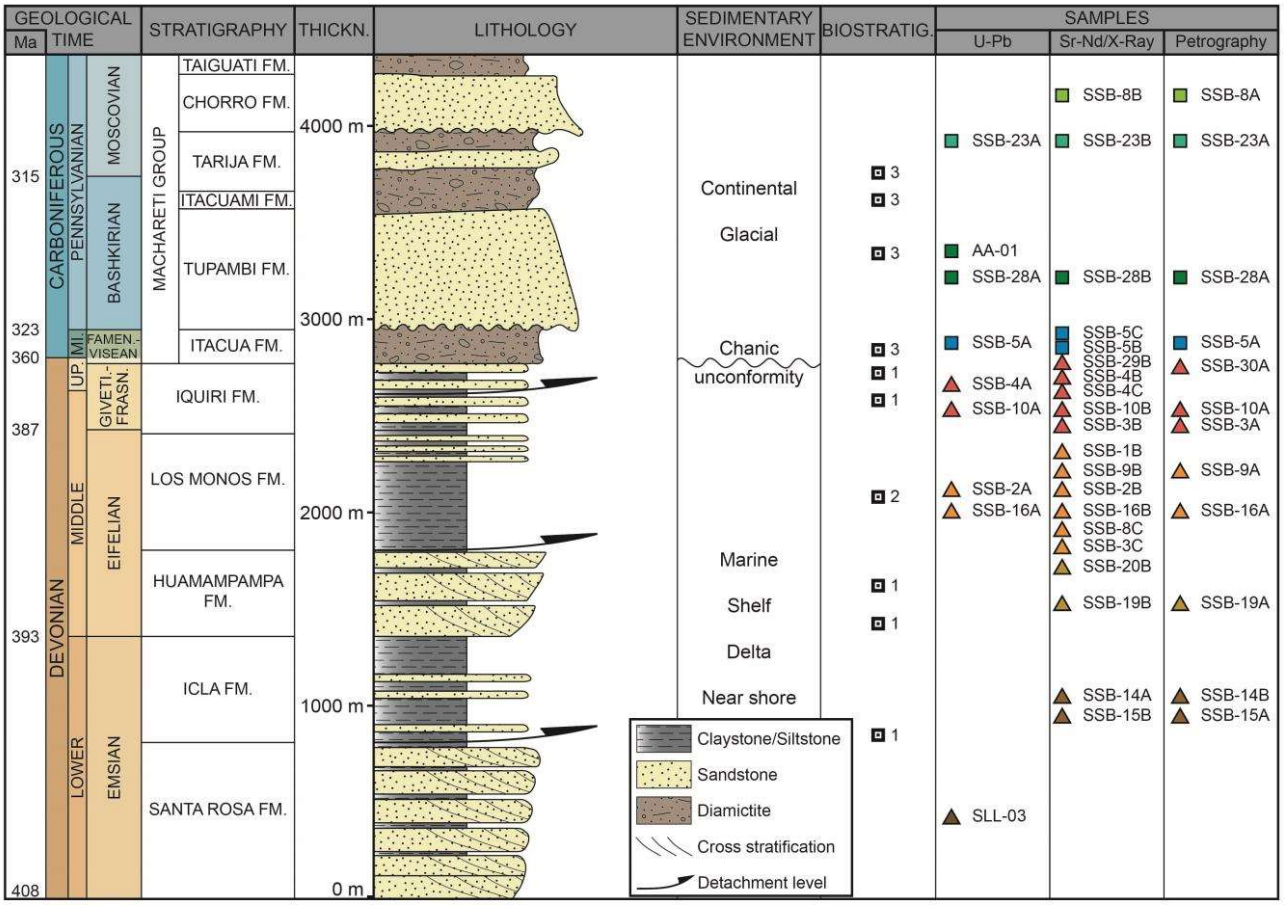
GEOLOGICAL TIME
Ma
CARBONIFEROUS
DEVONIAN
PENNSYLVANIAN
MOSCOVIAN
BASHKIRIAN
MI.
FAMEN.-VISEAN
UP.
GIVETI.-FRASN.
MIDDLE
EIFELIAN
LOWER
EMSIAN
315
323
360
387
393
408
STRATIGRAPHY
MACHARETI GROUP
TAIGUATI FM.
CHORRO FM.
TARIJA FM.
ITACUAMI FM.
TUPAMBI FM.
ITACUA FM.
IQUIRI FM.
LOS MONOS FM.
HUAMAMPAMPA FM.
ICLA FM.
SANTA ROSA FM.
THICKN.
4000 m
3000 m
2000 m
1000 m
0 m
LITHOLOGY
SEDIMENTARY ENVIRONMENT
Continental
Glacial
Chanic unconformity
Marine
Shelf
Delta
Near shore
BIOSTRATIG.
3
3
3
3
1
1
2
1
1
1
Claystone/Siltstone
Sandstone
Diamictite
Cross stratification
Detachment level
SAMPLES
U-Pb
Sr-Nd/X-Ray
Petrography
SSB-8B
SSB-8A
SSB-23A
SSB-23B
SSB-23A
AA-01
SSB-28A
SSB-28B
SSB-28A
SSB-5C
SSB-5B
SSB-29B
SSB-4B
SSB-4C
SSB-10B
SSB-3B
SSB-1B
SSB-9B
SSB-2B
SSB-16B
SSB-8C
SSB-3C
SSB-20B
SSB-19B
SSB-14A
SSB-15B
SSB-5A
SSB-4A
SSB-10A
SSB-2A
SSB-16A
SLL-03
SSB-5A
SSB-30A
SSB-10A
SSB-3A
SSB-9A
SSB-16A
SSB-19A
SSB-14B
SSB-15A

Fig. 3

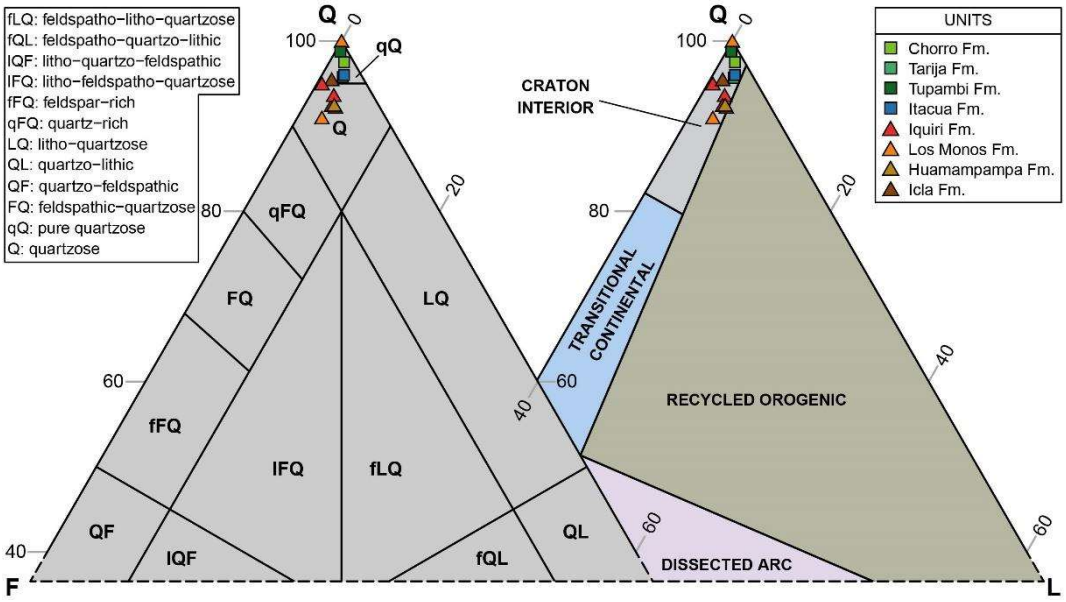
fLQ: feldspatho-litho-quartzose
fQL: feldspatho-quartzo-lithic
lQF: litho-quartzo-feldspathic
lFQ: litho-feldspatho-quartzose
fFQ: feldspar-rich
qFQ: quartz-rich
LQ: litho-quartzose
QL: quartzo-lithic
QF: quartzo-feldspathic
FQ: feldspathic-quartzose
qQ: pure quartzose
Q: quartzose
Q
qQ
qFQ
FQ
LQ
fFQ
lFQ
fLQ
QF
lQF
fQL
QL
F
L
CRATON INTERIOR
TRANSITIONAL CONTINENTAL
RECYCLED OROGENIC
DISSECTED ARC
UNITS
Chorro Fm.
Tarija Fm.
Tupambi Fm.
Itacua Fm.
Iquiri Fm.
Los Monos Fm.
Huamampampa Fm.
Icla Fm.

Fig. 4

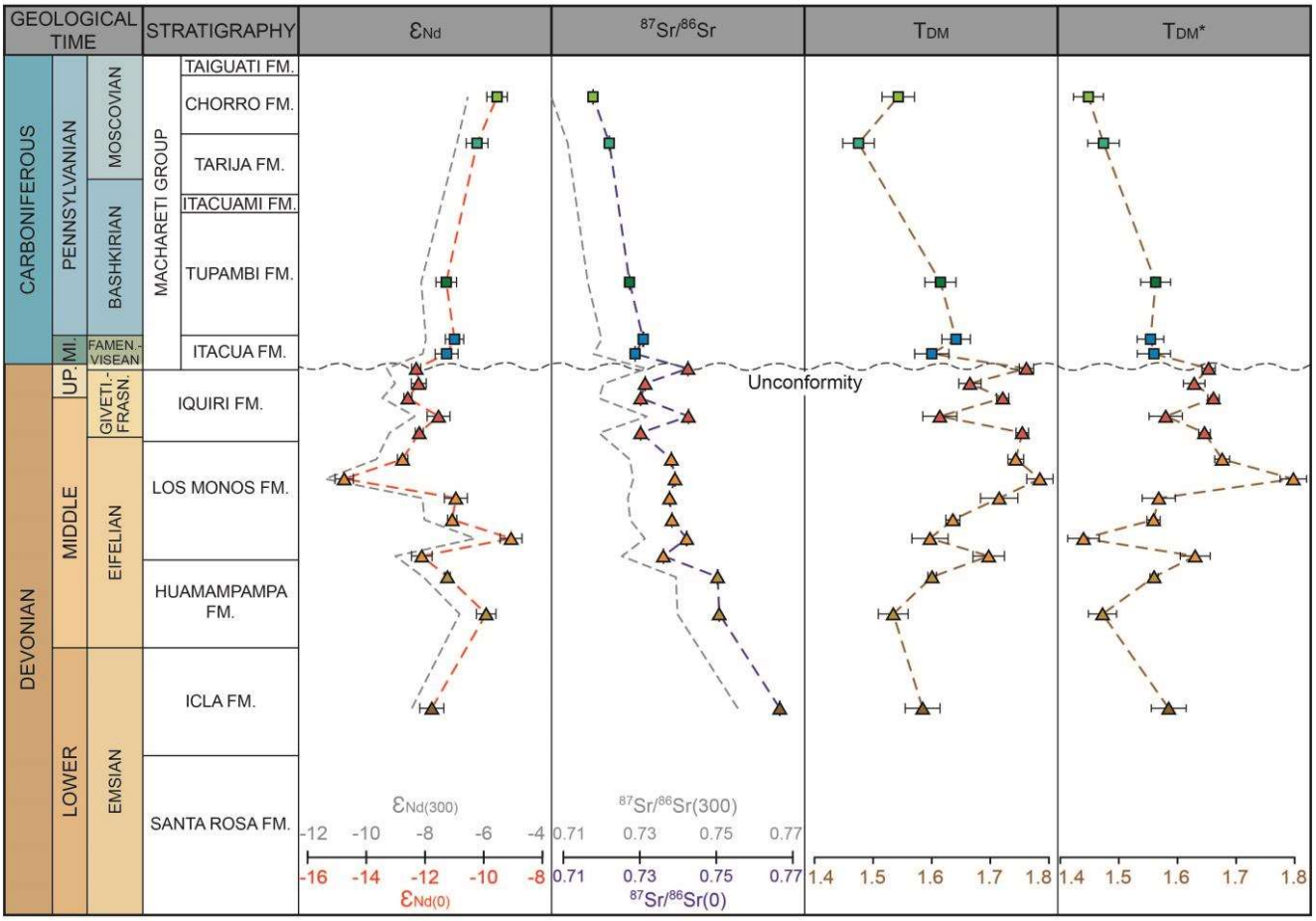
GEOLOGICAL TIME
STRATIGRAPHY
εNd
87Sr/86Sr
TDM
TDM*
CARBONIFEROUS
DEVONIAN
PENNSYLVANIAN
MOSCOVIAN
BASHKIRIAN
MI.
FAMEN.-VISEAN
UP.
MIDDLE
LOWER
GIVETI.-FRASN.
EIFELIAN
EMSIAN
MACHARETI GROUP
TAIGUATI FM.
CHORRO FM.
TARIJA FM.
ITACUAMI FM.
TUPAMBI FM.
ITACUA FM.
IQUIRI FM.
LOS MONOS FM.
HUAMAMPAMPA FM.
ICLA FM.
SANTA ROSA FM.
Unconformity
εNd(300)
εNd(0)
87Sr/86Sr(300)
87Sr/86Sr(0)

Fig. 5

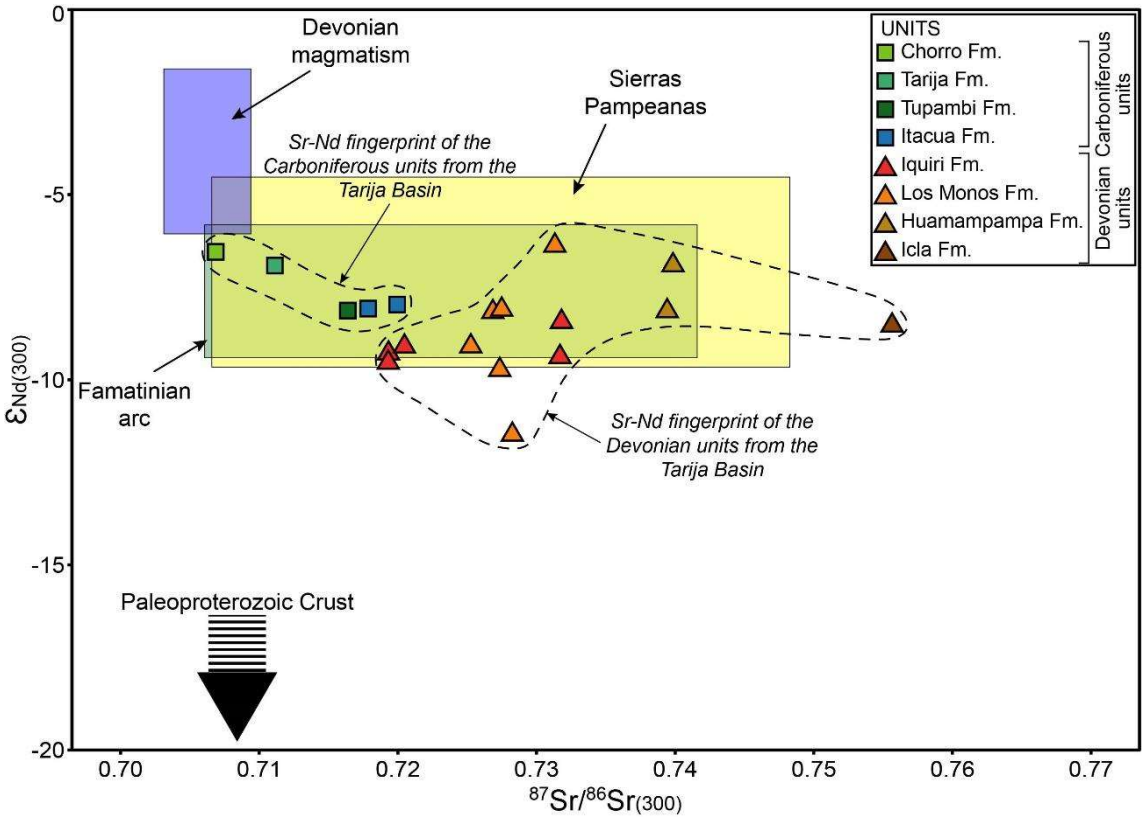
Devonian magmatism
Sierras Pampeanas
Sr-Nd fingerprint of the Carboniferous units from the Tarija Basin
Famatinian arc
Sr-Nd fingerprint of the Devonian units from the Tarija Basin
Paleoproterozoic Crust
UNITS
Chorro Fm.
Tarija Fm.
Tupambi Fm.
Itacua Fm.
Iquiri Fm.
Los Monos Fm.
Huamampampa Fm.
Icla Fm.
Carboniferous units
Devonian units
εNd(300)
87Sr/86Sr(300)

Fig. 6

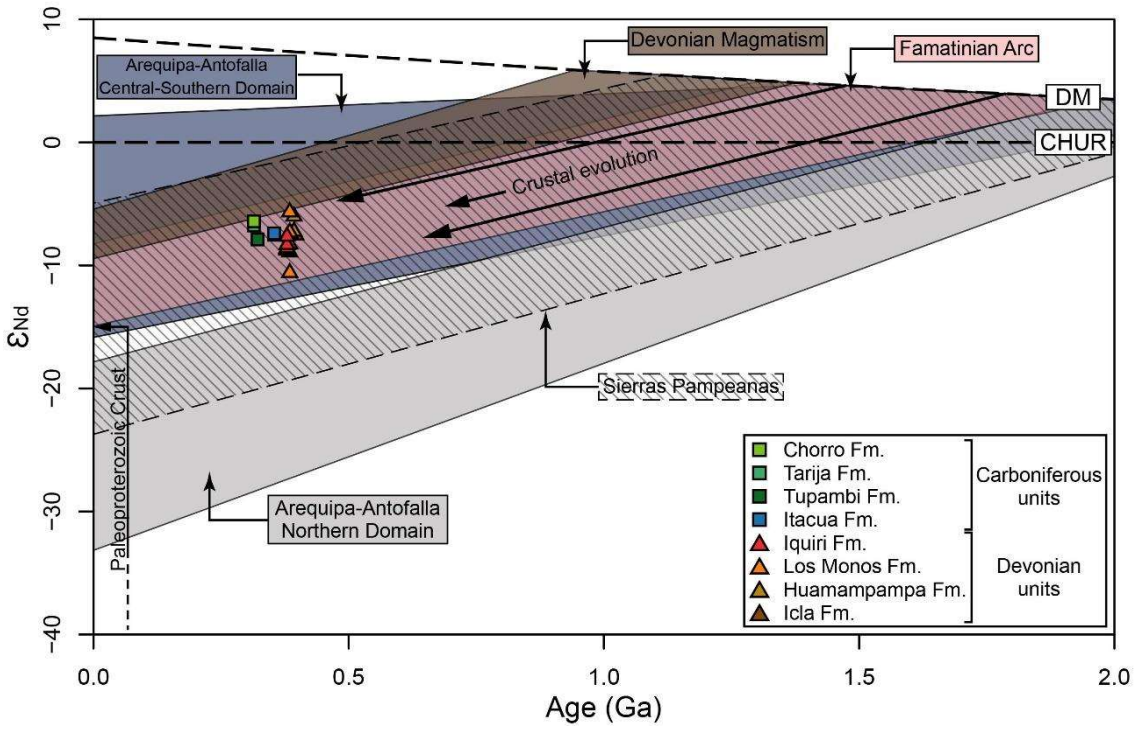
Devonian Magmatism
Famatinian Arc
Arequipa-Antofalla Central-Southern Domain
DM
CHUR
Crustal evolution
Sierras Pampeanas
Paleoproterozoic Crust
Arequipa-Antofalla Northern Domain
Chorro Fm.
Tarija Fm.
Tupambi Fm.
Itacua Fm.
Iquiri Fm.
Los Monos Fm.
Huamampampa Fm.
Icla Fm.
Carboniferous units
Devonian units
εNd
Age (Ga)

Fig. 7

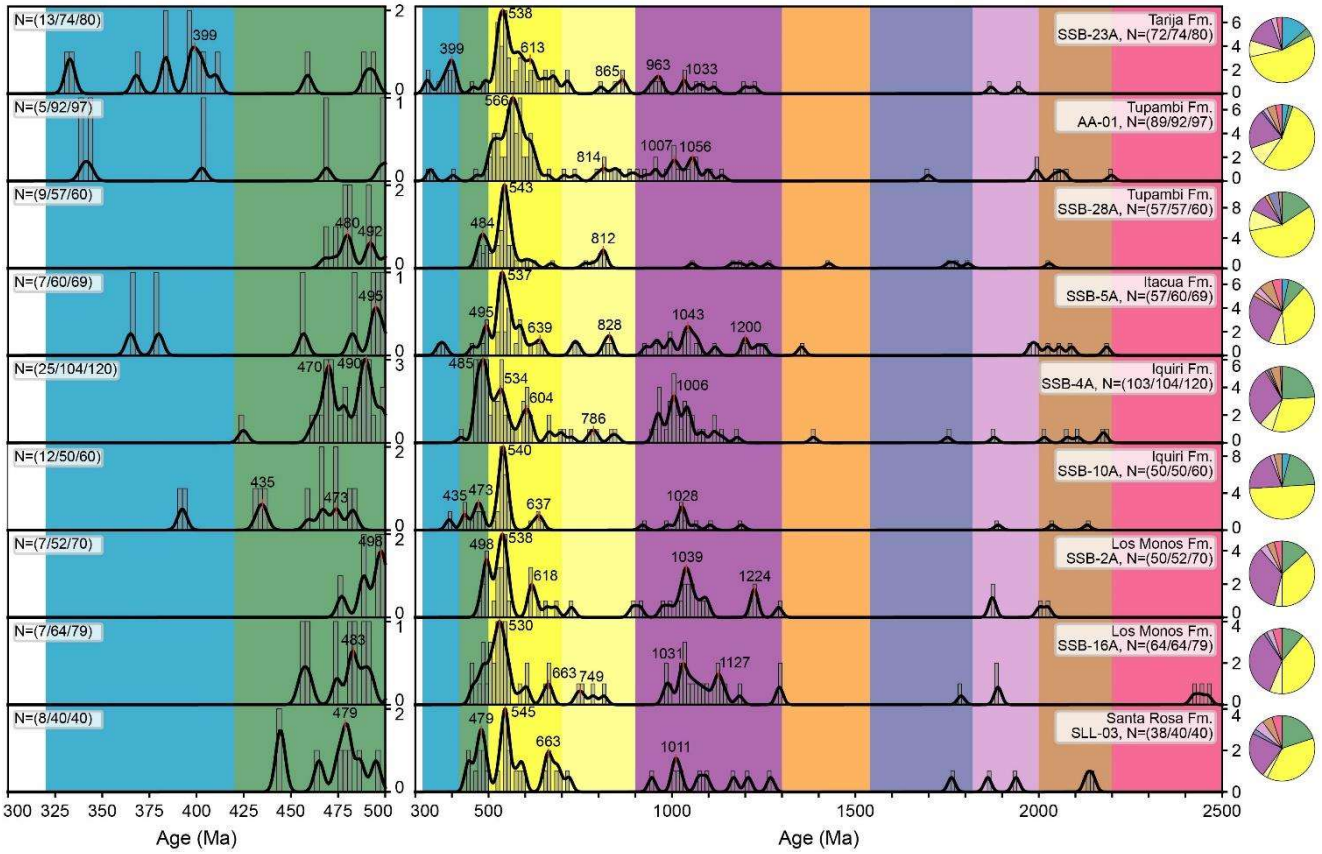
N=(13/74/80)
N=(5/92/97)
N=(9/57/60)
N=(7/60/69)
N=(25/104/120)
N=(12/50/60)
N=(7/52/70)
N=(7/64/79)
N=(8/40/40)
Tarija Fm. SSB-23A, N=(72/74/80)
Tupambi Fm. AA-01, N=(89/92/97)
Tupambi Fm. SSB-28A, N=(57/57/60)
Itacua Fm. SSB-5A, N=(57/60/69)
Iquiri Fm. SSB-4A, N=(103/104/120)
Iquiri Fm. SSB-10A, N=(50/50/60)
Los Monos Fm. SSB-2A, N=(50/52/70)
Los Monos Fm. SSB-16A, N=(64/64/79)
Santa Rosa Fm. SLL-03, N=(38/40/40)
Age (Ma)
Age (Ma)

Fig. 8

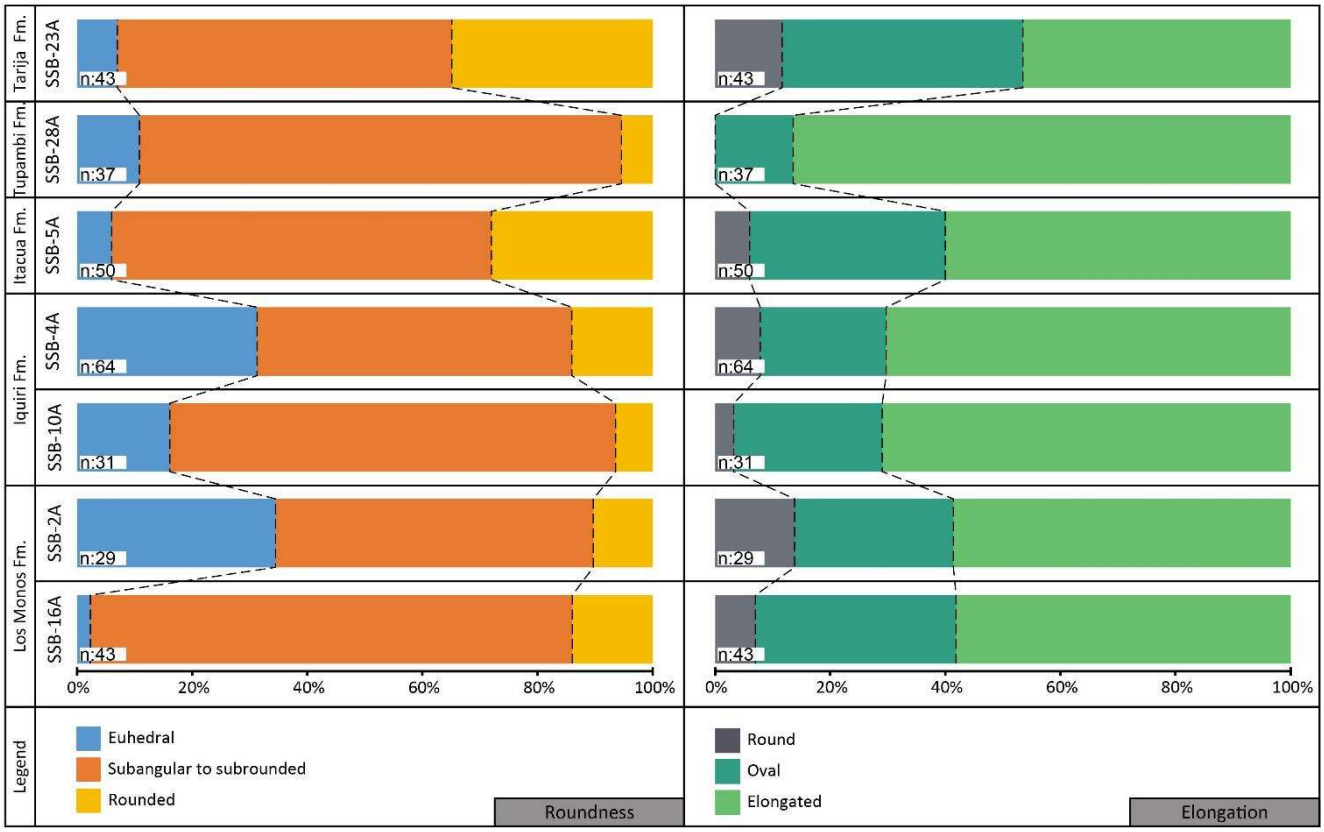
Tarija Fm.
Tupambi Fm.
Itacua Fm.
Iquiri Fm.
Los Monos Fm.
SSB-23A
SSB-28A
SSB-5A
SSB-4A
SSB-10A
SSB-2A
SSB-16A
n:43
n:37
n:50
n:64
n:31
n:29
n:43
0%
20%
40%
60%
80%
100%
Legend
Euhedral
Subangular to subrounded
Rounded
Roundness
Round
Oval
Elongated
Elongation

Fig. 9

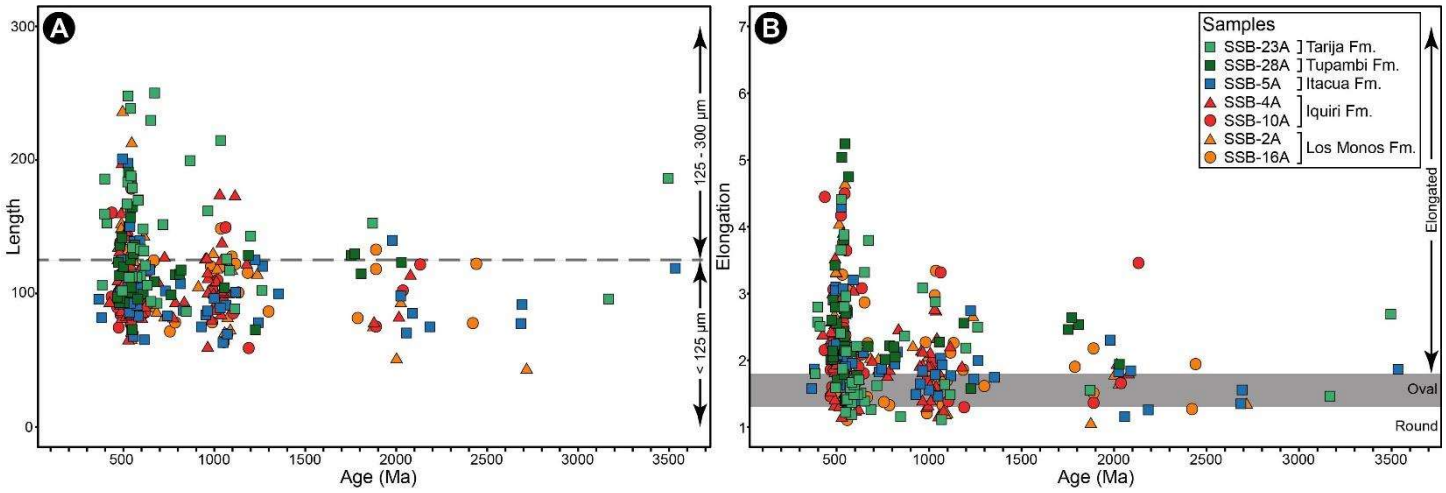
A
B
Length
Elongation
Age (Ma)
125 - 300 µm
< 125 µm
Elongated
Oval
Round
Samples
SSB-23A
SSB-28A
SSB-5A
SSB-4A
SSB-10A
SSB-2A
SSB-16A
Tarija Fm.
Tupambi Fm.
Itacua Fm.
Iquiri Fm.
Los Monos Fm.

Fig. 10

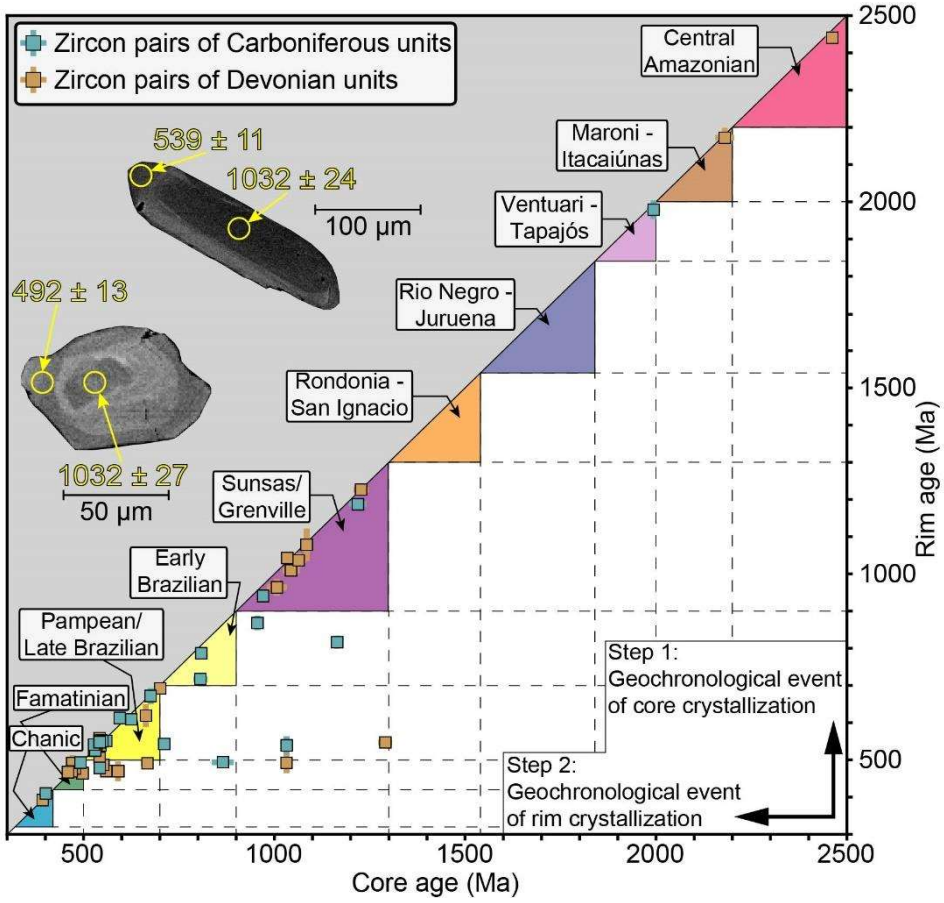
Zircon pairs of Carboniferous units
Zircon pairs of Devonian units
539 ± 11
1032 ± 24
100 µm
492 ± 13
1032 ± 27
50 µm
Central Amazonian
Maroni - Itacaiúnas
Ventuari - Tapajós
Rio Negro - Juruena
Rondonia - San Ignacio
Sunsas/ Grenville
Early Brazilian
Pampean/ Late Brazilian
Famatinian
Chanic
Step 1: Geochronological event of core crystallization
Step 2: Geochronological event of rim crystallization
Core age (Ma)
Rim age (Ma)

Fig. 11

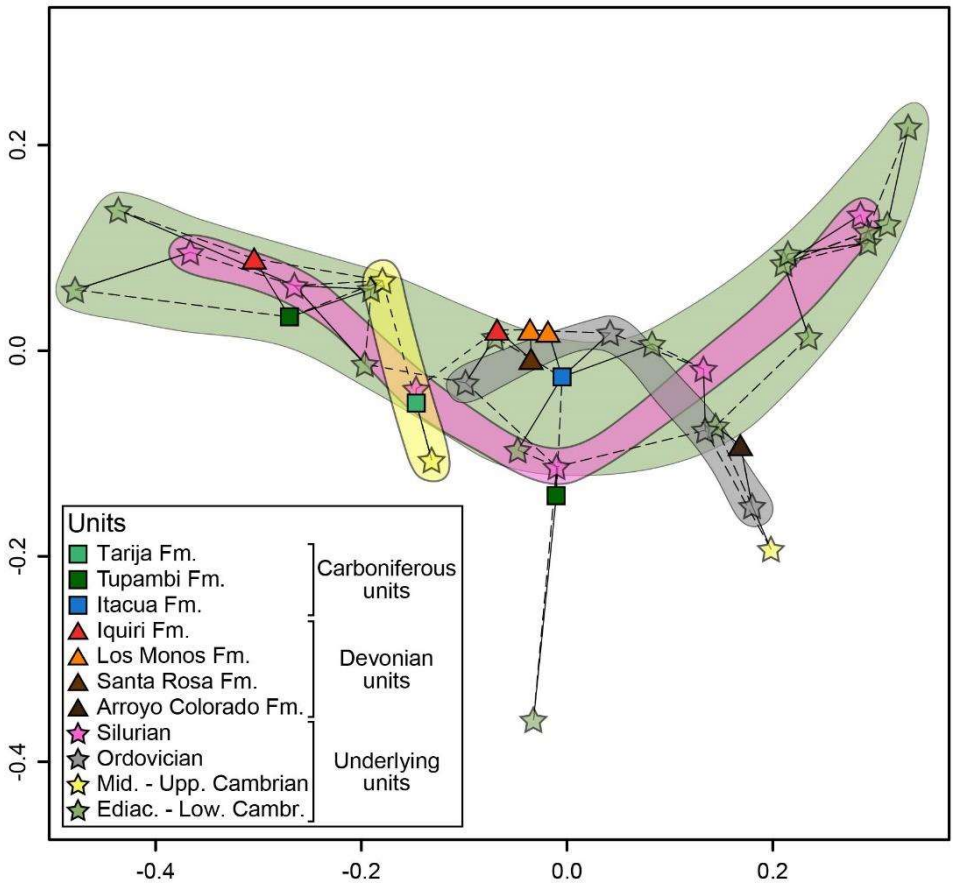
Units
Tarija Fm.
Tupambi Fm.
Itacua Fm.
Carboniferous units
Iquiri Fm.
Los Monos Fm.
Santa Rosa Fm.
Arroyo Colorado Fm.
Devonian units
Silurian
Ordovician
Mid. - Upp. Cambrian
Ediac. - Low. Cambr.
Underlying units
0.2
0.0
-0.2
-0.4
-0.4
-0.2
0.0
0.2

Fig. 12

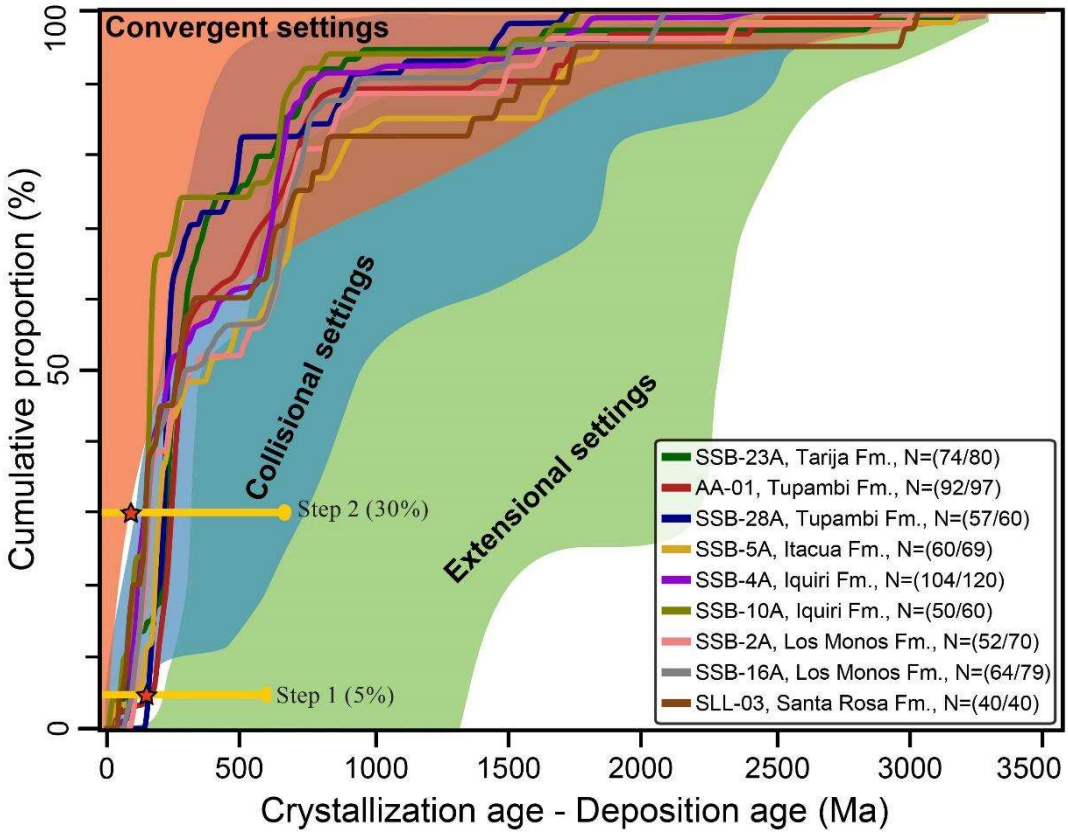
Convergent settings
Collisional settings
Extensional settings
Step 2 (30%)
Step 1 (5%)
SSB-23A, Tarija Fm., N=(74/80)
AA-01, Tupambi Fm., N=(92/97)
SSB-28A, Tupambi Fm., N=(57/60)
SSB-5A, Itacua Fm., N=(60/69)
SSB-4A, Iquiri Fm., N=(104/120)
SSB-10A, Iquiri Fm., N=(50/60)
SSB-2A, Los Monos Fm., N=(52/70)
SSB-16A, Los Monos Fm., N=(64/79)
SLL-03, Santa Rosa Fm., N=(40/40)
Cumulative proportion (%)
0
50
100
0
500
1000
1500
2000
2500
3000
3500
Crystallization age - Deposition age (Ma)

Fig. 13

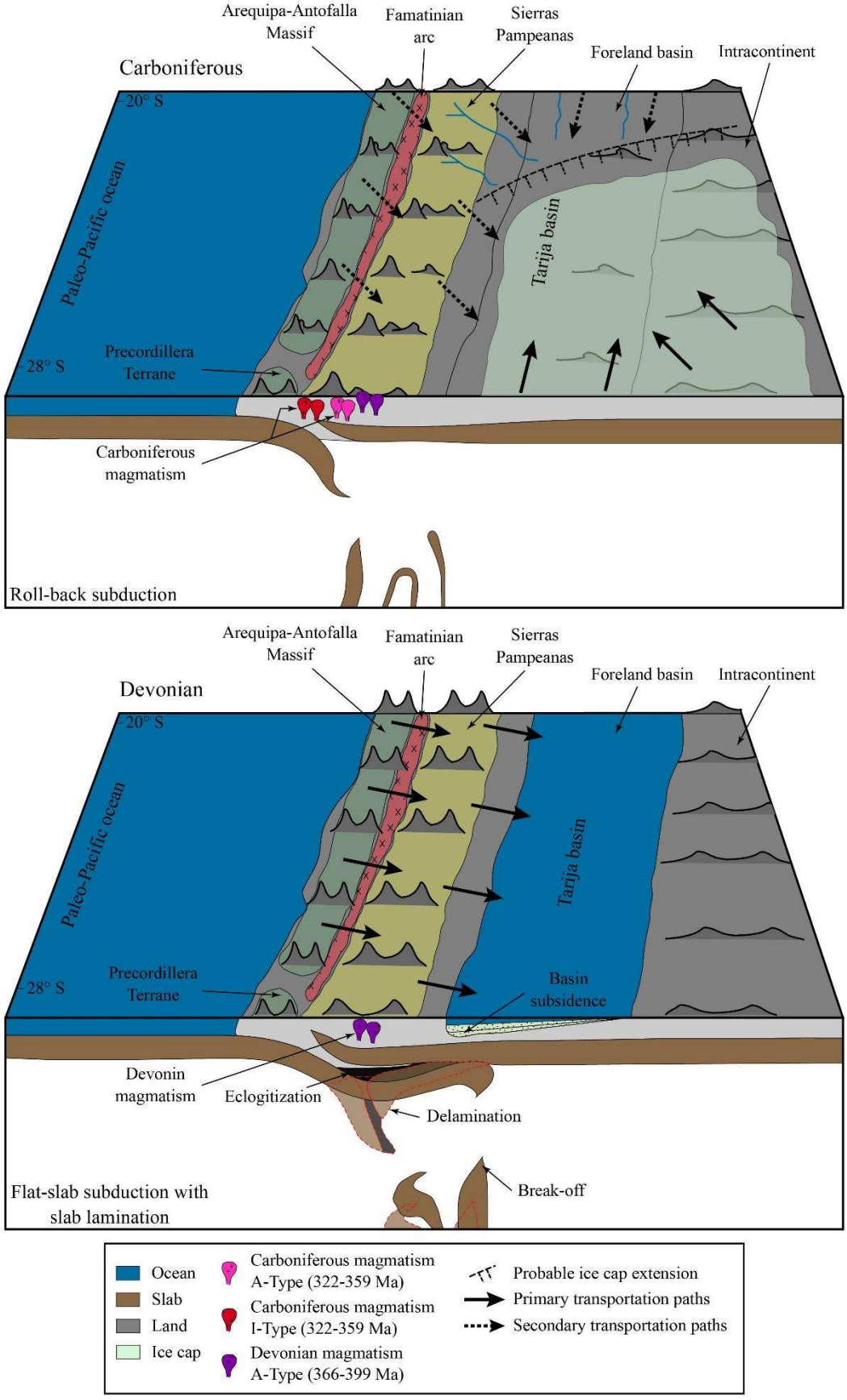
Carboniferous
Arequipa-Antofalla Massif
Famatinian arc
Sierras Pampeanas
Foreland basin
Intracontinent
20° S
28° S
Paleo-Pacific ocean
Tarija basin
Precordillera Terrane
Carboniferous magmatism
Roll-back subduction
Devonian
Devonin magmatism
Eclogitization
Delamination
Basin subsidence
Break-off
Flat-slab subduction with slab lamination
Ocean
Slab
Land
Ice cap
Carboniferous magmatism A-Type (322-359 Ma)
Carboniferous magmatism I-Type (322-359 Ma)
Devonian magmatism A-Type (366-399 Ma)
Probable ice cap extension
Primary transportation paths
Secondary transportation paths

Fig. 14

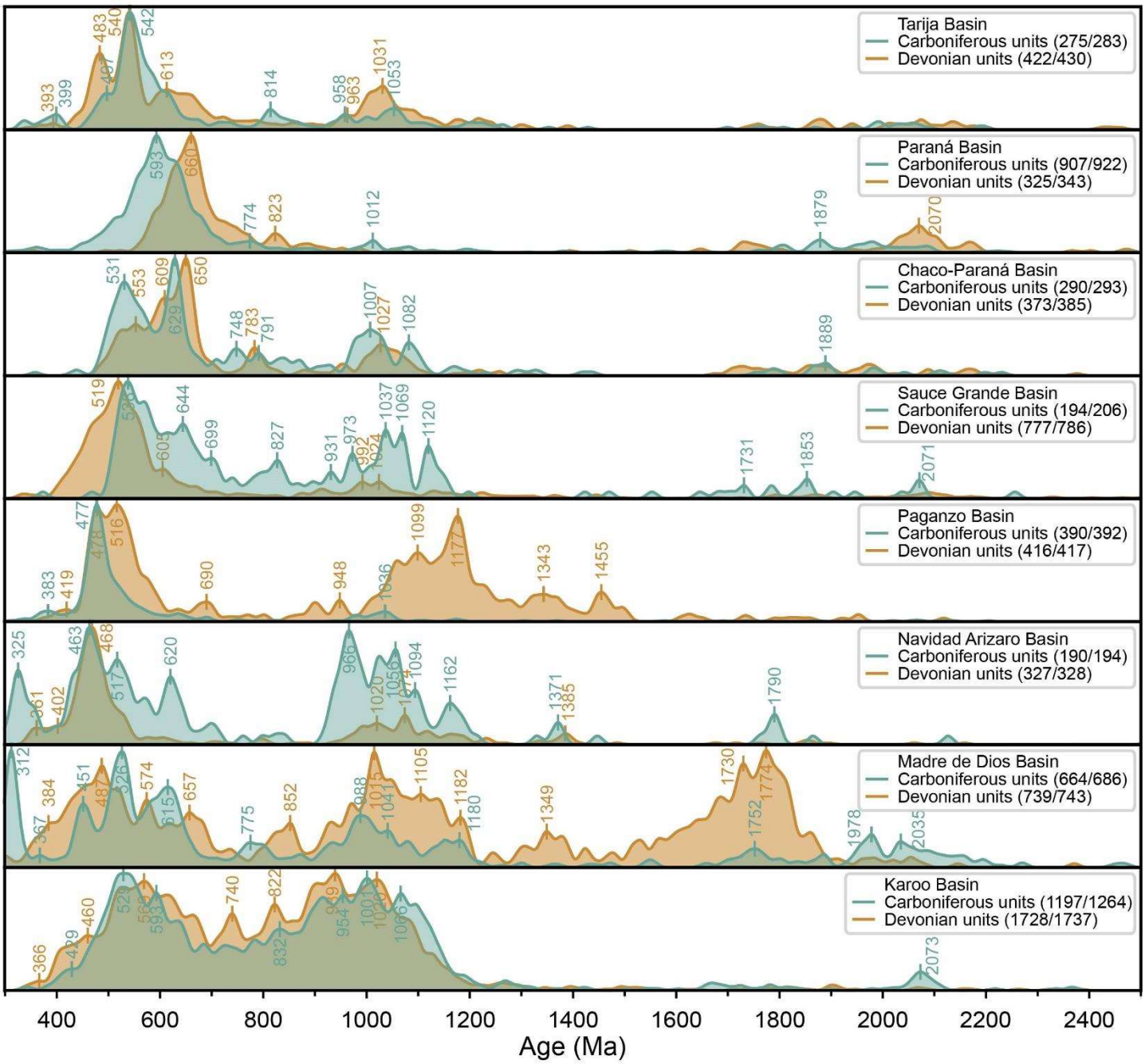
Tarija Basin
Carboniferous units (275/283)
Devonian units (422/430)
Paraná Basin
Carboniferous units (907/922)
Devonian units (325/343)
Chaco-Paraná Basin
Carboniferous units (290/293)
Devonian units (373/385)
Sauce Grande Basin
Carboniferous units (194/206)
Devonian units (777/786)
Paganzo Basin
Carboniferous units (390/392)
Devonian units (416/417)
Navidad Arizaro Basin
Carboniferous units (190/194)
Devonian units (327/328)
Madre de Dios Basin
Carboniferous units (664/686)
Devonian units (739/743)
Karoo Basin
Carboniferous units (1197/1264)
Devonian units (1728/1737)
400
600
800
1000
1200
1400
1600
1800
2000
2200
2400
Age (Ma)

Fig. 15

Supplementary data

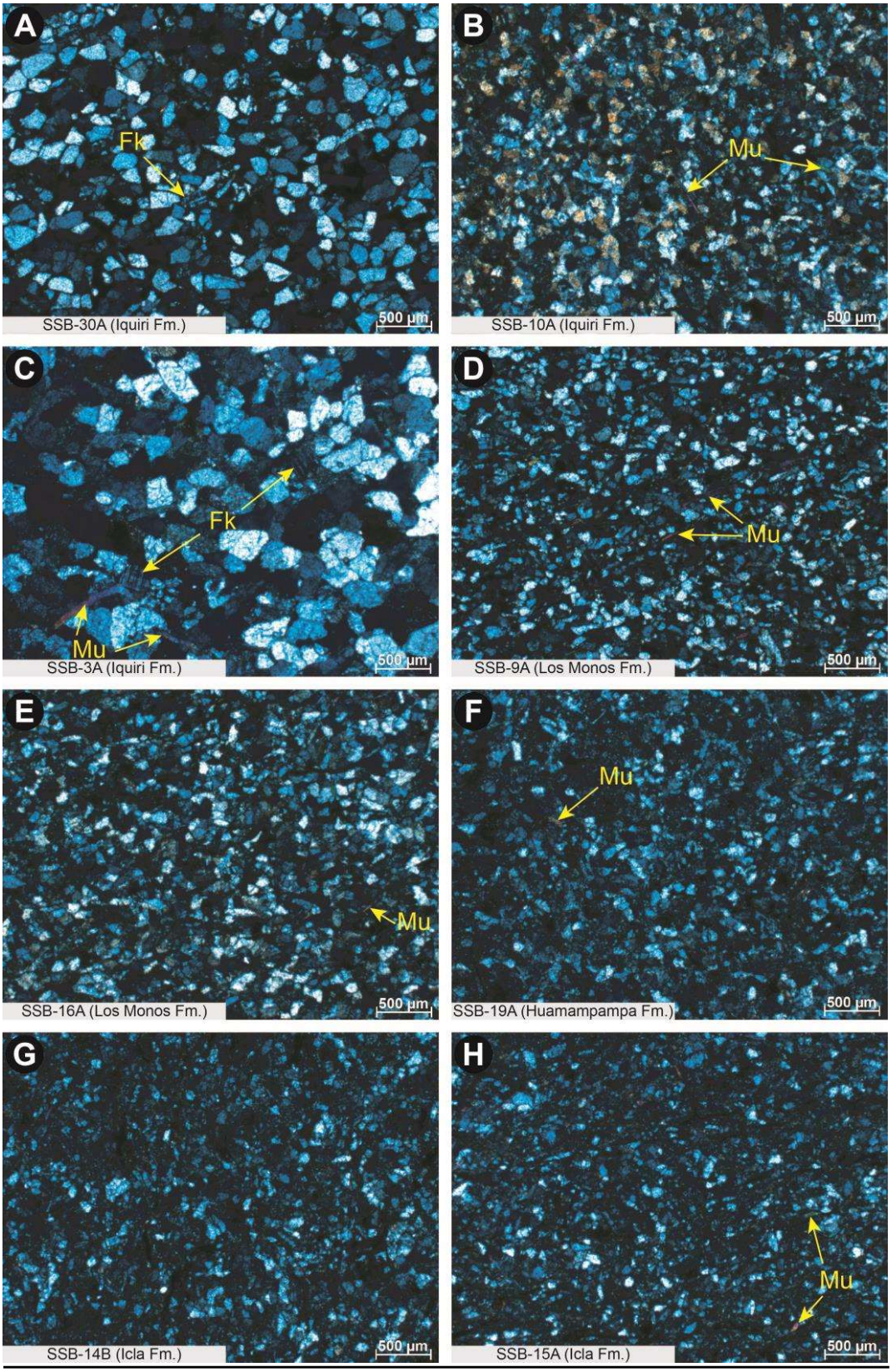

Supplementary Figure I1

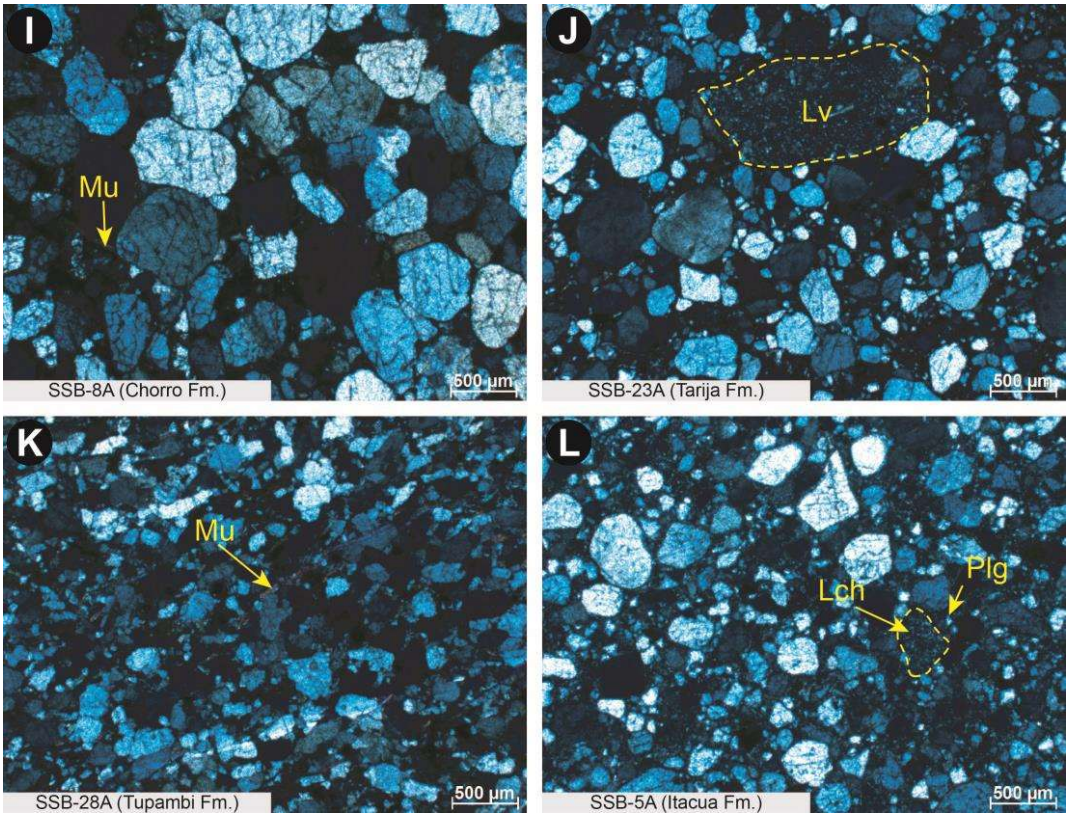

Supplementary Figure I1 (Continue)

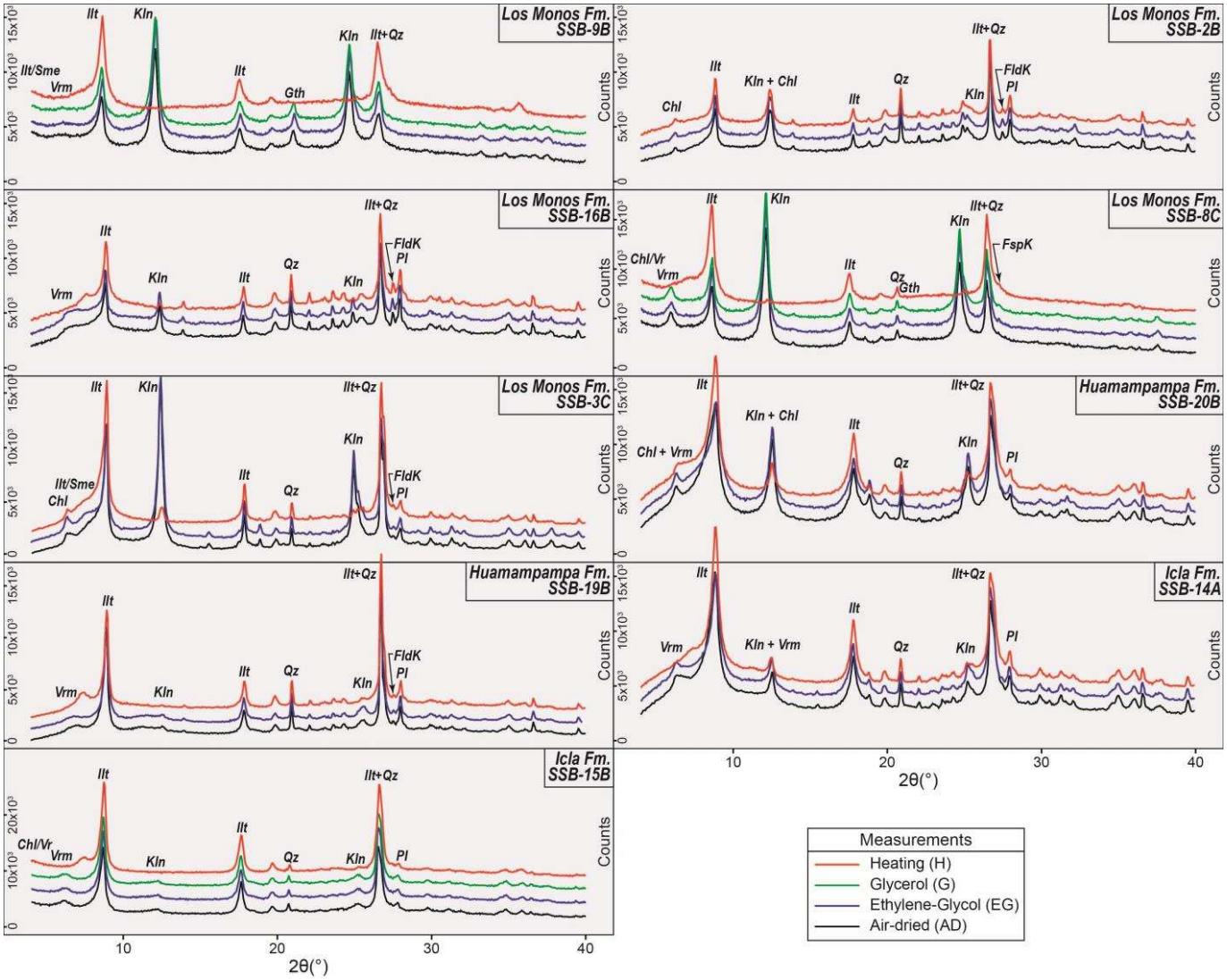

Supplementary Figure I2

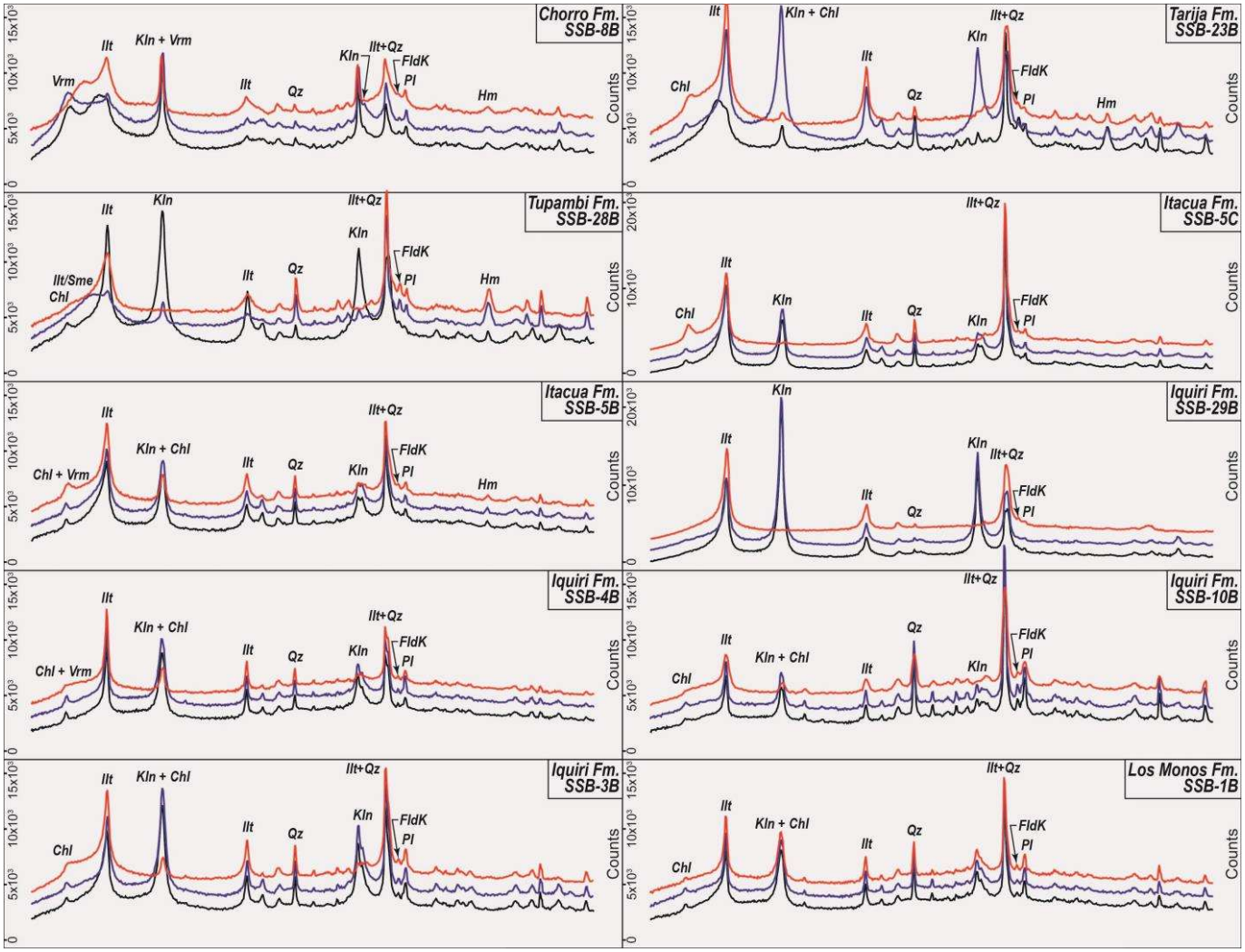

Supplementary Figure I2 (Continue)

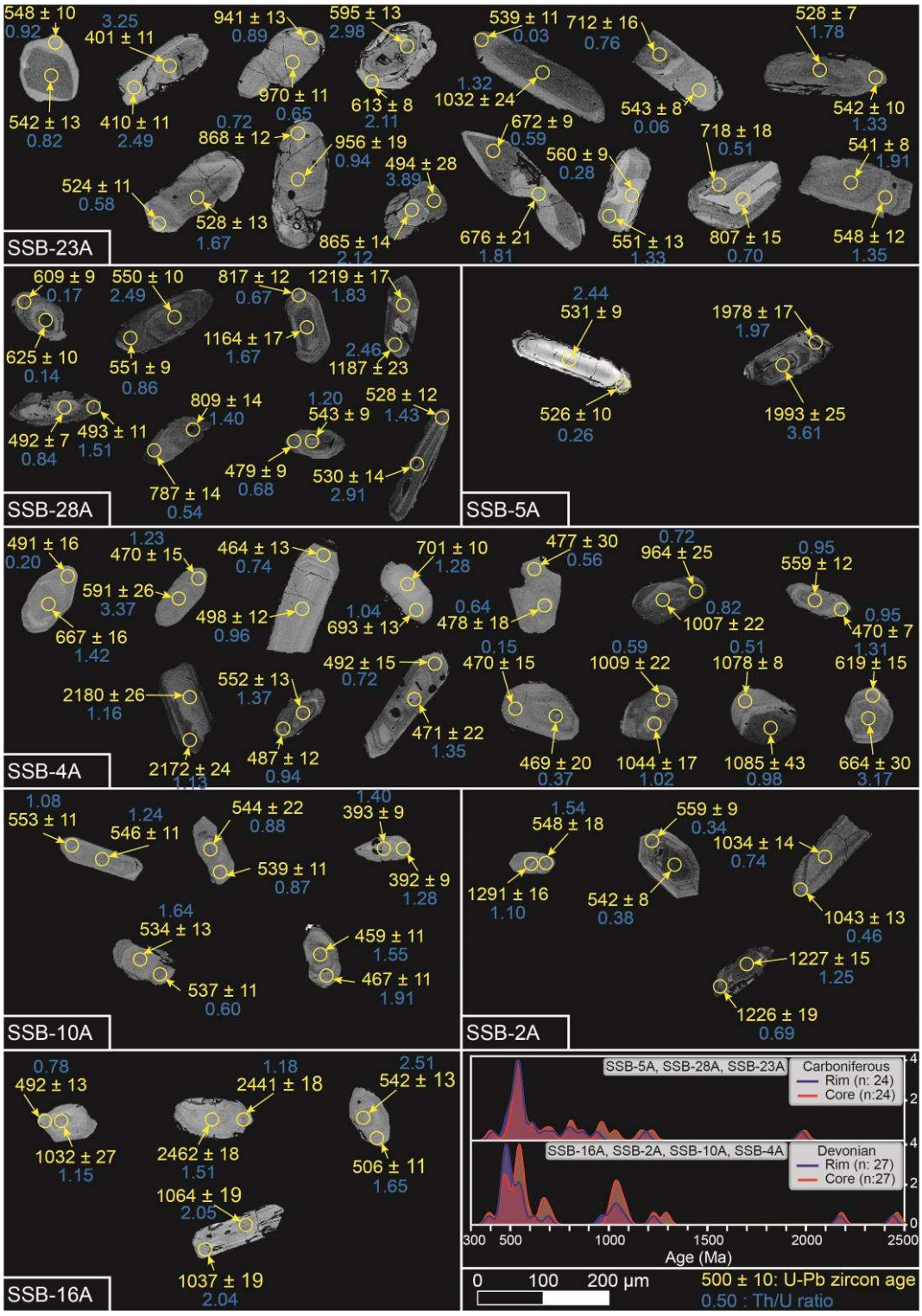

Supplementary Figure I3

Laboratory and Sample Preparation	
Laboratory name	Laboratório de Estudos Geodinâmicos, Geocronológicos e Ambientais, Instituto de Geociências, Universidade de Brasília (UnB)
Sample type/mineral	Zircon
Sample preparation	Conventional mineral separation, 0.5 cm resin mount, 1 µm polish to finish
Imaging	BSE, FEI Quanta 450, 10 nA, 20kV, 13.8 mm working distance
Laser ablation system	
Make, Model and type	ESI/New Wave Research, UP-213, Nd:YAG
Ablation cell and volume	Low volume cell, ca. 4 cm^3
Laser wavelength (nm)	213 nm
Pulse width (ns)	3 ns
Fluence (J cm^{-2})	3.0 - 3.5 J cm^{-2}
Repetition rate (Hz)	10 Hz (U-Pb)
Spot size	25 µm (U-Pb)
Sampling mode / pattern	single spot analyses
Carrier gas	100% He, Ar make-up gas combined using a Y-piece along the sample transport line close to the torch.
Pre-ablation laser warm-up (background collection)	10 s
Ablation duration (s)	40 s
Wash-out delay	20 s
Ablation pit depth / ablation rate	~10 µm pit depth
Cell carrier gas flow (l min^{-1})	0.40 l min^{-1} He
ICP-MS Instrument	
Make, Model and type	Thermo-Fischer, Neptune, MC-ICP-MS
Sample introduction	Ablation aerosol
RF power (W)	1050 W
Make-up gas flow (l min^{-1})	0.98 - 1.05 l min-1
Detection system	Mixed Faraday cups and multiple ion counting (MIC) array
Masses measured for U-Pb	Faraday ^{232}Th, ^{238}U and ^{206}Pb; MIC ^{202}Hg, ^{204}Pb, ^{207}Pb and ^{208}Pb
Integration time per peak/dwell times (ms); quadrupole settling time between mass jumps	#N.A.

Total integration time per output data point (s)	1.049 s
Dead time (ns)	#N.A.
Data Processing	
Gas blank	20 s
Calibration strategy	GJ1 used as primary reference material, 91500 used as secondary/validation
Reference Material info	GJ1 (Jackson et al. 2004, Horstwood et al. 2016)
	91500 (Wiedenbeck et al., 1995)
Data processing package used / Correction for LIEF	Iolite v.4.0 (Paton et al., 2011) & VizualAge (Petrus and Kamber, 2012) using exponential plus linear modelling for LIEF
Mass discrimination	Standard-sample bracketing with 207Pb/206Pb and 206Pb/238U ratios normalized to reference material GJ1
Common-Pb correction, composition and uncertainty	none
Uncertainty level and propagation	Ages are quoted at 2s absolute, propagation is by quadratic addition. Excess variance and age uncertainty of reference material are propagated where appropriate.
Quality control / Validation	91500 – Intercept age = 1073 ± 7 (2s, MSWD = 0.86, n = 36) Systematic uncertainty for propagation is 1% (2s).

Supplementary Table 1

Supplementary Table 2

Laboratório de Geocronologia, Universidade de Brasília								Data for Tera-Wasserburg plot[2]				Data for Wetherill plot[2]					Apparent Ages (Ma)							
Identifier	Spot number	f206c	^{206}Pb mV	U[1]	Th/U	^{206}Pb/^{204}Pb	1s	^{238}U/^{206}Pb	1s	^{207}Pb/^{206}Pb	1s	^{207}Pb/^{235}U	1s	^{206}Pb/^{238}U	1s	Rho	^{207}Pb/^{206}Pb *	2s	^{206}Pb/^{238}U	2s	^{207}Pb/^{235}U	2s	% conc[3]	% conc[4]
			(mV)	(ppm)			(%)		(%)		(%)		(%)		(%)			(abs)		(abs)		(abs)		
SSB-16A - Los Monos Fm. - Devonian																								
SSB-16A	#62	#N/A	0.003	219	1.96	54408	2.4	12.71	1.0	0.05669	0.7	0.6173	1.2	0.07869	1.0	0.83	478	29	488	10	488	18	102	100
SSB-16A	#74	#N/A	0.005	423	0.23	16626	3.7	12.86	1.0	0.05722	0.6	0.6120	1.2	0.07778	1.0	0.88	499	24	483	9	485	17	97	100
SSB-16A	#10	#N/A	0.002	199	2.72	3568	6.6	13.55	1.7	0.05735	1.2	0.5839	2.1	0.07390	1.7	0.81	503	53	460	15	467	30	91	98
SSB-16A	#11	#N/A	0.002	164	1.01	10603	2.4	13.10	1.2	0.05746	1.0	0.6069	1.5	0.07637	1.2	0.76	507	43	474	10	482	23	94	99
SSB-16A	#109	#N/A	0.003	280	0.35	29554	4.1	12.26	1.1	0.05762	0.7	0.6468	1.3	0.08160	1.1	0.86	514	28	506	11	506	20	98	100
SSB-16A	#63	#N/A	0.002	144	2.51	10230	7.9	11.41	1.3	0.05817	1.0	0.7042	1.6	0.08775	1.2	0.79	534	41	542	13	541	25	102	100
SSB-16A	#5	#N/A	0.002	145	1.98	18496	2.4	11.76	1.1	0.05827	0.7	0.6843	1.3	0.08503	1.1	0.84	539	29	526	10	529	20	98	99
SSB-16A	#75	#N/A	0.004	313	0.62	31384	5.4	11.08	1.0	0.05852	0.7	0.7287	1.2	0.09023	1.0	0.84	548	28	557	11	556	20	102	100
SSB-16A	#96	#N/A	0.003	232	1.32	21075	6.4	12.06	1.1	0.05859	0.9	0.6689	1.5	0.08298	1.2	0.79	550	38	514	11	520	23	93	99
SSB-16A	#50	#N/A	0.002	133	2.78	24761	4.4	11.60	1.3	0.05881	1.0	0.7012	1.7	0.08625	1.3	0.78	558	44	533	13	539	27	96	99
SSB-16A	#13	#N/A	0.007	553	2.10	36841	1.7	11.91	1.0	0.05882	0.7	0.6787	1.3	0.08394	1.0	0.81	559	32	520	10	526	20	93	99
SSB-16A	#91	#N/A	0.004	295	1.92	37824	0.8	11.26	1.0	0.05889	0.6	0.7211	1.2	0.08879	1.0	0.86	562	26	548	11	551	20	98	99
SSB-16A	#81	#N/A	0.002	152	3.56	124850	0.2	11.07	1.2	0.05891	0.9	0.7334	1.5	0.09041	1.2	0.81	562	37	558	12	559	24	99	100
SSB-16A	#92	#N/A	0.002	130	2.41	13501	7.2	11.85	1.1	0.05928	0.9	0.6877	1.4	0.08439	1.1	0.79	575	37	522	11	531	23	91	98
SSB-16A	#9	#N/A	0.002	135	1.89	7157	7.9	11.77	2.5	0.05930	0.8	0.6920	2.5	0.08515	2.3	0.94	577	36	527	23	534	40	91	99
SSB-16A	#43	#N/A	0.003	253	3.47	19082	11.1	11.55	1.1	0.05953	0.7	0.7078	1.3	0.08661	1.1	0.83	585	31	535	11	543	22	92	99
SSB-16A	#101	#N/A	0.007	552	1.30	12958	16.0	12.25	1.4	0.05970	0.8	0.6727	1.6	0.08171	1.4	0.87	591	34	506	14	522	25	86	97
SSB-16A	#65	#N/A	0.002	171	1.98	10490	9.5	11.45	1.2	0.05990	1.2	0.7216	1.7	0.08739	1.2	0.70	597	51	540	12	551	27	90	98
SSB-16A	#89	#N/A	0.003	258	1.58	7461	14.1	11.88	2.3	0.05989	1.0	0.6898	2.4	0.08436	2.2	0.92	598	40	522	22	532	38	87	98
SSB-16A	#12	#N/A	0.002	181	1.06	9335	6.7	11.25	1.1	0.05997	1.2	0.7340	1.6	0.08887	1.1	0.66	599	52	549	11	559	27	92	98
SSB-16A	#24	#N/A	0.007	509	0.11	31192	4.2	10.16	1.1	0.05999	0.6	0.8099	1.2	0.09844	1.0	0.87	602	25	605	12	602	21	100	100
SSB-16A	#25	#N/A	0.003	191	0.90	4856	9.4	11.66	1.0	0.06047	0.8	0.7164	1.3	0.08574	1.0	0.77	619	36	530	10	548	22	86	97
SSB-16A	#103	#N/A	0.002	212	1.85	3505	17.2	12.88	1.5	0.06063	1.2	0.6432	1.9	0.07767	1.5	0.77	624	52	482	14	504	30	77	96
SSB-16A	#64	#N/A	0.003	238	1.65	5003	8.3	12.26	1.2	0.06075	1.3	0.6796	1.7	0.08160	1.2	0.69	628	53	506	11	527	27	80	96
SSB-16A	#22	#N/A	0.002	156	3.00	4284	11.6	11.57	1.1	0.06092	0.9	0.7266	1.4	0.08648	1.1	0.77	634	37	535	11	555	23	84	96
SSB-16A	#37	#N/A	0.002	167	0.78	3677	26.7	12.61	1.4	0.06144	0.9	0.6739	1.6	0.07937	1.3	0.82	653	39	492	13	523	26	75	94

SSB-16A	#19	#N/A	0.002	132	2.33	36118	0.6	10.24	1.1	0.06202	0.9	0.8361	1.4	0.09772	1.1	0.78	673	37	601	13	617	26	89	97
SSB-16A	#48	#N/A	0.003	267	1.83	2892	4.2	13.66	1.1	0.06229	2.3	0.6323	2.6	0.07323	1.1	0.43	676	93	456	10	497	39	67	92
SSB-16A	#82	#N/A	0.001	41	6.87	5143	3.3	9.49	2.6	0.06256	2.1	0.9090	3.4	0.10623	2.6	0.77	684	93	651	32	656	64	95	99
SSB-16A	#110	#N/A	0.003	214	0.35	54016	2.6	9.17	1.1	0.06276	0.9	0.9427	1.4	0.10911	1.1	0.78	698	37	668	14	674	26	96	99
SSB-16A	#106	#N/A	0.003	256	2.89	3422	270.2	10.58	1.1	0.06362	1.6	0.8168	2.0	0.09449	1.1	0.57	727	68	582	12	606	35	80	96
SSB-16A	#108	#N/A	0.005	257	2.13	35905	3.4	8.04	1.0	0.06431	0.6	1.1019	1.2	0.12441	1.0	0.87	751	24	756	14	754	24	101	100
SSB-16A	#88	#N/A	0.001	46	1.42	68542	0.5	7.45	1.8	0.06794	1.1	1.2591	2.1	0.13465	1.8	0.85	864	45	814	27	827	46	94	98
SSB-16A	#39	#N/A	0.003	162	0.69	17648	1.9	7.73	1.1	0.06911	1.0	1.2232	1.5	0.12945	1.1	0.74	901	42	785	16	811	33	87	97
SSB-16A	#8	#N/A	0.009	517	0.44	22417	2.2	9.21	1.0	0.06992	0.6	1.0447	1.1	0.10856	1.0	0.87	925	23	664	12	726	23	72	91
SSB-16A	#49	#N/A	0.004	199	0.90	2999	6.4	8.27	3.8	0.07226	1.7	1.2201	4.1	0.12203	3.7	0.91	990	69	742	51	807	84	75	92
SSB-16A	#38	#N/A	0.006	216	1.74	36078	4.6	5.77	1.0	0.07258	0.6	1.7360	1.2	0.17336	1.0	0.87	1001	24	1031	19	1022	30	103	101
SSB-16A	#51	#N/A	0.009	356	0.96	85560	4.4	5.81	1.0	0.07322	0.6	1.7368	1.2	0.17211	1.0	0.86	1019	25	1024	19	1022	30	100	100
SSB-16A	#55	#N/A	0.008	304	1.40	61081	3.5	5.81	1.0	0.07358	0.6	1.7535	1.2	0.17219	1.0	0.86	1029	24	1024	19	1028	30	100	100
SSB-16A	#23	#N/A	0.006	252	1.31	28151	5.8	5.98	1.1	0.07388	0.6	1.7020	1.2	0.16715	1.1	0.88	1037	22	996	19	1009	30	96	99
SSB-16A	#54	#N/A	0.003	111	2.44	14961	12.2	6.04	1.2	0.07393	0.8	1.6970	1.4	0.16568	1.2	0.82	1038	32	988	21	1007	35	95	98
SSB-16A	#67	#N/A	0.003	125	1.55	16223	3.9	5.66	1.0	0.07429	0.6	1.8105	1.2	0.17666	1.0	0.85	1048	25	1049	20	1049	31	100	100
SSB-16A	#26	#N/A	0.006	224	0.92	16440	2.8	5.64	1.1	0.07517	0.6	1.8332	1.2	0.17735	1.1	0.87	1072	23	1052	20	1057	31	98	100
SSB-16A	#42	#N/A	0.002	75	2.70	33394	2.4	5.21	1.1	0.07611	0.7	2.0107	1.3	0.19206	1.1	0.85	1097	26	1133	22	1119	33	103	101
SSB-16A	#36	#N/A	0.002	65	1.15	14410	6.9	5.76	1.5	0.07618	1.2	1.8356	1.9	0.17361	1.5	0.76	1098	49	1032	27	1058	49	94	98
SSB-16A	#93	#N/A	0.009	352	1.32	15053	7.5	5.46	1.1	0.07615	0.6	1.9098	1.3	0.18314	1.1	0.87	1098	25	1084	22	1084	34	99	100
SSB-16A	#14	#N/A	0.001	22	1.17	4404	3.6	5.40	1.6	0.07629	1.5	1.9485	2.2	0.18547	1.6	0.73	1098	60	1097	32	1098	58	100	100
SSB-16A	#53	#N/A	0.001	36	6.04	4298	10.5	6.13	3.0	0.07670	2.1	1.7405	3.7	0.16444	3.0	0.82	1107	84	981	54	1021	88	89	96
SSB-16A	#78	#N/A	0.001	52	5.03	7824	1.8	5.30	1.2	0.07653	0.9	1.9924	1.5	0.18890	1.2	0.79	1107	35	1115	24	1113	39	101	100
SSB-16A	#90	#N/A	0.005	190	0.73	63953	1.7	5.25	1.1	0.07668	0.7	1.9983	1.3	0.19043	1.1	0.84	1112	27	1124	22	1115	33	101	101
SSB-16A	#66	#N/A	0.004	163	3.04	71737	2.1	5.23	1.1	0.07744	0.7	2.0351	1.3	0.19114	1.1	0.84	1131	26	1128	21	1127	33	100	100
SSB-16A	#104	#N/A	0.001	36	3.06	56855	0.4	5.54	2.0	0.07820	1.3	1.9375	2.4	0.18100	2.0	0.84	1149	51	1072	39	1094	62	93	98
SSB-16A	#77	#N/A	0.004	153	2.04	5142	5.1	5.73	1.0	0.07840	1.1	1.8945	1.5	0.17447	1.0	0.67	1155	44	1037	19	1079	39	90	96
SSB-16A	#87	#N/A	0.004	150	0.73	7480	13.4	5.14	1.1	0.07876	0.7	2.1188	1.3	0.19444	1.1	0.84	1165	28	1145	23	1155	35	98	99
SSB-16A	#27	#N/A	0.003	104	1.75	13395	10.8	4.96	1.1	0.07922	0.7	2.2036	1.3	0.20157	1.1	0.85	1176	26	1184	23	1182	35	101	100
SSB-16A	#76	#N/A	0.006	232	2.05	2543	35.6	5.57	1.0	0.08131	1.2	2.0005	1.5	0.17941	1.0	0.65	1227	45	1064	19	1116	40	87	95
SSB-16A	#94	#N/A	0.002	61	0.88	31166	1.4	4.50	1.1	0.08432	0.8	2.5728	1.4	0.22217	1.1	0.81	1298	31	1293	26	1293	39	100	100
SSB-16A	#21	#N/A	0.005	168	1.09	16577	13.0	4.50	1.0	0.08493	1.0	2.5828	1.4	0.22201	1.0	0.73	1312	37	1293	23	1296	40	98	100

SSB-16A	#20	#N/A	0.002	41	4.01	6577	7.2	3.19	1.2	0.10941	1.0	4.7015	1.5	0.31325	1.2	0.77	1788	35	1757	35	1767	50	98	99
SSB-16A	#6	#N/A	0.003	50	3.60	14134	5.2	2.97	1.1	0.11565	0.7	5.3837	1.3	0.33701	1.1	0.83	1889	26	1872	34	1882	43	99	99
SSB-16A	#107	#N/A	0.002	53	3.41	17951	7.5	2.97	1.1	0.11564	0.6	5.3465	1.3	0.33691	1.1	0.87	1889	22	1872	35	1876	42	99	100
SSB-16A	#102	#N/A	0.012	176	0.98	59486	6.4	2.16	1.1	0.15687	0.6	9.9704	1.3	0.46222	1.1	0.89	2421	19	2449	45	2432	45	101	101
SSB-16A	#57	#N/A	0.021	312	1.18	52053	10.7	2.27	1.0	0.15865	0.5	9.6754	1.1	0.44069	1.0	0.88	2441	18	2354	38	2404	40	96	98
SSB-16A	#56	#N/A	0.029	399	1.51	157574	11.3	2.11	1.0	0.16067	0.5	10.5481	1.2	0.47444	1.0	0.89	2462	18	2503	42	2484	42	102	101
SSB-16A	#29	#N/A	0.003	254	1.69	5265	20.9	10.88	3.0	0.06915	1.9	0.8725	3.7	0.09214	3.1	0.85	901	78	568	33	636	67	63	89
SSB-16A	#80	#N/A	0.002	182	0.39	4689	5.2	12.00	1.3	0.07129	0.8	0.8192	1.5	0.08340	1.3	0.83	964	33	516	12	607	26	54	85
SSB-16A	#41	#N/A	0.001	34	2.34	1988	6.6	8.46	2.9	0.07728	1.6	1.2589	3.2	0.11909	2.8	0.87	1124	63	725	38	827	70	64	88
SSB-16A	#95	#N/A	0.001	119	3.71	564	34.3	18.65	5.1	0.07882	4.1	0.5850	6.3	0.05444	4.7	0.75	1153	153	342	31	466	90	30	73
SSB-16A	#73	#N/A	0.004	395	1.13	844	24.1	12.58	1.5	0.08133	1.6	0.8887	2.2	0.07957	1.5	0.68	1226	61	494	14	646	40	40	76
SSB-16A	#7	#N/A	0.002	214	0.57	651	50.9	14.29	1.6	0.08176	1.2	0.7834	1.9	0.07001	1.6	0.80	1238	45	436	13	587	33	35	74
SSB-16A	##	#N/A	0.006	280	5.09	1606	24.4	6.83	3.2	0.08546	1.4	1.7214	3.4	0.14714	3.1	0.92	1324	52	885	51	1015	83	67	87
SSB-16A	#52	#N/A	0.011	566	0.67	1269	58.8	7.66	1.8	0.08660	0.9	1.5522	2.0	0.13071	1.8	0.89	1350	34	792	26	951	48	59	83
SSB-16A	#34	#N/A	0.002	100	0.80	1166	37.1	9.07	1.7	0.09212	2.8	1.4210	3.3	0.11036	1.7	0.51	1463	101	675	21	896	75	46	75
SSB-16A	#68	#N/A	0.008	820	1.13	480	43.1	14.97	1.8	0.09515	1.0	0.8740	2.0	0.06688	1.8	0.86	1530	39	417	14	637	37	27	65
SSB-16A	#105	#N/A	0.002	139	1.56	569	61.3	10.78	4.5	0.09909	1.5	1.2691	4.9	0.09382	4.7	0.95	1605	52	578	51	830	107	36	70
SSB-16A	#28	#N/A	0.004	375	2.26	455	45.2	14.75	3.8	0.09965	2.2	0.9414	4.2	0.06829	3.6	0.85	1614	79	426	29	672	78	26	63
SSB-16A	#35	#N/A	0.006	287	2.96	414	86.0	7.53	1.6	0.11509	2.1	2.1122	2.7	0.13288	1.6	0.59	1877	73	804	24	1153	72	43	70
SSB-16A	#79	#N/A	0.027	395	0.05	48178	10.4	2.08	1.9	0.27834	0.6	18.4680	2.0	0.48259	1.9	0.95	3353	19	2538	77	3013	71	76	84
SSB-16A	#40	#N/A	-	-	-	-	-	-	-	-	-	-	-	-	-	-	-	-	-	-	-	-	-	-
SSB-2A - Los Monos Fm. - Devonian																								
SSB-2A	#48	#N/A	0.002	131	2.16	12311	2.5	12.51	0.8	0.05678	0.6	0.6247	1.0	0.07995	0.8	0.82	482	25	496	8	493	11	103	101
SSB-2A	#56	#N/A	0.003	217	0.25	18844	8.9	13.03	0.8	0.05716	0.5	0.6022	0.9	0.07680	0.8	0.84	496	22	477	7	479	13	96	100
SSB-2A	#14	#N/A	0.002	198	1.05	14244	6.7	12.43	1.0	0.05755	0.7	0.6364	1.2	0.08053	1.0	0.81	511	31	499	9	500	15	98	100
SSB-2A	#78	#N/A	0.003	222	2.07	11168	16.4	12.69	0.7	0.05776	0.6	0.6230	1.0	0.07882	0.7	0.75	519	27	489	7	492	9	94	99
SSB-2A	#91	#N/A	0.004	329	1.56	53882	9.3	12.49	0.7	0.05784	0.9	0.6341	1.1	0.08004	0.7	0.65	522	38	496	7	499	14	95	100
SSB-2A	#80	#N/A	0.002	192	0.58	33998	3.9	11.60	0.7	0.05806	0.6	0.6908	0.9	0.08623	0.7	0.75	531	27	533	7	533	9	101	100
SSB-2A	#25	#N/A	0.002	120	1.04	14674	8.3	11.61	0.8	0.05821	0.7	0.6903	1.1	0.08620	0.9	0.77	536	30	533	9	533	10	100	100
SSB-2A	#98	#N/A	0.003	255	1.32	26162	2.7	11.74	0.8	0.05821	0.6	0.6805	1.0	0.08520	0.8	0.79	536	26	527	8	527	12	98	100
SSB-2A	#82	#N/A	0.001	91	1.25	12185	4.4	11.33	1.3	0.05849	1.4	0.7099	1.9	0.08839	1.4	0.70	544	59	546	14	545	12	100	100
SSB-2A	#39	#N/A	0.002	108	0.73	9153	8.0	11.53	0.9	0.05852	1.0	0.6980	1.3	0.08677	0.9	0.66	546	44	536	9	538	12	98	100

SSB-2A	#50	#N/A	0.002	165	0.38	42999	2.7	11.39	0.7	0.05856	0.7	0.7050	1.1	0.08778	0.7	0.71	549	32	542	8	542	10	99	100
SSB-2A	#8	#N/A	0.003	255	0.26	4981	24.2	12.72	0.9	0.05930	0.8	0.6301	1.2	0.07866	0.8	0.71	576	36	488	8	496	23	85	98
SSB-2A	#54	#N/A	0.001	88	5.49	11450	5.5	11.74	1.0	0.05942	1.0	0.6983	1.4	0.08530	1.0	0.70	579	42	528	10	538	12	91	98
SSB-2A	#40	#N/A	0.004	247	0.66	5426	8.9	11.36	0.8	0.05969	0.7	0.7238	1.1	0.08809	0.8	0.78	591	29	544	9	553	13	92	98
SSB-2A	#64	#N/A	0.011	707	0.41	27530	8.4	10.01	0.6	0.06018	0.5	0.8276	0.8	0.09995	0.6	0.80	609	20	614	7	612	10	101	100
SSB-2A	#47	#N/A	0.003	234	0.65	5535	17.9	11.31	1.2	0.06096	0.8	0.7399	1.4	0.08850	1.2	0.82	636	35	547	12	562	27	86	97
SSB-2A	#94	#N/A	0.002	155	2.28	9070	22.5	11.78	2.9	0.06131	2.2	0.7135	3.6	0.08513	2.8	0.78	646	95	527	28	547	39	81	96
SSB-2A	#63	#N/A	0.003	239	3.44	4180	4.6	12.05	0.7	0.06136	1.5	0.7010	1.6	0.08297	0.7	0.43	649	60	514	7	539	21	79	95
SSB-2A	#77	#N/A	0.002	161	3.22	59949	1.0	9.74	1.0	0.06170	0.7	0.8722	1.2	0.10274	1.0	0.80	662	30	630	11	637	12	95	99
SSB-2A	#84	#N/A	0.003	240	0.83	176300	1.4	10.01	0.8	0.06171	0.7	0.8458	1.1	0.09992	0.8	0.77	663	29	614	10	622	11	93	99
SSB-2A	#38	#N/A	0.005	257	4.50	10643	12.0	9.29	0.7	0.06185	0.4	0.9165	0.8	0.10764	0.7	0.85	668	17	659	8	660	11	99	100
SSB-2A	#97	#N/A	0.003	211	0.82	2331	16.9	12.41	0.8	0.06213	2.0	0.6920	2.2	0.08063	0.8	0.36	668	83	500	8	533	34	75	94
SSB-2A	#21	#N/A	0.003	174	2.25	25145	5.7	8.95	0.7	0.06233	0.5	0.9571	0.9	0.11174	0.7	0.84	684	20	683	9	682	11	100	100
SSB-2A	#51	#N/A	0.005	335	0.34	3071	38.8	11.05	0.8	0.06280	0.8	0.7797	1.2	0.09054	0.9	0.73	699	34	559	9	585	10	80	95
SSB-2A	#35	#N/A	0.003	204	1.54	2239	52.4	11.32	1.6	0.06619	2.0	0.7902	2.6	0.08866	1.7	0.66	803	76	548	18	591	36	68	93
SSB-2A	#52	#N/A	0.002	138	1.57	46251	1.5	8.39	1.0	0.06817	1.1	1.1145	1.5	0.11925	1.0	0.66	872	46	726	13	760	23	83	96
SSB-2A	#83	#N/A	0.000	14	1.52	13957	0.3	9.95	3.2	0.06882	4.0	0.9459	5.2	0.10084	3.2	0.63	886	163	619	37	676	19	70	92
SSB-2A	#69	#N/A	0.003	119	2.31	89311	2.1	6.00	0.7	0.07253	0.7	1.6700	1.0	0.16661	0.7	0.72	999	28	993	13	997	16	99	100
SSB-2A	#57	#N/A	0.007	338	1.72	10788	29.4	6.74	0.7	0.07261	0.7	1.4789	0.9	0.14844	0.6	0.70	1002	26	892	11	922	16	89	97
SSB-2A	#89	#N/A	0.002	93	1.70	14125	6.2	5.86	0.9	0.07325	0.5	1.7182	1.0	0.17064	0.9	0.85	1020	21	1016	16	1015	20	100	100
SSB-2A	#67	#N/A	0.007	263	0.74	108036	1.4	5.75	0.8	0.07336	0.4	1.7699	0.8	0.17399	0.8	0.89	1023	15	1034	14	1034	17	101	100
SSB-2A	#28	#N/A	0.006	206	1.21	268148	0.6	5.72	1.4	0.07416	0.5	1.7943	1.5	0.17531	1.4	0.94	1045	20	1041	27	1043	39	100	100
SSB-2A	#75	#N/A	0.004	146	1.64	34418	8.5	5.79	0.9	0.07428	0.5	1.7660	1.0	0.17296	0.9	0.86	1048	20	1028	16	1033	20	98	100
SSB-2A	#5	#N/A	0.002	68	1.51	24311	4.3	5.40	0.9	0.07463	0.6	1.9131	1.1	0.18543	0.9	0.84	1057	23	1097	18	1086	20	104	101
SSB-2A	#76	#N/A	0.003	128	1.15	20455	4.4	5.64	0.7	0.07469	0.6	1.8235	0.9	0.17733	0.7	0.79	1059	22	1052	13	1054	17	99	100
SSB-2A	#6	#N/A	0.004	152	1.41	29415	5.0	5.62	0.8	0.07473	0.7	1.8367	1.0	0.17807	0.8	0.77	1060	26	1056	15	1059	16	100	100
SSB-2A	#68	#N/A	0.008	315	0.46	8084	24.4	5.70	0.7	0.07487	0.5	1.8152	0.8	0.17557	0.7	0.82	1064	18	1043	13	1051	14	98	99
SSB-2A	#90	#N/A	0.001	21	1.35	4938	2.6	5.55	2.1	0.07609	2.0	1.8863	2.9	0.18119	2.1	0.73	1089	79	1073	41	1076	24	99	100
SSB-2A	#96	#N/A	0.001	53	1.17	32472	2.5	5.44	1.1	0.07620	0.8	1.9270	1.4	0.18391	1.1	0.80	1098	33	1088	22	1090	21	99	100
SSB-2A	#36	#N/A	0.001	36	2.57	2924	6.1	6.15	1.5	0.07863	1.6	1.7602	2.2	0.16304	1.5	0.66	1157	62	973	26	1031	30	84	94
SSB-2A	#12	#N/A	0.007	303	1.56	2431	25.9	6.58	0.8	0.07939	0.6	1.6533	1.0	0.15207	0.8	0.83	1181	21	913	14	991	16	77	92
SSB-2A	#9	#N/A	0.009	276	3.75	94572	3.0	4.80	0.8	0.08051	0.4	2.3067	0.9	0.20823	0.8	0.89	1208	15	1219	17	1214	18	101	100

SSB-2A	#93	#N/A	0.009	312	0.69	16883	5.2	4.77	0.9	0.08167	0.4	2.3533	1.0	0.20951	0.9	0.90	1237	16	1226	19	1228	21	99	100
SSB-2A	#92	#N/A	0.007	222	1.25	12757	5.3	4.77	0.7	0.08198	0.7	2.3644	0.9	0.20974	0.7	0.71	1244	26	1227	15	1232	19	99	100
SSB-2A	#34	#N/A	0.009	243	1.10	53124	7.8	4.51	0.7	0.08417	0.4	2.5661	0.8	0.22168	0.7	0.85	1295	17	1291	16	1291	18	100	100
SSB-2A	#10	#N/A	0.001	38	0.76	1318	19.7	5.75	1.3	0.08617	1.0	2.0594	1.7	0.17434	1.4	0.80	1340	40	1036	26	1135	39	77	91
SSB-2A	#20	#N/A	0.004	66	2.33	74748	3.3	2.87	0.7	0.11462	0.4	5.4899	0.8	0.34839	0.7	0.83	1873	16	1927	22	1899	18	103	101
SSB-2A	#41	#N/A	0.006	114	1.50	408263	0.7	3.04	0.8	0.11471	0.9	5.1706	1.2	0.32947	0.8	0.68	1874	31	1836	25	1848	20	98	99
SSB-2A	#24	#N/A	0.007	133	2.57	28366	11.3	2.75	2.2	0.12321	0.7	6.1510	2.3	0.36486	2.2	0.95	2002	26	2005	74	1996	87	100	100
SSB-2A	#11	#N/A	0.018	325	0.23	29074	23.2	2.65	0.6	0.12482	0.5	6.4725	0.8	0.37698	0.6	0.78	2025	18	2062	22	2042	23	102	101
SSB-2A	#42	#N/A	0.022	288	1.34	4175	28.4	2.03	0.7	0.18723	0.6	12.6605	0.9	0.49317	0.7	0.78	2717	18	2584	29	2655	27	95	97
SSB-2A	#81	#N/A	0.007	72	1.82	461208	0.6	1.62	0.9	0.28483	0.5	24.3302	1.0	0.61931	0.9	0.86	3389	16	3107	41	3281	37	92	95
SSB-2A	#95	#N/A	0.004	491	0.56	2037	48.6	17.86	2.4	0.06433	0.7	0.4959	2.6	0.05620	2.5	0.96	751	30	352	17	409	36	47	86
SSB-2A	#49	#N/A	0.003	222	0.68	1695	33.0	13.17	0.9	0.06665	1.9	0.6992	2.1	0.07596	0.8	0.41	817	75	472	8	538	33	58	88
SSB-2A	#79	#N/A	0.005	418	0.66	1860	24.2	12.54	0.8	0.06640	0.9	0.7264	1.2	0.07976	0.8	0.67	818	35	495	7	554	20	60	89
SSB-2A	#62	#N/A	0.004	347	1.12	908	8.9	15.27	1.2	0.07528	2.4	0.6833	2.7	0.06551	1.2	0.43	1072	93	409	9	529	36	38	77
SSB-2A	#53	#N/A	0.004	417	0.41	836	35.5	13.67	0.8	0.07755	2.1	0.7777	2.3	0.07318	0.8	0.36	1132	86	455	7	584	35	40	78
SSB-2A	#33	#N/A	0.009	436	0.25	1142	18.8	8.09	1.5	0.07804	1.7	1.3280	2.4	0.12398	1.6	0.69	1142	66	753	23	858	30	66	88
SSB-2A	#37	#N/A	0.007	396	1.40	1463	25.2	9.67	0.9	0.08272	1.0	1.1793	1.3	0.10348	0.9	0.69	1261	36	635	11	791	30	50	80
SSB-2A	#65	#N/A	0.005	221	0.72	33927	2.0	7.35	1.6	0.08549	1.0	1.6083	1.9	0.13616	1.6	0.84	1325	40	823	24	973	55	62	85
SSB-2A	#55	#N/A	0.002	100	0.78	18709	1.7	7.36	0.9	0.08585	0.7	1.6105	1.2	0.13602	0.9	0.78	1333	28	822	14	974	23	62	84
SSB-2A	#22	#N/A	0.006	240	0.37	16746	40.7	6.08	1.2	0.08659	1.5	1.9509	1.9	0.16450	1.2	0.61	1349	55	982	21	1098	59	73	89
SSB-2A	#7	#N/A	0.003	224	1.30	601	30.2	11.48	1.1	0.08899	4.0	1.0600	4.2	0.08716	1.1	0.26	1394	144	539	11	733	88	39	74
SSB-2A	#70	#N/A	0.005	416	0.28	525	68.6	13.08	0.7	0.09085	1.1	0.9585	1.3	0.07646	0.7	0.51	1440	42	475	6	682	23	33	70
SSB-2A	#27	#N/A	0.004	296	0.23	428	27.1	13.35	1.7	0.09535	2.8	0.9834	3.3	0.07508	1.8	0.55	1526	99	467	16	695	52	31	67
SSB-2A	#26	#N/A	0.003	209	0.73	281	40.5	12.14	2.1	0.11379	2.7	1.3086	3.4	0.08274	2.0	0.60	1850	93	512	20	846	93	28	61
SSB-2A	#13	#N/A	0.005	401	0.85	325	37.6	10.73	4.5	0.11794	2.2	1.5316	5.0	0.09448	4.5	0.90	1921	78	582	49	939	143	30	62
SSB-2A	#23	#N/A	0.012	231	1.39	6734	7.1	2.98	1.3	0.14097	0.5	6.5252	1.4	0.33629	1.3	0.92	2238	19	1868	41	2048	51	83	91
SSB-2A	#19	#N/A	0.002	52	2.60	1582	37.1	3.29	1.5	0.17836	0.6	7.5055	1.6	0.30499	1.5	0.93	2636	19	1715	45	2172	53	65	79
SSB-2A	#66	#N/A	0.007	387	0.23	67	27.5	8.79	1.3	0.30766	1.8	4.8278	2.3	0.11383	1.3	0.58	3507	55	695	17	1788	91	20	39
SSB-10A - Iquiri Fm. - Devonian																								
SSB-10A	#22	#N/A	0.003	336	1.40	14830	14.8	15.87	0.8	0.05505	0.7	0.4759	1.3	0.06279	1.1	0.85	422	42	393	9	395	17	93	99
SSB-10A	#41	#N/A	0.001	110	2.38	3075	8.7	14.42	1.1	0.05673	0.9	0.5453	1.4	0.06936	1.1	0.76	479	41	432	9	442	20	90	98
SSB-10A	#39	#N/A	0.001	106	1.89	10382	2.6	12.85	1.4	0.05689	1.4	0.6062	2.0	0.07791	1.4	0.69	484	62	484	13	481	30	100	101
SSB-10A	#80	#N/A	0.003	316	1.91	40393	1.0	13.30	1.2	0.05713	0.8	0.5929	1.5	0.07521	1.2	0.83	495	35	467	11	473	21	94	99

SSB-10A	#74	#N/A	0.002	189	0.49	14785	2.4	13.12	1.2	0.05716	0.8	0.6014	1.5	0.07626	1.2	0.83	496	35	474	11	478	21	96	99
SSB-10A	#79	#N/A	0.002	172	1.55	20188	2.5	13.55	1.2	0.05723	0.7	0.5873	1.4	0.07387	1.2	0.89	499	28	459	11	469	20	92	98
SSB-10A	#25	#N/A	0.001	65	4.53	3644	9.8	13.37	1.8	0.05741	1.8	0.5897	2.6	0.07503	1.9	0.71	501	78	466	17	470	38	93	99
SSB-10A	#63	#N/A	0.002	166	2.99	17810	4.3	13.10	1.3	0.05766	0.8	0.6026	1.5	0.07639	1.2	0.83	515	36	475	11	479	22	92	99
SSB-10A	#59	#N/A	0.003	247	2.24	16025	18.1	14.29	1.2	0.05776	0.8	0.5578	1.4	0.07001	1.1	0.82	519	34	436	9	450	19	84	97
SSB-10A	#24	#N/A	0.003	254	1.28	15405	8.8	11.41	1.1	0.05819	1.0	0.6997	1.5		1.1	0.72	535	44	542	11	539	24	101	101
SSB-10A	#12	#N/A	0.002	157	0.87	12549	5.4	11.48	1.1	0.05820	0.8	0.7001	1.3	0.08718	1.1	0.81	535	34	539	11	539	21	101	100
SSB-10A	#57	#N/A	0.002	187	1.50	36602	3.0	11.73	1.1	0.05821	0.8	0.6866	1.4	0.08531	1.1	0.81	536	34	528	11	531	22	98	99
SSB-10A	#71	#N/A	0.003	304	2.52	7609	15.0	12.89	1.1	0.05824	0.7	0.6232	1.3	0.07762	1.1	0.85	537	28	482	10	492	19	90	98
SSB-10A	#13	#N/A	0.003	176	1.68	12816	5.8	11.51	1.1	0.05827	0.9	0.7001	1.4	0.08689	1.1	0.75	538	39	537	11	539	23	100	100
SSB-10A	#05	#N/A	0.002	165	1.03	6354	11.3	11.50	1.1	0.05827	0.8	0.6972	1.4	0.08699	1.1	0.81	538	35	538	11	537	22	100	100
SSB-10A	#10	#N/A	0.003	210	1.08	53690	1.6	11.17	1.1	0.05841	0.8	0.7217	1.3	0.08952	1.1	0.82	543	33	553	11	552	22	102	100
SSB-10A	#50	#N/A	0.005	336	2.04	23781	4.2	11.40	1.0	0.05844	0.7	0.7094	1.2	0.08776	1.0	0.82	545	30	542	10	544	20	100	100
SSB-10A	#19	#N/A	0.001	86	1.06	8049	2.8	11.46	1.5	0.05853	1.4	0.7034	2.0	0.08737	1.4	0.71	545	60	540	14	541	32	99	100
SSB-10A	#09	#N/A	0.002	157	1.24	8055	7.5	11.32	1.1	0.05846	0.8	0.7115	1.4	0.08837	1.1	0.81	545	35	546	11	546	22	100	100
SSB-10A	#48	#N/A	0.003	191	2.11	11519	7.1	11.41	1.0	0.05850	0.8	0.7045	1.3	0.08765	1.0	0.79	547	35	542	11	541	21	99	100
SSB-10A	#26	#N/A	0.004	277	1.13	22331	4.4	11.37	1.0	0.05855	1.2	0.7029	1.6	0.08798	1.0	0.66	549	51	544	10	540	25	99	101
SSB-10A	#23	#N/A	0.003	345	1.28	5205	59.9	15.94	1.3	0.05874	3.1	0.5032	3.3	0.06274	1.3	0.38	550	126	392	9	414	43	71	95
SSB-10A	#76	#N/A	0.002	172	2.04	13715	6.8	11.63	1.2	0.05860	0.8	0.6968	1.5	0.08605	1.2	0.82	550	36	532	12	537	23	97	99
SSB-10A	#20	#N/A	0.001	53	2.45	7618	1.8	11.17	2.1	0.05885	2.0	0.7227	2.9	0.08984	2.1	0.73	555	85	555	22	552	48	100	100
SSB-10A	#08	#N/A	0.003	213	2.13	20730	6.3	11.17	1.0	0.05878	0.9	0.7210	1.4	0.08950	1.0	0.74	557	40	553	11	551	23	99	100
SSB-10A	#58	#N/A	0.002	186	2.10	32603	2.9	11.55	1.1	0.05897	0.8	0.6999	1.4	0.08658	1.1	0.78	564	36	535	11	539	22	95	99
SSB-10A	#42	#N/A	0.003	238	3.12	9747	2.0	14.34	1.2	0.05921	0.8	0.5680	1.5	0.06977	1.2	0.83	573	34	435	10	457	21	76	95
SSB-10A	#27	#N/A	0.001	100	1.64	16776	3.0	11.58	1.3	0.05951	1.1	0.7088	1.7	0.08642	1.3	0.77	583	45	534	13	544	27	92	98
SSB-10A	#21	#N/A	0.002	147	2.25	27899	4.5	11.47	1.1	0.05967	1.0	0.7098	1.5	0.08718	1.1	0.76	589	41	539	11	548	30	91	98
SSB-10A	#11	#N/A	0.001	76	0.88	2159	7.2	11.37	2.2	0.06050	1.9	0.7248	2.9	0.08801	2.2	0.76	620	79	544	22	553	47	88	98
SSB-10A	#38	#N/A	0.002	133	1.98	5798	9.1	11.94	1.2	0.06067	0.9	0.6948	1.5	0.08373	1.2	0.79	626	38	518	11	536	24	83	97
SSB-10A	#66	#N/A	0.005	340	1.28	1158077	0.0	9.91	1.0	0.06101	0.6	0.8484	1.2	0.10090	1.1	0.85	638	27	620	12	624	22	97	99
SSB-10A	#28	#N/A	0.002	175	0.60	11397	13.1	11.51	1.6	0.06150	2.8	0.7297	3.2	0.08698	1.6	0.50	651	113	538	16	556	53	83	97
SSB-10A	#33	#N/A	0.001	76	4.60	8338	6.6	9.48	1.2	0.06141	1.1	0.8934	1.6	0.10557	1.2	0.73	651	46	647	14	648	29	99	100
SSB-10A	#61	#N/A	0.002	113	1.76	15041	2.9	9.65	1.2	0.06158	0.9	0.8768	1.5	0.10369	1.2	0.81	658	36	636	14	639	27	97	99
SSB-10A	#54	#N/A	0.004	244	0.10	125185	0.8	9.69	1.7	0.06265	1.0	0.8960	2.0	0.10355	1.8	0.87	694	44	635	21	649	37	92	98
SSB-10A	#65	#N/A	0.003	214	2.26	3259	9.4	11.82	1.2	0.06319	1.1	0.7333	1.7	0.08464	1.2	0.72	712	47	524	12	558	27	74	94
SSB-10A	#53	#N/A	0.006	233	1.55	34472	5.4	6.03	1.0	0.07192	0.6	1.6525	1.1	0.16591	1.0	0.87	983	22	990	17	991	27	101	100

SSB-10A	#06	#N/A	0.007	258	1.16	161398	3.6	5.76	1.0	0.07367	0.8	1.7489	1.3	0.17351	1.0	0.78	1031	33	1031	19	1027	33	100	100
SSB-10A	#51	#N/A	0.006	229	2.73	38006	5.8	5.85	1.2	0.07391	0.7	1.7264	1.4	0.17093	1.2	0.85	1038	29	1017	22	1018	35	98	100
SSB-10A	#37	#N/A	0.009	335	3.50	19323	1.9	5.78	1.0	0.07402	0.7	1.7554	1.2	0.17312	1.0	0.82	1041	28	1029	19	1029	31	99	100
SSB-10A	#75	#N/A	0.009	402	1.35	12804	1.9	6.52	1.1	0.07419	0.7	1.5681	1.2	0.15341	1.0	0.83	1046	28	920	17	958	30	88	96
SSB-10A	#78	#N/A	0.003	108	1.07	30928	2.5	5.79	1.1	0.07472	0.8	1.7658	1.3	0.17284	1.1	0.80	1060	32	1028	20	1033	34	97	100
SSB-10A	#34	#N/A	0.002	89	1.80	10484	11.3	5.58	1.1	0.07496	0.7	1.8497	1.3	0.17915	1.1	0.85	1066	28	1062	22	1063	34	100	100
SSB-10A	#55	#N/A	0.002	79	1.30	191603	0.3	5.79	1.3	0.07569	0.7	1.8058	1.4	0.17294	1.3	0.88	1086	27	1028	24	1047	36	95	98
SSB-10A	#60	#N/A	0.002	66	4.56	9270	7.0	5.36	1.1	0.07677	0.9	1.9670	1.4	0.18674	1.1	0.78	1114	34	1104	22	1104	36	99	100
SSB-10A	#07	#N/A	0.003	93	2.95	48154	4.4	4.94	1.1	0.07770	0.7	2.1652	1.3	0.20260	1.1	0.84	1138	27	1189	23	1170	34	105	102
SSB-10A	#62	#N/A	0.007	148	3.08	34591	3.4	3.03	1.0	0.11566	0.6	5.2168	1.2	0.33036	1.0	0.84	1889	23	1840	31	1855	39	97	99
SSB-10A	#47	#N/A	0.010	199	0.83	35414	7.7	3.03	1.0	0.12563	0.6	5.6738	1.2	0.33012	1.0	0.85	2037	22	1839	32	1927	40	90	95
SSB-10A	#72	#N/A	0.013	242	0.55	16269	9.4	2.89	1.0	0.13262	0.6	6.3566	1.2	0.34642	1.0	0.87	2132	20	1917	34	2026	41	90	95
SSB-10A	#49	#N/A	0.001	106	3.37	1127	35.4	20.80	2.7	0.06313	2.0	0.4226	3.2	0.04848	2.5	0.78	704	83	305	15	357	37	43	85
SSB-10A	#40	#N/A	0.004	343	1.34	3411	10.8	14.44	2.5	0.06433	0.8	0.6176	2.6	0.06986	2.4	0.95	751	33	435	20	488	38	58	89
SSB-10A	#56	#N/A	0.008	781	0.96	2011	37.8	14.03	1.2	0.06495	1.2	0.6355	1.8	0.07133	1.2	0.70	770	52	444	10	499	26	58	89
SSB-10A	#73	#N/A	0.001	118	1.44	1498	10.2	11.73	1.4	0.06831	2.5	0.8043	2.8	0.08538	1.4	0.48	865	103	528	14	598	48	61	88
SSB-10A	#77	#N/A	0.006	565	1.13	1050	7.0	12.43	1.4	0.07398	1.4	0.8184	2.0	0.08048	1.4	0.69	1039	57	499	13	607	35	48	82
SSB-10A	#36	#N/A	0.000	38	2.58	529	16.9	17.90	3.5	0.07463	4.4	0.5781	5.4	0.05626	3.2	0.59	1042	166	353	22	463	79	34	76
SSB-10A	#52	#N/A	0.005	258	2.73	2976	12.4	7.74	1.3	0.07731	1.3	1.3837	1.9	0.12930	1.3	0.71	1127	51	784	19	882	43	70	89
SSB-10A	#64	#N/A	0.001	133	1.36	299	80.6	19.95	2.3	0.09368	2.0	0.6455	3.0	0.05036	2.3	0.76	1496	74	317	14	506	47	21	63
SSB-10A	#14	#N/A	0.002	183	1.02	317	20.2	14.11	1.0	0.10707	1.0	1.0465	1.4	0.07090	1.0	0.73	1749	35	442	9	727	29	25	61
SSB-10A	#35	#N/A	0.009	302	0.82	17815	6.8	4.92	1.2	0.11607	0.5	3.2398	1.3	0.20342	1.2	0.91	1896	19	1194	25	1467	39	63	81
SSB-4A - Iquiri Fm. - Devonian																								
SSB-4A_Comp	#13	#N/A	0.001	349	0.95	6467	2.8	13.36	0.7	0.05711	1.0	0.5930	1.2	0.07575	0.7	0.60	511	39	470	7	473	7	92	100
SSB-4A	#80	#N/A	0.001	434	1.90	4079	2.1	11.39	0.9	0.05840	1.1	0.7124	1.5	0.08815	1.0	0.68	543	47	544	10	546	11	100	100
SSB-4A	#63	#N/A	0.001	329	1.32	18185	1.3	13.47	1.5	0.05784	1.6	0.5954	2.2	0.07511	1.4	0.66	561	57	466	13	474	13	83	98
SSB-4A_Comp	#77	#N/A	0.001	392	0.37	10008	2.3	12.06	1.0	0.05931	1.3	0.6801	1.7	0.08329	1.1	0.65	568	54	516	11	526	13	91	98
SSB-4A	#78	#N/A	0.001	325	1.15	23088	0.7	11.53	1.3	0.05886	1.4	0.7086	2.0	0.08764	1.3	0.69	570	60	543	13	543	12	95	100
SSB-4A	#91	#N/A	0.001	268	0.12	31237	0.4	13.76	1.2	0.05805	1.4	0.5866	1.9	0.07422	1.3	0.66	581	54	461	11	468	11	79	98
SSB-4A	#33	#N/A	0.001	226	0.74	9122	1.8	13.78	1.5	0.05682	1.6	0.5805	2.2	0.07483	1.5	0.66	582	61	464	13	465	11	80	100
SSB-4A	#29	#N/A	0.001	249	0.48	66060	0.3	11.80	1.7	0.05972	2.1	0.6971	2.6	0.08735	1.5	0.60	587	58	539	16	536	14	92	101
SSB-4A	#25	#N/A	0.001	295	0.38	11557	2.1	13.47	1.4	0.05711	1.6	0.5900	2.1	0.07597	1.4	0.66	589	57	471	12	471	11	80	100
SSB-4A	#34	#N/A	0.001	232	0.96	17955	0.8	12.77	1.4	0.05766	1.5	0.6316	2.0	0.08034	1.3	0.64	590	52	498	12	498	11	84	100
SSB-4A_Comp	#34	#N/A	0.001	267	0.21	5310	2.1	13.07	1.3	0.05829	1.6	0.6130	2.1	0.07798	1.3	0.65	592	58	484	12	485	12	82	100

SSB-4A_Comp	#42	#N/A	0.001	251	1.37	7772	2.1	11.35	1.1	0.05959	1.4	0.7284	1.8	0.08919	1.2	0.65	594	52	552	13	556	12	93	99
SSB-4A_Comp	#14	#N/A	0.001	223	1.27	3353	7.0	11.76	1.1	0.05915	1.3	0.7000	1.7	0.08697	1.0	0.61	596	48	537	10	538	11	90	100
SSB-4A	#9	#N/A	0.001	418	0.16	172909	0.1	10.02	0.9	0.06015	1.0	0.8374	1.3	0.10017	0.8	0.64	600	41	615	10	617	10	103	100
SSB-4A_Comp	#58	#N/A	0.001	306	0.67	3080	3.4	12.92	0.9	0.06040	1.0	0.6538	1.3	0.07876	0.9	0.66	607	41	488	8	510	10	80	96
SSB-4A	#11	#N/A	0.001	250	0.70	17075	0.8	10.60	1.1	0.06006	1.3	0.7915	1.7	0.09582	1.1	0.66	617	50	590	12	592	12	96	100
SSB-4A_Comp	#63	#N/A	0.001	200	1.46	26652	0.5	12.61	1.4	0.05851	1.4	0.6503	1.9	0.08196	1.3	0.66	622	52	507	12	508	11	81	100
SSB-4A_Comp	#43	#N/A	0.001	205	0.94	14027	0.8	13.18	1.4	0.05972	1.6	0.6280	2.0	0.07854	1.3	0.64	646	59	487	12	495	11	75	98
SSB-4A	#44	#N/A	0.002	522	1.28	87743	0.5	8.72	0.8	0.06141	0.9	0.9773	1.2	0.11490	0.8	0.64	648	39	701	10	692	10	108	101
SSB-4A_Comp	#12	#N/A	0.001	181	0.95	19008	0.6	11.38	1.2	0.06091	1.4	0.7487	1.8	0.09059	1.2	0.65	650	52	559	12	566	13	86	99
SSB-4A_Comp	#59	#N/A	0.001	503	0.21	2150	8.5	14.83	0.9	0.06144	1.1	0.5737	1.4	0.06814	0.9	0.63	653	44	425	7	461	9	65	92
SSB-4A	#66	#N/A	0.001	206	0.80	7201	1.8	10.37	1.2	0.06106	1.5	0.8136	2.0	0.09815	1.2	0.64	660	56	603	14	604	14	91	100
SSB-4A_Comp	#41	#N/A	0.001	258	1.12	24474	0.6	12.24	1.1	0.06146	1.4	0.6997	1.7	0.08315	1.1	0.62	661	53	516	10	538	13	78	96
SSB-4A	#16	#N/A	0.000	166	3.10	4584	2.4	13.26	1.8	0.05824	1.8	0.6206	2.5	0.07897	1.7	0.68	666	68	489	16	489	14	73	100
SSB-4A_Comp	#45	#N/A	0.001	210	0.98	20459	0.8	12.89	1.5	0.05993	1.6	0.6492	2.2	0.08088	1.5	0.66	668	59	501	14	508	11	75	99
SSB-4A	#45	#N/A	0.001	337	1.04	284778	0.1	8.87	0.9	0.06258	1.0	0.9788	1.4	0.11346	0.9	0.66	677	43	693	12	693	11	102	100
SSB-4A_Comp	#57	#N/A	0.000	155	0.15	8162	1.3	14.54	2.7	0.06300	2.9	0.6030	3.4	0.07579	1.7	0.51	682	70	470	15	478	12	69	98
SSB-4A	#15	#N/A	0.000	178	1.23	3510	2.5	13.75	1.7	0.05964	1.9	0.6033	2.5	0.07575	1.6	0.65	683	70	470	15	478	13	69	98
SSB-4A_Comp	#48	#N/A	0.000	168	0.72	2271	5.4	13.35	2.0	0.06045	2.2	0.6278	2.8	0.07941	1.7	0.60	685	78	492	15	495	13	72	99
SSB-4A	#58	#N/A	0.000	180	1.72	5689	2.5	11.91	2.1	0.05964	2.5	0.6874	3.3	0.08620	2.1	0.64	694	94	532	21	530	18	77	100
SSB-4A	#13	#N/A	0.000	174	0.20	7423	1.5	13.05	1.7	0.05860	2.0	0.6222	2.7	0.07933	1.7	0.65	696	74	491	16	491	14	71	100
SSB-4A	#12	#N/A	0.001	174	1.42	19040	0.7	9.43	1.4	0.06205	1.5	0.9184	2.0	0.10922	1.3	0.65	705	54	667	16	661	14	95	101
SSB-4A	#61	#N/A	0.000	162	0.64	4015	3.2	13.81	2.3	0.06020	2.4	0.6140	3.1	0.07684	2.0	0.64	712	77	478	18	485	15	67	99
SSB-4A_Comp	#75	#N/A	0.000	155	1.72	15086	1.1	13.52	2.1	0.05990	2.0	0.6243	2.7	0.07940	1.7	0.65	721	71	491	16	492	12	68	100
SSB-4A	#92	#N/A	0.001	324	0.06	18868	0.9	12.12	1.8	0.06452	1.8	0.7448	2.5	0.08461	1.7	0.68	739	71	523	17	561	35	71	93
SSB-4A_Comp	#92	#N/A	0.001	251	1.31	2004	9.1	10.07	1.3	0.06523	1.4	0.8993	1.9	0.10094	1.3	0.69	756	55	619	15	651	14	82	95
SSB-4A	#60	#N/A	0.000	163	0.98	46106	0.3	11.22	2.7	0.06455	2.9	0.8013	3.8	0.09332	2.4	0.65	757	103	579	28	596	24	76	97
SSB-4A_Comp	#9	#N/A	0.001	153	1.89	17762	0.9	10.52	1.6	0.06430	1.9	0.8475	2.4	0.09857	1.5	0.62	761	67	605	17	622	16	80	97
SSB-4A_Comp	#33	#N/A	0.002	410	1.68	2710	4.3	10.40	0.7	0.06517	1.0	0.8764	1.2	0.09642	0.7	0.56	768	42	593	8	639	13	77	93
SSB-4A	#65	#N/A	0.000	132	0.61	2226	3.6	10.64	2.8	0.06650	3.4	0.8569	4.2	0.09945	2.5	0.59	786	110	610	28	625	31	78	98
SSB-4A_Comp	#90	#N/A	0.000	127	0.34	6711	1.7	13.49	2.0	0.06188	2.4	0.6283	3.0	0.07948	1.8	0.61	788	78	493	17	494	14	63	100
SSB-4A	#74	#N/A	0.000	169	0.52	57894	0.2	13.15	2.0	0.05973	2.3	0.6286	3.0	0.08048	1.9	0.63	789	89	498	18	495	15	63	101
SSB-4A_Comp	#95	#N/A	0.001	192	1.20	36232	0.3	7.73	0.9	0.06607	1.1	1.1926	1.4	0.13107	0.9	0.65	797	46	793	14	796	12	100	100
SSB-4A_Comp	#50	#N/A	0.000	150	0.37	7120	2.1	14.85	3.6	0.06332	3.6	0.5934	4.2	0.07583	2.2	0.53	822	99	469	20	474	13	57	99
SSB-4A_Comp	#89	#N/A	0.000	121	0.39	11270	0.9	13.87	2.7	0.06375	2.6	0.6474	3.4	0.07909	2.1	0.63	825	88	489	20	506	16	59	97

SSB-4A	#75	#N/A	0.000	125	0.89	12965	0.8	13.40	4.6	0.06465	4.7	0.6739	5.3	0.08422	2.3	0.44	838	93	521	23	522	18	62	100
SSB-4A	#57	#N/A	0.000	118	0.66	3269	3.1	14.79	3.1	0.06461	3.1	0.6186	4.0	0.07750	2.6	0.64	895	101	479	23	487	21	54	98
SSB-4A_Comp	#74	#N/A	0.000	104	3.03	5259	2.1	13.71	8.7	0.06927	9.3	0.7084	9.5	0.08716	2.3	0.24	909	93	536	23	542	14	59	99
SSB-4A	#50	#N/A	0.000	115	1.51	20674	0.5	13.49	3.1	0.06340	3.5	0.6523	4.3	0.08334	2.4	0.56	914	97	514	23	508	18	56	101
SSB-4A	#76	#N/A	0.000	137	0.41	7949	1.6	13.85	2.7	0.06212	2.9	0.6152	3.7	0.07886	2.3	0.61	922	105	487	21	485	16	53	100
SSB-4A_Comp	#93	#N/A	0.000	79	1.61	3476	2.8	8.34	2.2	0.07110	2.5	1.1774	3.1	0.13029	1.8	0.59	925	76	786	27	789	17	85	100
SSB-4A_Comp	#47	#N/A	0.000	112	1.35	71272	0.1	15.33	3.3	0.06692	3.9	0.5935	4.6	0.07615	2.4	0.53	927	109	471	22	472	15	51	100
SSB-4A_Comp	#49	#N/A	0.000	106	1.38	38059	0.3	11.25	2.4	0.07052	2.4	0.8803	3.0	0.09895	1.9	0.63	946	75	606	22	640	16	64	95
SSB-4A	#59	#N/A	0.001	224	0.54	96040	0.3	7.37	1.7	0.07157	1.5	1.3517	2.2	0.13844	1.6	0.73	948	63	835	25	866	27	88	96
SSB-4A	#14	#N/A	0.000	98	3.37	11926	0.9	12.00	5.0	0.06751	6.1	0.7881	6.5	0.09614	2.3	0.36	984	94	591	26	590	18	60	100
SSB-4A_Comp	#98	#N/A	0.001	226	3.09	4924	3.1	7.94	1.1	0.07249	1.1	1.2718	1.6	0.12781	1.1	0.71	985	45	775	16	831	21	79	93
SSB-4A	#98	#N/A	0.001	227	0.24	29383	1.0	6.23	1.0	0.07280	1.1	1.6265	1.5	0.16178	1.0	0.66	986	44	966	17	979	15	98	99
SSB-4A	#64	#N/A	0.001	154	1.01	9415	1.2	6.31	1.3	0.07257	1.4	1.6135	1.9	0.16152	1.3	0.67	1000	59	964	23	974	18	96	99
SSB-4A_Comp	#91	#N/A	0.000	68	3.17	11786	0.8	10.39	5.3	0.06662	5.6	0.8945	6.2	0.10866	2.4	0.40	1008	117	664	30	646	21	66	103
SSB-4A	#28	#N/A	0.002	357	0.16	20149	1.7	6.00	0.8	0.07302	0.9	1.7001	1.2	0.16675	0.8	0.65	1010	35	995	14	1008	13	98	99
SSB-4A_Comp	#25	#N/A	0.001	170	0.62	27160	0.8	6.39	1.0	0.07364	1.1	1.5996	1.5	0.15901	0.9	0.64	1014	39	950	16	970	13	94	98
SSB-4A	#93	#N/A	0.001	217	0.18	22584	1.0	5.90	0.9	0.07356	1.0	1.7306	1.4	0.17067	0.9	0.65	1016	41	1015	16	1019	15	100	100
SSB-4A_Comp	#11	#N/A	0.001	187	1.55	7145	3.1	5.97	0.6	0.07377	0.9	1.7176	1.1	0.16888	0.6	0.57	1016	35	1006	12	1015	13	99	99
SSB-4A	#43	#N/A	0.001	120	1.24	99860	0.1	6.02	3.9	0.07714	3.9	1.7549	4.1	0.17498	1.4	0.33	1019	59	1038	26	1028	19	102	101
SSB-4A	#48	#N/A	0.001	130	2.16	8765	1.6	6.01	1.2	0.07411	1.3	1.7145	1.8	0.16945	1.2	0.67	1019	54	1009	22	1013	16	99	100
SSB-4A	#96	#N/A	0.001	118	0.72	21242	0.8	6.35	1.4	0.07413	1.5	1.6266	2.1	0.16167	1.4	0.69	1020	61	964	25	980	18	94	98
SSB-4A	#41	#N/A	0.001	179	1.68	20345	0.8	5.78	1.0	0.07452	1.1	1.7828	1.5	0.17466	1.0	0.66	1033	43	1037	18	1038	15	100	100
SSB-4A	#95	#N/A	0.001	141	0.82	119284	0.1	6.01	1.2	0.07445	1.3	1.7323	1.7	0.16937	1.2	0.69	1034	51	1007	22	1020	16	97	99
SSB-4A	#31	#N/A	0.001	107	0.56	29038	0.4	6.14	1.6	0.07507	1.6	1.7253	2.2	0.16651	1.6	0.69	1035	62	997	28	1018	20	96	98
SSB-4A	#18	#N/A	0.001	187	0.45	500656	0.0	5.68	1.0	0.07406	1.1	1.8228	1.5	0.17724	0.9	0.64	1035	44	1051	18	1054	16	102	100
SSB-4A_Comp	#73	#N/A	0.004	668	0.56	27511	3.2	5.64	0.3	0.07391	0.6	1.8166	0.7	0.17739	0.3	0.45	1038	24	1053	6	1052	11	101	100
SSB-4A_Comp	#76	#N/A	0.001	97	0.96	3466	3.7	6.40	2.7	0.07555	2.3	1.6619	3.4	0.16627	2.6	0.75	1039	87	986	46	990	33	95	100
SSB-4A_Comp	#66	#N/A	0.001	100	0.59	12749	0.9	6.05	1.2	0.07560	1.4	1.7473	1.9	0.16988	1.2	0.64	1049	56	1009	22	1025	16	96	98
SSB-4A	#82	#N/A	0.000	71	0.75	4112	2.5	6.57	2.6	0.07755	2.7	1.6420	3.3	0.16799	1.9	0.57	1050	77	996	34	984	22	95	101
SSB-4A_Comp	#80	#N/A	0.002	314	0.51	63940	0.3	5.50	0.4	0.07482	0.8	1.8782	0.9	0.18208	0.4	0.49	1062	28	1078	8	1073	14	102	100
SSB-4A_Comp	#94	#N/A	0.001	85	0.91	22807	0.6	5.86	1.3	0.07673	1.5	1.8132	2.0	0.17602	1.3	0.65	1068	58	1042	24	1050	17	98	99
SSB-4A_Comp	#60	#N/A	0.000	81	0.45	11191	1.0	9.68	4.8	0.07980	5.6	1.1284	6.3	0.12003	2.8	0.45	1072	117	726	38	764	24	68	95
SSB-4A_Comp	#61	#N/A	0.001	170	1.18	12939	1.5	5.78	0.7	0.07550	0.9	1.8188	1.2	0.17466	0.7	0.64	1074	37	1038	14	1052	14	97	99
SSB-4A	#62	#N/A	0.000	108	0.56	4230	2.5	19.67	11.0	0.07715	7.3	0.6076	8.0	0.07739	3.3	0.42	1097	151	477	30	480	20	43	99

SSB-4A_Comp	#44	#N/A	0.002	313	0.71	24553	1.2	5.30	0.4	0.07649	0.7	2.0060	0.8	0.18896	0.4	0.50	1103	26	1115	8	1117	11	101	100
SSB-4A_Comp	#79	#N/A	0.000	59	0.98	5925	1.9	5.90	2.5	0.07927	2.8	1.8473	3.6	0.18356	2.2	0.62	1106	91	1084	43	1061	21	98	102
SSB-4A_Comp	#65	#N/A	0.001	130	1.02	8494	1.6	5.76	0.9	0.07755	1.1	1.8749	1.4	0.17562	0.9	0.61	1114	45	1044	17	1072	16	94	97
SSB-4A	#10	#N/A	0.001	202	0.89	17733	0.9	5.34	0.9	0.07747	1.0	2.0236	1.3	0.18877	0.9	0.66	1120	39	1114	17	1123	15	99	99
SSB-4A	#49	#N/A	0.001	102	0.92	12081	1.1	6.02	2.2	0.07831	2.3	1.7804	3.4	0.17050	2.4	0.72	1126	94	1011	44	1036	26	90	98
SSB-4A	#79	#N/A	0.000	74	1.55	167306	0.1	6.82	2.6	0.07907	2.7	1.6133	3.5	0.16141	2.2	0.62	1130	90	958	38	973	21	85	98
SSB-4A	#42	#N/A	0.001	92	1.02	4483	2.3	5.10	1.3	0.07922	1.4	2.1485	1.9	0.20058	1.2	0.65	1138	55	1178	26	1163	18	103	101
SSB-4A_Comp	#97	#N/A	0.001	134	0.64	115374	0.1	5.22	0.8	0.07844	0.9	2.0993	1.2	0.19322	0.8	0.65	1148	37	1137	16	1148	14	99	99
SSB-4A	#77	#N/A	0.000	93	0.76	4925	2.2	14.33	7.9	0.06660	7.2	0.6820	7.9	0.08705	3.2	0.41	1159	150	534	33	526	20	46	102
SSB-4A_Comp	#10	#N/A	0.000	71	1.10	5296	2.0	14.66	5.8	0.07257	6.0	0.6894	6.8	0.08567	3.2	0.47	1160	137	528	31	530	20	45	100
SSB-4A	#94	#N/A	0.000	106	1.22	4130	2.4	12.75	3.1	0.07725	3.4	0.8372	4.1	0.09138	2.4	0.58	1163	99	561	25	614	23	48	91
SSB-4A_Comp	#26	#N/A	0.000	50	0.97	3434	2.9	7.10	3.2	0.08277	3.2	1.6355	3.9	0.16309	2.3	0.58	1183	99	965	40	981	21	82	98
SSB-4A	#90	#N/A	0.001	116	1.76	6856	1.7	6.04	1.5	0.08061	1.7	1.8381	2.3	0.16918	1.5	0.68	1185	61	1006	28	1057	23	85	95
SSB-4A_Comp	#28	#N/A	0.000	43	0.89	3975	3.0	6.84	4.2	0.08589	4.2	1.7592	4.9	0.17539	2.6	0.53	1231	112	1030	49	1027	27	84	100
SSB-4A_Comp	#32	#N/A	0.000	71	2.17	772	10.4	15.56	9.3	0.09486	9.4	0.7889	10.0	0.08753	3.4	0.34	1279	133	535	34	583	31	42	92
SSB-4A_Comp	#82	#N/A	0.000	44	2.67	2510	4.0	8.79	8.7	0.08189	8.6	1.2916	9.9	0.14336	5.0	0.50	1347	202	849	78	837	36	63	101
SSB-4A_Comp	#64	#N/A	0.001	115	0.81	14013	1.4	4.08	1.2	0.08882	1.5	2.9924	1.9	0.24594	1.3	0.65	1385	51	1416	31	1405	19	102	101
SSB-4A_Comp	#78	#N/A	0.001	86	3.18	9426	1.3	3.41	1.3	0.10860	1.4	4.4387	1.9	0.29887	1.3	0.65	1751	51	1683	36	1718	22	96	98
SSB-4A_Comp	#81	#N/A	0.002	161	1.25	144484	0.1	2.86	0.5	0.11506	0.7	5.5663	0.9	0.34995	0.5	0.55	1878	25	1936	16	1911	16	103	101
SSB-4A	#97	#N/A	0.000	47	1.11	28616	0.4	3.04	1.8	0.12809	1.8	5.9472	2.5	0.34637	1.8	0.71	2015	57	1910	56	1961	37	95	97
SSB-4A	#89	#N/A	0.001	119	1.22	22685	1.3	2.81	0.9	0.12906	1.0	6.3668	1.3	0.35694	0.9	0.66	2078	33	1968	29	2027	19	95	97
SSB-4A	#47	#N/A	0.004	379	0.73	22181	4.0	2.76	0.8	0.13082	0.8	6.5224	1.1	0.36257	0.7	0.66	2107	29	1996	26	2048	19	95	97
SSB-4A_Comp	#31	#N/A	0.002	145	1.13	37395	1.0	2.43	0.5	0.13599	0.7	7.7427	0.9	0.41239	0.5	0.59	2172	24	2227	20	2201	16	103	101
SSB-4A_Comp	#30	#N/A	0.001	102	1.16	14185	1.9	2.46	0.6	0.13678	0.8	7.7005	0.9	0.40764	0.6	0.60	2180	26	2202	21	2196	16	101	100
SSB-4A	#32	#N/A	0.000	17	2.36	4443	2.7	1.83	5.6	0.20174	5.0	15.8215	5.8	0.60717	3.0	0.51	2742	85	3027	146	2842	66	110	107
SSB-4A	#27	#N/A	0.000	171	1.15	7213	1.4	24.79	4.4	0.05924	4.4	0.3351	5.2	0.04771	2.8	0.53	879	115	299	16	293	13	34	102
SSB-4A_Comp	#17	#N/A	0.001	272	0.71	3041	4.0	10.00	0.8	0.07199	1.1	0.9930	1.3	0.10106	0.8	0.59	965	42	620	9	700	12	64	89
SSB-4A	#26	#N/A	0.000	107	1.09	39363	0.2	27.05	17.6	0.06841	19.8	0.3338	20.2	0.05350	4.4	0.22	983	170	333	28	291	19	34	114
SSB-4A_Comp	#18	#N/A	0.000	85	1.30	29636	0.3	14.49	32.4	0.05980	34.4	0.6007	34.5	0.07698	2.9	0.08	1015	114	477	25	476	17	47	100
SSB-4A_Comp	#96	#N/A	0.002	483	1.05	1066	23.3	9.02	0.4	0.07951	0.7	1.2189	0.8	0.11122	0.4	0.51	1178	27	680	5	809	10	58	84
SSB-4A_Comp	#29	#N/A	0.006	1132	0.39	4949	24.2	6.95	0.2	0.08199	0.6	1.6243	0.6	0.14387	0.2	0.36	1243	23	866	4	980	11	70	88
SSB-4A_Comp	#62	#N/A	0.000	22	0.58	2838	3.6	5.36	22.9	0.03208	28.1	0.8588	30.4	0.10834	11.4	0.38	1358	283	638	152	616	71	47	104
SSB-4A	#17	#N/A	0.000	13	2.66	1234	6.9	1.64	107.8	0.02249	78.7	1.1377	83.9	0.10277	29.1	0.35	1376	380	412	366	729	136	30	57

SSB-4A	#73	#N/A	0.000	166	1.01	360	23.7	-1.97	-848.7	-0.00041	-1101.8	-0.0039	1105.0	0.00164	84.3	0.08	1402	405	11	18	-4	13	1	-287
SSB-4A	#81	#N/A	0.000	40	0.84	6603	1.7	9.83	31.6	0.06882	32.1	0.8450	33.4	0.10700	9.1	0.27	1437	303	645	114	613	53	45	105
SSB-4A_Comp	#16	#N/A	0.000	93	0.98	41	260.8	16.34	179.0	-0.00350	-304.9	0.0034	358.7	0.00106	189.0	0.53	1510	483	4	25	2	18	0	212
SSB-4A_Comp	#27	#N/A	0.000	19	16.72	1200	7.6	2.98	57.5	0.02082	53.4	0.7983	54.7	0.10273	11.7	0.21	1578	334	583	144	573	72	37	102
SSB-4A_Comp	#46	#N/A	0.007	1060	0.33	7071	2.6	4.79	0.6	0.10161	0.6	2.9436	0.8	0.20929	0.6	0.73	1652	21	1225	13	1392	24	74	88
SSB-4A_Comp	#15	#N/A	0.000	16	-20.47	971	9.2	7.65	50.2	0.04833	49.4	0.8984	50.8	0.10775	12.1	0.24	1879	343	557	151	612	77	30	91
SSB-4A	#30	#N/A	0.001	69	1.39	109569	0.1	3.38	1.6	0.12396	1.7	5.0970	2.4	0.30314	1.6	0.67	1987	61	1702	47	1834	25	86	93
SSB-4A	#46	#N/A	0.001	85	3.01	5161	3.0	3.21	1.1	0.14169	1.2	6.1474	1.6	0.31589	1.1	0.68	2232	39	1766	33	1995	23	79	89
SSB-5A - Itacua Fm. - Carboniferous																								
SSB-5A	#67	#N/A	0.006	661	2.27	57342	2.9	16.47	0.8	0.05382	0.6	0.4508	0.9	0.06070	0.8	0.80	362	25	380	5	378	11	105	101
SSB-5A	#94	#N/A	0.001	168	1.50	10100	6.7	17.18	1.0	0.05396	1.0	0.4338	1.4	0.05826	1.0	0.72	366	42	365	7	366	12	100	100
SSB-5A	#72	#N/A	0.001	58	3.10	58526	0.4	13.65	1.4	0.05585	1.3	0.5646	1.9	0.07342	1.4	0.72	442	58	457	12	455	14	103	100
SSB-5A	#49	#N/A	0.005	375	3.05	22866	9.0	12.53	0.7	0.05697	0.6	0.6280	0.9	0.07981	0.7	0.80	489	24	495	7	495	14	101	100
SSB-5A	#41	#N/A	0.004	304	1.89	59386	1.7	12.57	0.8	0.05717	0.6	0.6258	1.0	0.07960	0.8	0.80	497	27	494	8	493	13	99	100
SSB-5A	#115	#N/A	0.002	153	3.10	35587	1.7	11.65	1.0	0.05759	0.7	0.6869	1.3	0.08592	1.0	0.80	525	44	531	10	531	15	101	100
SSB-5A	#47	#N/A	0.002	158	2.44	18330	4.4	11.66	0.9	0.05813	0.8	0.6914	1.2	0.08581	0.9	0.74	533	34	531	9	534	16	100	99
SSB-5A	#109	#N/A	0.008	727	0.17	15439	25.2	11.72	0.9	0.05824	1.4	0.6816	1.7	0.08534	0.9	0.53	536	60	528	9	528	19	98	100
SSB-5A	#53	#N/A	0.001	79	1.38	34206	1.0	11.38	1.4	0.05796	1.2	0.7021	1.5	0.08736	1.0	0.63	542	36	540	10	540	17	100	100
SSB-5A	#51	#N/A	0.002	152	1.89	11240	14.1	11.55	0.9	0.05840	0.8	0.7000	1.2	0.08665	0.9	0.75	543	35	536	9	539	16	99	99
SSB-5A	#79	#N/A	0.003	228	2.66	16273	3.8	11.33	0.9	0.05838	0.6	0.7096	1.1	0.08832	0.9	0.82	543	26	546	9	545	15	101	100
SSB-5A	#23	#N/A	0.004	259	4.50	17795	3.4	11.60	0.8	0.05852	0.6	0.6957	1.0	0.08621	0.8	0.80	548	25	533	8	536	15	97	99
SSB-5A	#25	#N/A	0.002	133	1.23	17774	2.2	11.07	1.0	0.05866	0.8	0.7314	1.2	0.09036	0.9	0.77	553	32	558	10	557	14	101	100
SSB-5A	#34	#N/A	0.002	151	1.49	13660	13.3	11.11	1.0	0.05880	0.7	0.7303	1.2	0.09010	1.0	0.79	558	32	556	10	557	17	100	100
SSB-5A	#116	#N/A	0.002	151	0.99	17825	11.3	11.28	1.0	0.05848	0.9	0.7150	1.3	0.08870	1.0	0.72	561	52	548	10	548	18	98	100
SSB-5A	#48	#N/A	0.004	328	0.26	8760	18.9	11.78	1.0	0.05904	0.6	0.6944	1.2	0.08495	1.0	0.86	567	26	526	10	535	16	93	98
SSB-5A	#70	#N/A	0.001	48	1.72	3109	5.9	11.51	1.5	0.05919	1.8	0.7056	2.4	0.08697	1.5	0.63	569	81	538	15	542	26	94	99
SSB-5A	#55	#N/A	0.003	215	1.84	11501	4.5	12.44	1.4	0.05917	1.2	0.6612	1.8	0.08045	1.4	0.77	571	51	499	13	515	20	87	97
SSB-5A	#42	#N/A	0.006	416	0.14	39154	5.8	10.71	0.8	0.05927	0.6	0.7653	1.0	0.09339	0.8	0.79	576	26	576	8	577	17	100	100
SSB-5A	#33	#N/A	0.002	171	1.19	21370	2.9	11.51	0.8	0.05927	0.6	0.7102	1.0	0.08692	0.8	0.81	576	26	537	8	545	14	93	99
SSB-5A	#83	#N/A	0.001	108	2.53	12366	3.3	10.44	0.9	0.05959	0.7	0.7858	1.2	0.09584	0.9	0.78	587	32	590	10	589	17	101	100
SSB-5A	#69	#N/A	0.005	457	3.29	6299	8.8	12.87	1.2	0.05988	0.8	0.6404	1.4	0.07774	1.2	0.83	598	34	483	11	502	20	81	96
SSB-5A	#22	#N/A	0.003	164	3.34	11278	5.8	10.44	0.9	0.06052	0.6	0.7984	1.1	0.09579	0.9	0.83	621	25	590	10	596	16	95	99
SSB-5A	#20	#N/A	0.005	299	0.65	32582	3.6	10.55	0.9	0.06081	0.6	0.7945	1.1	0.09480	0.9	0.84	631	25	584	10	594	17	92	98

SSB-5A	#28	#N/A	0.001	58	2.19	5281	8.9	11.02	0.9	0.06133	1.3	0.7564	1.7	0.09032	1.1	0.65	645	55	557	12	572	19	86	97
SSB-5A	#40	#N/A	0.002	99	1.31	8256	7.3	9.51	1.0	0.06127	0.7	0.8888	1.2	0.10523	1.0	0.82	647	29	645	12	646	17	100	100
SSB-5A	#84	#N/A	0.005	345	0.10	23892	16.1	9.99	1.0	0.06193	0.6	0.8529	1.2	0.10021	1.0	0.87	671	24	616	12	626	21	92	98
SSB-5A	#114	#N/A	0.003	217	1.61	22873	5.8	9.67	0.8	0.06202	0.7	0.8785	1.1	0.10347	0.8	0.73	673	31	635	10	640	16	94	99
SSB-5A	#100	#N/A	0.001	72	1.13	11517	1.9	8.19	0.9	0.06310	0.7	1.0642	1.1	0.12221	0.9	0.78	710	30	743	12	736	19	105	101
SSB-5A	#74	#N/A	0.006	357	2.72	25811	4.5	8.33	0.7	0.06389	0.5	1.0565	0.9	0.11999	0.7	0.81	737	22	731	10	732	17	99	100
SSB-5A	#88	#N/A	0.003	238	0.44	3044	48.2	11.12	0.9	0.06554	1.2	0.8172	1.5	0.08995	0.9	0.60	789	49	555	9	606	25	70	92
SSB-5A	#99	#N/A	0.005	275	0.57	37382	8.2	7.29	0.9	0.07013	0.6	1.3246	1.1	0.13730	0.9	0.84	931	24	829	14	856	25	89	97
SSB-5A	#24	#N/A	0.002	87	1.79	4842	9.3	6.28	0.9	0.07114	0.8	1.5637	1.2	0.15944	0.9	0.78	960	30	954	16	956	25	99	100
SSB-5A	#111	#N/A	0.002	106	1.07	20158	4.2	7.27	1.9	0.07190	1.1	1.3663	2.2	0.13803	1.9	0.86	980	46	833	30	873	60	85	95
SSB-5A	#65	#N/A	0.009	336	0.75	27951	3.7	6.01	1.0	0.07227	0.8	1.6556	1.3	0.16649	1.0	0.76	992	33	993	18	991	39	100	100
SSB-5A	#81	#N/A	0.004	173	0.72	22920	1.7	6.46	0.9	0.07257	0.5	1.5462	1.0	0.15496	0.9	0.85	1001	21	929	15	949	23	93	98
SSB-5A	#54	#N/A	0.008	306	0.72	20686	6.5	5.74	0.9	0.07377	0.5	1.7783	1.0	0.17442	0.9	0.87	1034	21	1036	17	1037	24	100	100
SSB-5A	#27	#N/A	0.006	184	1.60	31504	10.4	5.74	1.0	0.07414	0.6	1.7823	1.0	0.17378	0.8	0.80	1044	23	1033	14	1039	23	99	99
SSB-5A	#68	#N/A	0.005	180	1.17	9962	9.3	5.67	0.9	0.07419	0.7	1.8018	1.1	0.17652	0.9	0.78	1045	28	1048	17	1046	22	100	100
SSB-5A	#26	#N/A	0.002	85	2.76	125408	1.1	5.97	1.2	0.07420	0.8	1.7024	1.4	0.16760	1.2	0.83	1046	31	999	21	1009	35	96	99
SSB-5A	#93	#N/A	0.011	422	1.22	74718	4.4	5.58	0.7	0.07445	0.6	1.8343	0.9	0.17921	0.7	0.80	1053	22	1063	14	1058	23	101	100
SSB-5A	#39	#N/A	0.013	515	1.40	22418	23.2	6.21	1.5	0.07491	0.5	1.6639	1.5	0.16132	1.4	0.95	1065	18	964	25	994	40	91	97
SSB-5A	#35	#N/A	0.002	84	1.83	17835	6.1	5.53	0.9	0.07567	0.7	1.8891	1.1	0.18087	0.9	0.80	1085	27	1072	18	1077	24	99	99
SSB-5A	#112	#N/A	0.003	139	0.86	2627	9.3	7.46	2.5	0.07709	1.2	1.4333	2.8	0.13478	2.5	0.90	1121	48	815	38	902	67	73	90
SSB-5A	#71	#N/A	0.006	194	2.28	41641	1.1	5.28	0.8	0.07905	0.5	2.0700	0.9	0.18931	0.8	0.84	1172	19	1118	15	1139	24	95	98
SSB-5A	#66	#N/A	0.007	223	2.90	25669	6.5	4.89	0.9	0.08027	0.6	2.2495	1.1	0.20439	0.9	0.83	1203	23	1199	19	1197	25	100	100
SSB-5A	#87	#N/A	0.005	184	1.70	2324	7.9	5.67	0.8	0.08099	0.7	1.9678	1.1	0.17650	0.8	0.75	1220	27	1048	15	1104	28	86	95
SSB-5A	#97	#N/A	0.015	531	0.08	279304	3.4	4.89	0.8	0.08115	0.5	2.2804	1.0	0.20464	0.8	0.84	1224	21	1200	18	1206	30	98	100
SSB-5A	#96	#N/A	0.009	293	3.01	53165	5.3	4.67	0.7	0.08189	0.6	2.4066	1.0	0.21406	0.7	0.78	1242	23	1250	17	1245	25	101	100
SSB-5A	#82	#N/A	0.004	115	3.62	31661	6.1	4.76	1.0	0.08289	0.7	2.4098	1.2	0.21036	1.0	0.82	1265	25	1231	21	1245	33	97	99
SSB-5A	#80	#N/A	0.002	59	0.05	13213	2.2	4.47	1.4	0.08677	1.0	2.6869	1.8	0.22408	1.4	0.81	1353	39	1303	33	1323	62	96	98
SSB-5A	#107	#N/A	0.023	438	1.97	16667	10.1	2.94	0.8	0.12156	0.5	5.7360	0.9	0.34002	0.8	0.84	1978	17	1887	24	1937	30	95	97
SSB-5A	#102	#N/A	0.009	188	3.61	20128	10.1	2.87	0.9	0.12234	0.5	5.8986	1.0	0.34866	0.9	0.88	1993	25	1928	29	1961	32	97	98
SSB-5A	#110	#N/A	0.011	214	2.21	91121	5.3	2.78	0.8	0.12477	0.5	6.2024	0.9	0.35987	0.7	0.83	2025	18	1982	25	2005	29	98	99
SSB-5A	#86	#N/A	0.002	43	1.24	9836	24.3	2.90	1.0	0.12712	0.9	6.0478	1.3	0.34450	1.0	0.73	2057	33	1908	32	1982	40	93	96
SSB-5A	#85	#N/A	0.009	194	2.28	60373	8.2	2.79	1.0	0.12949	1.9	6.3408	2.2	0.35841	1.0	0.47	2090	67	1975	34	2024	46	94	98
SSB-5A	#52	#N/A	0.010	158	1.97	76587	2.5	2.53	0.8	0.13670	0.5	7.4919	0.9	0.39476	0.8	0.82	2185	18	2145	28	2172	32	98	99
SSB-5A	#98	#N/A	0.004	48	0.89	23373	4.4	1.95	0.9	0.18370	0.6	13.0433	1.1	0.51419	0.9	0.81	2686	20	2674	37	2683	37	100	100

SSB-5A	#21	#N/A	0.010	120	3.48	46861	8.3	1.98	0.9	0.18446	0.9	12.7653	1.2	0.50528	0.9	0.70	2692	28	2636	36	2662	48	98	99
SSB-5A	#73	#N/A	0.011	102	1.67	53193	11.0	1.41	0.8	0.31296	0.5	30.7643	1.0	0.71143	0.9	0.86	3535	16	3464	45	3511	36	98	99
SSB-5A	#108	#N/A	0.001	63	1.45	3234	31.3	13.76	2.3	0.06698	2.5	0.6744	3.4	0.07336	2.4	0.69	822	98	456	20	523	30	56	87
SSB-5A	#113	#N/A	0.001	98	0.59	951	59.9	11.88	2.2	0.06748	1.9	0.7854	2.9	0.08457	2.2	0.76	847	78	523	22	588	20	62	89
SSB-5A	#101	#N/A	0.004	348	1.29	2337	30.4	10.52	1.8	0.07115	0.8	0.9300	2.0	0.09526	1.8	0.92	960	31	587	20	667	29	61	88
SSB-5A	#95	#N/A	0.001	80	2.73	4251	11.6	7.29	1.6	0.08116	0.9	1.5284	1.8	0.13738	1.6	0.86	1224	35	830	24	941	47	68	88
SSB-5A	#37	#N/A	0.004	208	0.30	4245	6.1	7.71	1.0	0.10976	0.5	1.9581	1.2	0.12976	1.0	0.89	1795	19	786	15	1101	31	44	71
SSB-5A	#50	#N/A	0.015	697	0.75	664	70.9	6.90	1.0	0.13525	1.1	2.7023	1.5	0.14502	1.0	0.70	2166	36	873	16	1329	30	40	66
SSB-5A	#38	#N/A	0.006	90	2.70	273	50.9	2.86	1.1	0.16176	0.7	7.8862	1.3	0.34982	1.1	0.86	2473	22	1934	37	2218	48	78	87
SSB-5A	#56	#N/A	0.013	198	1.15	81307	1.3	2.39	0.8	0.17029	0.5	9.8155	1.0	0.41823	0.8	0.83	2560	18	2252	30	2417	36	88	93
SSB-5A	#36	#N/A	0.004	69	1.34	28575	8.4	2.97	3.3	0.23684	0.8	11.0568	3.4	0.34012	3.3	0.97	3098	26	1885	105	2524	118	61	75
SSB-28A - Tupambi Fm. - Carboniferous																								
SSB-28A	#5	#N/A	0.001	113	1.81	55552	1.1	12.98	1.1	0.05629	0.9	0.6036	1.4	0.07714	1.1	0.78	461	38	479	10	479	14	104	100
SSB-28A	#22	#N/A	0.002	208	3.54	17975	4.6	13.14	0.8	0.05644	0.7	0.5928	1.0	0.07614	0.8	0.77	468	29	473	7	473	13	101	100
SSB-28A	#75	#N/A	0.003	301	0.34	69028	1.8	12.40	0.8	0.05672	0.6	0.6320	1.0	0.08066	0.8	0.82	479	24	500	8	497	14	104	101
SSB-28A	#14	#N/A	0.003	311	1.12	73388	2.6	12.90	0.8	0.05673	0.7	0.6072	1.0	0.07751	0.8	0.75	480	30	481	7	482	13	100	100
SSB-28A	#81	#N/A	0.003	286	1.82	29480	5.8	13.29	0.9	0.05675	0.7	0.5888	1.1	0.07524	0.9	0.77	480	30	468	8	470	14	97	99
SSB-28A	#76	#N/A	0.003	306	1.76	63402	1.5	12.91	0.8	0.05698	0.7	0.6105	1.0	0.07744	0.8	0.76	489	30	481	7	484	14	98	99
SSB-28A	#37	#N/A	0.005	407	0.84	18203	5.4	12.60	0.8	0.05722	0.6	0.6266	1.0	0.07936	0.8	0.78	498	27	492	7	494	14	99	100
SSB-28A	#47	#N/A	0.003	267	0.68	8330	9.8	12.98	1.0	0.05727	0.7	0.6088	1.2	0.07709	1.0	0.84	500	28	479	9	483	16	96	99
SSB-28A	#20	#N/A	0.003	271	1.38	18570	2.7	12.64	0.9	0.05728	0.7	0.6260	1.1	0.07913	0.9	0.78	501	30	491	8	494	15	98	99
SSB-28A	#68	#N/A	0.002	168	3.36	69190	1.7	10.93	1.0	0.05738	0.6	0.7257	1.2	0.09156	1.0	0.84	505	28	565	11	554	16	112	102
SSB-28A	#38	#N/A	0.001	117	1.51	8299	6.2	12.60	1.2	0.05778	1.1	0.6337	1.6	0.07951	1.2	0.74	518	47	493	11	498	14	95	99
SSB-28A	#64	#N/A	0.002	185	3.03	13146	12.9	11.34	1.0	0.05794	0.7	0.7060	1.2	0.08823	1.0	0.83	526	30	545	10	542	16	104	100
SSB-28A	#70	#N/A	0.003	246	0.42	8264	3.9	12.29	0.8	0.05796	0.7	0.6476	1.1	0.08137	0.8	0.74	527	31	504	8	507	15	96	99
SSB-28A	#51	#N/A	0.001	98	0.95	6414	5.1	11.53	1.2	0.05805	1.1	0.6952	1.6	0.08681	1.2	0.75	529	47	537	12	536	16	101	100
SSB-28A	#84	#N/A	0.001	108	1.53	8992	5.3	11.47	1.2	0.05809	1.1	0.6983	1.6	0.08727	1.2	0.73	530	46	539	12	538	16	102	100
SSB-28A	#48	#N/A	0.002	198	1.19	10047	5.1	11.40	0.9	0.05814	0.8	0.7023	1.2	0.08777	0.9	0.73	533	36	542	9	540	15	102	100
SSB-28A	#53	#N/A	0.002	172	0.59	16695	2.3	11.80	0.9	0.05816	0.7	0.6806	1.1	0.08480	0.9	0.78	534	31	525	9	527	15	98	100
SSB-28A	#55	#N/A	0.001	95	2.79	8918	2.8	11.39	1.2	0.05825	1.4	0.7045	1.8	0.08793	1.2	0.66	535	57	543	12	541	19	101	100
SSB-28A	#21	#N/A	0.002	159	2.50	28729	3.4	11.85	1.0	0.05831	0.8	0.6794	1.3	0.08443	1.0	0.79	540	34	522	10	526	14	97	99
SSB-28A	#9	#N/A	0.002	129	2.49	16676	6.7	11.24	0.9	0.05832	0.7	0.7180	1.2	0.08903	1.0	0.81	540	30	550	10	549	15	102	100
SSB-28A	#27	#N/A	0.003	292	2.05	42946	1.7	11.56	1.0	0.05832	1.0	0.6935	1.4	0.08656	1.0	0.71	540	43	535	10	535	18	99	100
SSB-28A	#34	#N/A	0.003	279	1.17	12564	1.7	11.39	1.0	0.05835	1.0	0.7065	1.4	0.08782	1.0	0.70	541	44	543	10	543	15	100	100

SSB-28A	#10	#N/A	0.001	107	0.86	16480	3.9	11.22	0.9	0.05840	0.8	0.7207	1.2	0.08920	0.9	0.74	543	36	551	9	551	16	101	100
SSB-28A	#50	#N/A	0.001	82	1.55	9256	3.7	11.45	1.4	0.05852	1.4	0.7051	2.0	0.08757	1.4	0.72	544	59	541	14	542	17	99	100
SSB-28A	#41	#N/A	0.004	301	1.83	28514	5.7	11.38	0.9	0.05845	0.6	0.7084	1.1	0.08792	0.9	0.82	545	26	543	9	544	15	100	100
SSB-28A	#79	#N/A	0.001	114	2.91	5951	6.9	11.67	1.3	0.05859	1.7	0.6894	2.2	0.08575	1.4	0.64	548	73	530	14	532	18	97	100
SSB-28A	#83	#N/A	0.006	488	3.04	16634	8.2	11.39	0.9	0.05855	0.9	0.7060	1.2	0.08779	0.9	0.71	549	37	542	9	542	16	99	100
SSB-28A	#19	#N/A	0.001	124	3.40	6207	3.4	11.49	1.1	0.05857	1.0	0.7019	1.4	0.08710	1.1	0.74	550	41	538	11	540	15	98	100
SSB-28A	#82	#N/A	0.003	280	1.66	34322	3.5	11.13	0.8	0.05863	0.6	0.7270	1.0	0.08988	0.8	0.80	552	25	555	8	555	16	101	100
SSB-28A	#63	#N/A	0.002	136	1.24	732597	0.2	11.27	1.7	0.05883	1.5	0.7196	2.1	0.08891	1.6	0.73	557	60	549	16	550	17	99	100
SSB-28A	#67	#N/A	0.001	100	2.79	6334	8.4	11.41	1.1	0.05883	1.1	0.7135	1.6	0.08776	1.1	0.70	557	50	542	11	547	18	97	99
SSB-28A	#8	#N/A	0.003	187	1.58	28356	2.5	11.11	0.9	0.05878	0.7	0.7321	1.1	0.09003	0.9	0.77	557	31	556	9	558	15	100	100
SSB-28A	#42	#N/A	0.002	203	1.20	7925	5.1	11.38	0.9	0.05910	0.8	0.7151	1.2	0.08786	0.9	0.73	569	34	543	9	548	16	95	99
SSB-28A	#49	#N/A	0.002	190	2.11	9101	2.3	10.99	0.9	0.05931	1.2	0.7413	1.5	0.09097	0.8	0.57	576	52	561	9	563	26	97	100
SSB-28A	#6	#N/A	0.003	183	0.14	38041	3.9	9.82	0.9	0.05972	0.8	0.8406	1.2	0.10187	0.9	0.74	592	34	625	10	619	17	106	101
SSB-28A	#80	#N/A	0.002	138	1.43	6327	10.5	11.73	1.2	0.06027	1.1	0.7083	1.6	0.08536	1.2	0.75	611	47	528	12	544	18	86	97
SSB-28A	#7	#N/A	0.008	549	0.17	11083	6.0	10.10	0.8	0.06068	0.5	0.8277	1.0	0.09906	0.8	0.85	627	21	609	9	612	17	97	99
SSB-28A	#77	#N/A	0.001	82	1.23	2892	19.1	11.02	1.3	0.06179	3.3	0.7505	3.5	0.09087	1.3	0.37	646	128	561	14	568	33	87	99
SSB-28A	#23	#N/A	0.004	255	0.29	9413	13.7	9.13	0.8	0.06137	0.9	0.9335	1.2	0.10959	0.8	0.67	650	38	670	10	669	22	103	100
SSB-28A	#78	#N/A	0.002	202	0.77	3480	32.4	10.30	1.3	0.06184	2.4	0.8231	2.7	0.09716	1.3	0.47	665	99	598	14	610	38	90	98
SSB-28A	#62	#N/A	0.005	387	1.24	4485	36.7	10.64	1.1	0.06406	0.4	0.8248	1.2	0.09402	1.1	0.92	743	19	579	12	611	20	78	95
SSB-28A	#40	#N/A	0.002	133	0.54	14090	9.5	7.71	0.9	0.06569	0.7	1.1767	1.2	0.12980	1.0	0.79	795	31	787	14	790	22	99	100
SSB-28A	#28	#N/A	0.005	266	1.03	40321	9.8	7.41	0.8	0.06568	0.5	1.2286	0.9	0.13501	0.8	0.81	795	22	816	11	814	20	103	100
SSB-28A	#39	#N/A	0.002	106	1.40	22572	4.7	7.49	0.9	0.06572	0.8	1.2108	1.2	0.13365	0.9	0.76	796	31	809	14	806	20	102	100
SSB-28A	#24	#N/A	0.004	192	1.44	20605	4.3	7.48	0.8	0.06584	0.6	1.2164	1.0	0.13379	0.8	0.79	800	26	809	12	808	20	101	100
SSB-28A	#26	#N/A	0.006	314	0.67	14963	3.6	7.41	0.8	0.06599	0.9	1.2317	1.2	0.13504	0.8	0.68	804	35	817	12	815	20	102	100
SSB-28A	#11	#N/A	0.004	258	0.61	8903	13.3	7.96	0.9	0.06600	0.8	1.1396	1.2	0.12558	0.9	0.74	805	34	763	13	772	25	95	99
SSB-28A	#33	#N/A	0.002	68	2.45	25093	2.4	5.63	1.2	0.07479	1.1	1.8377	1.6	0.17784	1.2	0.75	1060	42	1055	23	1059	26	100	100
SSB-28A	#25	#N/A	0.006	189	1.67	143400	1.7	5.05	0.8	0.07659	0.7	2.1065	1.0	0.19798	0.8	0.78	1109	26	1164	17	1151	28	105	101
SSB-28A	#36	#N/A	0.004	140	2.46	19041	10.0	4.95	1.0	0.07953	0.6	2.2122	1.2	0.20221	1.1	0.85	1184	25	1187	23	1185	28	100	100
SSB-28A	#35	#N/A	0.005	181	1.83	24892	8.5	4.81	0.8	0.08070	0.7	2.3032	1.1	0.20812	0.8	0.72	1213	29	1219	17	1213	25	100	100
SSB-28A	#66	#N/A	0.004	150	2.05	16125	4.7	4.63	0.6	0.08122	0.6	2.4058	1.1	0.21488	1.0	0.85	1226	23	1261	13	1244	27	103	101
SSB-28A	#52	#N/A	0.008	220	1.35	28539	6.7	3.92	0.9	0.09017	0.5	3.1794	1.0	0.25517	0.9	0.88	1428	18	1465	23	1452	31	103	101
SSB-28A	#65	#N/A	0.004	99	2.47	22933	9.3	3.13	0.8	0.10728	0.6	4.7189	1.0	0.31923	0.8	0.79	1753	21	1786	24	1770	31	102	101
SSB-28A	#12	#N/A	0.004	91	3.65	11785	9.2	3.17	1.0	0.10840	0.7	4.7126	1.2	0.31603	1.0	0.83	1772	24	1770	30	1769	31	100	100
SSB-28A	#56	#N/A	0.005	115	2.83	8435	4.4	3.17	0.9	0.11054	0.6	4.8131	1.1	0.31535	0.9	0.84	1807	21	1767	28	1787	34	98	99

SSB-28A	#69	#N/A	0.013	274	0.89	45235	3.7	2.83	0.8	0.12508	0.7	6.0933	1.0	0.35337	0.8	0.74	2029	24	1951	26	1989	40	96	98
SSB-28A	#54	#N/A	0.003	275	2.47	1822	6.2	13.57	1.3	0.06882	2.3	0.6981	2.6	0.07376	1.3	0.48	888	90	459	11	537	39	52	85
SSB-28A	#13	#N/A	0.004	123	1.33	268012	1.5	3.73	0.9	0.10885	1.0	4.0099	1.4	0.26835	0.9	0.68	1779	35	1532	25	1636	38	86	94
SSB-28A	#61	#N/A	0.003	61	0.72	13023	14.7	2.83	1.2	0.14031	1.0	6.7900	1.5	0.35315	1.2	0.79	2230	32	1950	40	2084	61	87	94
SSB-23A - Tarija Fm. - Carboniferous																								
SSB-23A	#79	#N/A	0.004	432	1.17	13020	12.2	18.93	0.8	0.05353	0.5	0.3901	1.0	0.05285	0.8	0.82	350	24	332	5	334	8	95	99
SSB-23A	#19	#N/A	0.005	508	1.44	22527	3.7	18.83	0.7	0.05355	0.5	0.3910	0.9	0.05313	0.8	0.81	351	24	334	5	335	8	95	100
SSB-23A	#95	#N/A	0.002	212	1.56	114971	0.5	17.03	0.9	0.05374	0.7	0.4355	1.1	0.05875	0.9	0.80	358	30	368	6	367	9	103	100
SSB-23A	#36	#N/A	0.004	391	1.45	64238	1.4	16.30	0.7	0.05437	0.5	0.4597	0.8	0.06137	0.7	0.80	385	22	384	5	384	7	100	100
SSB-23A	#11	#N/A	0.001	80	7.01	64027	0.4	16.34	1.0	0.05455	1.2	0.4598	1.6	0.06126	1.0	0.64	389	53	383	8	384	11	98	100
SSB-23A	#69	#N/A	0.002	194	2.51	8487	2.5	15.49	0.8	0.05532	0.7	0.4915	1.1	0.06459	0.8	0.74	423	32	403	6	406	9	95	99
SSB-23A	#20	#N/A	0.001	87	1.61	7374	5.4	13.57	1.2	0.05643	1.0	0.5726	1.5	0.07378	1.2	0.76	466	42	459	10	460	10	98	100
SSB-23A	#34	#N/A	0.003	281	1.17	5135	28.5	15.75	1.2	0.05694	2.5	0.4948	2.8	0.06354	1.2	0.43	482	113	397	9	408	25	82	97
SSB-23A	#70	#N/A	0.003	301	2.81	7897	10.1	15.73	0.8	0.05691	0.7	0.4979	1.0	0.06359	0.8	0.77	487	28	397	6	410	7	82	97
SSB-23A	#10	#N/A	0.001	121	2.49	3928	19.6	15.25	1.3	0.05756	1.5	0.5214	2.0	0.06568	1.3	0.68	509	64	410	11	426	19	81	96
SSB-23A	#81	#N/A	0.001	55	1.33	58269	0.5	11.22	1.3	0.05775	1.2	0.7098	1.7	0.08930	1.2	0.72	517	52	551	13	545	12	107	101
SSB-23A	#109	#N/A	0.002	115	2.60	13093	3.6	11.77	0.8	0.05781	0.7	0.6783	1.1	0.08498	0.8	0.73	520	32	526	8	526	11	101	100
SSB-23A	#114	#N/A	0.002	134	1.91	16290	10.3	11.42	0.8	0.05795	0.7	0.7001	1.1	0.08759	0.8	0.73	526	32	541	8	539	11	103	100
SSB-23A	#53	#N/A	0.002	134	0.58	12870	5.4	11.82	1.1	0.05801	0.9	0.6755	1.4	0.08473	1.2	0.80	527	38	524	11	524	15	99	100
SSB-23A	#52	#N/A	0.001	75	1.67	19478	0.7	11.72	1.3	0.05808	1.6	0.6796	2.0	0.08543	1.3	0.64	527	69	528	13	526	14	100	100
SSB-23A	#80	#N/A	0.001	99	0.90	6897	5.2	11.90	0.9	0.05805	0.9	0.6682	1.2	0.08406	0.9	0.71	529	37	520	9	520	13	98	100
SSB-23A	#62	#N/A	0.002	147	1.10	14815	5.2	11.60	1.2	0.05812	0.7	0.6901	1.4	0.08640	1.2	0.85	532	32	534	12	533	14	100	100
SSB-23A	#82	#N/A	0.004	286	0.28	13885	27.5	11.03	0.9	0.05842	0.9	0.7264	1.2	0.09071	0.9	0.71	544	38	560	9	554	14	103	101
SSB-23A	#101	#N/A	0.003	224	0.92	12036	11.6	11.25	0.8	0.05853	1.1	0.7173	1.4	0.08894	0.8	0.55	546	47	549	8	549	19	101	100
SSB-23A	#113	#N/A	0.002	124	0.88	42702	1.5	10.88	0.8	0.05851	0.7	0.7419	1.1	0.09193	0.8	0.75	547	30	567	9	564	11	104	101
SSB-23A	#6	#N/A	0.001	49	0.82	5797	1.7	11.41	1.2	0.05862	1.2	0.7072	1.7	0.08779	1.3	0.73	550	53	542	13	543	15	99	100
SSB-23A	#7	#N/A	0.010	654	0.92	34132	13.2	11.28	0.9	0.05862	0.5	0.7156	1.1	0.08873	1.0	0.88	552	22	548	10	548	18	99	100
SSB-23A	#47	#N/A	0.001	87	1.33	42490	1.2	11.42	1.0	0.05888	0.8	0.7093	1.3	0.08767	1.0	0.78	560	34	542	10	544	13	97	100
SSB-23A	#23	#N/A	0.002	157	1.70	7599	5.5	11.58	0.8	0.05886	0.6	0.7007	1.0	0.08641	0.8	0.82	560	25	534	8	539	13	95	99
SSB-23A	#115	#N/A	0.001	84	1.35	14654	3.8	11.29	1.1	0.05897	1.3	0.7213	1.7	0.08870	1.2	0.66	561	56	548	12	551	14	98	99
SSB-23A	#42	#N/A	0.001	92	1.78	34283	1.0	11.73	0.7	0.05891	0.7	0.6928	1.0	0.08528	0.7	0.73	562	29	528	7	534	10	94	99
SSB-23A	#96	#N/A	0.004	299	2.87	7427	4.0	12.67	0.8	0.05919	0.6	0.6444	1.0	0.07892	0.8	0.81	573	24	490	7	505	11	86	97
SSB-23A	#112	#N/A	0.001	55	5.36	3258	4.5	10.64	1.7	0.05942	1.7	0.7710	2.4	0.09432	1.7	0.69	576	73	581	18	580	22	101	100
SSB-23A	#85	#N/A	0.002	119	2.36	12753	1.8	10.61	1.2	0.05932	0.8	0.7689	1.5	0.09434	1.2	0.81	577	37	581	13	579	23	101	100

SSB-23A	#63	#N/A	0.000	30	3.11	3689	2.6	10.68	2.9	0.06002	2.8	0.7722	4.3	0.09464	3.2	0.76	589	120	583	35	581	19	99	100
SSB-23A	#40	#N/A	0.002	165	2.03	7209	12.8	11.63	1.0	0.05973	0.8	0.7078	1.3	0.08606	1.0	0.79	591	33	532	10	543	13	90	98
SSB-23A	#26	#N/A	0.002	105	0.03	5626	15.1	11.48	1.0	0.05978	0.8	0.7188	1.3	0.08721	1.0	0.80	593	34	539	11	550	17	91	98
SSB-23A	#9	#N/A	0.001	92	3.25	2856	6.1	15.63	1.4	0.05990	1.5	0.5283	2.1	0.06418	1.4	0.70	594	65	401	11	431	20	68	93
SSB-23A	#39	#N/A	0.001	66	8.62	8982	3.8	11.10	1.2	0.05988	1.1	0.7437	1.6	0.09023	1.2	0.74	596	48	557	13	565	11	93	99
SSB-23A	#27	#N/A	0.002	154	2.55	10608	12.8	11.83	0.9	0.05988	0.8	0.6969	1.3	0.08460	1.0	0.77	597	34	523	9	537	17	88	98
SSB-23A	#65	#N/A	0.001	36	1.81	14730	1.2	9.08	1.7	0.05999	1.3	0.9097	2.1	0.11057	1.7	0.79	599	56	676	21	657	19	113	103
SSB-23A	#83	#N/A	0.001	82	1.21	10606	5.2	10.74	1.2	0.06002	0.9	0.7685	1.5	0.09322	1.2	0.79	602	37	575	12	579	11	95	99
SSB-23A	#37	#N/A	0.002	119	0.55	23188	1.9	10.37	1.1	0.06005	0.7	0.7995	1.3	0.09661	1.1	0.85	603	30	594	12	596	20	99	100
SSB-23A	#38	#N/A	0.003	212	0.94	13302312	0.0	10.37	0.9	0.06014	0.5	0.7983	1.0	0.09653	0.9	0.87	607	21	594	10	596	14	98	100
SSB-23A	#108	#N/A	0.000	22	3.80	4483	2.4	9.99	2.8	0.06055	2.7	0.8354	4.0	0.10105	3.0	0.73	609	122	620	34	617	18	102	101
SSB-23A	#116	#N/A	0.003	211	1.81	27737	3.5	10.03	0.8	0.06040	0.5	0.8292	1.0	0.09972	0.8	0.87	617	20	613	10	613	12	99	100
SSB-23A	#64	#N/A	0.001	85	2.09	81132	0.4	9.89	1.1	0.06067	0.9	0.8443	1.5	0.10126	1.2	0.77	625	39	622	13	621	17	100	100
SSB-23A	#50	#N/A	0.007	429	0.03	27561	6.2	9.72	0.8	0.06099	0.4	0.8636	0.9	0.10290	0.8	0.90	638	17	631	10	632	13	99	100
SSB-23A	#67	#N/A	0.003	214	2.76	131477	0.6	10.10	0.7	0.06105	0.5	0.8304	0.9	0.09901	0.7	0.78	640	23	609	8	614	11	95	99
SSB-23A	#61	#N/A	0.001	47	3.89	3134	26.6	12.68	3.2	0.06136	2.1	0.6674	3.7	0.07969	3.0	0.81	643	89	494	28	519	32	77	95
SSB-23A	#87	#N/A	0.000	18	4.83	5126	1.5	10.95	5.9	0.06198	6.2	0.7766	8.2	0.09273	5.4	0.66	647	249	571	58	584	18	88	98
SSB-23A	#22	#N/A	0.003	147	2.11	9178	15.4	10.01	0.5	0.06148	0.7	0.8455	1.0	0.09971	0.7	0.71	654	30	613	8	622	13	94	98
SSB-23A	#94	#N/A	0.001	81	2.20	15347	4.9	9.42	1.2	0.06195	1.2	0.9065	1.7	0.10624	1.2	0.69	669	53	651	14	655	21	97	99
SSB-23A	#24	#N/A	0.004	243	1.19	20873	12.6	9.41	0.9	0.06193	0.5	0.9100	1.1	0.10636	0.9	0.88	671	21	652	11	657	19	97	99
SSB-23A	#5	#N/A	0.004	188	2.21	29350	5.9	8.92	1.0	0.06261	0.7	0.9649	1.2	0.11216	0.9	0.80	693	30	685	12	686	22	99	100
SSB-23A	#66	#N/A	0.008	482	0.59	52433	6.2	9.10	0.7	0.06264	0.5	0.9446	0.9	0.10986	0.7	0.85	695	19	672	9	675	13	97	100
SSB-23A	#21	#N/A	0.002	133	2.98	4421	27.0	10.36	1.2	0.06384	1.2	0.8550	1.6	0.09665	1.1	0.70	734	49	595	13	627	13	81	95
SSB-23A	#98	#N/A	0.010	538	0.51	13767	15.1	8.51	1.3	0.06421	0.9	1.0476	1.6	0.11775	1.3	0.82	746	38	718	18	727	40	96	99
SSB-23A	#28	#N/A	0.003	153	0.76	32539	1.8	8.57	1.2	0.06445	0.6	1.0319	1.3	0.11670	1.2	0.91	755	23	712	16	720	19	94	99
SSB-23A	#33	#N/A	0.011	727	0.03	2030	37.1	11.39	0.9	0.06613	0.7	0.8030	1.1	0.08788	0.8	0.75	808	30	543	8	598	20	67	91
SSB-23A	#99	#N/A	0.007	312	0.70	8924	24.0	7.51	1.0	0.06752	0.9	1.2517	1.3	0.13329	1.0	0.76	852	35	807	15	824	21	95	98
SSB-23A	#86	#N/A	0.003	140	0.86	24964	13.9	7.14	0.7	0.06863	0.7	1.3304	1.0	0.14015	0.7	0.74	886	28	845	12	859	16	95	98
SSB-23A	#55	#N/A	0.004	181	0.72	15941	12.1	6.94	0.8	0.07012	0.8	1.3887	1.1	0.14412	0.8	0.71	931	31	868	12	884	19	93	98
SSB-23A	#13	#N/A	0.011	399	0.65	59323	5.7	6.16	0.6	0.07125	0.4	1.5919	0.7	0.16246	0.6	0.87	964	15	970	11	967	13	101	100
SSB-23A	#14	#N/A	0.004	123	0.89	26316	7.3	6.37	0.7	0.07149	0.7	1.5525	1.0	0.15712	0.7	0.74	970	27	941	13	951	17	97	99
SSB-23A	#56	#N/A	0.005	243	2.12	40027	8.8	6.97	0.9	0.07174	0.4	1.4185	1.0	0.14360	0.9	0.90	978	18	865	14	897	22	88	96
SSB-23A	#54	#N/A	0.004	178	0.94	67503	4.8	6.27	1.1	0.07343	0.6	1.6177	1.2	0.15979	1.1	0.87	1024	24	956	19	977	23	93	98
SSB-23A	#51	#N/A	0.005	186	0.74	15308	9.4	6.20	0.8	0.07352	0.5	1.6314	0.9	0.16137	0.8	0.85	1027	19	964	13	982	16	94	98

SSB-23A	#102	#N/A	0.011	393	1.27	9589	22.4	5.75	0.7	0.07374	0.7	1.7703	1.0	0.17397	0.7	0.75	1033	25	1034	14	1035	14	100	100
SSB-23A	#48	#N/A	0.002	80	1.06	14509	5.9	5.56	0.9	0.07497	0.5	1.8580	1.0	0.18002	0.9	0.87	1067	19	1067	17	1066	21	100	100
SSB-23A	#25	#N/A	0.001	32	1.32	2492	11.4	5.77	1.3	0.07506	1.3	1.7930	1.8	0.17369	1.3	0.71	1067	51	1032	24	1043	25	97	99
SSB-23A	#88	#N/A	0.004	122	3.65	32029	9.3	5.46	0.9	0.07531	0.5	1.9054	1.0	0.18319	0.9	0.86	1076	21	1084	18	1083	23	101	100
SSB-23A	#93	#N/A	0.006	215	0.84	29594	3.7	5.30	0.7	0.07720	0.4	2.0071	0.8	0.18863	0.7	0.87	1125	16	1114	14	1118	16	99	100
SSB-23A	#97	#N/A	0.005	152	3.50	167201	0.5	4.89	0.7	0.07954	0.5	2.2419	0.8	0.20447	0.7	0.82	1184	18	1199	14	1194	16	101	100
SSB-23A	#8	#N/A	0.006	163	2.29	21265	7.6	4.78	0.9	0.08274	0.4	2.3710	1.0	0.20918	0.9	0.91	1262	16	1224	20	1234	24	97	99
SSB-23A	#107	#N/A	0.001	14	3.84	5285	5.6	2.87	2.5	0.11461	1.4	5.5225	3.1	0.35126	2.7	0.88	1870	51	1939	88	1901	78	104	102
SSB-23A	#84	#N/A	0.005	97	6.29	12432	16.5	3.08	0.7	0.11922	0.5	5.3295	0.8	0.32448	0.7	0.84	1944	16	1812	22	1873	23	93	97
SSB-23A	#68	#N/A	0.003	37	6.55	30981	7.3	1.78	2.1	0.24742	0.6	19.2751	1.3	0.55502	1.2	0.88	3167	20	2845	54	3053	75	90	93
SSB-23A	#110	#N/A	0.010	98	1.57	81566	4.5	1.56	0.7	0.30518	0.4	26.9602	0.8	0.64019	0.7	0.85	3496	13	3190	35	3382	27	91	94
SSB-23A	#41	#N/A	0.005	375	1.95	2409	47.0	12.87	1.0	0.06643	0.7	0.7160	1.2	0.07772	1.0	0.81	819	29	483	9	548	17	59	88
SSB-23A	#35	#N/A	0.008	1227	2.51	647	63.3	26.58	1.7	0.08263	1.5	0.4294	2.2	0.03781	1.6	0.73	1254	56	239	7	363	8	19	66
SSB-23A	#12	#N/A	0.011	504	1.39	957	28.3	8.38	1.4	0.08539	1.5	1.4050	2.0	0.11963	1.4	0.69	1320	56	728	19	891	31	55	82
SSB-23A	#100	#N/A	0.009	224	0.86	14082	51.9	4.04	1.6	0.10243	0.5	3.5248	1.7	0.24805	1.6	0.96	1668	18	1428	40	1532	49	86	93
SSB-23A	#49	#N/A	0.007	258	0.74	6054	14.3	5.64	1.6	0.10658	0.8	2.6135	1.7	0.17766	1.5	0.89	1740	29	1054	29	1303	59	61	81
SSB-23A	#111	#N/A	0.008	94	0.55	42061	5.4	1.64	0.8	0.29534	0.6	24.7235	1.0	0.60865	0.8	0.81	3445	18	3064	39	3297	42	89	93

CAPÍTULO 5

CONCLUSÕES

O estudo de proveniência sedimentar efetuado no intervalo Devoniano – Carbonífero da bacia de Tarija permitiram concluir:

- As unidades devonianas (formações Icla, Huamampampa, Los Monos e Iquiri) da bacia de Tarija possuem valores de $\varepsilon_{Nd(300)}$ entre -9.65 até -6.82 e razões $^{87}Sr/^{86}Sr_{(300)}$ entre 0.71931 e 0.75565. Enquanto as unidades carboníferas (formações Itacua, Tupambi, Tarija e Chorro) possuem valores de $\varepsilon_{Nd(300)}$ entre -8.13 até -6.54 e razões $^{87}Sr/^{86}Sr_{(300)}$ entre 0.70686 e 0.71996. Esses valores são similares aos valores obtidos em amostras das Sierras Pampeanas, o domínio central e sul do maciço de Arequipa-Antofalla, e o Arco Famatiniano.
- As idades U-Pb dos grãos de zircão detrítico das unidades devonianas e carboníferas sinalam como principais fontes aos eventos Pampeano (700 – 500 Ma), Sunsas/Grenvillian (1300 – 900 Ma) e Famatiniano (500 – 420 Ma).
- Além disso, os conteúdos menos radiogênicos e os grãos de zircão com idades entre 420 e 320 Ma (evento Chánico) das rochas das unidades carboníferas indicam o aporte de uma fonte mais jovem, o que poderia sinalar como fonte ao magmatismo Devoniano no noroeste Argentino.
- No entanto, os dados de paleocorrentes para o norte e noroeste em combinação com nossos dados (XRD em pelitos, petrografia de arenitos, morfologia dos grão de zircão, isótopos de Sr-Nd, idades U-Pb, e as análises MDS) poderiam sustentar o retrabalho de unidades subjacentes como potenciais fontes de sedimentos desde o sudeste da bacia e com um aporte menor desde o oeste representado pelas Sierras Pampeanas, o domínio central e sul do maciço de Arequipa-Antofalla, o arco Famatiniano e as rocas magmáticas devonianas do noroeste Argentino.
- Nossos dados de proveniência sedimentar em combinação com informação publicada de paleocorrentes, padrões de subsidência e dados do desenvolvimento de uma faixa de dobra e cavalgamentos durante o

Paleozoico, permitiram interpretar a existência de uma bacia de antepaís relacionada a uma margem convergente, a qual experimentou modificações no comportamento e interação das placas durante o Devoniano e o Carbonífero. Além disso, o Carbonífero está representado por um importante aporte sedimentário desde a região intracontinental como produto do transporte glacial.

- A análise do registro detrítico sedimentário da bacia de Tarija e a comparação com as diferentes bacias sedimentares contemporâneas localizadas na margem sudoeste de Gondwana nos permitem interpretar que essa margem possuía uma forte segmentação, como resposta ao modificações no comportamento e interação entre as placas. Para o norte de 20° S, considerando os dados disponíveis, a existência de um arco magmático durante o Devoniano não pode ser descartado. Entre 20° S e 28° S não existe evidencia de atividade magmática até agora; no entanto existe evidencia de uma importante subsidência e encurtamento tectônico na bacia de Tarija durante o Devoniano e o Carbonífero, o qual suporta a Idea de uma subducção tipo *flat-slab* na região. Para o sul de 28° S, a informação existente sugere a existência de uma subducção tipo *flat-slab*, a qual foi caracterizada pelo desenvolvimento de um magmatismo intracontinental durante o Devoniano que mudou para um magmatismo de arco durante o Carbonífero como consequência de uma subducção tipo *flat-slab* e processos de delaminação da placa.
- Finalmente, as características geodinâmicas na margem sudoeste de Gondwana durante o Devoniano são complexas; no entanto, o estabelecimento de uma margem passiva nesse setor de Gondwana não consegue explicar as evidencias que sustentam a existência de uma margem ativa. Nesse trabalho propõe-se que a ausência do arco magmático durante o Devoniano é consequência das características de uma subducção tipo *flat-slab*.

BIBLIOGRAFIA

Albarède, F., Telouk, P., Blichert-Toft, J., Boyet, M., Agranier, A., Nelson, B., 2004. Precise and accurate isotopic measurements using multiple-collector ICPMS. Geochim. Cosmochim. Acta 68, 2725–2744. https://doi.org/10.1016/j.gca.2003.11.024

Allen, P.A., Armitage, J.J., 2012. Cratonic basins, in: Busby, C., Azor, A. (Eds.), Tectonics of Sedimentary Basins: Recent Advances. Blackwell Publishing Ltd., pp. 602–620.

Allen, P.A., Homewood, P., Williams, G.D., 1986. Foreland Basins: An Introduction, in: Allen, P.A., Homewood, P. (Eds.), Foreland Basins. Blackwell Publishing Ltd., Oxford, UK, pp. 3–12. https://doi.org/10.1002/9781444303810.ch

Allmendinger, R., Zapata, T., 2000. The footwall ramp of the Subandean decollement, northernmost Argentina, from extended correlation of seismic reflection data. Tectonophysics 321, 37–55. https://doi.org/10.1016/S0040-1951(00)00077-9

Alves, D.B., 1987. Desenvolvimento da metodologia de preparação de amostras para análise difratométrica de argilominerais no Centro de Pesquisas da Petrobrás. Bol. Geociências da Petrobrás 1, 157–175.

Anderson, R.B., Long, S.P., Horton, B.K., Calle, A.Z., Ramirez, V., 2017. Shortening and structural architecture of the Andean fold-thrust belt of southern Bolivia (21°S): Implications for kinematic development and crustal thickening of the central Andes. Geosphere 13, 538–558. https://doi.org/10.1130/GES01433.1

Anderson, R.B., Long, S.P., Horton, B.K., Calle, A.Z., Soignard, E., 2021. Late Paleozoic Gondwanide deformation in the Central Andes: Insights from RSCM thermometry and thermal modeling, southern Bolivia. Gondwana Res. 94, 222–242. https://doi.org/10.1016/j.gr.2021.03.002

Augustsson, C., Münker, C., Bahlburg, H., Fanning, C.M., 2006. Provenance of late Palaeozoic metasediments of the SW South American Gondwana margin: a combined U–Pb and Hf-isotope study of single detrital zircons. J. Geol. Soc. London. 163, 983–995. https://doi.org/10.1144/0016-76492005-149

Augustsson, C., Voigt, T., Bernhart, K., Kreißler, M., Gaupp, R., Gärtner, A., Hofmann, M., Linnemann, U., 2018. Zircon size-age sorting and source-area effect : The German Triassic Buntsandstein Group. Sediment. Geol. 375, 218–231. https://doi.org/10.1016/j.sedgeo.2017.11.004

Baby, P., Hérail, G., Salinas, R., Sempere, T., 1992. Geometry and kinematic evolution of passive roof duplexes deduced from cross section balancing: Example from the foreland thrust system of the southern Bolivian Subandean Zone. Tectonics 11, 523–536. https://doi.org/10.1029/91TC03090

Bahlburg, H., Hervé, F., 1997. Geodynamic evolution and tectonostratigraphic terranes of northwestern Argentina and northern Chile. Geol. Soc. Am. Bull. 109, 869–884. https://doi.org/10.1130/0016-7606(1997)109<0869:GEATTO>2.3.CO;2

Bahlburg, H., Vervoort, J.D., Du Frane, S.A., Bock, B., Augustsson, C., Reimann, C., 2009. Timing of crust formation and recycling in accretionary orogens: Insights learned from the western margin of South America. Earth-Science Rev. 97, 215–241. https://doi.org/10.1016/j.earscirev.2009.10.006

Basu, A.R., Sharma, M., DeCelles, P.G., 1990. Nd, Sr-isotopic provenance and trace element geochemistry of Amazonian foreland basin fluvial sands, Bolivia and Peru: implications for ensialic Andean orogeny. Earth Planet. Sci. Lett. 100, 1–17. https://doi.org/10.1016/0012-821X(90)90172-T

Belotti, H.J., Saccavino, L.L., Schachner, G.A., 1995. Structural Styles and Petroleum Occurrence in the Sub-Andean Fold and Thrust Belt of Northern Argentina. Pet. Basins South Am. https://doi.org/10.1306/M62593C28

Benedetto, J.L., 2019. El continente de Gondwana a través del tiempo, una introducción a la Geología Histórica, 3°. ed. Academia Nacional de Ciencias, Córdoba, Argentina.

Bock, B., Bahlburg, H., Worner, G., Zimmermann, U., 2000. Tracing crustal evolution in the Southern Central Andes from Late Precambrian to Permian with geochemical and Nd and Pb isotope data. J. Geol. 108, 515–535. https://doi.org/10.1086/314422

Bouchez, J., Gaillardet, J., France-Lanord, C., Maurice, L., Dutra-Maia, P., 2011. Grain size control of river suspended sediment geochemistry: Clues from Amazon River depth profiles. Geochemistry, Geophys. Geosystems 12, n/a-n/a. https://doi.org/10.1029/2010GC003380

Calle, A.Z., 2013. Neogene sedimentation and provenance record of the Subandean zone and Chaco foreland basin, southern Bolivia. The University of Texas at Austin.

Calle, A.Z., Horton, B.K., Limachi, R., Stockli, D.F., Uzeda-Orellana, G. V., Anderson, R.B., Long, S.P., 2018. Cenozoic Provenance and Depositional Record of the Sub-Andean Foreland Basin during Growth of the Central Andean Fold-Thrust Belt, Southern Bolivia, in: Zamora, G., McClay, K.R., Ramos, V.A. (Eds.), Petroleum Basins and Hydrocarbon Potential of the Andes of Perú and Bolivia. The American Association of Petroleum Geologist and Repsol, pp. 483–530. https://doi.org/10.1306/13622132M1173777

Cardona, A., 2006. Reconhecimento da evolução tectônica da proto-margem andina do centro-norte peruano, baseada em dados geoquímicos e isotópicos do embasamento da Cordilheira Oriental na região de Huánuco-La Unión. Universidade de São Paulo.

Cardona, A., Cordani, U.G., Ruiz, J., Valencia, V.A., Armstrong, R., Chew, D., Nutman, A., Sanchez, A.W., 2009. U-Pb Zircon Geochronology and Nd Isotopic Signatures of the Pre-Mesozoic Metamorphic Basement of the Eastern Peruvian Andes: Growth and Provenance of a Late Neoproterozoic to Carboniferous Accretionary Orogen on the Northwest Margin of Gondwana. J. Geol. 117, 285–305. https://doi.org/10.1086/597472

Casquet, C., Baldo, E., Pankhurst, R.J., Rapela, C.W., Galindo, C., Fanning, C.M., Saavedra, J., 2001. Involvement of the Argentine Precordillera terrane in the Famatinian mobile belt: U-Pb SHRIMP and metamorphic evidence from the Sierra de Pie de Palo. Geology 29, 703. https://doi.org/10.1130/0091-7613(2001)029<0703:IOTAPT>2.0.CO;2

Casquet, C., Pankhurst, R.J., Rapela, C.W., Galindo, C., Fanning, C.M., Chiaradia, M., Baldo, E., González-Casado, J.M., Dahlquist, J.A., 2008. The Mesoproterozoic Maz terrane in the Western Sierras Pampeanas, Argentina, equivalent to the Arequipa–Antofalla block of southern Peru? Implications for West Gondwana margin evolution. Gondwana Res. 13, 163–175. https://doi.org/10.1016/j.gr.2007.04.005

Catuneanu, O., Beaumont, C., Waschbusch, P., 1997. Interplay of static loads and subduction dynamics in foreland basins: Reciprocal stratigraphies and the "missing" peripheral bulge. Geology 25, 1087. https://doi.org/10.1130/0091-7613(1997)025<1087:IOSLAS>2.3.CO;2

Cawood, P.A., 2005. Terra Australis Orogen: Rodinia breakup and development of the Pacific and Iapetus margins of Gondwana during the Neoproterozoic and Paleozoic. Earth-Science Rev. 69, 249–279. https://doi.org/10.1016/j.earscirev.2004.09.001

Cawood, P.A., Hawkesworth, C.J., Dhuime, B., 2012. Detrital zircon record and tectonic setting. Geology 40, 875–878. https://doi.org/10.1130/G32945.1

Chew, D.M., Magna, T., Kirkland, C.L., Mišković, A., Cardona, A., Spikings, R., Schaltegger, U., 2008. Detrital zircon fingerprint of the Proto-Andes : Evidence for a Neoproterozoic active margin? Precambrian Res. 167, 186–200.

https://doi.org/10.1016/j.precamres.2008.08.002

Chew, D.M., Pedemonte, G., Corbett, E., 2016. Proto-andean evolution of the eastern Cordillera of Peru. Gondwana Res. 35, 59–78.

Chew, D.M., Schaltegger, U., Kosler, J., Whitehouse, M.J., Gutjahr, M., Spikings, R.A., Miskovic, A., 2007. U-Pb geochronologic evidence for the evolution of the Gondwanan margin of the north-central Andes. Geol. Soc. Am. Bull. 119, 697–711. https://doi.org/10.1130/B26080.1

Corfu, F., Hanchar, J.M., Hoskin, P.W.., Kinny, P., 2003. Atlas of Zircon Textures. Rev. Mineral. Geochemistry 53, 469–500. https://doi.org/10.2113/0530469

Craddock, J.P., Ojakangas, R.W., Malone, D.H., Konstantinou, A., Mory, A., Bauer, W., Thomas, R.J., Affinati, S.C., Pauls, K., Zimmerman, U., Botha, G., Rochas-Campos, A., Santos, P.R. dos, Tohver, E., Riccomini, C., Martin, J., Redfern, J., Horstwood, M., Gehrels, G., 2019. Detrital zircon provenance of Permo-Carboniferous glacial diamictites across Gondwana. Earth-Science Rev. 192, 285–316. https://doi.org/10.1016/j.earscirev.2019.01.014

Cruz, C.E., Sylwan, C.A., Villar, H.J., 2002. La cuenca de Tarija, Bolivia y noroeste de Argentina: ¿Sistema petrolero único o múltiples sistemas petroleros?, in: V Congreso de Exploración y Desarrollo de Hidrocarburos. Instituto Argentino del Petróleo y del Gas, Mar del Plata, p. 19.

Cruz, C.E., Veramendi, J.O., Di Benedetto, M., Pereira, M., Villar, H.J., 2008. Los Sistemas Petroleros Devonicos Del Subandino Sur Y Pie De Monte De La Cuenca De Tarija. Bolivia, in: Cruz, C.E., Rodríguez, J.F., Hechem, J.J., J, V.H. (Eds.), VII Congreso de Exploración y Desarrollo de Hidrocarburos (Simposio de Sistemas Petroleros de Las Cuencas Andinas). Instituto Argentino del Petróleo y del Gas, Buenos Aires, p. 29.

Cullers, R.L., 2000. The geochemistry of shales, siltstones and sandstones of Pennsylvanian–Permian age, Colorado, USA: implications for provenance and metamorphic studies. Lithos 51, 181–203. https://doi.org/10.1016/S0024-4937(99)00063-8

Dahlquist, J.A., Alasino, P.H., Basei, M.A.S., Morales Cámera, M.M., Macchioli Grande, M., da Costa Campos Neto, M., 2018. Petrological, geochemical, isotopic, and geochronological constraints for the Late Devonian–Early Carboniferous magmatism in SW Gondwana (27–32°LS): an example of geodynamic switching. Int. J. Earth Sci. 107, 2575–2603. https://doi.org/10.1007/s00531-018-1615-9

Dahlquist, J.A., Macchioli Grande, M., Alasino, P.H., Basei, M.A.S., Galindo, C., Moreno, J.A., Morales Cámera, M.M., 2019. New geochronological and isotope data for the Las Chacras – Potrerillos and Renca batholiths: A contribution to the Middle-Upper Devonian magmatism in the pre-Andean foreland (Sierras Pampeanas, Argentina), SW Gondwana. J. South Am. Earth Sci. 93, 348–363. https://doi.org/10.1016/j.jsames.2019.04.026

Dalenz-Farjat, A., Alvarez, L.A., Hernández, R.M., Albariño, L.M., 2002. Cuenca Siluro-Devónica del sur de Bolivia y del noroeste argentino: algunas interpretaciones. V Congr. Explor. y Desarro. Hidrocarburos 18.

DeCelles, P.G., 2012. Foreland basin systems revisited: Variations in response to tectonic settings, in: Busby, C., Azor, A. (Eds.), Tectonics of Sedimentary Basins: Recent Advances. Blackwell Publishing Ltd. Chichester, UK, pp. 405–426.

DeCelles, P.G., Giles, K.A., 1996. Foreland basin systems. Basin Res. 8, 105–123.

di Pasquo, M., 2007. Asociaciones palinológicas en las formaciones Los Monos (Devónico) e Itacua (Carbonífero Inferior) en Balapuca (Cuenca Tarija), sur de Bolivia: Parte 1. Formación Los Monos. Rev. geológica Chile 34. https://doi.org/10.4067/S0716-02082007000100006

di Pasquo, M.M., Anderson Folnagy, H. j, Isaacson, P.E., Grader, G.W., 2019. Late Paleozoic carbonates and glacial deposits in Bolivia and Northern Argentina: Significant paleoclimatic changes, in: Latitudinal Controls on Stratigraphic Models and Sedimentary Concepts. Society for Sedimentary Geology, Tulsa, Olkahoma, pp. 185–203. https://doi.org/10.2110/sepmsp.108.10

Diaz-Martinez, E., 1996. Síntesis Estratigráfica y Geodinámica del Carbonífero de Bolivia. Memorias del XII Congr. Geológico Boliv. (Tarija, Boliv. 1, 355–367.

Diaz-Martinez, E., Limachi, R., Goitia, V.H., Sarmiento, D., Arispe, O., Montecinos, R., 1996. Relacion entre tectonica y sedimentacion en la cuenca de antepais del Paleozoico medio de los Andes centrales de Bolivia (14 a 22° S). Memorias del XII Congr. Geológico Boliv. (Tarija, Boliv. 1, 97–102.

Dickinson, W.R., 1985. Interpreting Provenance Relations from Detrital Modes of Sandstones, in: Provenance of Arenites. Springer Netherlands, Dordrecht, pp. 333–361. https://doi.org/10.1007/978-94-017-2809-6_15

Dickinson, W.R., 1974. Tectonics and Sedimentation, Tectonics and Sedimentation. SEPM (Society for Sedimentary Geology). https://doi.org/10.2110/pec.74.22

Dickinson, W.R., Gehrels, G.E., 2009. Use of U–Pb ages of detrital zircons to infer maximum depositional ages of strata: A test against a Colorado Plateau Mesozoic database. Earth Planet. Sci. Lett. 288, 115–125. https://doi.org/10.1016/j.epsl.2009.09.013

Dorobek, S.L., 1995. Synorogenic carbonate platforms and reefs in foreland basins: controls on stratigraphic evolution and platform/reef morphology.

Dunn, J.F., Hartshorn, K.G., Hartshon, P.W., 1995. Structural Styles and Hydrocarbon Potential of the Sub-Andean Thrust Belt of Southern Bolivia, in: Tankard, A.J., Suárez, S., Welsink, H.J. (Eds.), Petroleum Basins of South America. American Association of Petroleum Geologist Memoir 62. pp. 523–543.

Echavarria, L., Hernández, R., Allmendinger, R., Reynolds, J., 2003. Subandean thrust and fold belt of northwestern Argentina: Geometry and timing of the Andean evolution. Am. Assoc. Pet. Geol. Bull. 87, 965–985. https://doi.org/10.1306/01200300196

Einsele, G., 2000. Sedimentary Basins, 2nd ed. Springer-Verlag Berlin Heidelberg, Berlin, Heidelberg. https://doi.org/10.1007/978-3-662-04029-4

Fedorchuk, N.D., Griffis, N.P., Isbell, J.L., Goso, C., Rosa, E.L.M., Montañez, I.P., Yin, Q.-Z., Huyskens, M.H., Sanborn, M.E., Mundil, R., Vesely, F.F., Iannuzzi, R., 2021. Provenance of late Paleozoic glacial/post-glacial deposits in the eastern Chaco-Paraná Basin, Uruguay and southernmost Paraná Basin, Brazil. J. South Am. Earth Sci. 106, 102989. https://doi.org/10.1016/j.jsames.2020.102989

Fernández Seveso, F., Vistalli, M.C., Viñes, R., 1998. The Silurian-Devonian Chaco Basin: A review for reservoir correlation in Argentina and Bolivia. Ext. Abstr. Vol. AAPG Int. Conf. Exhib. 452–453.

Fernández Seveso, F., Vistalli, M.C., Viñes, R.F., 2000. Correlación de reservorios en la cuenca silúrica-devónica del Chaco: Una revisión integrada previa a la adquisición de bloques exploratorios en Bolivia. Boletín Inf. Pet. Terc. Época XVII, 152–166.

Figueiredo, J., Hoorn, C., van der Ven, P., Soares, E., 2009. Late Miocene onset of the Amazon River and the Amazon deep-sea fan: Evidence from the Foz do Amazonas Basin. Geology 37, 619–622. https://doi.org/10.1130/G25567A.1

Fuentes, F., Rocha, E., Starck, D., 2018. Geometry and kinematics of structures of the southern sub-Andean fold-thrust belt of Bolivia. AAPG Mem. 117, 443–463.

https://doi.org/10.1306/13622130M1173775

Garzanti, E., 2019. Petrographic classification of sand and sandstone. Earth-Science Rev. 192, 545–563. https://doi.org/10.1016/j.earscirev.2018.12.014

Giampaoli, P., Rojas Vera, E., 2018. Fold Growth and Lateral Linkage in the Southern Sub-Andean Fold-and-Thrust Belt of Argentina and Bolivia, in: AAPG Memoir 117: Petroleum Basins and Hydrocarbon Potential of the Andes of Peru and Bolivia. AAPG Special Volumes.

Giles, K.A., Dickinson, W.R., 1995. The interplay of eustasy and lithospheric flexure in forming stratigraphic sequences in foreland settings: An example from the Antler foreland, Nevada and Utah.

Gioia, S.M.C.., Pimentel, M.., 2000. The Sm-Nd isotopic method in the geochronology laboratory of the University of Brasília. An. Acad. Bras. Cienc. 72, 219–245. https://doi.org/10.1590/S0001-37652000000200009

Gohrbandt, K.H.A., 1993. Paleozoic paleogeographic and depositional developments on the central proto-Pacific margin of Gondwana: Their importance to hydrocarbon accumulation. J. South Am. Earth Sci. 6, 267–287.

Goldstein, J.I., Newbury, D.E., Echlin, P., Joy, D.C., Romig, A.D., Lyman, C.E., Fiori, C., Lifshin, E., 1992. Electron-specimen interactions, in: Goldstein et al (Ed.), Scanning Electron Microscopy and X-Ray Microanalysis. Plenum Press, New York, pp. 69–147.

Goldstein, S.L., O'Nions, R.K., Hamilton, P.J., 1984. A Sm-Nd isotopic study of atmospheric dusts and particulates from major river systems. Earth Planet. Sci. Lett. 70, 221–236. https://doi.org/https://doi.org/10.1016/0012-821X(84)90007-4

Govindaraju, K., 1994. 1994 Compilatiom of working values and sample description for 383 geostandards. Geostand. Geoanalytical Res. 18, 1–158. https://doi.org/10.1046/j.1365-2494.1998.53202081.x-i1

Grahn, Y., 2003. Silurian and Devonian chitinozoan assemblages from the Chaco-Parana Basin, northeastern Argentina and central Uruguay. Rev. española Micropaleontol. 35, 1–8.

Gromet, L.P., Haskin, L.A., Korotev, R.L., Dymek, R.F., 1984. The "North American shale composite": Its compilation, major and trace element characteristics. Geochim. Cosmochim. Acta 48, 2469–2482. https://doi.org/10.1016/0016-7037(84)90298-9

Gulbranson, E.L., Montañez, I.P., Schmitz, M.D., Limarino, C.O., Isbell, J.L., Marenssi, S.A., Crowley, J.L., 2010. High-precision U-Pb calibration of Carboniferous glaciation and climate history, Paganzo Group, NW Argentina. Bull. Geol. Soc. Am. 122, 1480–1498. https://doi.org/10.1130/B30025.1

Haq, B.U., Schutter, S.R., 2008. A chronology of Paleozoic sea-level changes. Science (80-.). 322, 64–68.

Heredia, N., García-Sansegundo, J., Gallastegui, G., Farias, P., Giacosa, R., Hongn, F., Tubía, J.M., Alonso, J.J., Busquets, P., Charrier, R., Clariana, P., Colombo, F., Cuesta, A., Gallastegui, J., Giambiagi, L., González-Menéndez, L., Limarino, O., Martín-González, F., Pedreira, D., Quintana, L., Rodríguez-Fernández, L.R., Rubio-Ordóñez, Á., Seggiaro, R., Serra-Varela, S., Spalletti, L., Cardó, R., Ramos, V.A., 2018a. The Pre-Andean Phases of Construction of the Southern Andes Basement in Neoproterozoic–Paleozoic Times, in: Folguera, A., Contreras-Reyes, E., Heredia, N., Encinas, A., B. Iannelli, S., Oliveros, V., M. Dávila, F., Collo, G., Giambiagi, L., Maksymowicz, A., Iglesia Llanos, M.P., Turienzo, M., Naipauer, M., Orts, D., D. Litvak, V., Alvarez, O., Arriagada, C. (Eds.), The Evolution of the Chilean-Argentinean Andes. Springer International Publishing, Cham, pp. 111–131. https://doi.org/10.1007/978-3-319-67774-3_5

Heredia, N., García-Sansegundo, J., Gallastegui, G., Farias, P., Giacosa, R.E., Giambiagi, L.B., Busquets, P., Colombo, F., Charrier, R., Cuesta, A., Rubio-Ordóñez, Á., Ramos, V.A., 2018b. Review of the geodynamic evolution of the SW margin of Gondwana preserved in the Central Andes of Argentina and Chile (28°-38° S latitude). J. South Am. Earth Sci. 87, 87–94. https://doi.org/10.1016/j.jsames.2017.11.019

Hernández, R.M., Galli, C.I., Reynolds, J., Omarini, R., Viramonte, J., 1999. Estratigrafía del Terciario en el noroeste Argentino. Geol. del Noroeste Argentino Relat. XIV Congr. Geológico Argentino 1, 316–328.

Hernández, R.M., Jordan, T.E., Dalenz Farjat, A., Echavarría, L., Idleman, B.D., Reynolds, J.H., 2005. Age, distribution, tectonics, and eustatic controls of the Paranense and Caribbean marine transgressions in southern Bolivia and Argentina. J. South Am. Earth Sci. 19, 495–512. https://doi.org/10.1016/j.jsames.2005.06.007

Hulka, C., Gräfe, K.-U., Sames, B., Uba, C.E., Heubeck, C., 2006. Depositional setting of the Middle to Late Miocene Yecua Formation of the Chaco Foreland Basin, southern Bolivia. J. South Am. Earth Sci. 21, 135–150. https://doi.org/10.1016/j.jsames.2005.08.003

Hurtado, C., Roddaz, M., Santos, R.V., Baby, P., Antoine, P.-O., Dantas, E.L., 2018. Cretaceous-early Paleocene drainage shift of Amazonian rivers driven by Equatorial Atlantic Ocean opening and Andean uplift as deduced from the provenance of northern Peruvian sedimentary rocks (Huallaga basin). Gondwana Res. 63, 152–168.

Ingersoll, R. V, 2011. Tectonics of Sedimentary Basins, with Revised Nomenclature, in: Busby, C., Azor, A. (Eds.), Tectonics of Sedimentary Basins: Recent Advances. John Wiley & Sons, Ltd, Chichester, UK, pp. 1–43. https://doi.org/10.1002/9781444347166.ch1

Ingersoll, R. V, Bullard, T.F., Ford, R.L., Grimm, J.P., Pickle, S.W., 1984. The Effect of Grain Size on Detrital Modes: A Test of the Gazzi-Dickinson Point-Counting Method. SEPM J. Sediment. Res. 54, 103–116. https://doi.org/10.1306/212F83B9-2B24-11D7-8648000102C1865D

Isaacson, P.E., Diaz-Martinez, E., 1995. Evidence for a Middle-Late Paleozoic Foreland Basin and Significant Paleolatitudinal Shift, Central Andes. Pet. Basins South Am. https://doi.org/10.1306/M62593C10

Jackson, S.E., Pearson, N.J., Griffin, W.L., Belousova, E.A., 2004. The application of laser ablation-inductively coupled plasma-mass spectrometry to in situ U–Pb zircon geochronology. Chem. Geol. 211, 47–69. https://doi.org/10.1016/j.chemgeo.2004.06.017

Jaillard, E., Hérail, G., Monfret, T., Díaz-Martínez, E., Baby, P., Lavenu, A., Dumont, J.F., 2000. Tectonic evolution of the Andes of Ecuador, Peru, Bolivia and northernmost Chile. Tecton. Evol. South Am. 31, 481–559.

Jiménez, N., López-Velásquez, S., Santiváñez, R., 2009. Evolución tectonomagmática de los Andes Bolivianos. Rev. la Asoc. Geol. Argentina 65, 36–67.

Kley, J., 1996. Transition from basement-involved to thin-skinned thrusting in the Cordillera Oriental of southern Bolivia. Tectonics 15, 763–775. https://doi.org/10.1029/95TC03868

Kley, J., Gangui, A.H., Krüger, D., 1996. Basement-involved blind thrusting in the eastern Cordillera Oriental, southern Bolivia: evidence from cross-sectional balancing, gravimetric and magnetotelluric data. Tectonophysics 259, 171–184. https://doi.org/10.1016/0040-1951(95)00067-4

Kołtonik, K., Isaacson, P., Pisarzowska, A., Paszkowski, M., Augustsson, C., Szczerba, M., Slama, J., Budzyń, B., Stachacz, M., Krawczyński, W., 2019. Provenance of upper Paleozoic siliciclastics rocks from two high-latitude glacially influenced intervals in Bolivia. J. South Am. Earth Sci. 92, 12–31. https://doi.org/10.1016/j.jsames.2019.02.023

Leighton, M.W., Kolara, D.R., Oltz, D.F., Eidel, J.J., 1990. Interior cratonic basins.

Liew, T.C., Hofmann, A.W., 1988. Precambrian crustal components, plutonic associations, plate environment of the Hercynian Fold Belt of central Europe: Indications from a Nd and Sr isotopic study. Contrib. to Mineral. Petrol. 98, 129–138. https://doi.org/10.1007/BF00402106

Limarino, C.O., Spalletti, L.A., 2006. Paleogeography of the upper Paleozoic basins of southern South America : An overview. J. South Am. Earth Sci. 22, 134–155. https://doi.org/10.1016/j.jsames.2006.09.011

Linol, B., de Wit, M.J., Kasanzu, C.H., da Silva Schmitt, R., Corrêa-Martins, F.J., Assis, A., 2016. Correlation and paleogeographic reconstruction of the Cape-Karoo Basin sequences and their equivalents across central west Gondwana, in: Linol, B, de Wit, M. (Eds.), Origin and Evolution of the Cape Mountains and Karoo Basin. Springer, pp. 183–192.

Linol, B., de Wit, M.J., Milani, E.J., Guillocheau, F., Scherer, C., 2015. New regional correlations between the Congo, Paraná and Cape-Karoo basins of southwest Gondwana, in: Geology and Resource Potential of the Congo Basin. Springer, pp. 245–268.

Loewy, S.L., Connelly, J.N., Dalziel, I.W.D., 2004. An orphaned basement block: The Arequipa-Antofalla Basement of the central Andean margin of South America. Geol. Soc. Am. Bull. 116, 171. https://doi.org/10.1130/B25226.1

López de Luchi, M.G., Siegesmund, S., Wemmer, K., Nolte, N., 2017. Petrogenesis of the postcollisional Middle Devonian monzonitic to granitic magmatism of the Sierra de San Luis, Argentina. Lithos 288–289, 191–213. https://doi.org/10.1016/j.lithos.2017.05.018

Marsaglia, K.M., 1995. Interarc and backarc basins, in: Busby, C., Ingersoll, R. V (Eds.), Tectonics of Sedimentary Basins. Blackwell Science, Oxford, pp. 299–329.

McLennan, S.M., Hemming, S., McDaniel, D. K.Hanson, G., 1993. Geochemical approaches to sedimentation, provenance, and tectonics, in: Johnsson, M.J., Basu, A. (Eds.), Processes Controlling the Composition of Clastic Sediments. Geological Society of America, Boulder, Colorado, pp. 21–40.

Miall, A.D., 2000. Principles of Sedimentary Basin Analysis. Springer Berlin Heidelberg, Berlin, Heidelberg. https://doi.org/10.1007/978-3-662-03999-1

Milani, E.J., De Wit, M.J., 2008. Correlations between the classic Paraná and Cape–Karoo sequences of South America and southern Africa and their basin infills flanking the Gondwanides: du Toit revisited. Geol. Soc. London, Spec. Publ. 294, 319–342.

Milani, E.J., Ramos, V.A., 1998. Orogenias paleozóicas no domínio sul-ocidental do Gondwana e os ciclos de subsidência da Bacia do Paraná. Rev. Bras. Geociências 28, 473–484.

Moore, D.M., Reynolds, R.C., 1997. X-ray Diffraction and the Identification and Analysis of Clay Minerals. Oxford University Press, New York.

Morata, D., Castro de Machuca, B., Arancibia, G., Pontoriero, S., Fanning, C.M., 2010. Peraluminous Grenvillian TTG in the Sierra de Pie de Palo, Western Sierras Pampeanas, Argentina: Petrology, geochronology, geochemistry and petrogenetic implications. Precambrian Res. 177, 308–322. https://doi.org/10.1016/j.precamres.2010.01.001

Mukasa, S.B., Henry, D.J., 1990. The San Nicolás batholith of coastal Peru: early Palaeozoic continental arc or continental rift magmatism? J. Geol. Soc. London. 147, 27–39. https://doi.org/10.1144/gsjgs.147.1.0027

Nie, J., Horton, B.K., Saylor, J.E., Mora, A., Mange, M., Garzione, C.N., Basu, A., Moreno, C.J., Caballero, V., Parra, M., 2012. Integrated provenance analysis of a convergent retroarc

foreland system: U-Pb ages, heavy minerals, Nd isotopes, and sandstone compositions of the Middle Magdalena Valley basin, northern Andes, Colombia. Earth-Science Rev. 110, 111–126. https://doi.org/10.1016/j.earscirev.2011.11.002

Pankhurst, R.J., Rapela, C.W., 1998. The proto-Andean margin of Gondwana: an introduction. Geol. Soc. London, Spec. Publ. 142, 1–9.

Pankhurst, R.J., Rapela, C.W., Saavedra, J., Baldo, E., Dahlquist, J., Pascua, I., Fanning, C.M., 1998. The Famatinian magmatic arc in the central Sierras Pampeanas : an Early to Mid-Ordovician continental arc on the Gondwana margin. Early to Mid-Ordovician Cont. arc Gondwana margin 343–367.

Patchett, P.J., Roth, M.A., Canale, B.S., de Freitas, T.A., Harrison, J.C., Embry, A.F., Ross, G.M., 1999. Nd isotopes, geochemistry, and constraints on sources of sediments in the Franklinian mobile belt, Arctic Canada. Geol. Soc. Am. Bull. 111, 578–589. https://doi.org/10.1130/0016-7606(1999)111<0578:NIGACO>2.3.CO;2

Paton, C., Hellstrom, J., Paul, B., Woodhead, J., Hergt, J., 2011. Iolite: Freeware for the visualisation and processing of mass spectrometric data. J. Anal. At. Spectrom. 26, 2508. https://doi.org/10.1039/c1ja10172b

Petrus, J.A., Kamber, B.S., 2012. VizualAge: A Novel Approach to Laser Ablation ICP-MS U-Pb Geochronology Data Reduction. Geostand. Geoanalytical Res. 36, 247–270. https://doi.org/10.1111/j.1751-908X.2012.00158.x

Powers, M.C., 1953. A New Roundness Scale for Sedimentary Particles. J. Sediment. Res. 23, 117–119. https://doi.org/https://doi.org/10.1306/D4269567-2B26-11D7-8648000102C1865D

Price, R.A., 1973. Large-scale gravitational flow of supracrustal rocks, southern Canadian Rockies. Gravity and tectonics 491–502.

Ramos, V.A., 2018. Tectonic evolution of the Central Andes: from terrane accretion to crustal delamination, in: Zamora, G., McClay, K.M., Ramos, V.A. (Eds.), Petroleum Basins and Hydrocarbon Potential of the Andes of Perú and Bolivia. AAPG Memoir 117, pp. 1–34. https://doi.org/10.1306/13622115M1172855

Ramos, V.A., 2015. La orogenia famatiniana (Ordovícico medio a tardío) en el margen continental protoandino de América del Sur: nuevas evidencias y sus implicancias tectónicas, in: XIV Congreso Geológico Chileno. La Serena, pp. 106–109.

Ramos, V.A., 1988. Late Proterozoic - Early Paleozoic of South America - a Collisional History. Episodes 11, 168–174.

Ramos, V.A., 1986. El Diastrofismo Oclóyico: Un ejemplo de tectónica de colisión durante el Eopaleozoico en el Noroeste Argentino. Rev. del Inst. Geol. y Minería 6, 13–28.

Ramos, V.A., Aleman, A., 2000. Tectonic evolution of the Andes, in: Cordani, U.G., Milani, E.J., Filho, A.M., Campos, D.A. (Eds.), Tectonic Evolution of the Andes. Rio de Janeiro, pp. 636–685.

Ramos, V.A., Chemale, F., Naipauer, M., Pazos, P.J., 2014. A provenance study of the Paleozoic Ventania System (Argentina): Transient complex sources from Western and Eastern Gondwana. Gondwana Res. 26, 719–740. https://doi.org/10.1016/j.gr.2013.07.008

Rapela, C.W., Pankhurst, R.J., Casquet, C., Baldo, E., Saavedra, J., Galindo, C., Fanning, C.M., 1998. The Pampean Orogeny of the southern proto-Andes: Cambrian continental collision in the Sierras de Córdoba. Geol. Soc. London, Spec. Publ. 142, 181–217. https://doi.org/10.1144/gsl.sp.1998.142.01.10

Rapela, C.W., Pankhurst, R.J., Fanning, C.M., Grecco, L.E., 2003. Basement evolution of the Sierra de la Ventana Fold Belt: New evidence for Cambrian continental rifting along the southern margin of Gondwana. J. Geol. Soc. London. 160, 613–628. https://doi.org/10.1144/0016-764902-112

Reimann, C.R., Bahlburg, H., Carlotto, V., Boekhout, F., Berndt, J., Lopez, S., 2015. Journal of South American Earth Sciences Multi-method provenance model for early Paleozoic sedimentary basins of southern Peru and northern Bolivia (13 e 18 S). J. South Am. Earth Sci. 64, 94–115. https://doi.org/10.1016/j.jsames.2015.08.013

Reimann, C.R., Bahlburg, H., Kooijman, E., Berndt, J., Gerdes, A., Carlotto, V., López, S., 2010. Geodynamic evolution of the early Paleozoic Western Gondwana margin 14°–17°S reflected by the detritus of the Devonian and Ordovician basins of southern Peru and northern Bolivia. Gondwana Res. 18, 370–384. https://doi.org/10.1016/j.gr.2010.02.002

Rocha, E., 2013. Estilos estructurales del Subandino Sur de Bolivia. Universidad de Buenos Aires, Tese de Doutoramento, 204 p.

Roddaz, M., Viers, J., Brusset, S., Baby, P., Hérail, G., 2005. Sediment provenances and drainage evolution of the Neogene Amazonian foreland basin. Earth Planet. Sci. Lett. 239, 57–78. https://doi.org/10.1016/j.epsl.2005.08.007

Roddaz, M., Viers, J., Moreira-Turcq, P., Blondel, C., Sondag, F., Guyot, J.-L., Moreira, L., 2014. Evidence for the control of the geochemistry of Amazonian floodplain sediments by stratification of suspended sediments in the Amazon. Chem. Geol. 387, 101–110. https://doi.org/10.1016/j.chemgeo.2014.07.022

Rubatto, D., 2017. Zircon: the metamorphic mineral. Rev. Mineral. geochemistry 83, 261–295.

Sempere, T., 1995. Phanerozoic evolution of Bolivia and adjacent regions, in: Petroleum Basins of South America. American Association of Petroleum Geologist Memoir 62. pp. 207–230. https://doi.org/https://doi.org/10.1306/M62593C9

Sharman, G.R., Sharman, J.P., Sylvester, Z., 2018. detritalPy: A Python-based toolset for visualizing and analysing detrital geo-thermochronologic data. Depos. Rec. 4, 202–215. https://doi.org/10.1002/dep2.45

Sloss, L.L., 1988. Introduction, in: Sloss, L.L. (Ed.), Sedimentary Cover-North American Craton. Geological Society of America, Boulder, Colorado, pp. 1–3. https://doi.org/10.1130/DNAG-GNA-D2

Sloss, L.L., Speed, R.C., 1974. Relationships of Cratonic and Continental - Margin Tectonic episodes, in: Dickinson, W.R. (Ed.), Tectonics and Sedimentation, Volume 22. SEPM (Society for Sedimentary Geology), pp. 98–119. https://doi.org/10.2110/pec.74.22.0098

Starck, D., 1999. Los sistemas petroleros de la Cuenca de Tarija, in: IV Congreso de Exploración y Desarrollo de Hidrocarburos. Mar del Plata, pp. 63–82.

Starck, D., 1995. Silurian-Jurassic stratigraphy and basin evolution of northwestern Argentina, in: Tankard, A.J., Suárez, R., Welsink, H.J. (Eds.), Petroleum Basins of South America. American Association of Petroleum Geologists Memoir 62, pp. 251–267. https://doi.org/https://doi.org/10.1306/M62593C11

Starck, D., Del Papa, C., 2006. The northwestern Argentina Tarija Basin: Stratigraphy, depositional systems, and controlling factors in a glaciated basin. J. South Am. Earth Sci. 22, 169–184. https://doi.org/10.1016/j.jsames.2006.09.013

Starck, D., Gallardo, E., Schulz, A., 1993. The pre-Carboniferous unconformity in the Argentine portion of the Tarija Basin, in: International Congress of Carboniferous-Permian. pp. 373–384.

Starck, D., Gallardo, E., Schulz, A., 1992. La cuenca de Tarija: Estratigrafía de la porción Argentina. Boletín Inf. Pet. 30, 2–14.

Starck, D., Rodríguez, A., Constantini, L., 2002. Las rocas reservorio Carbónicas de la Cuenca de Tarija (Cuenca de Tarija "Sensu Stricto"), in: Schiuma, M., Hinterwimmer, G., Vergani, G. (Eds.), Rocas Reservorio de Las Cuencas Productivas de La Argentina. Instituto Argentino del Petróleo y Gas, Buenos Aires, pp. 699–716.

Suárez Soruco, R., Díaz Martínez, E., 1996. Léxico estratigráfico de Bolivia. Rev. Ténica Yacimientos Pet. Fisc. Boliv. 17, 227.

Taylor, B., Karner, G.D., 1983. On the evolution of marginal basins. Rev. Geophys. 21, 1727. https://doi.org/10.1029/RG021i008p01727

Torsvik, T.H., Cocks, L.R.M., 2013. Gondwana from top to base in space and time. Gondwana Res. 24, 999–1030. https://doi.org/10.1016/j.gr.2013.06.012

Troth, I., Marshall, J.E.A., Racey, A., Becker, R.T., 2011. Devonian sea-level change in Bolivia: A high palaeolatitude biostratigraphical calibration of the global sea-level curve. Palaeogeogr. Palaeoclimatol. Palaeoecol. 304, 3–20. https://doi.org/10.1016/j.palaeo.2010.10.008

Uba, C.E., Hasler, C.-A., Buatois, L.A., Schmitt, A.K., Plessen, B., 2009a. Isotopic, paleontologic, and ichnologic evidence for late Miocene pulses of marine incursions in the central Andes. Geology 37, 827–830. https://doi.org/10.1130/G30014A.1

Uba, C.E., Heubeck, C., Hulka, C., 2006. Evolution of the late Cenozoic Chaco foreland basin, Southern Bolivia. Basin Res. 18, 145–170. https://doi.org/10.1111/j.1365-2117.2006.00291.x

Uba, C.E., Heubeck, C., Hulka, C., 2005. Facies analysis and basin architecture of the Neogene Subandean synorogenic wedge, southern Bolivia. Sediment. Geol. 180, 91–123. https://doi.org/10.1016/j.sedgeo.2005.06.013

Uba, C.E., Kley, J., Strecker, M.R., Schmitt, A.K., 2009b. Unsteady evolution of the Bolivian Subandean thrust belt: The role of enhanced erosion and clastic wedge progradation. Earth Planet. Sci. Lett. 281, 134–146. https://doi.org/10.1016/j.epsl.2009.02.010

Uriz, N.J., Cingolani, C.A., Basei, M.A.S., Blanco, G., Abre, P., Portillo, N.S., Siccardi, A., 2016. Provenance and paleogeography of the Devonian Durazno Group, southern Paraná Basin in Uruguay. J. South Am. Earth Sci. 66, 248–267.

Valdez, V., Pablo, J., Sergio, P., Paim, G., Paulo, R., Danielski, C., Cagliari, J., Chemale, F., Kneller, B., 2020. Timing of the Late Palaeozoic glaciation in western Gondwana : New ages and correlations from Paganzo and Paraná basins. Palaeogeogr. Palaeoclimatol. Palaeoecol. 544, 23. https://doi.org/10.1016/j.palaeo.2020.109624

Van der Lelij, R., Spikings, R., Ulianov, A., Chiaradia, M., Mora, A., 2016. Palaeozoic to Early Jurassic history of the northwestern corner of Gondwana, and implications for the evolution of the Iapetus, Rheic and Pacific Oceans. Gondwana Res. 31, 271–294. https://doi.org/10.1016/j.gr.2015.01.011

Varela, R., Sato, A.M., Basei, M.A.S., Siga Jr, O., 2003. Proterozoico medio y Paleozoico inferior de la sierra de Umango, antepaís andino (29 S), Argentina: edades U-Pb y caracterizaciones isotópicas. Rev. geológica Chile 30, 265–284.

Vargas, M., Santos, A., Bressane, A., Francisco, R.S., Faccion, J.E., Paim, P.S., 2020. The Devonian of the Paraná Basin, Brazil: Sequence stratigraphy, paleogeography, and SW Gondwana interregional correlations. Sediment. Geol. 408, 14. https://doi.org/10.1016/j.sedgeo.2020.105768

Vaughan, A.P.M., Leat, P.T., Pankhurst, R.J., 2005. Terrane processes at the margins of Gondwana: introduction. Geol. Soc. London, Spec. Publ. 246, 1–21.

Viers, J., Roddaz, M., Filizola, N., Guyot, J.-L., Sondag, F., Brunet, P., Zouiten, C., Boucayrand, C., Martin, F., Boaventura, G.R., 2008. Seasonal and provenance controls on Nd–Sr isotopic compositions of Amazon rivers suspended sediments and implications for Nd and Sr fluxes exported to the Atlantic Ocean. Earth Planet. Sci. Lett. 274, 511–523. https://doi.org/10.1016/j.epsl.2008.08.011

Vistalli, M.C., 1990. La Cuenca Siluro Devónica del Noroeste. En: G. Chebli & LA Spalletti. Ser. Correlación Geológica Nº 6 Cuencas Sedimentarias Argentinas 19–41.

Wiedenbeck, M., Allé, P., Corfu, F., Griffin, W.L., Meier, M., Oberli, F., Quadt, A. Von, Roddick, J.., Spiegel, W., 1995. Three natural zircon standards for U-Th-Pb, Lu-Hf, trace element and REE analyses. Geostand. Geoanalytical Res. 19, 1–23. https://doi.org/10.1111/j.1751-908X.1995.tb00147.x

Xie, X., Heller, P.L., 2009. Plate tectonics and basin subsidence history. Geol. Soc. Am. Bull. 121, 55–64.

Yakymchuk, C., Kirkland, C.L., Clark, C., 2018. Th/U ratios in metamorphic zircon. J. Metamorph. Geol. 36, 715–737. https://doi.org/10.1111/jmg.12307

Zalán, P.V., Wolff, S., Astolfi, M.A.M., Vieira, I.S., Concelcao, J.C.J., Appi, V.T., Neto, E.V.S., Cerqueira, J.R., Marques, A., 1990. The Parana Basin, Brazil, in: Leighton, M.W., Kolata, D.R., Oltz, D.F., Fidel, J.J. (Eds.), Interior Cratonic Basins. American Association of Petroleum Geologists Memoir 51, pp. 681–708.